Fluid-Structure Interaction in the Cardiovascular System. Numerical Analysis and Simulation

Matteo Astorino

Interaction Fluide-Structure dans le Système Cardiovasculaire. Analyse Numérique et Simulation

THÈSE DE DOCTORAT

Présentée par

Matteo Astorino

pour obtenir le grade de

DOCTEUR DE
L' UNIVERSITÉ PIERRE ET MARIE CURIE - Paris VI

Spécialité : Mathématiques Appliquées

Soutenue publiquement le 13 Avril 2010 devant le jury composé de :

Jean-Frédéric Gerbeau	Directeur de thèse
Céline Grandmont	Directeur de thèse
Bruno Koobus	Rapporteur
Georges-Henri Cottet	President du jury
Jean-Marie Le Gouez	Examinateur
Frédéric Hecht	Examinateur
Yvon Maday	Invité

Après avis favorables des rapporteurs : Sunčica Čanić et Bruno Koobus.

Thèse préparée au sein de l'équipe-projet REO
Centre de Recherche INRIA Paris-Rocquencourt
Domaine de Voluceau, BP 105
78153 Le Chesnay CEDEX

Remerciements

Nissuna umana investigazione si pò dimandare vera scienzia,
s'essa non passa per le matematiche dimostrazioni.
Leonardo da Vinci

Je tiens en premier lieu à remercier mes directeurs de thèse, Jean-Frédéric Gerbeau et Celine Grandmont, pour m'avoir donné la possibilité de travailler au sein du projet REO sur un sujet très interessant comme l'interaction fluide-structure. Jour après jour, leur expérience et leurs conseils m'ont permis d'apprendre et de travailler sur différents aspects de ce fascinant problème mathématique. Leurs enseignements seront toujours un exemple à suivre dans ma vie professionnelle et personnelle.
Avec Jean-Frédéric j'ai fait mes premiers pas dans le monde de la recherche, pour cette raison je le remercie ici d'avoir été un guide et une source d'inspiration dans mon travail, mais aussi pour avoir toujours trouvé un moment pour m'écouter et me conseiller. La passion et l'énergie de Celine m'ont toujours transporté et ses encouragements m'ont aidé à surpasser beaucoup de difficultés. Sa disponibilité et patience à m'expliquer les secrets de l'analyse numerique ont été precieuses.
Merci aussi à Franz Chouly, Miguel Fernández, Olivier Pantz, Shawn Shadden, Karim Traoré et Irene Vignon-Clementel, avec lesquelles j'ai eu la chance de collaborer durant ces trois années.
Je remercie très sincèrement les professeurs Sunčica Čanić et Bruno Koobus, pour avoir pris le temps de rapporter cette thèse, ainsi que Georges-Henri Cottet, Jean-Marie Le Gouez et Frédéric Hecht et Yvon Maday pour avoir accepté de faire partie de mon jury.
Je tiens également à remercier les chercheurs, les post-docs, les doctorants et les ingénieurs des équipes REO, BANG, GAMMA et MACS qui ont contribué de manière unique à l'atmosphère scientifique et humaine du batiment 16 de l'INRIA Paris-Rocquencourt. Un remerciement particulier à Miguel, pour ses conseils, pour tous les retours vers Paris faits ensemble en bus B ou en voiture, mais surtout pour son amitié.
J'exprime aussi ma gratitude à l'équipe MACS pour les codes structure et à l'équipe GAMMA pour les mailleurs. Un remerciement particulier à Marina et Philippe pour avoir toujours répondu prontement à mes questions sur l'utilisation de leurs codes. Un double merci à Marina - my best coffee-dealer - pour n'avoir jamais été à court de café Lavazza, élément essentiel pour la vie d'un Italien à l'étranger.
Je n'oublie pas mes "co-bureautiers" - Antoine, Nuno, Nejib, Geraldine, Cristobal (Franco scorpion) et Anne-Claire - avec lesquels j'ai souvent partagé les petits succèss ainsi que les difficultés. Merci aussi à Adrien, Alfonso (Franco sportif), Annabelle (Gina), Asven, Ayman, Filippo, Joaquin, Julien, Nick, Radomir, Thomas, William et tous les autres de la pause café. Les meilleurs moments à Paris, je l'ai vécus avec eux et pour cela je leur suis reconnaissainte. Mais pour moi Paris ca veut dire aussi la Cité Universitaire, merci alors à toutes les personnes que j'ai rencontré et qui m'ont fait me sentir citoyen du monde.
Et maintenant les derniers remerciements dans ma langue maternelle. Un ringraziamento va agli "amici di sempre" Davide, Luca, Marco e Roberta. Pur essendo spesso lontani, ho sempre saputo di poter contare su di loro...e anche stavolta me lo hanno dimostrato. Il ringraziamento piú grande lo rivolgo alla mia famiglia e a Maike per l'affetto e il sostegno che non mi hanno mai fatto mancare. A loro dedico la mia tesi di dottorato.

Interaction Fluide-Structure dans le Système Cardiovasculaire. Analyse Numérique et Simulation

Resumé: Dans cette thèse, nous proposons et analysons des méthodes numériques partitionnées pour la simulation de phénomènes d'interaction fluide-structure (IFS) dans le système cardiovasculaire. Nous considérons en particulier l'interaction mécanique du sang avec la paroi des grosses artères, avec des valves cardiaques et avec le myocarde.

Dans les algorithmes IFS partitionnés, le couplage entre le fluide et la structure peut être imposé de manière implicite, semi-implicite ou explicite. Dans la première partie de cette thèse, nous faisons l'analyse de convergence d'un algorithme de projection semi-implicite. Puis, nous proposons une nouvelle version de ce schéma qui possède de meilleures propriétés de stabilité. La modification repose sur un couplage Robin-Robin résultant d'une ré-interprétation de la formulation de Nitsche.

Dans la seconde partie, nous nous intéressons à la simulation de valves cardiaques. Nous proposons une stratégie partionnée permettant la prise en compte du contact entre plusieurs structures immergées dans un fluide. Nous explorons également l'utilisation d'une technique de post-traitement récente, basée sur la notion de structures Lagrangiennes cohérentes, pour analyser qualitativement l'hémodynamique complexe en aval des valves aortiques.

Dans la dernière partie, nous proposons un modèle original de valves cardiaques. Ce modèle simplifié offre un compromis entre les approches "0D" classiques et les simulations complexes d'interaction fluide-structure 3D. Diverses simulations numériques sont présentées pour illustrer l'efficacité et la robustesse de ce modèle, qui permet d'envisager des simulations réalistes de l'hémodynamique cardiaque, à un coût de calcul modéré.

Mots-clés: Interaction fluide-structure, couplage semi-implicite, schéma de projection de Chorin-Temam, méthode de Nitsche, contact, valves cardiaques, structures Lagrangiennes cohérentes, surfaces résistives immergées, ventricule gauche.

Fluid-Structure Interaction in the Cardiovascular System. Numerical Analysis and Simulation

Abstract: In this thesis we focus on the numerical analysis and the development of efficient partitioned algorithms for fluid-structure interaction (FSI) problems arising in hemodynamics. In particular we consider the mechanical interaction of the blood with the large arteries, with the cardiac valves and with the myocardium.

In partitioned FSI procedures the coupling between the fluid and the structure can be enforced in different ways: implicit, semi-implicit or explicit. In the first part of this thesis, the convergence properties of a projection semi-implicit coupling scheme are investigated from the theoretical and numerical viewpoints. Then, for the same scheme, we propose a modification that aims at improving its stability properties. This modification relies on the reinterpretation of the Nitsche's interface coupling as a particular Robin-Robin coupling.

In the second part fluid-structure interaction problems with cardiac valves are addressed. For these problems we devise a modular partitioned strategy for the numerical simulation of 3D FSI problems where contact among multiple elastic solids can occur. For the analysis of the computational results, we also investigate the use of an advanced post-processing technique based on the notion of Lagrangian coherent structures.

Finally, in the last part, a new reduced model for cardiac valves simulations is presented. This new model offers a compromise between standard lumped parameter models and fully 3D FSI problems. Various numerical experiments are presented to validate its efficiency and robustness. With this model, numerical simulations of the cardiac hemodynamics can be performed with a reduced computational cost.

Keywords: Fluid-structure interaction, semi-implicit coupling, Chorin-Temam projection scheme, Nitsche's method, contact, cardiac valves, Lagrangian coherent structures, resistive immersed surfaces, left ventricle.

Contents

Fluid-structure interaction in the cardiovascular system

Chapter 1

Introduction

Contents

The cardiovascular system has a very complex structure typically characterized by multiple physical scales both in space and in time. In space, the vascular geometry varies from micrometers (*e.g.* the capillary wall and blood cell size) to centimeters (*e.g.* the vessel length). In time, the physiological activities range from milliseconds, for the fast chemical processes, to days, for remodeling phenomena.

The aim of this work is the mathematical and numerical investigation of some of the fluid-structure interaction (FSI) problems arising in hemodynamics. More precisely, we are interested in FSI problems characterized by a macroscopic space scale (*i.e.* order of centimeters), and with time scales comparable to that of the cardiac cycle (*i.e.* approximatively seconds).

In this chapter, we introduce the general framework of the thesis. In Section 1.1, notions on the cardiovascular system are given, in order to provide the reader with the essential medical vocabulary that we shall make use of in the following. For a more comprehensive presentation we refer to [Thi08a, Thi08b]. Note that, in all the physiological and pathological phenomena we will describe, a fluid - the blood - interacts with one or multiple structures (*e.g.* vessels, cardiac valves and heart wall). In Section 1.2, we give an overview of the recent achievements made in the simulations of cardiovascular FSI problems. Three different groups of cardiovascular applications are considered: blood - vessel wall interaction, blood - cardiac valves interaction and blood - myocardium interaction. This introductory chapter ends with the outline of the thesis and its main contributions, Section 1.3.

1.1 The cardiovascular system

Elements of cardiovascular anatomy. The heart is made of muscular tissue, *the myocardium*, characterized by specialized muscle cells, the *cardiomyocytes*, which have a high resistance to fatigue. It has four cavities: two atria, right (RA) and left (LA), and two ventricles, right (RV) and left (LV). A longitudinal cross-section of the heart with the corresponding cavities is represented in Figure 1.1. The two atria, RA and LA, respectively collect the blood from the body and from the lungs. Whereas the two ventricles, RV and LV, respectively pumps the blood to the lungs and to the body. Both ventricles receive the blood from the corresponding atria (*i.e.* LV from LA and RV from RA).

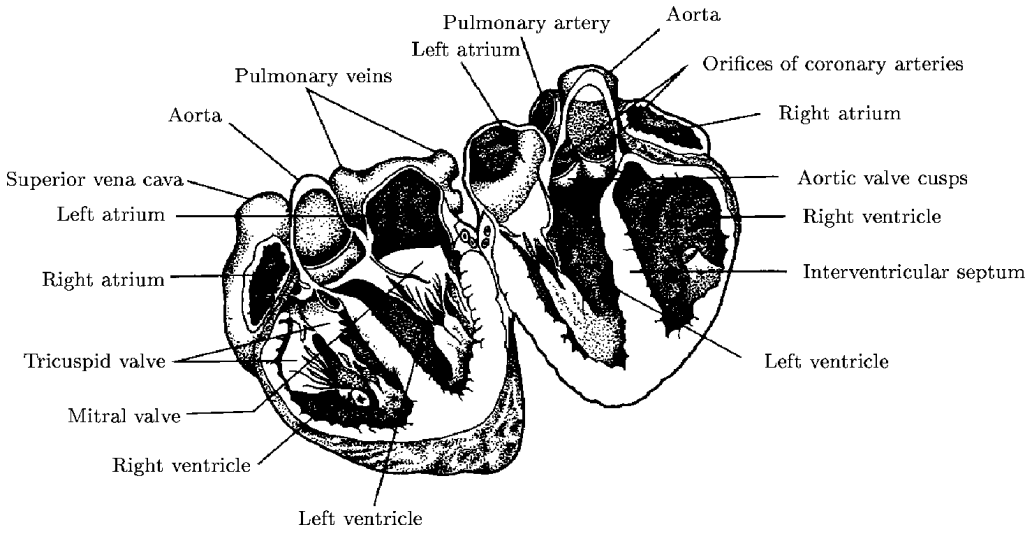

Figure 1.1: Longitudinal cross-section of the heart. From [NH00].

The ensemble of the LV and LA (resp. RV and RA) defines the so-called *left heart* (resp. *right heart*). The left heart (LH) releases highly pressurized blood, approximatively at 100 mmHg, through the *systemic circulation*. The right heart (RH) propels the blood through the *pulmonary circulation* and it is characterized by a lower pressure than the systemic circulation. A schematic representation of the system is given in Figure 1.2. In this work, we mainly focus on the systemic circulation, and in particular in the LV and the aorta.

At the exit of each heart cavity, a valve prevents the backflow of the blood into the corresponding cavity. There are four valves: the *mitral valve* and the *aortic valve* for the LH, the *tricuspid valve* and the *pulmonary valve* for the RH. In the LH, the mitral valve prevents the backflow of the blood from the LV to the LA. This valve is made of two leaflets, that are attached to the inner side of the LV through the *chordae tendinae* - biological attachments that prevent the mitral valve prolapse during its closure. The aortic valve separates the LV from the aorta - the major systemic artery. It is made of three leaflets respectively fixed to three

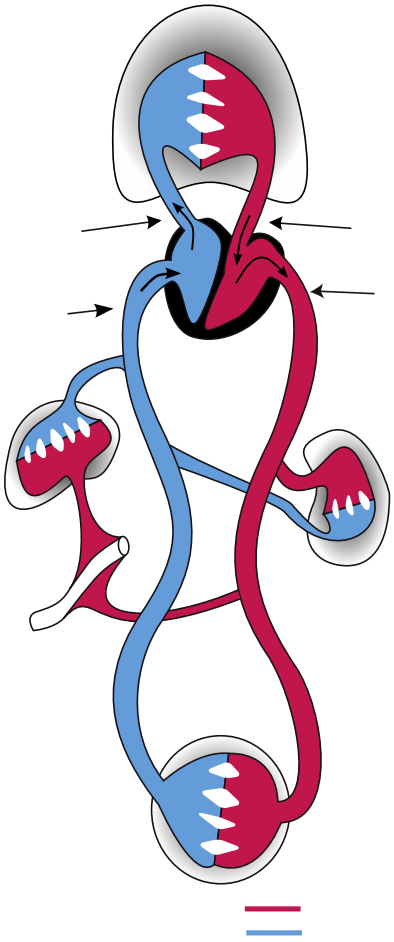

Figure 1.2: The cardiovascular system. Adapted from [Moi08].

hemispherical bulges of the aortic root, the so-called *sinuses of Valsalva*. From two of the sinuses originate the coronary arteries, which are responsible for the perfusion of the heart (see Figure 1.3). Differently from the mitral valve, the aortic valve has no attachments and the leaflets provide a mutual support when the valve is closed. In the RH, the tricuspid and the pulmonary valves have respectively the same role as the mitral and the aortic valves in the LH. As a matter of fact, the tricuspid valve regulates the blood flow between the RA and the RV, while the pulmonary valve controls the flow between the RV and the main pulmonary artery.

The cardiac cycle. The cardiac dynamics is set by an electrical signal generated because of the flow of ions, principally sodium, potassium and calcium, across the cell membrane of the heart wall. The electrical current spreads first across the atria, leading to the contraction of the atrial muscle. Then, it continues to the ventricles, entailing the contraction of the ventricular myocardium and the corresponding ejection of blood into the systemic and pulmonary circulations.

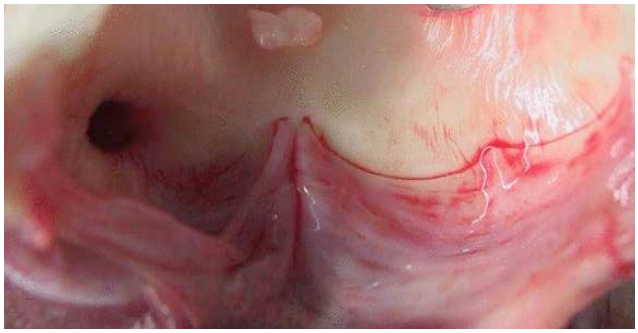

Figure 1.3: Valsalva sinuses of the aortic root with view on the coronary ostium. Two of the leaflets of the aortic valve are visible. From [Thi08b].

In normal conditions, the cardiac cycle runs less than one second (approximatively 70 heart beats per minute) and can be mainly decomposed in two subsequent phases, each one divided in two more sub-phases. Let us briefly describe them with respect to the LH.

At the beginning of the first phase - the *ventricular systole* - the aortic valve is closed and the ventricle is filled with blood, which came from the atrium. This phase starts with the contraction of the ventricle and the corresponding closure of the mitral valve. During the ventricular systole two sub-phases can be distinguished:

I. the *isovolumic contraction*, that is characterized by a rapid increase of the ventricular pressure. In this phase the mitral and aortic valves are closed.

II. the *systolic ejection*, which begins when the pressure in the ventricle reaches the one of the aorta. With a further increase of pressure, the aortic valve opens and the blood flows from the ventricle to the vessel network.

Notice also that during the ventricular systole, the atrium is refilled with blood coming from the vessel network. The second phase - the *ventricular diastole* - starts at the end of the systole. The ventricle contraction ends and a negative pressure gradient induces a modification of the flow conditions which causes the closure of the aortic valve. Like for the systole, also in the diastole we have two sub-phases:

III. the *isovolumic relaxation*, that starts at the closure of the aortic valve. Here, the LV valves remain closed until the pressure of the ventricle is bounded by the ones of the artery and atrium. During this period, the ventricle relaxes and its pressure smoothly reduces.

IV. the *ventricular filling*, which begins when the ventricular pressure is lower than the one of the atrium. In this phase, the blood flows from the atrium to the ventricle.

In Figure 1.4, the different phases are represented together with the main cardiac indices related to the LH. Clearly a similar cycle acts symmetrically also for the RH.

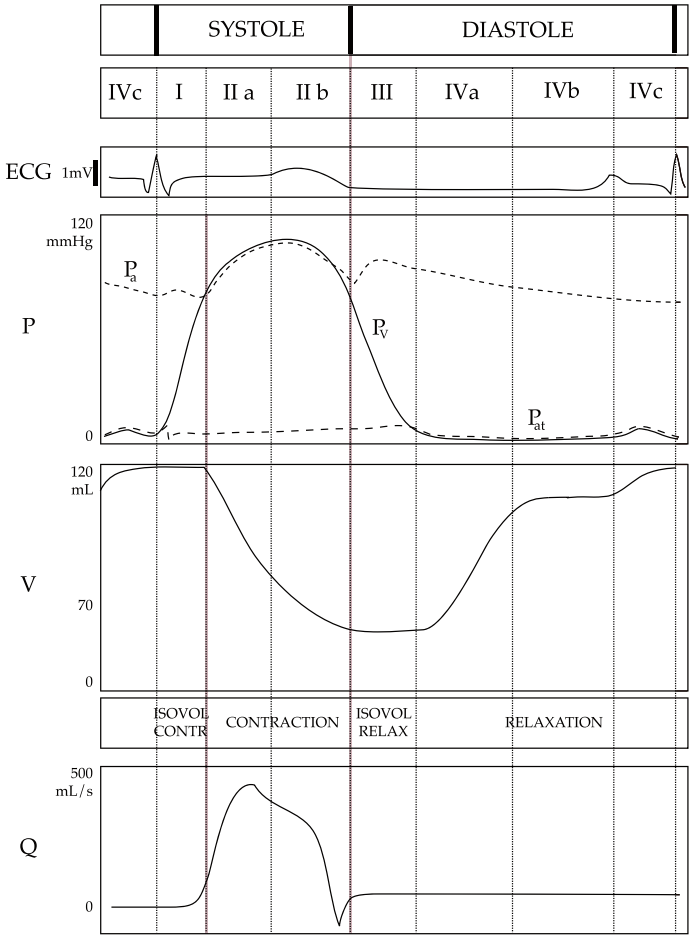

Figure 1.4: Main cardiac phases and behavior of the different cardiac indices: electrocardiogram (ECG), pressure (P), volume (V), aortic flow (Q). The pressures P_a, P_V and P_{at} represent respectively the aortic, the LV and the LA pressures. Adapted from [Moi08].

Cardiovascular pathologies. There are many different cardiovascular abnormalities and diseases, which can have varying effects, ranging from benign conditions to death. Here we mention only some of them. We refer to [LBMZ08] for a complete review.

Common examples of vessel diseases are the *arteriosclerosis* and the *aneurysms*. Arteriolosclerosis refers in general to a stiffening (loss of elasticity) of the vessel wall. It typically affects the small arteries and arterioles and it is often associated with hypertension. The aneurysm is a localized, blood-filled dilatation of the vessel wall. Aneurysms most commonly occur in arteries at the base of the brain (*the circle of Willis*) and in the aorta. The rupture of an aneurysm results in hemorrhage, that could lead to death in the worst cases. In Chapter 4, a numerical simulation of an idealized abdominal aortic aneurysm (AAA) is presented.

Stroke, ischemia, coronary artery disease, valvular disease and arrhythmia are among the most common causes of heart failure. Focusing on valves, *valvular regurgitation* and *stenosis* are considered main pathologies. Valvular regurgitation is a condition in which the malfunction of one (or more) of the leaflets provokes an improper closure of the valve and leads to blood leaking. The nature and severity of the leakage may prevent a correct functioning of the heart.

The stenosis is an abnormal narrowing of the valve opening, which can result from various causes such as calcification, congenital or rheumatic diseases. Once this condition develops, high pressure builds up in the left ventricle and can seriously injure the heart. In Chapter 6, the techniques available for the estimation of its severity are presented and new directions based on advanced computational techniques are introduced.

1.2 Numerical simulation of fluid-structure interaction problems arising in hemodynamics: state-of-the-art

In this section the recent achievements in fluid-structure interaction are briefly presented from the application viewpoint. Three different applications are considered:

Blood - vessel interaction. The simulation of blood flows in compliant large vessels is a very active research topic. The development of advanced numerical methods, together with the modern three-dimensional imaging techniques and the increase of computational resources, has led to the achievement of very important results. In particular, it is now possible to easily construct and simulate patient-specific geometric models starting from medical imaging data. The works [GVF05, TOK+08, BGH+09, TF09] are representative of the different numerical techniques employed in the computation of blood flows in arteries for physiological and pathological conditions. Other works focus on the interaction between the blood and implanted medical devices (*e.g.* stents [CRCK+05, DZ07, FGM08]).

Among the most common computational techniques for the simulation of blood flows in compliant vessels, we recall the *arbitrary Lagrangian-Eulerian* (ALE) approach (see *e.g.* [FQV09] and references therein), the coupled momentum method [FVCJ+06], the *space-time* (DSD/ST) approach [TS07], and the *isogeometric analysis* [BCZH06]. Referring in particular to the ALE approach, different solution schemes have been developed to address these FSI problems, each one with its costs and benefits. These schemes can be divided in two groups: *monolithic* and *partitioned* procedures. In a monolithic approach, the equations governing the flow and the structure are solved simultaneously, with a single solver. In a partitioned approach, distinct solvers are used for the fluid and the structure. A comparison between these two procedures, for some of the coupling schemes used in biomedical FSI problems, is presented in [KGF+09]. In this thesis we mainly focus on partitioned methods and an overview of the most recent advances in this field is given in

Section 2.5.3.

Blood - cardiac valves interaction. Despite the important progresses realized in the last decades in the simulations of the interaction between the blood and cardiac valves, this type of FSI problems still remains very challenging. On the one hand, the mechanical properties of the valves are very complex (see Section 2.2.2, p. 27). On the other hand, the development of robust, reliable and efficient computational methods is difficult.

For this type of interaction, only a few computational procedures are based on the ALE approach [CBHP06, MÖ9, SB09]. As a matter of fact, the large structural displacements of the valve imply important deformations of the fluid mesh and frequent remeshing can be required. Moreover, at the closure of the valve, the change of topology makes the definition of the ALE formulation difficult.

For this reason, other approaches, such as the Immersed Boundary method [MPY82, Pes02] or the Fictitious Domain method [GPP94, Baa01], are usually preferred. In such methods the fluid domain is generally discretized in a fixed computational grid, while the structure domain is discretized in a separate grid. Fluid and structure meshes are therefore totally independent. The two methods, similar in the underling idea, differ for the chosen mathematical formulation.

The Immersed Boundary (IB) method has been proposed in order to investigate the blood flow into the heart and through heart valves [MPY82, Pes02, GHMP07]. The immersed solid is accounted for in the surrounding fluid by adding body forces to the governing fluid equations. Body forces are distributed on all nodes of the fluid mesh *via* a discrete Dirac measure that has the effect to smear, or diffuse, the solid boundary over several fluid nodes in the vicinity of the interface. Applications of the IB method are reported for instance in [MP01, VCMP08, WLY+08].

The Fictitious Domain (FD) method gets rid of the discrete Dirac measures in the FSI coupling, by using a variational approach in which the continuity of the displacements between fluid and structure is enforced through Lagrange multipliers. This method has been much investigated in [GPP94, GPHJ99, GPH+01]. In fluid-structure interaction problems, the FD method was originally used for rigid particles and has been extended later to flexible structures, either using Lagrange multiplier located on the structure surface [Baa01, dHPSB03, vLADB04, vLAvdV06, dSGB08] or on the structure volume [Yu05]. Among others, we remark the computational methods proposed in [vLAvdV06, dSGB08] that take into account, within the FD method, the *contact* between a valve and a rigid wall and the *chordae tendinae*. Moreover in [dSGB08] the use of partitioned procedures has been introduced.

Blood - heart wall interaction. The fluid-structure interaction in the heart is a very challenging problem. To the best of our knowledge, only Peskin's research group performed numerical simulations of the fluid-structure in the heart (LV and RV) with flexible valves. Among their pioneering works, based on the IB method, we recall for example [MP00, KMP01]. More recently other research groups have considered

the fluid-structure interaction in the heart. Important results have been achieved in [WHS+02, WSKH04] where multiphysics simulations of the left ventricle (electro-fluid-mechanical coupling) have been performed. In these works, the influence of valves has been simulated using lumped parameter models.

Considering only the fluid-dynamics of the heart, *i.e.* the wall displacements are imposed, interesting results concerning the characterization of the vorticity in the LV are given in [DPB05, NWY06].

1.3 Thesis outline and main contributions

Funding. This PhD thesis has been funded by the CardioSense3D project. CardioSense3D is a 4-year Large Initiative Action launched in 2005 and funded by the French national research center INRIA which focuses on the electro-mechanical modeling of the heart. This Action groups four INRIA research teams: ASCLEPIOS, MACS, REO and SISYPHE. The first team is located in Sophia-Antipolis while the other teams are located in Paris-Rocquencourt. ASCLEPIOS team focuses on cardiac image analysis, MACS on bio-solid simulation and estimation, REO on bio-fluid and electrophysiology simulation, and SISYPHE on cardiac control and modeling. In the Cardiosense3D project, three main research topics are considered:

Multiphysics coupling. The aim is to integrate four physiological phenomena: electrophysiology, cardiac mechanics, arterial and ventricular flow, and perfusion.

Patient-specific modeling based on identifiable parameters. The aim is the creation of a patient-specific heart model based on the estimate of its characteristic parameters from clinically available data (images and signals).

Therapy planning applications. The aim is the development of applications for the solution of clinical and industrial problems.

This Action involves also multiple clinical, industrial and academic partners (see `http://www-sop.inria.fr/CardioSense3D/` for further details).

The results presented in this thesis take part to the development of the first topic - the multiphysics coupling. In this work we focus on the numerical analysis and simulation of fluid-structure interaction problems arising in hemodynamics. The main contributions of this thesis are reported in Chapters 3, 4, 5, 6 and 7 and are summarized here below.

The coupled FSI problem. From a general viewpoint, the fluid-structure problem that we consider throughout this thesis, reads:
Find the fluid velocity $\mathbf{u} : \Omega^{\mathrm{f}} \times \mathbb{R}^+ \to \mathbb{R}^d$, the pressure $p : \Omega^{\mathrm{f}} \times \mathbb{R}^+ \to \mathbb{R}$, the solid displacement $\hat{\boldsymbol{d}} : \hat{\Omega}^{\mathrm{s}} \times \mathbb{R}^+ \to \mathbb{R}^d$ and the solid velocity $\hat{\mathbf{u}}^{\mathrm{s}} : \hat{\Omega}^{\mathrm{s}} \times \mathbb{R}^+ \to \mathbb{R}^d$ such that

- Fluid sub-problem (Navier-Stokes equations):

$$\begin{cases} \rho^{\mathrm{f}} \dfrac{\partial \mathbf{u}}{\partial t}\Big|_{\mathcal{A}} + \rho^{\mathrm{f}}(\mathbf{u}-\mathbf{w})\cdot\nabla\mathbf{u} - \operatorname{div}\boldsymbol{\sigma}^{\mathrm{f}}(\mathbf{u},p) = \mathbf{0}, \quad \text{in} \quad \Omega^{\mathrm{f}}(t), \\ \qquad\qquad \operatorname{div}\mathbf{u} = 0, \quad \text{in} \quad \Omega^{\mathrm{f}}(t), \end{cases} \tag{1.1}$$

- Solid sub-problem (*e.g.* Elastodynamic equations):

$$\begin{cases} \rho_0^{\mathrm{s}}\partial_t\hat{\mathbf{u}}^{\mathrm{s}} - \operatorname{div}_{\hat{\mathbf{x}}}\hat{\boldsymbol{\Pi}}(\hat{\boldsymbol{d}}) = \mathbf{0}, \quad \text{in} \quad \hat{\Omega}^{\mathrm{s}}, \\ \qquad\qquad \hat{\mathbf{u}}^{\mathrm{s}} = \partial_t\hat{\boldsymbol{d}}, \quad \text{in} \quad \hat{\Omega}^{\mathrm{s}}, \end{cases} \tag{1.2}$$

- Coupling conditions:

$$\begin{cases} \hat{\boldsymbol{d}}^{\mathrm{f}} = \operatorname{Ext}(\hat{\boldsymbol{d}}_{|\Sigma}), \quad \hat{\mathbf{w}} = \partial_t\hat{\boldsymbol{d}}^{\mathrm{f}} \quad \text{in} \quad \hat{\Omega}^{\mathrm{f}}, \quad \Omega^{\mathrm{f}}(t) = (\mathbf{I}_{\Omega^{\mathrm{f}}} + \hat{\boldsymbol{d}}^{\mathrm{f}})(\hat{\Omega}^{\mathrm{f}}), \\ \mathbf{u} = \mathbf{w}, \quad \text{on} \quad \Sigma(t), \\ \hat{\boldsymbol{\Pi}}\hat{\mathbf{n}}^{\mathrm{s}} = \hat{J}^{\mathrm{f}}\hat{\boldsymbol{\sigma}}^{\mathrm{f}}(\hat{\boldsymbol{F}}^{\mathrm{f}})^{-\mathrm{T}}\hat{\mathbf{n}}^{\mathrm{s}}, \quad \text{on} \quad \hat{\Sigma}. \end{cases} \tag{1.3}$$

where Ω^{f}, Ω^{s} and Σ denote respectively the fluid domain, the structure domain and the fluid-structure interface. The fluid and structure densities are given by ρ^{f} and ρ_0^{s}, $\boldsymbol{\sigma}^{\mathrm{f}}(\mathbf{u},p)$ is the fluid Cauchy stress tensor and $\boldsymbol{\Pi}(\hat{\boldsymbol{d}})$ the Piola-Kirchhoff stress tensor for the structure. In (1.1), $\cdot|_{\mathcal{A}}$ represents the ALE time derivative. We denote with $\hat{\cdot}$, quantities written in the Lagrangian formulation for the structure, or in the ALE formulation for the fluid, the Eulerian framework is assumed otherwise. The same notation is used in Chapter 2, in all the other chapters this distinction is neglected in order to simplify the notation. In (1.3) $\operatorname{Ext}(\cdot)$ is any reasonable extension operator in the fluid domain and $\hat{\boldsymbol{F}}^{\mathrm{f}}$ defines the deformation gradient of the fluid domain, $\hat{J}^{\mathrm{f}}$ being its determinant.

The coupled FSI problem and the notation used are described in greater detail in Chapter 2. There, the mathematical modeling and the numerical discretization of the fluid-structure interaction problem are considered. The fluid and solid models and the resulting coupled problem are presented. Then, different variational formulations for the coupled FSI problem are given. For the sake of clarity, the space and time discretizations of the problem are addressed separately. The finite element approach is used for the discretization in space. For the numerical resolution of the FSI problem we consider partitioned procedures, which allow the use of distinct fluid and structure solvers. In Section 2.5.3, the partitioned procedures are regrouped depending on the type of coupling enforced between fluid and structure: *implicit* coupling, *semi-implicit* coupling, *explicit* coupling. For each group the state-of-the-art is presented.

1.3.1 A semi-implicit projection coupling for FSI problems: analysis and numerics (Part I)

Among the different partitioned schemes, the semi-implicit coupling schemes offer an excellent compromise between stability and efficiency. As a matter of fact

these are faster than the common implicit procedures, but more stable than *standard*[1] explicit coupling schemes, which are unstable when the added-mass effect becomes important [CGN05]. Examples of semi-implicit coupling schemes are given in the following works [FGG06, FGG07, QQ07, BQQ08, SM08]. Considering the first semi-implicit scheme [FGG06, FGG07], its efficiency relies upon a convenient implicit-explicit splitting performed with the Chorin-Temam projection scheme [Cho68, Tem68, Cho69] in the fluid: at each time step the projection sub-step (carried out in a known fluid domain) is implicitly coupled with the structure, so accounting for the added-mass effect in an implicit way, while the expensive ALE-advection-viscous sub-step is explicit.

For a linearized version of problem (1.1)-(1.3), the authors proved that the scheme is stable under the condition (see [FGG07, Theorem 1]):

$$\rho^{\mathrm{s}} \geq C\left(\rho^{\mathrm{f}}\frac{h}{H^{\alpha}}+\frac{\mu\tau}{hH^{\alpha}}\right), \quad \text{with} \quad \alpha \overset{\text{def}}{=} \begin{cases} 0, & \text{if} \quad \overline{\Omega^{\mathrm{s}}} = \Sigma, \\ 1, & \text{if} \quad \overline{\Omega^{\mathrm{s}}} \neq \Sigma, \end{cases} \tag{1.4}$$

where μ, τ, h and H are respectively the fluid viscosity, the time-step and the fluid and structure space discretization steps. Although condition (1.4) depends on the fluid-structure density ratio (*i.e.* it is still related to the added-mass effect [CGN05]) and it holds for a dissipative time-advancing method within the structure, the scheme is stable for a wide range of cardiovascular FSI problems, even with the use of a conservative scheme within the structure.

In Part I of this thesis, we first investigate the convergence properties of the scheme, then we propose a modification that allows for the scheme to be stable independently of the added mass effect. This last modification allows for the method to be used in a wider range of FSI problems.

Convergence analysis of the semi-implicit projection scheme (Chapter 3). A number of works is devoted to the numerical analysis of FSI coupling schemes (*e.g.* [Gra98, GM00, LTM00, Tak02, DGHL03]). However, to our best knowledge, none of these considers the convergence analysis of semi-implicit FSI coupling schemes. In Chapter 3, we analyze the convergence of the semi-implicit projection scheme for a linearized version of problem (1.1)-(1.3). The problem is the same used for the stability proof in [FGG07]: the fluid is described by the Stokes equations, the structure by the classical linear elastodynamic equations (linearized elasticity, plate or shell models) and all changes of geometry are neglected. The fluid and structure equations are fully discretized in time and space. In time, the non-incremental Chorin-Temam projection scheme is used for the fluid, the Leap-Frog scheme for the structure. In space, we assume finite element approximations with a non-conforming matching at the interface. As a consequence an interface matching operator π_h

[1] Recently an explicit coupling scheme whose stability properties are independent of the added-mass effect has been proposed in [BF07, BF09]. Its stability relies on the Nitsche's method to impose the coupling conditions and on a time penalty term giving an L^2-control on the fluid pressure variations at the interface.

is introduced at the fluid-structure interface. The convergence is proved for two different matching operators: a finite element interpolation operator and a mortar operator. Assuming for these operators the properties defined in Section 3.3.3, p. 68, the following convergence result holds

Theorem 1.1 (Chapter 3, p. 76) *Under the stability condition (1.4), and if the solution of the linear coupled problem is smooth enough in space and time, then the error in the semi-implicit projection scheme is of order* $\sqrt{\tau} + h^k + H^m + h^l$. *The indices* k, m, l *are related to the fluid velocity, to the structure and to the interface matching operator, respectively. More precisely, the index* k *is the polynomial degree of the approximation for the fluid velocity. The index* m *depends on the choice of the finite element approximation space for the structure and, for* $\boldsymbol{v}^{\mathrm{s}}$ *smooth enough, is such that*

$$\inf_{\boldsymbol{v}_H \in V_H^{\mathrm{s}}} \|\boldsymbol{v}^{\mathrm{s}} - \boldsymbol{v}_H\|_{V^{\mathrm{s}}} \leq C H^m;$$

with

$$V^{\mathrm{s}} \subseteq \left\{ \boldsymbol{v}^{\mathrm{s}} \in [H^1(\Omega^{\mathrm{s}})]^d \,:\, \boldsymbol{v}^{\mathrm{s}} = \boldsymbol{0} \text{ on } \Gamma_D^{\mathrm{s}} \right\},$$

V_H^{s} *being the corresponding finite element space. The index* l *depends on the choice of the matching operator* π_h, *that is,*

- $l \leq \min\left(r - \frac{\alpha}{2}, k+1\right)$ *for the pointwise-type operator,*
- $\frac{1}{2} \leq l \leq k$ *for the mortar-type operator,*

where α *is defined in (1.4) and* r *is* 1 *or* 2 *depending on the considered structure (*i.e. *linearized elasticity, plate or shell).*

The proof of the theorem is reported in same chapter. We also discuss the optimality in space of the error estimate and we provide numerical experiments for the optimality in time.

A Robin based semi-implicit projection scheme (Chapter 4). As already mentioned, the semi-implicit projection scheme is robust and efficient for cardiovascular applications. Nonetheless, for problems where the added-mass effect is very important the scheme may still be unstable. As a matter of fact, the stability condition still depends on the fluid-structure density ratio. In addition from a theoretical viewpoint, the stability is proved only for a non-conservative scheme within the structure (for conservative schemes the proof is not trivial). It is interesting to observe that these two aspects are strictly related to the strong enforcement of the coupling kinematic condition in the explicit step of the scheme (*i.e.* in the ALE-advection-diffusion step of the fluid problem). In Chapter 4, we aim at removing these two limitations. In order to enhance stability, we propose to replace the strong enforcement of the kinematic condition in the explicit step by a Robin-Robin coupling derived from Nitsche's penalty method (see *e.g.* [Nit71, BHS03, BF07]). This reinterpretation of the Nitsche's coupling as a Robin-Robin coupling represents an

important element of novelty with respect to other schemes based either on a pure Nitsche's method [BF07, BF09] or on Robin-Robin scalings derived by reduced structure models [BNV08]. The implicit part of the scheme (*i.e.* the pressure-structure coupling) is eventually discretized in space in a standard fashion. The stability of this new scheme is proved for the linearized version of problem (1.1)-(1.3) (with a conservative time-advancing scheme for the structure), and the following result holds

Theorem 1.2 (Chapter 4, p. 108) *The Robin based semi-implicit coupling scheme is stable, in the energy-norm, under the conditions:*

$$\gamma \geq 2C_{\mathrm{ti}}, \quad \gamma\mu\tau = \mathcal{O}(h), \tag{1.5}$$

where γ is the Nitsche's parameter and C_{ti} the constant of the trace inverse inequality

$$||\boldsymbol{v}_h^{\mathrm{f}}||^2_{0,\partial K} \leq C_{\mathrm{ti}} h^{-1} ||\boldsymbol{v}_h^{\mathrm{f}}||^2_{0,K} \quad \forall \boldsymbol{v}_h^{\mathrm{f}} \in X_h^{\mathrm{f}}, \tag{1.6}$$

X_h^{f} being the finite element approximation of the space $[H^1(\Omega^{\mathrm{f}})]^d$.

Since the stability condition (1.5) does depend neither on the fluid-solid density ratio nor on the geometry of the domain, the semi-implicit coupling scheme (4.22)-(4.24) remains stable irrespectively of the added-mass effect. Moreover, thanks to the natural interface dissipation of the Robin coupling, a diffusive time marching in the structure is no longer needed to ensure stability. In Chapter 4, we give the proof of Theorem 1.2, and we analyze also other mathematical formulations for the same coupling algorithm. Numerical experiments that validate this new approach in two and three dimensions are also presented.

1.3.2 Numerical simulation of FSI problems with cardiac valves (Part II)

In Part II of this thesis we consider the numerical simulation of the interaction between blood and cardiac valves. This problem offers extraordinary challenges from the modeling, the mathematical and the numerical viewpoints. Examples are the highly non-linear constitutive laws, the intense unsteadiness and strong pressure gradients in the blood flow, but also the contact among the leaflets and the modeling of the *chordae tendineae* (for the mitral valves).

In this field, many works consider two-dimensional fluid-structure problems, only a few three-dimensional problems. The ones considering three dimensional fluid-structure interaction problems frequently assume simplifications in the model in order to reduce its complexity. A typical simplification is the use of planes of symmetry for the leaflets. As a result, only one leaflet is effectively simulated, the behaviors of the others, as well as the flow distribution, are retrieved by symmetry. This approach could be used for example in the simulation prosthetic valves, the leaflets being symmetric. Nonetheless, native valves are naturally non-symmetric and the flow behavior is inherently three dimensional. In addition, in view of the

simulation of particular diseases, such as stenosis for example, the whole three-dimensional complexity of the problem has to be taken into account. In this work we consider fully 3D valves simulations, focusing in particular on the aortic valve. The other valves can be clearly handled within the same general approach.

A partitioned scheme for FSI and multi-body contact (Chapter 5). The use of fully three-dimensional simulations introduces automatically new complexities that must be handled in order to have reliable results. This is the case of the contact among multiple elastic solids (*i.e.* the leaflets). From a mathematical viewpoint, the contact problem is itself very difficult. As a matter of fact, the constraint of non-penetration among the immersed structures defines a *non-convex* optimization problem. In our work the complexity is increased by the interaction with the blood. In Chapter 5, we propose a unified modular framework to solve both the FSI and the multi-body contact problems. The contact algorithm, which can handle multi-structure and auto contacts, has been implemented in an independent C++ software. The modularity ensures the maximum of flexibility in code development: the fluid and the structure solvers are assumed "black-boxes", for whom the only requirement is the capability to exchange forces and velocities. The chapter concludes with a numerical experiment on an idealized aortic valve that validates our approach.

Computational analysis of an aortic valve jet with Lagrangian coherent structures (Chapter 6). In Chapter 6, we apply the modular algorithm previously described to the computation of the flow through a realistic deformable, three-dimensional aortic valve. The data obtained from this simulation are analyzed with the Lagrangian coherent structures (LCS) method. This is an advanced post-processing technique that can be used to reveal dominant flow features, such as vortex boundaries or separation profiles, or uncover kinematic processes organizing fluid mixing [Hal01, SLM05, LSM07]. From a medical point of view, the knowledge of these kind of transport features is particularly appealing. As a matter of fact, disturbed flow conditions, including vortical or separated flow, are known to influence health maintenance and disease progression [ST08, WK99]. In the particular case of the aortic valve, LCS can be used to characterize flow separation downstream of the valve and identify the time-dependent bounding surface of the blood flow jet. The minimal cross-section of this jet is the so-called "effective orifice area", or jet size, which is in fact one of the indices that the medical community considers reliable in the assessment of valvular stenosis. Note however that these indices rely on basic physical principles, such as Torricelli's law, Bernoulli's law and conservation of mass and provide a little insight into the actual transport structures. The advantage of the computational framework proposed is twofold: on the one hand it can be used to evaluate the quality and effectiveness of existing clinical indices, on the other hand, as an ultimate goal, to provide a computational-based assessment of valve stenosis.

1.3.3 Towards the fluid-structure interaction in the heart (Part III)

The fluid-structure interaction in the heart is a very fascinating problem which contains itself all the difficulties related to the interaction of the blood with the wall and with the cardiac valves. From the modeling point of view, an accurate description of the heart and valves mechanics is required. Advances in this direction are for example given in [HPS03, CFG+09] for the heart and in [WKM05, PSH07] for valves. From the numerical point of view, techniques such as the ones introduced in Chapters 4 and 5 have to be included in a single framework in order to consider all the possible interactions: blood - heart wall and blood - heart valves. This is feasible (see for example [dS07, Chapter 6] for preliminary results in two-dimensions) but in three-dimensions it could become so computationally intensive that it may not be the best option to address some clinical problems for which a precise mechanical description of all the elements is not required. If the mechanics of the heart itself is the principal point of interest, one could be motivated to replace the complex three-dimensional simulations of the valves with reduced valve models, which take into account the opening and closing behavior of the heart valves. Nonetheless the use of standard lumped parameter models has inherent limitations due to the introduction of artificial boundaries in regions where high variability in the fluid dynamics quantities is experienced. In the last part of the thesis, we propose a new reduced model for cardiac valves, which improves the accuracy of standard lumped models and the robustness and efficiency of 3D FSI models.

Resistive immersed surfaces for heart valves modeling (Chapter 7). The new reduced model for heart valves is presented in Chapter 7. In this approach, the mechanics of valves is not considered. Instead, valves are replaced by immersed surfaces acting as resistances on the fluid. The mathematical formulation is based on the model proposed in [FGM08] to deal with immersed stents. This allows for a precise computation of the pressure discontinuity across the valve even with the use of continuous finite element approximations. The immersed surfaces are part of the fluid mesh, the opening and the closing of the valve are controlled by resistance coefficients that vary depending on the fluid-dynamics status of the system. The geometry of the resistive surface are defined as the real three-dimensional valve geometries in their closed and fully open configurations. The surfaces corresponding to the open position is of course equipped with a zero resistance, *i.e.* they are "invisible", when the valves are closed. Doing so, the geometrical domain seen by the fluid is realistic for the most part of the cardiac cycle (see Figure 1.5 for an example of closed and open valves).

Various numerical experiments are presented for different realistic configurations. All the simulations involve an incompressible viscous fluid either in a rigid domain or in a moving domain (with imposed displacements). A preliminary example in fluid-structure interaction problems is also given for the sake of completeness.

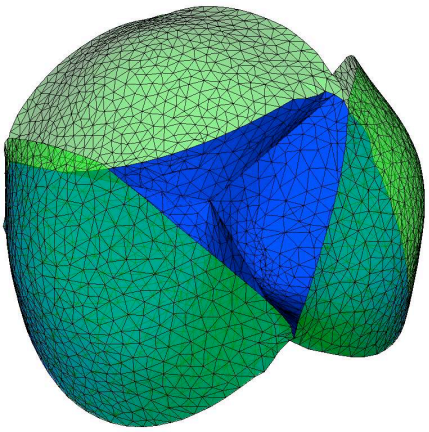

Figure 1.5: Open (green) and closed (blue) configurations of an aortic valve.

Conclusions and perspectives. This thesis is completed by concluding remarks and perspectives. Moreover, in Appendix A, we illustrate a simple but effective reduced model to take into account external tissues in cardiovascular FSI problems.

Chapter 2

Mathematical modeling and numerical discretization of the coupled fluid-structure interaction problem

Contents

2.1 Introduction

In continuum mechanics, a material body, such as the fluid and/or the solid, is defined as a *continuum medium* which occupies a bounded, open and simply connected domain $\hat{\Omega} \subset \mathbb{R}^d$, $d = 2, 3$. We shall refer to $\hat{\Omega}$ as the *reference configuration* of the medium under consideration.

Any change in time of the configuration of the continuum body is the result of a *motion*, that is, the result of the application of a smooth map $\boldsymbol{\varphi} : \hat{\Omega} \times \mathbb{R}^+ \to \mathbb{R}^d$ associating each point $\hat{\mathbf{x}} \in \hat{\Omega}$ to a new position $\mathbf{x} = \boldsymbol{\varphi}(\hat{\mathbf{x}}, t)$ for all time $t \geq 0$. For any fixed time $\tau \geq 0$, $\boldsymbol{\varphi}_\tau \stackrel{\text{def}}{=} \boldsymbol{\varphi}(\hat{\mathbf{x}}, \tau)$ defines a *deformation* of the continuum body and the set $\Omega(\tau) = \{\mathbf{x} \in \mathbb{R}^d : \mathbf{x} = \boldsymbol{\varphi}(\hat{\mathbf{x}}, \tau), \hat{\mathbf{x}} \in \hat{\Omega}\}$ is the corresponding *current configuration*.

When we analyze the deformation or motion of solids, or the flow of fluids, it is necessary to describe the evolution in time of the associated physical quantities.

These quantities can be defined alternatively on the reference or on the current configuration. In the former case, the so-called *Lagrangian description* (or *Lagrangian formulation*) of the continuum medium is employed; the physical quantities are defined on $\hat{\Omega}$ and $(\hat{\mathbf{x}}, t)$ are adopted as independent variables. Note that, in the following, we adopt the usual convention to denote with the superscript $\hat{\cdot}$ a Lagrangian field. In the latter case, the so-called *Eulerian description* (or *Eulerian formulation*) is used and the physical quantities refer to the $(\mathbf{x}, t)$ pair on the current domain $\Omega(t)$. Depending on the context, one formulation may be more convenient than the other. In solid mechanics the Lagrangian formulation is adopted. Computationally, this description allows an easy tracking of interfaces and facilitates the treatment of material with history-dependent constitutive relations. In fluid mechanics, instead, the Eulerian formulation is usually preferred since the large distortions that characterize the fluid motion can be handled with relative ease. From a computational point of view, this formulation naturally leads to choose as computational domain a fixed open bounded set $\Omega \subset \mathbb{R}^d$ such that $\Omega \subset \Omega(t)$ for all times t we observe the motion. As a consequence, in situations involving moving boundaries/interfaces (*e.g.* fluid-structure interaction, free-surface flows or multi-fluid flows), an Eulerian description of the fluid could become computationally troublesome due to the difficulty of precisely tracking the moving interface. Whenever possible, it is therefore preferable to use a different frame of reference, the well-known *arbitrary Lagrangian-Eulerian formulation*, that could be seen as a "compromise" between the Eulerian and Lagrangian descriptions [DHPRF04]. As a matter of fact, in the arbitrary Lagrangian-Eulerian description, the computational domain is neither fixed, as often assumed in the Eulerian framework, nor governed by the fluid motion, like in the Lagrangian framework, but its movement is governed by that of the boundary/interface.

In the numerical simulation of fluid-structure interaction problems, the need of coupling at the interface the two descriptions - Lagrangian and Eulerian - lead to the development of different approximation techniques. We mention, among others, the *arbitrary Lagrangian-Eulerian* (ALE) approach [HLZ81], based on the aforementioned ALE formulation of the fluid problem, the *Lagrange multiplier/fictitious domain* (FD) method [GPP94], the *space-time* (DSD/ST) approach [TBL92] and the *immersed boundary* (IB) method [Pes02].

In this chapter we address the mathematical modeling and the numerical discretization of the coupled fluid-structure interaction problem for two different techniques: the arbitrary Lagrangian-Eulerian approach and the fictitious domain method. The presentation is essentially based on [FFGQ09] and [FG09].

In Section 2.2, the fluid and structure models are presented. The fluid is supposed to be homogeneous, incompressible and Newtonian and its equations are given both in the Eulerian and ALE formulations. For the sake of simplicity, in view of the presentation of the coupled FSI problem and of the coupling algorithms, we assume the solid to be governed by the classical elastodynamics equations written in Lagrangian coordinates. Even so, specific models for vessel wall, cardiac valves

and heart wall are briefly reviewed.

In Section 2.3, the coupled fluid-structure interaction problem in the ALE frame and the corresponding coupling conditions (or *transmission conditions*) are introduced. In Section 2.4, two variational formulations of the FSI problem are given. The two differ for the functional spaces chosen and in the way of imposing the coupling conditions. In the first one the coupling conditions are imposed in a strong form, in the second one they are imposed weakly by means of a Lagrange multiplier technique. The two formulations are mathematically equivalent, since they describe variationally the same physical problem. Nonetheless, from a numerical point of view, they lead to different computational methods to solve the FSI problem. The former leads to the use of the ALE technique, the latter is used to introduce the FD method, and one should be preferred to the other depending on the considered application. For example, as briefly discussed in Chapter 1, the ALE technique is more indicated for FSI problems where the structure displacements are not very large (*e.g.* in blood - wall interaction). Instead the FD method is more suited to deal with very large displacements and contact (*e.g.* in blood - valve interaction).

The purpose of Section 2.5 is to address the numerical discretization of the coupled FSI problem for the ALE and FD techniques. For the sake of clarity the discretizations in space and time are introduced separately. The former using a finite element approximation, the latter with a finite difference approach. A particular attention is given to the discretization of the coupling conditions since, as we will see later, it plays a key role in the development of stable and efficient numerical algorithms.

From the computational viewpoint, we focus on *partitioned* procedures, which allow the use of different solvers for the fluid and structure problems. Among the partitioned schemes, we distinguish the *strongly coupled* ones from the *weakly coupled*, discussing the role of the *added-mass effect* [CGN05, FWR07] as a partial theoretical explanation of the fact that classical weakly coupled schemes may exhibit instabilities in blood flow simulations. Three different classes of partitioned schemes, on which rely the results of the following chapters, are finally presented.

2.2 Fluid and solid modeling

2.2.1 Fluid model

The blood is a complex non-Newtonian fluid, characterized by a suspension of living cells in a liquid, *the plasma*, made by water approximatively for the 90% of its volume. The particulate phase of blood consists mainly of erythrocytes (*red blood cells*), leukocytes (*white blood cells*) and platelets. The aggregatable and deformable nature of red blood cells, that occupy almost half of the total blood volume, is the main responsible for the non-Newtonian behavior [Thi08a].

Since the beginning of the 20^{th} century, important hemodynamic effects such as shear thinning, thixotropy, viscoelasticity and yield stress have been investigated both experimentally and theoretically (see *e.g.* [CLW06, YG08] for an overview).

The results obtained indicate that non-Newtonian effects significantly affect local hemodynamics in the small vasculature (where the shear rate is low and the vessel calibre is comparable with the cell size), while they could be neglected for the medium and large vasculature, whenever the finer details of the flow aren't the main object of the analysis. In the latter case, the Newtonian model is a suitable approximation of the blood behavior [FQV09].

This work focuses on the large vasculature (heart ventricles, cardiac valves and large arteries), therefore, even if it is worth keeping in mind that in some regions non-Newtonian effects could be important (*e.g.* valve hinges and leakage jet during valve closure [SB09]), it seems reasonable to model the blood as a homogeneous, incompressible, and Newtonian fluid governed by the Navier-Stokes equations.

The incompressible Navier-Stokes equations in the Eulerian frame. Let $\Omega^{\mathrm{f}}(t)$ be a bounded time-dependent domain of $\mathbb{R}^d$, $d = 2, 3$, with a Lipschitz continuous boundary $\partial\Omega^{\mathrm{f}}(t)$, and denote by $\mathbf{n}^{\mathrm{f}}$ the unit outward normal on $\partial\Omega^{\mathrm{f}}(t)$. Assuming the time $t \in \mathbb{R}^+$, the incompressible Navier-Stokes equations in their Eulerian formulation write:
Find the fluid velocity $\mathbf{u} = \mathbf{u}(\mathbf{x}, t) : \Omega^{\mathrm{f}}(t) \times \mathbb{R}^+ \to \mathbb{R}^d$ and the pressure $p = p(\mathbf{x}, t) : \Omega^{\mathrm{f}}(t) \times \mathbb{R}^+ \to \mathbb{R}$, such that

$$\begin{cases} \rho^{\mathrm{f}} \left(\dfrac{\partial \mathbf{u}}{\partial t} + (\mathbf{u} \cdot \nabla)\mathbf{u} \right) - \operatorname{div} \boldsymbol{\sigma}^{\mathrm{f}}(\mathbf{u}, p) = \mathbf{f}, & \text{in} \quad \Omega^{\mathrm{f}}(t), \\ \operatorname{div} \mathbf{u} = 0, & \text{in} \quad \Omega^{\mathrm{f}}(t), \end{cases} \tag{2.1}$$

where $\boldsymbol{\sigma}^{\mathrm{f}} = \boldsymbol{\sigma}^{\mathrm{f}}(\mathbf{u}, p) \overset{\text{def}}{=} 2\mu\boldsymbol{\varepsilon}(\mathbf{u}) - p\mathbf{I}$ is the Cauchy stress tensor with $\boldsymbol{\varepsilon}(\mathbf{u}) \overset{\text{def}}{=} \frac{1}{2}(\nabla\mathbf{u} + \nabla^{\mathrm{T}}\mathbf{u})$ the strain tensor and $\mathbf{I}$ the identity tensor. The quantity $\mathbf{f} = \mathbf{f}(\mathbf{x}, t)$ is a body force that will be assumed equal to $\mathbf{0}$ if not specified. The hypotheses of homogeneous, incompressible and newtonian fluid imply that the density ρ^{f} and the viscosity μ are constant in space and time.

Problem (2.1) is eventually completed with an initial condition for the velocity unknowns $\mathbf{u}(\mathbf{x}, 0) = \mathbf{u}_0$ in $\Omega^{\mathrm{f}}(0)$, and with suitable boundary conditions. Assuming Γ^{f}_D and Γ^{f}_N to be two non-overlapping subsets of $\partial\Omega^{\mathrm{f}}(t)$, such that $\Gamma^{\mathrm{f}}_D \cup \Gamma^{\mathrm{f}}_N = \partial\Omega^{\mathrm{f}}(t)$, the set of equations

$$\begin{cases} \mathbf{u} = \mathbf{u}_D & \text{on} \quad \Gamma^{\mathrm{f}}_D \subset \partial\Omega^{\mathrm{f}}, \\ \boldsymbol{\sigma}^{\mathrm{f}}\mathbf{n}^{\mathrm{f}} = \boldsymbol{g}_N & \text{on} \quad \Gamma^{\mathrm{f}}_N \subset \partial\Omega^{\mathrm{f}}, \end{cases} \tag{2.2}$$

defines respectively the Dirichlet boundary condition, $(2.2)_1$, and the Neumann boundary condition, $(2.2)_2$; with $\mathbf{u}_D$ and $\boldsymbol{g}_N$ given vector functions. Other boundary conditions, such as Robin boundary conditions, are possible and will be used in Chapter 4.

The incompressible Navier-Stokes equations in the ALE frame. In this paragraph we provide only the essential notions on the ALE formulation in order to reformulate the incompressible Navier-Stokes equations in this frame. For an extensive presentation of the ALE formulation we refer to [Nob01] and [FG09].

The ALE description is based on the introduction of an appropriate mapping $\mathcal{A}$ from a reference fixed configuration $\hat{\Omega}^{\mathrm{f}}$ (*e.g.* $\hat{\Omega}^{\mathrm{f}} = \Omega^{\mathrm{f}}(0)$) to the current moving domain $\Omega^{\mathrm{f}}(t)$:

$$\mathcal{A} : \hat{\Omega}^{\mathrm{f}} \times \mathbb{R}^+ \to \Omega^{\mathrm{f}}(t), \quad (\hat{\mathbf{x}}, t) \to \mathbf{x} = \mathcal{A}(\hat{\mathbf{x}}, t),$$

such that $\Omega^{\mathrm{f}}(t) = \mathcal{A}(\hat{\Omega}^{\mathrm{f}}, t)$ for all $t > 0$.

Remark 2.1 *The choice of the mapping is in general rather arbitrary, provided that the given law for the domain boundary movement is respected. As a result, a classical approach is to build the map $\mathcal{A}$ from the evolution of the boundary $\partial\Omega^{\mathrm{f}}(t)$ of the fluid domain $\Omega^{\mathrm{f}}(t)$.*

Noticing that the ALE map $\mathcal{A}_t(\hat{\mathbf{x}}) \overset{\text{def}}{=} \mathcal{A}(\hat{\mathbf{x}}, t)$ represents the deformation of the domain at any time $t > 0$, we can define the corresponding domain velocity as $\hat{\mathbf{w}}(\hat{\mathbf{x}}, t) \overset{\text{def}}{=} \partial_t \mathcal{A}(\hat{\mathbf{x}}, t)$. We also indicate the deformation gradient with $\hat{\boldsymbol{F}}^{\mathrm{f}}(\hat{\mathbf{x}}, t) \overset{\text{def}}{=} \nabla_{\hat{\mathbf{x}}} \mathcal{A}(\hat{\mathbf{x}}, t)$, where $\nabla_{\hat{\mathbf{x}}}$ is the gradient with respect to $\hat{\mathbf{x}}$, and its determinant with $\hat{J}^{\mathrm{f}}(\hat{\mathbf{x}}, t) \overset{\text{def}}{=} \det \hat{\boldsymbol{F}}^{\mathrm{f}}(\hat{\mathbf{x}}, t)$.

For any given function $\hat{f} : \hat{\Omega}^{\mathrm{f}} \times \mathbb{R}^+ \to \mathbb{R}$ defined in the ALE reference domain, its Eulerian description is given by

$$f(\mathbf{x}, t) = \hat{f}(\mathbf{x}, t) \circ \mathcal{A}_t^{-1} = \hat{f}(\mathcal{A}_t^{-1}(\mathbf{x}), t), \quad \forall \mathbf{x} \in \Omega^{\mathrm{f}}(t), \quad t > 0;$$

conversely

$$\hat{f}(\hat{\mathbf{x}}, t) = f(\mathcal{A}_t(\hat{\mathbf{x}}), t), \quad \forall \hat{\mathbf{x}} \in \hat{\Omega}^{\mathrm{f}}.$$

Therefore on a given point $\mathbf{x}$ of domain $\Omega^{\mathrm{f}}(t)$, we have that $\mathbf{w}(\mathbf{x}, t) = \hat{\mathbf{w}}(\hat{\mathbf{x}}, t)$, where $\mathbf{w}(\mathbf{x}, t)$ is the velocity of the domain in the current configuration, note that in general $\mathbf{w}(\mathbf{x}, t) \neq \mathbf{u}(\mathbf{x}, t)$.

In order to effectively apply the ALE formulation to the problem (2.1) we still need to introduce the relation between the *Eulerian time derivative* of an Eulerian field q, $\partial_t q$, and the corresponding *ALE time-derivative*, $\partial_t q|_{\mathcal{A}}$. The following proposition, based on the application of the chain rule for the composition of functions, yields the awaited result.

Proposition 2.1 *For any given Eulerian field q, the following identity holds*

$$\frac{\partial q}{\partial t}\Big|_{\mathcal{A}} = \mathbf{w} \cdot \nabla q + \frac{\partial q}{\partial t}. \tag{2.3}$$

A direct application of the identity (2.3) yields the following ALE formulation for the incompressible Navier-Stokes equations:
Find the fluid velocity $\mathbf{u} = \mathbf{u}(\mathbf{x}, t) : \Omega^{\mathrm{f}}(t) \times \mathbb{R}^+ \to \mathbb{R}^d$ and the pressure $p = p(\mathbf{x}, t) : \Omega^{\mathrm{f}}(t) \times \mathbb{R}^+ \to \mathbb{R}$, such that

$$\begin{cases} \rho^{\mathrm{f}} \left(\dfrac{\partial \mathbf{u}}{\partial t}\Big|_{\mathcal{A}} + (\mathbf{u} - \mathbf{w}) \cdot \nabla \mathbf{u} \right) - \operatorname{div} \boldsymbol{\sigma}^{\mathrm{f}}(\mathbf{u}, p) = \mathbf{f}, & \text{in} \quad \Omega^{\mathrm{f}}(t), \\ \operatorname{div} \mathbf{u} = 0, & \text{in} \quad \Omega^{\mathrm{f}}(t), \end{cases} \tag{2.4}$$

The formulation presented is the so-called *non-conservative* form and is not the only possible in the ALE context. A *conservative* form can be obtained by replacing equation $(2.4)_1$ with

$$(J^{\mathrm{f}})^{-1}\rho^{\mathrm{f}}\frac{\partial(J^{\mathrm{f}}\mathbf{u})}{\partial t}\Big|_{\mathcal{A}} + \operatorname{div}\left(\mathbf{u}\otimes(\mathbf{u}-\mathbf{w}) - \boldsymbol{\sigma}^{\mathrm{f}}(\mathbf{u},p)\right) = \mathbf{f}, \quad \text{in} \quad \Omega^{\mathrm{f}}(t).$$

We refer to [FFGQ09] for its derivation.

2.2.2 Solid models

Biological structures, such as vessel wall, cardiac valves and the heart wall, are in general characterized by very complex non-linear mechanical behaviors. These are often made of a fibrous network embedded in a multiple structure layers, each one characterized by a specific mechanical behavior. First, in view of the presentation of the coupled FSI problem and of the coupling algorithms, a general three-dimensional elastic model is introduced. Later, specific models for the biological structures considered in this work are briefly reviewed.

The elastodynamics equations. We denote the deformation of the solid medium by

$$\boldsymbol{\varphi}^{\mathrm{s}} : \hat{\Omega}^{\mathrm{s}} \times [0,T] \longrightarrow \Omega^{\mathrm{s}}(t).$$

We then introduce the corresponding deformation gradient $\hat{\boldsymbol{F}}^{\mathrm{s}}(\hat{\mathbf{x}},t) \stackrel{\mathrm{def}}{=} \nabla_{\hat{\mathbf{x}}}\boldsymbol{\varphi}^{\mathrm{s}}(\hat{\mathbf{x}},t)$, and its determinant $\hat{J}^{\mathrm{s}}(\hat{\mathbf{x}},t) \stackrel{\mathrm{def}}{=} \det\hat{\boldsymbol{F}}^{\mathrm{s}}(\hat{\mathbf{x}},t)$. The displacement of the domain is given by $\hat{\boldsymbol{d}}(\hat{\mathbf{x}},t) \stackrel{\mathrm{def}}{=} \boldsymbol{\varphi}^{\mathrm{s}}(\hat{\mathbf{x}},t) - \hat{\mathbf{x}}$. Within the structure, the velocity of a material point $\hat{\mathbf{x}}$, $\partial_t\boldsymbol{\varphi}^{\mathrm{s}}(\hat{\mathbf{x}},t) = \partial_t\hat{\boldsymbol{d}}(\hat{\mathbf{x}},t)$, is denoted by $\hat{\mathbf{u}}^{\mathrm{s}}(\hat{\mathbf{x}},t)$.

Assuming the structure governed by the elastodynamics equations in the Lagrangian formulation, the solid problem writes:
Find the solid displacement $\hat{\boldsymbol{d}} = \hat{\boldsymbol{d}}(\hat{\mathbf{x}},t) : \hat{\Omega}^{\mathrm{s}} \times \mathbb{R}^+ \to \mathbb{R}^d$ and the velocity $\hat{\mathbf{u}}^{\mathrm{s}} = \hat{\mathbf{u}}^{\mathrm{s}}(\hat{\mathbf{x}},t) : \hat{\Omega}^{\mathrm{s}} \times \mathbb{R}^+ \to \mathbb{R}^d$ such that

$$\begin{cases} \hat{\rho}^{\mathrm{s}}_0\dfrac{\partial\hat{\mathbf{u}}^{\mathrm{s}}}{\partial t} - \operatorname{div}_{\hat{\mathbf{x}}}\hat{\boldsymbol{\Pi}}(\hat{\boldsymbol{d}}) = \hat{\rho}^{\mathrm{s}}_0\hat{\mathbf{f}}^{\mathrm{s}}, \quad \text{in} \quad \hat{\Omega}^{\mathrm{s}}, \\ \partial_t\hat{\boldsymbol{d}} = \hat{\mathbf{u}}^{\mathrm{s}}, \quad \text{in} \quad \hat{\Omega}^{\mathrm{s}}, \end{cases} \tag{2.5}$$

with $\hat{\rho}^{\mathrm{s}}_0 \stackrel{\mathrm{def}}{=} \hat{J}^{\mathrm{s}}\hat{\rho}^{\mathrm{s}}$, $\hat{\rho}^{\mathrm{s}}$ the structure density, and $\hat{\mathbf{f}}^{\mathrm{s}}$ a given body force. The tensor $\hat{\boldsymbol{\Pi}} = \hat{\boldsymbol{\Pi}}(\hat{\boldsymbol{d}})$ is called the *first Piola-Kirchhoff tensor* and is related to the Cauchy stress tensor by the following relation:

$$\hat{\boldsymbol{\Pi}} \stackrel{\mathrm{def}}{=} \hat{J}^{\mathrm{s}}\hat{\boldsymbol{\sigma}}^{\mathrm{s}}(\hat{\boldsymbol{F}}^{\mathrm{s}})^{-\mathrm{T}}, \tag{2.6}$$

where $\hat{\boldsymbol{\sigma}}^{\mathrm{s}} \stackrel{\mathrm{def}}{=} \boldsymbol{\sigma}^{\mathrm{s}} \circ \boldsymbol{\varphi}^{\mathrm{s}}$. Unlike the Cauchy stress tensor $\hat{\boldsymbol{\sigma}}^{\mathrm{s}}$, the first Piola-Kirchhoff tensor $\hat{\boldsymbol{\Pi}}$ is non-symmetric. Notice also that the first Piola-Kirchhoff tensor is the *Piola transform* of the tensor $\hat{\boldsymbol{\sigma}}^{\mathrm{s}}$ and is related to $\hat{\boldsymbol{d}}$ through an appropriate constitutive law. The following proposition states the main properties of the Piola transform [FFGQ09]:

Proposition 2.2 *Let $\boldsymbol{\sigma}$ be an Eulerian second order tensor field in a given Lipschitz bounded domain $\Omega(t)$ and $\hat{\mathbf{\Pi}}$ its Piola transformation. Then*

$$\operatorname{div}_{\hat{\mathbf{x}}} \hat{\mathbf{\Pi}} = \hat{J} \operatorname{div} \hat{\boldsymbol{\sigma}} \quad in \quad \hat{\Omega}, \tag{2.7}$$

where $\hat{\boldsymbol{\sigma}} = \boldsymbol{\sigma} \circ \boldsymbol{\varphi}$. As a result, for all $\hat{V} \subset \hat{\Omega}$ we have

$$\int_{\partial V} \boldsymbol{\sigma}\mathbf{n}\, \mathrm{d}\gamma = \int_{\partial \hat{V}} \hat{\mathbf{\Pi}}\hat{\mathbf{n}}\, \mathrm{d}\hat{\gamma}, \tag{2.8}$$

$$\int_{\partial V} \mathbf{n}\, \mathrm{d}\gamma = \int_{\partial \hat{V}} \hat{J}(\hat{\boldsymbol{F}})^{-\mathrm{T}}\hat{\mathbf{n}}\, \mathrm{d}\hat{\gamma}, \tag{2.9}$$

$$\mathrm{d}\gamma = \hat{J}|(\hat{\boldsymbol{F}})^{-\mathrm{T}}\hat{\mathbf{n}}|\, \mathrm{d}\hat{\gamma}, \tag{2.10}$$

$$\mathbf{n} = \frac{(\hat{\boldsymbol{F}})^{-\mathrm{T}}\hat{\mathbf{n}}}{|(\hat{\boldsymbol{F}})^{-\mathrm{T}}\hat{\mathbf{n}}|}. \tag{2.11}$$

Here, $\mathbf{n}$ and $\hat{\mathbf{n}}$ stand for the outward unit normal vectors to ∂V and $\partial \hat{V}$, respectively.

Problem (2.5) has to be completed by the following initial conditions:

$$\hat{\boldsymbol{d}}(\hat{\mathbf{x}}, 0) = \hat{\boldsymbol{d}}_0, \quad \hat{\mathbf{u}}^{\mathrm{s}}(\hat{\mathbf{x}}, 0) = \hat{\mathbf{u}}^{\mathrm{s}}_0,$$

and the boundary conditions

$$\begin{cases} \hat{\boldsymbol{d}} = \hat{\boldsymbol{d}}_D & \text{on} \quad \hat{\Gamma}^{\mathrm{s}}_D \subset \partial\hat{\Omega}^{\mathrm{s}}, \\ \hat{\mathbf{\Pi}}\hat{\mathbf{n}}^{\mathrm{s}} = \hat{J}^{\mathrm{s}}||(\hat{\boldsymbol{F}}^{\mathrm{s}})^{-\mathrm{T}}\hat{\mathbf{n}}^{\mathrm{s}}||\hat{\mathbf{h}}^{\mathrm{s}} & \text{on} \quad \hat{\Gamma}^{\mathrm{s}}_N \subset \partial\hat{\Omega}^{\mathrm{s}}, \end{cases} \tag{2.12}$$

being $\hat{\boldsymbol{d}}_D$ and $\mathbf{h}^{\mathrm{s}}$ given functions and $\hat{\mathbf{n}}^{\mathrm{s}}$ the unit outward normal on $\partial\hat{\Omega}^{\mathrm{s}}$, $\hat{\Gamma}^{\mathrm{s}}_D \cup \hat{\Gamma}^{\mathrm{s}}_N = \partial\hat{\Omega}^{\mathrm{s}}$. Equation $(2.12)_1$ sets the displacements on the part $\hat{\Gamma}^{\mathrm{s}}_D$ of the boundary, while $(2.12)_2$ imposes the surface stresses on the part $\hat{\Gamma}^{\mathrm{s}}_N$ and is the Lagrangian equivalent of the boundary condition

$$\boldsymbol{\sigma}^{\mathrm{s}}\mathbf{n}^{\mathrm{s}} = \mathbf{h}^{\mathrm{s}} \quad \text{on} \quad \Gamma^{\mathrm{s}}_N \subset \partial\Omega^{\mathrm{s}},$$

written in the Eulerian frame.

Remark 2.2 *For the sake of simplicity, in the following we assume $\hat{\boldsymbol{d}}_D = \mathbf{0}$, which corresponds to a fixed boundary for the structure domain.*

Remark 2.3 *Other boundary conditions may be of interest for the structure in cardiovascular applications. An important example is provided in Appendix A, where a simple but effective reduced model has been proposed to provide an adequate representation of the external tissues in FSI problems. It can be shown that the model proposed can be interpreted numerically as a particular Robin boundary condition for the structure.*

Many constitutive laws can be devised for a solid. Here for instance, we provide the general formulation of a hyperelastic material. Specific models for vessels, valves and the heart wall are also briefly addressed below.

To introduce the hyperelastic formulation, a symmetric tensor, the so-called *second Piola-Kirchhoff tensor*

$$\hat{\boldsymbol{\Sigma}} \stackrel{\text{def}}{=} (\hat{\boldsymbol{F}}^{\text{s}})^{-1}\hat{\boldsymbol{\Pi}} = \hat{J}^{\text{s}}(\hat{\boldsymbol{F}}^{\text{s}})^{-1}\hat{\boldsymbol{\sigma}}^{\text{s}}(\hat{\boldsymbol{F}}^{\text{s}})^{-\text{T}}, \tag{2.13}$$

is used. Note that $\hat{\boldsymbol{\Sigma}}$ is usually preferred to $\hat{\boldsymbol{\Pi}}$ because of its symmetry. As a matter of fact, constitutive laws are often better expressed in terms of symmetric stress tensors. For a general hyperelastic material $\hat{\boldsymbol{\Sigma}}$ and $\hat{\boldsymbol{d}}$ are related by

$$\hat{\boldsymbol{\Sigma}}(\hat{\boldsymbol{E}}) = \frac{\partial \mathcal{W}(\hat{\boldsymbol{E}})}{\partial \hat{\boldsymbol{E}}},$$

where $\mathcal{W} = \mathcal{W}(\hat{\boldsymbol{E}}) : \mathbb{R}^{3\times 3} \to \mathbb{R}^{+}$ is the *density of elastic energy* of the solid and $\hat{\boldsymbol{E}}$ the *Green-Lagrange strain tensor*, defined as

$$\hat{\boldsymbol{E}} \stackrel{\text{def}}{=} \frac{1}{2}\left((\boldsymbol{F}^{\text{s}})^{\text{T}}\boldsymbol{F}^{\text{s}} - \mathbf{I}\right). \tag{2.14}$$

As a simple example, we can consider the Saint-Venant-Kirchhoff three-dimensional elastic model, which is characterized by the energy density

$$\mathcal{W}(\hat{\boldsymbol{E}}) = \frac{L_1}{2}(\operatorname{tr}\hat{\boldsymbol{E}})^2 + L_2 \operatorname{tr}\hat{\boldsymbol{E}}^2, \tag{2.15}$$

and by the Green-Lagrange strain tensor

$$\hat{\boldsymbol{\Sigma}}(\hat{\boldsymbol{E}}) = L_1(\operatorname{tr}\hat{\boldsymbol{E}})\mathbf{I} + 2L_2\hat{\boldsymbol{E}}. \tag{2.16}$$

In (2.15) and (2.16), L_1 and L_2 denote the first and second *Lamé coefficients*, which are related to properties specific of an elastic material, the *Young modulus* E and *Poisson coefficient* ν, by the following relations

$$E = L_2\frac{3L_1 + 2L_2}{L_1 + L_2}, \qquad \nu = \frac{1}{2}\frac{L_1}{L_1 + L_2}, \tag{2.17}$$

and

$$L_1 = \frac{E\nu}{(1-2\nu)(1+\nu)}, \qquad L_2 = \frac{E}{2(1+\nu)}. \tag{2.18}$$

In Part I of this work, a linearized Saint-Venant-Kirchhoff elastic model is used for all the numerical experiments. In this model, the Cauchy stress tensor $\boldsymbol{\sigma}^{\text{s}}$ is defined as

$$\boldsymbol{\sigma}^{\text{s}}(\boldsymbol{d}) = 2L_1(\operatorname{tr}\boldsymbol{\varepsilon}(\boldsymbol{d}))\mathbf{I} + 2L_2\boldsymbol{\varepsilon}(\boldsymbol{d}), \tag{2.19}$$

where the linearized strain tensor is given by

$$\boldsymbol{\varepsilon}(\boldsymbol{d}) = \frac{1}{2}\left(\nabla\boldsymbol{d} + \nabla^{\text{T}}\boldsymbol{d}\right). \tag{2.20}$$

Despite its simplicity, this model contains the essential features, common to more complex structure models, that must be taken into account in the analysis and development of fluid-structure interaction algorithms. Notice also that a simple Saint-Venant-Kirchhoff elasticity model can be adopted in fluid-structure interaction problems only when one is not really interested in the details of the stress, which is the case of this work. In all the other situations more complex models should be considered. An overview for vessels, cardiac valves and heart wall is given below.

Vessel wall models. Blood vessels exhibit numerous complex characteristics. Among others, we mention the heterogeneous multi-layered structure of the wall, the inherent residual stress and the smooth muscle contractility. Various constitutive models have been developed, each one aiming to model specific behaviors of the vessel wall. In [VD03], the different constitutive models have been classified in four main classes:

- *Pseudoelastic models*, conceived after observing repeatable loading and unloading curves in biological tissues [FFP79], treat the vessel as an hyperelastic material in loading and another material in unloading. In general, the application of these models is however limited by difficulties in the estimation of model parameters due to the multicollinearity (large strains - large stresses), that is typically observed in data sets obtained with the incremental method of loading.

- *Randomly elastic models*, using data collected according to a statistical design from both the loading and unloading cycles, try to remove the limiting factors of the pseudoelastic models. The data for such models generally appears "noisier" than traditionally collected data, but minimizing multicollinearity benefits the estimation of model parameters.

- *Poroelastic models*, well-suited to model wall transport, treat a blood vessel as a fluid-saturated porous medium. They include measures of both the solid and fluid components in the kinematic and conservation equations. Experiments are usually performed to assess the solid response in the presence and absence of fluid, as well as to assess the hydraulic conductivity. We refer to [Ken79] as one of the first work using the poroelastic approach in blood vessel mechanics.

- *Viscoelastic models*, useful for modeling creep, stress relaxation and hysteresis, include time-dependent responses in the constitutive equation. The simplest linear viscoelastic models are attributed to Maxwell, Voight and Kelvin [Fun93]. Among the developments in viscoelastic modeling we recall the works [ABL+95, VVA+00, HGS02]. Despite using linear approaches, these studies also include other observed arterial behaviors, such as heterogeneity and internal pressurization.

Valve models. Numerous works have been devoted to the study of the mechanical properties of natural and prosthetic cardiac valves. Here we mainly focus on the modeling of the natural ones, referring to [CLK04, HNP+06, SB05, SB09] for a general overview on prosthetic valves.

Cardiac valves consist of a fibrous tissue network, mainly collagen and elastin, saturated with a fluid that is mostly water. The fibrous network, being wavy and uniaxially aligned, causes a highly anisotropic stress-strain response of the leaflets. Numerous constitutive models trying to incorporate valve tissue characteristics have been proposed in the past decade. A survey is proposed in [WKM05] and four different classes of models have been identified:

- *Phenomenological models*, typically developed by guessing either a form of the stress-strain response or of the strain-energy function. The resulting stress-strain response is then fitted to experimental stress-strain data.
- *Transversely isotropic models*, that determine strain-energy functions based on the assumption of transverse isotropy and in terms of strain invariants. Among these, we mention the transversely isotropic hyperelastic model introduced in [PSH07] for the modeling of the mitral valve.
- *Aligned fiber models*, based on geometric assumption, extrapolate the overall tissue behavior from the behavior of a single (or bundle of) fiber(s).
- *Unit-cell models*, that derive the entire model from knowledge of the material microstructure.

In [WKM05], the transversely isotropic and the unit-cell constitutive models are said to be the most applicable to describe the behavior of heart valve tissue. Similar good results have indeed been achieved by fitting the two models to experimental data. Nonetheless, it is also observed that they could be significantly improved by including the layered characteristic of heart valve tissue and by providing separate curves for loading and unloading phases. The multi-layered structure of valves has been taken into account in [WKM07b, WKM08], where a set of multiscale simulations has been realized to examine the dynamic behavior of the human aortic valve at the cell, tissue and organ length scales.

In Part II, in view of the ratio thickness/size of the valves, we have chosen to model the leaflets as co-dimensional one structures (*i.e.* $(d-1)$-dimensional models, being d the dimension of the problem under analysis). In three dimensions a shell model has been used to avoid the locking phenomenon. We refer to [Bat96, CB03] for the general theory of shells. For what concerns the constitutive model, we used a generalized Hook law characterized by the following internal stored energy in the reference configuration $\hat{\Omega}^{\mathrm{s}}$:

$$\mathcal{W}(\hat{\boldsymbol{E}}) = \frac{1}{2}\int_{\hat{\Omega}^{\mathrm{s}}} \left[C^{\alpha\beta\lambda\mu} e_{\alpha\beta} e_{\lambda\mu} + D^{\alpha\lambda} e_{\alpha z} e_{\lambda z}\right] dV, \tag{2.21}$$

where $\hat{\boldsymbol{E}} = (e_{\alpha\beta})$. In equation (2.21) the Greek symbols varying from 1 to 2 are used for the tangential components to the surface, z is the third direction, and

$$C^{\alpha\beta\lambda\mu} = \frac{E}{2(1+\nu)}\left(g^{\alpha\lambda}g^{\beta\mu} + g^{\alpha\mu}g^{\beta\lambda} + \frac{2\nu}{1-\nu}g^{\alpha\beta}g^{\lambda\mu}\right), \tag{2.22}$$

$$D^{\alpha\lambda} = \frac{8E}{t_{\mathrm{s}}^2(1+\nu)}g^{\alpha\lambda}, \tag{2.23}$$

being t_{s} the thickness and $g^{\alpha\lambda}$ the contravariant components of the metric tensor.

In two dimension an inextensible 1D solid with deformation energy

$$\mathcal{W} = \frac{1}{2}\int_0^L EI \left|\frac{\partial^2 \mathbf{x}}{\partial s^2}\right|^2 ds, \tag{2.24}$$

has been used. In (2.24), $\mathbf{x}(s)$ represents the position vector of a point along the structure, and the quantities L and I denote, respectively, the length and the moment of inertia of the leaflet. We refer to [dSGB08] for more details on the model.

Even if the models proposed cannot be considered as optimal models for biological valves, they are nevertheless sufficient to illustrate the numerical techniques introduced in Chapters 5 and 6.

Heart wall models. The key ingredients in the description of the electromechanical behavior of the heart wall are the modeling of the electrical activity and of the mechanical constitutive law. The coupling of these two elements leads to a complex multiscale problem, that goes from the cellular to the macroscopic level of the myocardial tissue. A general overview on the main cardiac modeling issues is reported in [HPS03].

Much attention has been given to the modeling of the electrical function of the heart. The goal of integrative modeling of the electrical activity of the heart is to understand the genesis of the myocardial activation sequence, from models of cellular ion currents and tissue conductivity, and to study the process of generation of the body surface potentials, which in turn generate the ECG. We refer to [Zem09] for some recent advances in this field.

For what concerns the mechanical constitutive law, the latter must be able to account for both the active and passive aspects of the muscle dynamics. For the active part, most of the existing models of myofiber excitation-contraction mainly rely on heuristic approaches and experimental testing (see *e.g.* [WH99, Sac04, SH06]). Recently, a large displacement and large strains model, consistent with key thermomechanical requirements, has been proposed in [SMCCS06] and applied to elecromechanical simulations in [Moi08, CFG+09]. The model combines an active law, based on a chemically-controlled constitutive law of cardiac myofibre mechanics [BCS01], and a passive component which relies on the hyperelastic and viscolelastic laws. In Part III, the physiological displacements obtained from the simulations realized in [Moi08, CFG+09] are used to investigate the fluid-dynamics in the left-ventricle. The simulations are performed with a new reduced model for valves described in Chapter 7.

2.3 The coupled FSI problem

In order to introduce the general non-linear fluid-structure problem, let us consider a time-dependent domain $\Omega(t) \subset \mathbb{R}^d$. We assume, for all time t, that $\overline{\Omega(t)} = \overline{\Omega^{\mathrm{f}}(t)} \cup \overline{\Omega^{\mathrm{s}}(t)}$ and $\Omega^{\mathrm{f}}(t) \cap \Omega^{\mathrm{s}}(t) = \emptyset$, where $\Omega^{\mathrm{f}}(t)$ is occupied by an incompressible viscous fluid and $\Omega^{\mathrm{s}}(t)$ by an elastic solid. The reference configuration of the system is defined by $\hat{\Omega} = \hat{\Omega}^{\mathrm{f}} \cup \hat{\Omega}^{\mathrm{s}}$ and the fluid-structure interface is denoted by $\Sigma(t) = \overline{\Omega^{\mathrm{f}}(t)} \cap \overline{\Omega^{\mathrm{s}}(t)}$. A two-dimensional sketch of the considered domain is reported in Figure 2.1.

For the fluid, since we are dealing with a moving interface, we consider the incompressible Navier-Stokes equations in its ALE formulation (2.4). For the struc-

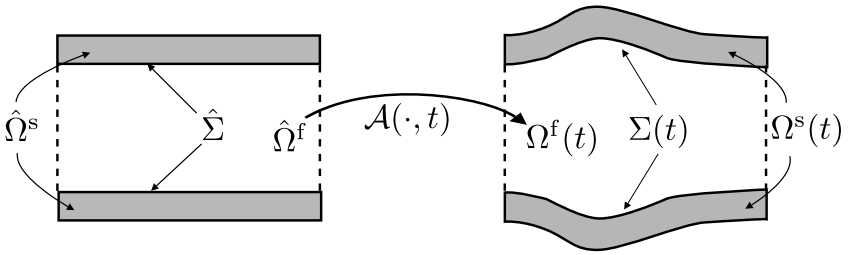

Figure 2.1: Geometry description.

ture, we take account of its motion with the elastodynamics equations (2.5). Both problems are completed with proper initial conditions and boundary conditions (on $\Gamma^{\mathrm{f}}_D(t)$ and $\Gamma^{\mathrm{f}}_N(t)$, for the fluid, and on Γ^{s}_D and Γ^{s}_N for the structure).

From the geometrical point of view, to ensure the compatibility between the two formulations we enforce that the fluid control volume follows the interface motion, *i.e.*

$$\mathcal{A}(\hat{\mathbf{x}},t) = \boldsymbol{\varphi}^{\mathrm{s}}(\hat{\mathbf{x}},t), \quad \text{on} \quad \hat{\Sigma}. \tag{2.25}$$

Since we describe the motion of the solid in terms of its displacement $\hat{\boldsymbol{d}}$, it is also useful to describe the ALE map in terms of the displacement of the control volume, $\hat{\boldsymbol{d}}^{\mathrm{f}} : \hat{\Omega}^{\mathrm{f}} \times \mathbb{R}^+ \to \mathbb{R}^d$, defined by

$$\hat{\boldsymbol{d}}^{\mathrm{f}}(\hat{\mathbf{x}},t) \stackrel{\mathrm{def}}{=} \mathcal{A}(\hat{\mathbf{x}},t) - \hat{\mathbf{x}}, \quad \forall \hat{\mathbf{x}} \in \hat{\Omega}^{\mathrm{f}}.$$

Thus, (2.25) reduces to

$$\hat{\boldsymbol{d}}^{\mathrm{f}}(\hat{\mathbf{x}},t) = \hat{\boldsymbol{d}}(\hat{\mathbf{x}},t), \quad \text{on} \quad \hat{\Sigma}. \tag{2.26}$$

Note that this equation defines a geometrical coupling between the two problems. Finally, by differentiating equality (2.26) with respect to t, we also have that

$$\hat{\mathbf{w}}(\hat{\mathbf{x}},t) = \hat{\mathbf{u}}^{\mathrm{s}}(\hat{\mathbf{x}},t), \quad \text{on} \quad \hat{\Sigma}. \tag{2.27}$$

Remark 2.4 *Although equations (2.26) and (2.27) are used in practice, only*

$$\hat{\boldsymbol{d}}^{\mathrm{f}}(\hat{\mathbf{x}},t) \cdot \mathbf{n} = \hat{\boldsymbol{d}}(\hat{\mathbf{x}},t) \cdot \mathbf{n}, \quad \textit{on} \quad \hat{\Sigma},$$
$$\hat{\mathbf{w}}(\hat{\mathbf{x}},t) \cdot \mathbf{n} = \hat{\mathbf{u}}^{\mathrm{s}}(\hat{\mathbf{x}},t) \cdot \mathbf{n}, \quad \textit{on} \quad \hat{\Sigma},$$

are theoretically required.

Apart from the constraint of satisfying (2.26), the displacement of the fluid control volume $\hat{\boldsymbol{d}}^{\mathrm{f}}$ (and hence $\mathcal{A}$) can be chosen rather arbitrarily. As a matter of fact, it can be any reasonable extension of $\hat{\boldsymbol{d}}_{|\hat{\Sigma}}$ over $\hat{\Omega}^{\mathrm{f}}$. In the sequel we will denote this operation by

$$\hat{\boldsymbol{d}}^{\mathrm{f}} = \mathrm{Ext}(\hat{\boldsymbol{d}}_{|\hat{\Sigma}}). \tag{2.28}$$

For instance, the operator Ext can be given in terms of an harmonic extension, by solving:

$$\begin{cases} -\Delta\hat{\boldsymbol{d}}^{\mathrm{f}} = \mathbf{0}, & \text{in} \quad \hat{\Omega}^{\mathrm{f}}, \\ \hat{\boldsymbol{d}}^{\mathrm{f}} = \mathbf{0}, & \text{on} \quad \partial\hat{\Omega}^{\mathrm{f}}\backslash\hat{\Sigma}, \\ \hat{\boldsymbol{d}}^{\mathrm{f}} = \hat{\boldsymbol{d}}, & \text{on} \quad \hat{\Sigma}, \end{cases} \tag{2.29}$$

where the boundaries of the fluid domain not belonging to Σ are assumed fixed along the motion. As a consequence, The current configuration of the fluid domain, $\Omega^{\mathrm{f}}(t)$, is parametrized by the ALE map

$$\mathcal{A}(\hat{\mathbf{x}}, t) = \hat{\mathbf{x}} + \mathrm{Ext}(\hat{\boldsymbol{d}}_{|\hat{\Sigma}}),$$

that is

$$\Omega^{\mathrm{f}}(t) = \mathcal{A}_t(\hat{\Omega}^{\mathrm{f}}) = (\mathbf{I}_{\hat{\Omega}^{\mathrm{f}}} + \hat{\boldsymbol{d}}^{\mathrm{f}})(\hat{\Omega}^{\mathrm{f}}).$$

From the mechanical point of view, the coupling between the two systems of differential equations is realized by imposing the following transmission conditions at the interface:

$$\mathbf{u} = \mathbf{u}^{\mathrm{s}}, \quad \text{on} \quad \Sigma(t), \tag{2.30}$$

$$\boldsymbol{\sigma}^{\mathrm{f}}\mathbf{n}^{\mathrm{f}} + \boldsymbol{\sigma}^{\mathrm{s}}\mathbf{n}^{\mathrm{s}} = \mathbf{0}, \quad \text{on} \quad \Sigma(t), \tag{2.31}$$

Equation (2.30) ensures the continuity of the velocity at the interface, since the fluid is assumed to be viscous and perfectly sticking to the interface $\Sigma(t)$. Equation (2.31) enforces the continuity of stress and in a Lagrangian description is given by:

$$\hat{\boldsymbol{\Pi}}\hat{\mathbf{n}}^{\mathrm{s}} + \hat{J}^{\mathrm{f}}\hat{\boldsymbol{\sigma}}^{\mathrm{f}}(\hat{\boldsymbol{F}}^{\mathrm{f}})^{-\mathrm{T}}\mathbf{n}^{\mathrm{f}} = \mathbf{0}, \quad \text{on} \quad \hat{\Sigma}. \tag{2.32}$$

Using the coupling conditions (2.28), (2.30) and (2.32) the non-linear fluid-structure problem under consideration reads as follows (see *e.g.* [FFGQ09]):
Find the fluid velocity $\mathbf{u} : \Omega^{\mathrm{f}} \times \mathbb{R}^+ \to \mathbb{R}^d$, the pressure $p : \Omega^{\mathrm{f}} \times \mathbb{R}^+ \to \mathbb{R}$, the solid displacement $\hat{\boldsymbol{d}} : \hat{\Omega}^{\mathrm{s}} \times \mathbb{R}^+ \to \mathbb{R}^d$ and the solid velocity $\hat{\mathbf{u}}^{\mathrm{s}} : \hat{\Omega}^{\mathrm{s}} \times \mathbb{R}^+ \to \mathbb{R}^d$ such that

- Fluid sub-problem:

$$\begin{cases} \rho^{\mathrm{f}}\dfrac{\partial\mathbf{u}}{\partial t}\Big|_{\mathcal{A}} + \rho^{\mathrm{f}}(\mathbf{u}-\mathbf{w})\cdot\nabla\mathbf{u} - 2\mu\,\mathrm{div}(\boldsymbol{\varepsilon}(\mathbf{u})) + \nabla p = \mathbf{0}, & \text{in} \quad \Omega^{\mathrm{f}}(t), \\ \mathrm{div}\,\mathbf{u} = 0, & \text{in} \quad \Omega^{\mathrm{f}}(t), \\ \mathbf{u} = \mathbf{u}_D, & \text{on} \quad \Gamma^{\mathrm{f}}_D, \\ \boldsymbol{\sigma}^{\mathrm{f}}\mathbf{n}^{\mathrm{f}} = \mathbf{g}, & \text{on} \quad \Gamma^{\mathrm{f}}_N, \end{cases} \tag{2.33}$$

- Solid sub-problem:

$$\begin{cases} \rho^{\mathrm{s}}_0\partial_t\hat{\mathbf{u}}^{\mathrm{s}} - \mathrm{div}_{\hat{\mathbf{x}}}\,\hat{\boldsymbol{\Pi}}(\hat{\boldsymbol{d}}) = \mathbf{0}, & \text{in} \quad \hat{\Omega}^{\mathrm{s}}, \\ \hat{\mathbf{u}}^{\mathrm{s}} = \partial_t\hat{\boldsymbol{d}}, & \text{in} \quad \hat{\Omega}^{\mathrm{s}}, \\ \hat{\boldsymbol{d}} = \hat{\boldsymbol{d}}_D, & \text{on} \quad \hat{\Gamma}^{\mathrm{s}}_D, \\ \hat{\boldsymbol{\Pi}}\hat{\mathbf{n}}^{\mathrm{s}} = \hat{J}^{\mathrm{s}}||(\hat{\boldsymbol{F}}^{\mathrm{s}})^{-\mathrm{T}}\hat{\mathbf{n}}^{\mathrm{s}}||\hat{\mathbf{h}}, & \text{on} \quad \hat{\Gamma}^{\mathrm{s}}_N, \end{cases} \tag{2.34}$$

- Coupling conditions:

$$\begin{cases} \hat{\boldsymbol{d}}^{\mathrm{f}} = \mathrm{Ext}(\hat{\boldsymbol{d}}_{|\Sigma}), \quad \hat{\mathbf{w}} = \partial_t \hat{\boldsymbol{d}}^{\mathrm{f}} \quad \text{in} \quad \hat{\Omega}^{\mathrm{f}}, \quad \Omega^{\mathrm{f}}(t) = (\mathbf{I}_{\Omega^{\mathrm{f}}} + \hat{\boldsymbol{d}}^{\mathrm{f}})(\hat{\Omega}^{\mathrm{f}}), \\ \mathbf{u} = \mathbf{w}, \quad \text{on} \quad \Sigma(t), \\ \hat{\boldsymbol{\Pi}}\hat{\mathbf{n}}^{\mathrm{s}} = \hat{J}^{\mathrm{f}} \hat{\boldsymbol{\sigma}}^{\mathrm{f}} (\hat{\boldsymbol{F}}^{\mathrm{f}})^{-\mathrm{T}} \hat{\mathbf{n}}^{\mathrm{s}}, \quad \text{on} \quad \hat{\Sigma}. \end{cases} \tag{2.35}$$

Remark 2.5 *Note that in the problem (2.33)-(2.35) we have supposed the body forces for the fluid and for the structure to be equal to* $\mathbf{0}$*. For hemodynamic applications it means that the effects of gravity are ignored.*

Remark 2.6 *In practice, as detailed in Section 2.5.3, most of the numerical schemes based on partitioned procedures, that solve the coupled problem (2.33)-(2.35), rely on a Dirichlet-Neumann domain decomposition strategy [QV99]. A Dirichlet boundary condition (*i.e. $(2.35)_2$*) is imposed at the interface for the fluid sub-problem, whereas the structure sub-problem is supplemented with a Neumann boundary condition (*i.e. $(2.35)_3$*).*

We finally observe that from an energetic point of view, the following proposition holds for the coupled problem (2.33)-(2.35):

Proposition 2.3 *Assume that the coupled fluid-structure system is isolated, i.e.* $\mathbf{u} = \mathbf{0}$ *on* $\partial\Omega^{\mathrm{f}}(t)\backslash\Sigma(t)$, $\hat{\boldsymbol{\Pi}}\hat{\mathbf{n}}^{\mathrm{s}} = \mathbf{0}$ *on* $\partial\hat{\Omega}^{\mathrm{s}}\backslash\hat{\Sigma}$*, then the following energy balance holds:*

$$\frac{\mathrm{d}}{\mathrm{d}t}\Bigg[\underbrace{\int_{\Omega^{\mathrm{f}}(t)} \frac{\rho^{\mathrm{f}}}{2}|\mathbf{u}|^2 \,\mathrm{d}\mathbf{x} + \int_{\hat{\Omega}^{\mathrm{s}}} \frac{\hat{\rho}_0^{\mathrm{s}}}{2}|\hat{\mathbf{u}}^{\mathrm{s}}|^2 \,\mathrm{d}\hat{\mathbf{x}}}_{\textit{Kinetic energy}} + \underbrace{\int_{\hat{\Omega}^{\mathrm{s}}} \mathcal{W}(\hat{\boldsymbol{E}}) \,\mathrm{d}\hat{\mathbf{x}}}_{\textit{Elastic potential energy}} \Bigg] + \underbrace{\int_{\Omega^{\mathrm{f}}(t)} 2\mu|\boldsymbol{\varepsilon}(\mathbf{u})|^2 \,\mathrm{d}\mathbf{x}}_{\textit{Dissipated viscous power}} = 0. \tag{2.36}$$

For a proof of (2.36) we refer to [FG09], here we only observe that the dissipation in the system only comes from the fluid viscosity and that the power exchanged by the fluid and the structure exactly balances at the interface. This balance is a direct consequence of the fulfillment of the coupling conditions $(2.35)_2$ and $(2.35)_3$.

2.4 Variational formulations of the coupled FSI problem

2.4.1 Elements of functional analysis

We give here some elements of functional analysis necessary to introduce the variational setting for the coupled problem (2.33)-(2.35). We refer to any standard functional analysis text (*e.g.* [Bre83]) for a more comprehensive presentation.

Let $\Omega \subset \mathbb{R}^d$, $d = 2, 3$, be a bounded domain, Lipschitz at least. We denote with $\mathcal{C}^0(\Omega)$ the space of functions that are continuous in Ω and with $\mathcal{C}^k(\Omega)$ the space of

functions that are k-times continuously Fréchet-differentiable on Ω. The space $\mathcal{D}(\Omega)$ represents the set of $\mathcal{C}^\infty$ functions whose support is compact in Ω. $\mathcal{D}(\Omega)$ is dense in $L^p(\Omega)$, $1 \leq p < +\infty$, which denotes the space of functions whose p-th power is absolutely integrable with respect to the Lebesgue measure on Ω. Let $\mathbb{M}(\Omega)$ be the space of scalar-valued functions on Ω that are Lebesgue-measurable, the spaces $L^p(\Omega)$, $1 \leq p \leq \infty$, are defined as

$$L^p(\Omega) \stackrel{\text{def}}{=} \{f \in \mathbb{M}(\Omega) : \|f\|_{L^p(\Omega)} < +\infty\},$$

with

$$\begin{aligned} \|f\|_{L^p(\Omega)} &= \left(\int_\Omega |f|^p \, \mathrm{d}\mathbf{x} \right)^{\frac{1}{p}}, \qquad && \forall\ 1 \leq p < \infty, \\ \|f\|_{L^\infty(\Omega)} &= \text{ess sup}_\Omega |f|, && p = \infty. \end{aligned}$$

The Sobolev space $W^{m,p}(\Omega)$ is the space of functions in $L^p(\Omega)$ whose distributional derivatives of order less than or equal to m belong to $L^p(\Omega)$, $m \geq 0$ being an integer and $1 \leq p \leq \infty$. When $p = 2$, $H^m(\Omega) = W^{m,2}(\Omega)$ is a Hilbert space if equipped with the scalar product

$$(f, v)_{m,\Omega} = \sum_{|\boldsymbol{\alpha}| \leq m} \int_\Omega D^{\boldsymbol{\alpha}} f \, D^{\boldsymbol{\alpha}} v \, \mathrm{d}\mathbf{x},$$

where $D^{\boldsymbol{\alpha}}$ denotes the distributional derivative with $\boldsymbol{\alpha} = [\alpha_1, ..., \alpha_d]$ a *multi-index* of non-negative integers. The associated norm is given by

$$\|f\|_{H^m(\Omega)} = \|f\|_{m,\Omega} = \sum_{|\boldsymbol{\alpha}| \leq m} \|D^{\boldsymbol{\alpha}} f\|_{L^p(\Omega)},$$

and the semi-norm by

$$|f|_{m,\Omega} = \left(\sum_{|\boldsymbol{\alpha}| = m} \|D^{\boldsymbol{\alpha}} f\|_{L^2(\Omega)} \right)^{\frac{1}{2}}.$$

Note that $L^2(\Omega) = H^0(\Omega)$ is a Hilbert space endowed with the scalar product

$$(f, v)_\Omega = \int_\Omega f \, v \, \mathrm{d}\mathbf{x},$$

and with the induced norm $\|f\|_{L^2(\Omega)} = \|f\|_{0,\Omega} = (f, f)^{\frac{1}{2}}$.

In the following, we also make use of the H^m subspaces

$$H_0^m(\Omega) \stackrel{\text{def}}{=} \{f \in H^m(\Omega) : f|_{\partial\Omega} = 0\}$$

and

$$H_{0,\Gamma}^m(\Omega) \stackrel{\text{def}}{=} \{f \in H^m(\Omega) : f|_\Gamma = 0,\ \Gamma \subseteq \partial\Omega\}.$$

The space $H_0^m(\Omega)$ (resp. $H_{0,\Gamma}^m(\Omega)$) consists of functions of $H^m(\Omega)$ with zero *trace* on the boundary $\partial\Omega$ (resp. $\Gamma \subseteq \partial\Omega$). A precise definition of trace for scalar and vector functions is reported for example in [QV97, Section 1.3]. Here, we limit ourselves to recall that any function belonging to $H^{m-1/2}(\Gamma)$, $m > 1/2$, is the trace on $\Gamma \subseteq \Omega$ of a function in $H^m(\Omega)$. For the space $H^1(\Omega)$, the associated trace operator on Γ is denoted with

$$\mathrm{Tr}_\Gamma : H^1(\Omega) \to H^{\frac{1}{2}}(\Gamma).$$

We finally mention that in the sequel, the symbol $[H^m(\Omega)]^d$ is used to indicate the space of d-dimensional vector functions whose components belong to $H^m(\Omega)$ (*e.g.* $[H^m(\Omega)]^3 = H^m(\Omega) \times H^m(\Omega) \times H^m(\Omega)$).

2.4.2 A first variational formulation

We aim at writing a first variational formulation for the problem (2.33)-(2.35). To this end, we first introduce the weak form for the fluid and the structure parts, (2.33) and (2.34) respectively, then we give the variational formulation of the whole coupled problem taking into account the coupling conditions (2.35). In view of the numerical discretization of the coupled problem, we assume here that the kinematic condition is imposed as a Dirichlet boundary condition for the fluid; whereas the continuity of stress is applied as a Neumann boundary condition for the structure (see Remark 2.6).

Formally, for the fluid, we define the functional spaces

$$\hat{V}^{\mathrm{f}} \stackrel{\mathrm{def}}{=} \left\{ \hat{\boldsymbol{v}}^{\mathrm{f}} : \hat{\Omega}^{\mathrm{f}} \to \mathbb{R}^d, \hat{\boldsymbol{v}}^{\mathrm{f}} \in [H^1(\hat{\Omega}^{\mathrm{f}})]^d \right\}, \tag{2.37}$$

$$V^{\mathrm{f}} \stackrel{\mathrm{def}}{=} \left\{ \boldsymbol{v}^{\mathrm{f}}(t) : \Omega^{\mathrm{f}}(t) \to \mathbb{R}^d,\ \boldsymbol{v}^{\mathrm{f}} = \hat{\boldsymbol{v}}^{\mathrm{f}} \circ \mathcal{A}_t^{-1}, \hat{\boldsymbol{v}}^{\mathrm{f}}|_{\Gamma_D^{\mathrm{f}}} = \mathbf{0} \right\}, \tag{2.38}$$

$$V_0^{\mathrm{f}} \stackrel{\mathrm{def}}{=} \left\{ \boldsymbol{v}^{\mathrm{f}}(t) : \Omega^{\mathrm{f}}(t) \to \mathbb{R}^d,\ \boldsymbol{v}^{\mathrm{f}} = \hat{\boldsymbol{v}}^{\mathrm{f}} \circ \mathcal{A}_t^{-1}, \hat{\boldsymbol{v}}^{\mathrm{f}}|_{\Gamma_D^{\mathrm{f}} \cup \hat{\Sigma}} = \mathbf{0} \right\}, \tag{2.39}$$

$$\hat{Q} \stackrel{\mathrm{def}}{=} \left\{ \hat{q} : \hat{\Omega}^{\mathrm{f}} \to \mathbb{R}^d, \hat{q} \in L^2(\hat{\Omega}^{\mathrm{f}}) \right\}, \tag{2.40}$$

$$Q \stackrel{\mathrm{def}}{=} \left\{ q(t) : \Omega^{\mathrm{f}}(t) \to \mathbb{R}^d, q = \hat{q} \circ \mathcal{A}_t^{-1} \right\}, \tag{2.41}$$

Notice that, contrary to the test functions $\hat{\boldsymbol{v}}^{\mathrm{f}} \in \hat{V}^{\mathrm{f}}$ and $\hat{q} \in \hat{Q}$ defined on the fixed domain $\hat{\Omega}^{\mathrm{f}}$, the functions $\boldsymbol{v}^{\mathrm{f}} \in V^{\mathrm{f}}$ and $q \in Q$ are time dependent. However, since $\hat{\boldsymbol{v}}^{\mathrm{f}}$ is independent of t, $\boldsymbol{v}^{\mathrm{f}}$ has zero ALE time-derivative

$$\left.\frac{\partial \boldsymbol{v}^{\mathrm{f}}}{\partial t}\right|_{\mathcal{A}} = \mathbf{0}. \tag{2.42}$$

The same property holds for q. For the sake of clarity and to avoid technicalities, we will simply denote the space of the unknowns by $X^{\mathrm{f}} \stackrel{\mathrm{def}}{=} [H^1(\Omega^{\mathrm{f}}(t))]^d$ and $M \stackrel{\mathrm{def}}{=} L^2(\Omega^{\mathrm{f}}(t))$, although the non cylindrical shape of the space-time domain would require a more precise notation.

By multiplying the fluid equation $(2.33)_{1,2}$ by $(\boldsymbol{v}^{\mathrm{f}}, q) \in V_0^{\mathrm{f}} \times Q$, integrating by parts and taking into account the boundary conditions, we get

$$\int_{\Omega^{\mathrm{f}}(t)} \rho^{\mathrm{f}} \frac{\partial \mathbf{u}}{\partial t}\Big|_{\mathcal{A}} \cdot \boldsymbol{v}^{\mathrm{f}} \,\mathrm{d}\mathbf{x} + \int_{\Omega^{\mathrm{f}}(t)} \rho^{\mathrm{f}} (\mathbf{u} - \mathbf{w}) \cdot \nabla \mathbf{u} \cdot \boldsymbol{v}^{\mathrm{f}} \,\mathrm{d}\mathbf{x} + \int_{\Omega^{\mathrm{f}}(t)} \boldsymbol{\sigma}^{\mathrm{f}}(\mathbf{u}, p) : \nabla \boldsymbol{v}^{\mathrm{f}} \,\mathrm{d}\mathbf{x} - \int_{\Gamma_N^{\mathrm{f}}} \mathbf{g} \cdot \boldsymbol{v}^{\mathrm{f}} \,\mathrm{d}\boldsymbol{\gamma} + \int_{\Omega^{\mathrm{f}}(t)} q \,\mathrm{div}\, \mathbf{u} \,\mathrm{d}\mathbf{x} = 0. \quad (2.43)$$

Using a change of variables in the first integral in combination with (2.42) and since ρ^{f} is assumed to be constant, it can be shown that

$$\int_{\Omega^{\mathrm{f}}(t)} \rho^{\mathrm{f}} \frac{\partial \mathbf{u}}{\partial t}\Big|_{\mathcal{A}} \cdot \boldsymbol{v}^{\mathrm{f}} \,\mathrm{d}\mathbf{x} = \frac{\mathrm{d}}{\mathrm{d}t} \int_{\Omega^{\mathrm{f}}(t)} \rho^{\mathrm{f}} \mathbf{u} \cdot \boldsymbol{v}^{\mathrm{f}} \,\mathrm{d}\mathbf{x} - \int_{\Omega^{\mathrm{f}}(t)} \rho^{\mathrm{f}} (\mathrm{div}\, \mathbf{w}) \mathbf{u} \cdot \boldsymbol{v}^{\mathrm{f}} \,\mathrm{d}\mathbf{x}.$$

Therefore, by inserting this equality in (2.43), the variational formulation for the fluid sub-problem reads:
For all $(\boldsymbol{v}^{\mathrm{f}}, q) \in V_0^{\mathrm{f}} \times Q$ and $t \in \mathbb{R}^+$, find $(\mathbf{u}(t), p(t)) \in X^{\mathrm{f}} \times M$, *a.e.* in t, satisfying $\mathbf{u} = \mathbf{w}$ on $\Sigma(t)$ and $\mathbf{u} = \mathbf{u}_D$ on Γ_D^{f}, and such that

$$\frac{\mathrm{d}}{\mathrm{d}t} \int_{\Omega^{\mathrm{f}}(t)} \rho^{\mathrm{f}} \mathbf{u} \cdot \boldsymbol{v}^{\mathrm{f}} \,\mathrm{d}\mathbf{x} + \int_{\Omega^{\mathrm{f}}(t)} \rho^{\mathrm{f}} (\mathbf{u} - \mathbf{w}) \cdot \nabla \mathbf{u} \cdot \boldsymbol{v}^{\mathrm{f}} \,\mathrm{d}\mathbf{x} - \int_{\Omega^{\mathrm{f}}(t)} \rho^{\mathrm{f}} (\mathrm{div}\, \mathbf{w}) \mathbf{u} \cdot \boldsymbol{v}^{\mathrm{f}} \,\mathrm{d}\mathbf{x} + \int_{\Omega^{\mathrm{f}}(t)} \boldsymbol{\sigma}^{\mathrm{f}}(\mathbf{u}, p) : \nabla \boldsymbol{v}^{\mathrm{f}} \,\mathrm{d}\mathbf{x} + \int_{\Omega^{\mathrm{f}}(t)} q \,\mathrm{div}\, \mathbf{u} \,\mathrm{d}\mathbf{x} = \int_{\Gamma_N^{\mathrm{f}}} \mathbf{g} \cdot \boldsymbol{v}^{\mathrm{f}} \,\mathrm{d}\boldsymbol{\gamma}. \quad (2.44)$$

For practical purposes, in the following, the variational formulation (2.44) will be replaced by the shorthand notation

$$A^{\mathrm{f}}(\mathbf{u}, p; \boldsymbol{v}^{\mathrm{f}}, q) = F^{\mathrm{f}}(\boldsymbol{v}^{\mathrm{f}}), \quad (2.45)$$

where

$$A^{\mathrm{f}}(\mathbf{u}, p; \boldsymbol{v}^{\mathrm{f}}, q) \stackrel{\mathrm{def}}{=} \frac{\mathrm{d}}{\mathrm{d}t} \int_{\Omega^{\mathrm{f}}(t)} \rho^{\mathrm{f}} \mathbf{u} \cdot \boldsymbol{v}^{\mathrm{f}} \,\mathrm{d}\mathbf{x} + \int_{\Omega^{\mathrm{f}}(t)} \rho^{\mathrm{f}} (\mathbf{u} - \mathbf{w}) \cdot \nabla \mathbf{u} \cdot \boldsymbol{v}^{\mathrm{f}} \,\mathrm{d}\mathbf{x} - \int_{\Omega^{\mathrm{f}}(t)} \rho^{\mathrm{f}} (\mathrm{div}\, \mathbf{w}) \mathbf{u} \cdot \boldsymbol{v}^{\mathrm{f}} \,\mathrm{d}\mathbf{x} + \int_{\Omega^{\mathrm{f}}(t)} \boldsymbol{\sigma}^{\mathrm{f}}(\mathbf{u}, p) : \nabla \boldsymbol{v}^{\mathrm{f}} \,\mathrm{d}\mathbf{x} + \int_{\Omega^{\mathrm{f}}(t)} q \,\mathrm{div}\, \mathbf{u} \,\mathrm{d}\mathbf{x},$$

and

$$F^{\mathrm{f}}(\boldsymbol{v}^{\mathrm{f}}) \stackrel{\mathrm{def}}{=} \int_{\Gamma_N^{\mathrm{f}}} \mathbf{g} \cdot \boldsymbol{v}^{\mathrm{f}} \,\mathrm{d}\boldsymbol{\gamma}.$$

The functional spaces associated with the structure problem are indicated with $\hat{V}^{\mathrm{s}}$ and $V^{\mathrm{s}} \stackrel{\mathrm{def}}{=} \hat{V}^{\mathrm{s}} \circ \boldsymbol{\varphi}_t^{-1}$. In the particular case of the elastodynamics equations they reads:

$$\hat{V}^{\mathrm{s}} \stackrel{\mathrm{def}}{=} \left\{ \hat{\boldsymbol{v}}^{\mathrm{s}} : \hat{\Omega}^{\mathrm{s}} \to \mathbb{R}^d, \hat{\boldsymbol{v}}^{\mathrm{s}} \in [H^1(\hat{\Omega}^{\mathrm{s}})]^d, \ \hat{\boldsymbol{v}}^{\mathrm{s}}|_{\hat{\Gamma}_D^{\mathrm{s}}} = \mathbf{0} \right\}, \quad (2.46)$$

$$V^{\mathrm{s}} \stackrel{\mathrm{def}}{=} \left\{ \boldsymbol{v}^{\mathrm{s}}(t) : \Omega^{\mathrm{s}}(t) \to \mathbb{R}^d, \ \boldsymbol{v}^{\mathrm{s}} = \hat{\boldsymbol{v}}^{\mathrm{s}} \circ \boldsymbol{\varphi}_t^{-1} \right\}. \quad (2.47)$$

Multiplying by $\hat{\boldsymbol{v}}^{\mathrm{s}} \in \hat{V}^{\mathrm{s}}$ the solid equation $(2.34)_1$, integrating by parts and taking into account the boundary conditions $(2.34)_{3,4}$ and the interface condition $(2.35)_3$, we get

$$\int_{\hat{\Omega}^{\mathrm{s}}} \hat{\rho}_0^{\mathrm{s}} \frac{\partial \hat{\mathbf{u}}^{\mathrm{s}}}{\partial t} \cdot \hat{\boldsymbol{v}}^{\mathrm{s}} \, \mathrm{d}\hat{\mathbf{x}} + \int_{\hat{\Omega}^{\mathrm{s}}} \hat{\boldsymbol{\Pi}} : \nabla_{\hat{\mathbf{x}}} \hat{\boldsymbol{v}}^{\mathrm{s}} \, \mathrm{d}\hat{\mathbf{x}} = \int_{\hat{\Gamma}_N^{\mathrm{s}}} \hat{J}^{\mathrm{s}} ||(\hat{\boldsymbol{F}}^{\mathrm{s}})^{-\mathrm{T}} \hat{\mathbf{n}}^{\mathrm{s}}|| \hat{\mathbf{h}} \cdot \hat{\boldsymbol{v}}^{\mathrm{s}} \, \mathrm{d}\hat{\boldsymbol{\gamma}} + \int_{\hat{\Sigma}} \hat{J}^{\mathrm{s}} \hat{\boldsymbol{\sigma}}^{\mathrm{f}} (\hat{\boldsymbol{F}}^{\mathrm{S}})^{-\mathrm{T}} \hat{\mathbf{n}}^{\mathrm{s}} \cdot \hat{\boldsymbol{v}}^{\mathrm{s}} \, \mathrm{d}\hat{\boldsymbol{\gamma}}. \quad (2.48)$$

Replacing $(2.34)_2$ in (2.48) and using the property (2.8) of the Piola transform, we obtain the following variational formulation for the structure sub-problem:
For all $\hat{\boldsymbol{v}}^{\mathrm{s}} \in \hat{V}^{\mathrm{s}}$, find $\hat{\boldsymbol{d}}(t) \in \hat{V}^{\mathrm{s}}$ such that

$$\int_{\hat{\Omega}^{\mathrm{s}}} \hat{\rho}_0^{\mathrm{s}} \frac{\partial^2 \hat{\boldsymbol{d}}}{\partial t^2} \cdot \hat{\boldsymbol{v}}^{\mathrm{s}} \, \mathrm{d}\hat{\mathbf{x}} + \int_{\hat{\Omega}^{\mathrm{s}}} \hat{\boldsymbol{\Pi}} : \nabla_{\hat{\mathbf{x}}} \hat{\boldsymbol{v}}^{\mathrm{s}} \, \mathrm{d}\hat{\mathbf{x}} = \int_{\hat{\Gamma}_N^{\mathrm{s}}} \hat{J}^{\mathrm{s}} ||(\hat{\boldsymbol{F}}^{\mathrm{s}})^{-\mathrm{T}} \hat{\mathbf{n}}^{\mathrm{s}}|| \hat{\mathbf{h}} \cdot \hat{\boldsymbol{v}}^{\mathrm{s}} \, \mathrm{d}\hat{\boldsymbol{\gamma}} - \int_{\Sigma(t)} \boldsymbol{\sigma}^{\mathrm{f}} \mathbf{n}^{\mathrm{f}} \cdot \boldsymbol{v}^{\mathrm{s}} \, \mathrm{d}\boldsymbol{\gamma}. \quad (2.49)$$

Also for the structure, we introduce the shorthand notation

$$A^{\mathrm{s}}(\hat{\boldsymbol{d}}; \hat{\boldsymbol{v}}^{\mathrm{s}}) = F^{\mathrm{s}}(\hat{\boldsymbol{v}}^{\mathrm{s}}) - \int_{\Sigma(t)} \boldsymbol{\sigma}^{\mathrm{f}} \mathbf{n}^{\mathrm{f}} \cdot \boldsymbol{v}^{\mathrm{s}} \, \mathrm{d}\boldsymbol{\gamma}, \quad (2.50)$$

where

$$A^{\mathrm{s}}(\hat{\boldsymbol{d}}; \hat{\boldsymbol{v}}^{\mathrm{s}}) \stackrel{\mathrm{def}}{=} \int_{\hat{\Omega}^{\mathrm{s}}} \hat{\rho}_0^{\mathrm{s}} \frac{\partial^2 \hat{\boldsymbol{d}}}{\partial t^2} \cdot \hat{\boldsymbol{v}}^{\mathrm{s}} \, \mathrm{d}\hat{\mathbf{x}} + \int_{\hat{\Omega}^{\mathrm{s}}} \hat{\boldsymbol{\Pi}} : \nabla_{\hat{\mathbf{x}}} \hat{\boldsymbol{v}}^{\mathrm{s}} \, \mathrm{d}\hat{\mathbf{x}},$$

and

$$F^{\mathrm{s}}(\hat{\boldsymbol{v}}^{\mathrm{s}}) \stackrel{\mathrm{def}}{=} \int_{\hat{\Gamma}_N^{\mathrm{s}}} \hat{J}^{\mathrm{s}} ||(\hat{\boldsymbol{F}}^{\mathrm{s}})^{-\mathrm{T}} \hat{\mathbf{n}}^{\mathrm{s}}|| \hat{\mathbf{h}} \cdot \hat{\boldsymbol{v}}^{\mathrm{s}} \, \mathrm{d}\hat{\boldsymbol{\gamma}}.$$

Before giving the variational formulation of the coupled problem, it must be observed that the last term on the right-hand side of (2.49) is not appropriate from the numerical point of view. Indeed, a direct approximation of $\int_{\Sigma(t)} \boldsymbol{\sigma}^{\mathrm{f}} \mathbf{n}^{\mathrm{s}} \cdot \hat{\boldsymbol{v}}^{\mathrm{s}} \, \mathrm{d}\boldsymbol{\gamma}$ might introduce a spurious energy at interface, leading to unstable numerical schemes. As a consequence, it is usually preferred to compute the fluid interface load as a residual of the fluid variational formulation, obtained by testing (2.44) with appropriate no vanishing test functions on $\Sigma(t)$. In detail, introducing a continuous linear lifting operator $\hat{\mathcal{L}} : [H^1(\hat{\Omega}^{\mathrm{s}})]^d \to [H^1(\hat{\Omega}^{\mathrm{f}})]^d$ such that $\hat{\mathcal{L}}\hat{\boldsymbol{v}}^{\mathrm{s}}$ satisfies

$$\begin{cases} \hat{\mathcal{L}}\hat{\boldsymbol{v}}^{\mathrm{s}} = \hat{\boldsymbol{v}}^{\mathrm{s}} & \text{on} \quad \hat{\Sigma}, \\ \hat{\mathcal{L}}\hat{\boldsymbol{v}}^{\mathrm{s}} = \mathbf{0} & \text{on} \quad \partial\hat{\Omega}^{\mathrm{f}} \backslash \hat{\Sigma}, \end{cases} \quad (2.51)$$

we have

$$\begin{aligned} \int_{\Sigma(t)} \boldsymbol{\sigma}^{\mathrm{f}} \mathbf{n}^{\mathrm{f}} \cdot \hat{\boldsymbol{v}}^{\mathrm{s}} \, \mathrm{d}\boldsymbol{\gamma} \quad = \quad & \frac{\mathrm{d}}{\mathrm{d}t} \int_{\Omega^{\mathrm{f}}(t)} \rho^{\mathrm{f}} \mathbf{u} \cdot \mathcal{L}\boldsymbol{v}^{\mathrm{s}} \, \mathrm{d}\mathbf{x} + \int_{\Omega^{\mathrm{f}}(t)} \rho^{\mathrm{f}} (\mathbf{u} - \mathbf{w}) \cdot \nabla \mathbf{u} \cdot \mathcal{L}\boldsymbol{v}^{\mathrm{s}} \, \mathrm{d}\mathbf{x} \\ & - \int_{\Omega^{\mathrm{f}}(t)} \rho^{\mathrm{f}} (\operatorname{div} \mathbf{w}) \mathbf{u} \cdot \mathcal{L}\boldsymbol{v}^{\mathrm{s}} \, \mathrm{d}\mathbf{x} + \int_{\Omega^{\mathrm{f}}(t)} \boldsymbol{\sigma}^{\mathrm{f}}(\mathbf{u}, p) : \nabla \mathcal{L}\boldsymbol{v}^{\mathrm{s}} \, \mathrm{d}\mathbf{x}, \end{aligned}$$

where $\mathcal{L}\boldsymbol{v}^{\mathrm{s}} \overset{\text{def}}{=} \hat{\mathcal{L}}\hat{\boldsymbol{v}}^{\mathrm{s}} \circ \mathcal{A}_t^{-1}$.

In summary, under variational formulation, the problem (2.33)-(2.35) can be rewritten as
For all $(\boldsymbol{v}^{\mathrm{f}}, q, \hat{\boldsymbol{v}}^{\mathrm{s}}) \in V_0^{\mathrm{f}} \times Q \times \hat{V}^{\mathrm{s}}$ and $t \in \mathbb{R}^+$, find $(\mathbf{u}(t), p(t), \hat{\boldsymbol{d}}(t)) \in X^{\mathrm{f}} \times M \times \hat{V}^{\mathrm{s}}$, satisfying $\mathbf{u} = \mathbf{w}$ on $\Sigma(t)$, $\mathbf{u} = \mathbf{u}_D$ on Γ_D^{f}, and such that

- Geometry sub-problem:

$$\hat{\boldsymbol{d}}^{\mathrm{f}} = \mathrm{Ext}(\hat{\boldsymbol{d}}_{|\Sigma}), \quad \hat{\mathbf{w}} = \partial_t \hat{\boldsymbol{d}}^{\mathrm{f}} \quad \text{in} \quad \hat{\Omega}^{\mathrm{f}}, \quad \Omega^{\mathrm{f}}(t) = (\mathbf{I}_{\Omega^{\mathrm{f}}} + \hat{\boldsymbol{d}}^{\mathrm{f}})(\hat{\Omega}^{\mathrm{f}}), \tag{2.52}$$

- Fluid sub-problem:

$$A^{\mathrm{f}}(\mathbf{u}, p; \boldsymbol{v}^{\mathrm{f}}, q) = F^{\mathrm{f}}(\boldsymbol{v}^{\mathrm{f}}), \tag{2.53}$$

- Solid sub-problem:

$$A^{\mathrm{s}}(\hat{\boldsymbol{d}}; \hat{\boldsymbol{v}}^{\mathrm{s}}) = F^{\mathrm{s}}(\hat{\boldsymbol{v}}^{\mathrm{s}}) - \langle \mathcal{R}(\mathbf{u}, p), \mathcal{L}\boldsymbol{v}^{\mathrm{s}} \rangle, \tag{2.54}$$

where we introduced the notation

$$\begin{aligned} \langle \mathcal{R}(\mathbf{u}, p), \mathcal{L}\boldsymbol{v}^{\mathrm{s}} \rangle \overset{\text{def}}{=} & \frac{\mathrm{d}}{\mathrm{d}t} \int_{\Omega^{\mathrm{f}}(t)} \rho^{\mathrm{f}} \mathbf{u} \cdot \mathcal{L}\boldsymbol{v}^{\mathrm{s}} \, \mathrm{d}\mathbf{x} + \int_{\Omega^{\mathrm{f}}(t)} \rho^{\mathrm{f}} (\mathbf{u} - \mathbf{w}) \cdot \nabla \mathbf{u} \cdot \mathcal{L}\boldsymbol{v}^{\mathrm{s}} \, \mathrm{d}\mathbf{x} \\ & - \int_{\Omega^{\mathrm{f}}(t)} \rho^{\mathrm{f}} (\operatorname{div} \mathbf{w}) \mathbf{u} \cdot \mathcal{L}\boldsymbol{v}^{\mathrm{s}} \, \mathrm{d}\mathbf{x} + \int_{\Omega^{\mathrm{f}}(t)} \boldsymbol{\sigma}^{\mathrm{f}}(\mathbf{u}, p) : \nabla \mathcal{L}\boldsymbol{v}^{\mathrm{s}} \, \mathrm{d}\mathbf{x}. \end{aligned}$$

Remark 2.7 *For the sake of simplicity, the notation introduced in (2.50) for the structure sub-problem and the corresponding functional spaces V^{s}, $\hat{V}^{\mathrm{s}}$ will be used in the following to identify a general structure problem that could be defined by the elastodynamics equations as well as by a reduced model (*e.g. *1D models in 2D or shell models in 3D). We refer for example to [dSGB08] for a proper definition of the variational formulation of a possible 1D structure model and to [CB03] for shell models.*

2.4.3 A second formulation based on Lagrange multipliers

The specificity of the variational formulation introduced above relies on the particular choice of the functional spaces (2.37)-(2.41) and (2.46)-(2.47). Nonetheless other choices could be done. In this second formulation we make a different choice of the functional spaces and we relax the kinematic constraint imposed strongly in (2.52)-(2.54): the kinematic constraint is weakly imposed by means of a Lagrange multiplier technique.

Let us consider for the fluid and structure test functions the spaces V^{f} and $\hat{V}^{\mathrm{s}}$, respectively. We observe that this choice of spaces does not specify the way to couple fluid and structure. In this case a possible way to enforce the coupling is to introduce at the interface a third space, the Lagrange multiplier space, formally:

$$\Lambda \overset{\text{def}}{=} \left\{ \boldsymbol{\mu} : \Sigma(t) \to \mathbb{R}^d, \boldsymbol{\mu} \in [H^{-1/2}(\Sigma(t))]^d \right\}, \tag{2.55}$$

associated with the constraint $\mathrm{Tr}_\Sigma\, \boldsymbol{v}^{\mathrm{f}} = \mathrm{Tr}_\Sigma\, \boldsymbol{v}^{\mathrm{s}}$. The corresponding variational formulation reads:
For all $(\boldsymbol{v}^{\mathrm{f}}, q, \hat{\boldsymbol{v}}^{\mathrm{s}}, \boldsymbol{\mu}) \in V^{\mathrm{f}} \times Q \times \hat{V}^{\mathrm{s}} \times \Lambda$ and $t \in \mathbb{R}^+$, find $(\mathbf{u}(t), p(t), \hat{\boldsymbol{d}}(t), \boldsymbol{\lambda}(t)) \in X^{\mathrm{f}} \times M \times \hat{V}^{\mathrm{s}} \times \Lambda$, satisfying $\mathbf{u} = \mathbf{u}_D$ on Γ_D^{f}, and such that

- Geometry sub-problem:

$$\hat{\boldsymbol{d}}^{\mathrm{f}} = \mathrm{Ext}(\hat{\boldsymbol{d}}_{|\Sigma}), \quad \hat{\mathbf{w}} = \partial_t \hat{\boldsymbol{d}}^{\mathrm{f}} \quad \text{in} \quad \hat{\Omega}^{\mathrm{f}}, \quad \Omega^{\mathrm{f}}(t) = (\mathbf{I}_{\Omega^{\mathrm{f}}} + \hat{\boldsymbol{d}}^{\mathrm{f}})(\hat{\Omega}^{\mathrm{f}}), \tag{2.56}$$

- Fluid sub-problem:

$$A^{\mathrm{f}}(\mathbf{u}, p; \boldsymbol{v}^{\mathrm{f}}, q) + \langle \boldsymbol{\lambda}, \boldsymbol{v}^{\mathrm{f}} \rangle_\Sigma = F^{\mathrm{f}}(\boldsymbol{v}^{\mathrm{f}}), \tag{2.57}$$

- Solid sub-problem:

$$A^{\mathrm{s}}(\hat{\boldsymbol{d}}; \hat{\boldsymbol{v}}^{\mathrm{s}}) - \langle \boldsymbol{\lambda}, \boldsymbol{v}^{\mathrm{s}} \rangle_\Sigma = F^{\mathrm{s}}(\hat{\boldsymbol{v}}^{\mathrm{s}}), \tag{2.58}$$

- Coupling condition:

$$\langle \boldsymbol{\mu}, \mathbf{u} \rangle_\Sigma = \langle \boldsymbol{\mu}, \mathbf{w} \rangle_\Sigma, \tag{2.59}$$

where $\langle \cdot, \cdot \rangle_\Sigma$ denotes the duality pairing on $[H^{-1/2}(\Sigma(t))]^d \times [H^{1/2}(\Sigma(t))]^d$. Note that within this formalism, the coupling condition $(2.35)_3$ is implicitly handled since $\langle \boldsymbol{\lambda}, \boldsymbol{v}^{\mathrm{f}} \rangle_\Sigma$ and $\langle \boldsymbol{\lambda}, \boldsymbol{v}^{\mathrm{s}} \rangle_\Sigma$ represent the variational forms of the load acting on the fluid and on the structure respectively. As a matter of fact, integrating by parts the fluid and structure sub-problems, it can be shown that $\boldsymbol{\lambda} = -\boldsymbol{\sigma}^{\mathrm{f}} \mathbf{n}^{\mathrm{f}}$ and $\boldsymbol{\lambda} = \boldsymbol{\sigma}^{\mathrm{s}} \mathbf{n}^{\mathrm{s}}$ respectively (see for example [LTM00]).

A Lagrange Multiplier/Fictitious Domain method for immersed structures. The use of Lagrange multipliers to take into account the coupling between a fluid and an immersed structure (rigid or flexible) is the base of the so-called Lagrange Multiplier/Fictitious Domain method [GPP94]. Originally developed to efficiently solve Dirichlet problems characterized by complex domains [GPP94], it has been extended to the simulations of fluid flows interacting with moving immersed rigid particles in [GPHJ99, GPH+01]. Later it has also been applied to the interaction with immersed flexible structures, either using Lagrange multipliers located on the structure surface (see [Baa01, dH04, vLADB04, dSGB08]), or Lagrange multipliers located on the structure volume for thick solids [Yu05].

The general idea of the method could be summarized in these two steps:

1. Extend the problem defined on a geometrically complex (possibly time-dependent) domain Ω to a larger, simpler domain Ω_{FD} (the "fictitious domain"), embedding the original one ($\Omega \subseteq \Omega_{FD}$).

2. To ensure that the solution on Ω_{FD} matches the original one on Ω, solve the extended problem enforcing the boundary/interface conditions of the original problem on $\partial\Omega$ by means of Lagrange multipliers.

The FD formulation for fluid-structure interaction problems is here presented in the case where the fluid interacts with an immersed thin structure (see Figure 2.2). In this configuration, the structure domain Ω^{s} is coincident with the fluid-structure interface Σ, that is $\Omega^{\mathrm{s}} \equiv \Sigma \subset \mathbb{R}^d$, and $\Omega^{\mathrm{f}} = (\Omega^{\mathrm{f}^+} \cup \Omega^{\mathrm{f}^-} \cup \Sigma) \subset \mathbb{R}^d$ is fixed.

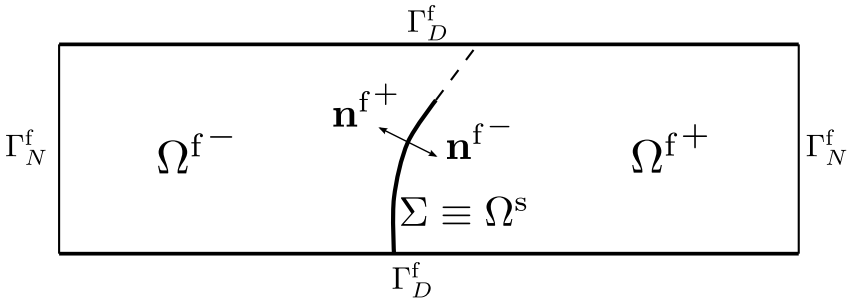

Figure 2.2: Geometry description.

Note that in this case the fluid domain overlaps the physical region occupied by the immersed structure domain (*i.e.* $\Omega^{\mathrm{s}} \equiv \Sigma \subset \Omega^{\mathrm{f}}$). The fluid domain represents therefore the fictitious domain Ω_{FD} and the Lagrange multipliers are used to prescribe the coupling conditions on Σ. The FD variational formulation of the fluid-structure interaction problem considered reads:
For all $(\boldsymbol{v}^{\mathrm{f}}, q, \hat{\boldsymbol{v}}^{\mathrm{s}}, \boldsymbol{\mu}) \in V^{\mathrm{f}} \times Q \times \hat{V}^{\mathrm{s}} \times \Lambda$ and $t \in \mathbb{R}^+$, find $(\mathbf{u}(t), p(t), \hat{\boldsymbol{d}}(t), \boldsymbol{\lambda}(t)) \in X^{\mathrm{f}} \times M \times \hat{V}^{\mathrm{s}} \times \Lambda$, satisfying $\mathbf{u} = \mathbf{u}_D$ on Γ_D^{f}, and such that

- Fluid sub-problem:

$$A^{\mathrm{f}}(\mathbf{u}, p; \boldsymbol{v}^{\mathrm{f}}, q) + \langle \boldsymbol{\lambda}, \boldsymbol{v}^{\mathrm{f}} \rangle_{\Sigma} = F^{\mathrm{f}}(\boldsymbol{v}^{\mathrm{f}}), \tag{2.60}$$

- Solid sub-problem:

$$A^{\mathrm{s}}(\hat{\boldsymbol{d}}; \hat{\boldsymbol{v}}^{\mathrm{s}}) - \langle \boldsymbol{\lambda}, \boldsymbol{v}^{\mathrm{s}} \rangle_{\Sigma} = F^{\mathrm{s}}(\hat{\boldsymbol{v}}^{\mathrm{s}}), \tag{2.61}$$

- Coupling condition:

$$\langle \boldsymbol{\mu}, \mathbf{u} \rangle_{\Sigma} = \langle \boldsymbol{\mu}, \partial_t \boldsymbol{d} \rangle_{\Sigma}, \tag{2.62}$$

Apart from the fluid domain considered and from the choice of the structure model, it is important to observe that the variational problem (2.60)-(2.62) is formally equivalent to (2.57)-(2.59). However it must be noticed that in this case, the Lagrange multipliers $\boldsymbol{\lambda}$ define the jump of the hydrodynamic stress through the immersed solid:

$$\boldsymbol{\lambda} = -(\boldsymbol{\sigma}^{\mathrm{f}^-}\mathbf{n}^{\mathrm{f}^-} + \boldsymbol{\sigma}^{\mathrm{f}^+}\mathbf{n}^{\mathrm{f}^+}).$$

This can be proved by splitting the fluid problem in two subproblems defined on the left hand side and on the right hand side of the structure, respectively on Ω^{f^-} and on Ω^{f^+}, and using the Green's formula in the integrals over Ω^{f^-} and Ω^{f^+} together with the fact that $(\mathbf{u}, p)$ is solution of the fluid problem (see [CDdSG+05, Remark 3.1]).

2.5 Numerical discretization of the coupled FSI problem

2.5.1 Semi-discretization in space

Space discretization techniques for fluid-structure problems can be roughly divided in two families: moving grid and fixed grid methods.

In moving grid methods, the fluid mesh moves and deforms to follow the structure. The Arbitrary Lagrangian-Eulerian (ALE) formulation is used for the fluid equations, which provides an accurate and reliable approach for the computation of the fluid loads on the structure. In computational hemodynamics, this approach is common for blood - artery wall (see *e.g.* [FFGQ09]) and blood - myocardium interaction. For blood - valves interaction some results have been reported both for natural and prosthetic valves [CBHP06, MÖ9, SB09]. However, the large structural displacements of the valve imply important deformations of the fluid mesh and frequent remeshing. Moreover, at the closure of the valve, the change of topology makes the proper definition of the ALE formulation difficult.

Fixed grid methods are more versatile at simulating FSI problems involving large structural displacements with possible topological changes. In such methods the fluid domain is generally discretized in a fixed computational grid, while the structure domain is discretized in a separate grid. Fluid and structure meshes are therefore totally independent. The coupling can be done in different ways depending on the chosen mathematical formulation. The most common approaches are the Immersed Boundary method [MPY82, Pes02] and the FD method [GPP94, Baa01]. Major drawbacks of fixed grid methods are that they could lead to leaking across the immersed solid or introduce inaccuracies in the computation of shear stresses on the solid if not properly discretized. We refer to [dS07] and to Chapter 6 for a discussion on space discretization issues for the FD approach.

Space discretization of the fluid and solid sub-problems. We use the finite element method to discretize in space the variational formulations of the fluid-structure problem. Assuming $\hat{\Omega}^{\mathrm{f}}$ (resp. $\hat{\Omega}^{\mathrm{s}}$) a polygonal (in 2D) or polyhedral (in 3D) domain, let $\{\mathcal{T}_h^{\mathrm{f}}\}_{0\leq h\leq 1}$ (resp. $\{\mathcal{T}_H^{\mathrm{s}}\}_{0\leq H\leq 1}$) be the family of triangulations of the domain $\hat{\Omega}^{\mathrm{f}}$ (resp. $\hat{\Omega}^{\mathrm{s}}$). For each triangulation the subscripts $h, H \in (0,1]$ refer to the level of refinement of the triangulation. In particular, h is defined as

$$h \stackrel{\mathrm{def}}{=} \max_{K\in\mathcal{T}_h^{\mathrm{f}}} h_K,$$

with h_K the diameter of the element K. We define H in an analogous way. In addition, we assume that both families of triangulations are quasi-uniform. For instance, for $\{\mathcal{T}_h^{\mathrm{f}}\}_{0<h\leq 1}$, it implies that

$$\frac{h_K}{\rho_K} < C_R, \quad h_K \geq C_U h, \quad \forall K \in \mathcal{T}_h^{\mathrm{f}}, \quad \forall h \in (0,1], \tag{2.63}$$

where ρ_K stands for the diameter of the largest inscribed ball in K and $C_R, C_U > 0$ are fixed constants. We also define $\{\mathcal{T}_h^{\mathrm{f}}(t)\}_{0\leq h\leq 1}$, for every $t > 0$, as a suitable

family of triangulations of the domain $\Omega^{\mathrm{f}}(t)$ derived from $\{\mathcal{T}_h^{\mathrm{f}}\}_{0\leq h\leq 1}$ through the ALE mapping.

Considering the discretization of the fluid sub-problem, let $\hat{Q}_h$ be an internal Lagrange finite element approximation of $L^2(\hat{\Omega}^{\mathrm{f}})$, and $\hat{X}_h^{\mathrm{f}}$ an internal $\mathcal{C}^0$ finite element approximation of $\hat{X}^{\mathrm{f}}$. We also introduce in the same way the spaces X_h^{f}, V_h^{f} and $V_{h,0}^{\mathrm{f}}$ in the current configuration. In general, the spaces X_h^{f} and Q_h, used to approximate respectively the velocity and the pressure unknowns, should be chosen in such a way that every couple $(\boldsymbol{v}_h^{\mathrm{f}}, q_h)$ in $X_h^{\mathrm{f}} \times Q_h$ satisfies the well-known *inf-sup condition* (or LBB condition) [Bre74, BF91]. Admissible choices of the finite element spaces are for example the pairs $\mathbb{P}_2 - \mathbb{P}_1$, $(\mathbb{P}_2 iso \mathbb{P}_1) - \mathbb{P}_1$ and $\mathbb{P}_1^b - \mathbb{P}_1$. An alternative to using inf-sup stable space pairs is to resort to stabilization techniques (*e.g.* [FF92]), which modify the discrete problem so that it is stable for equal order velocity-pressure interpolations. Note that for simplicity the same notation is used for the test functions and the unknowns spaces for the pressure, which is an abuse of notation in the framework of the ALE formulation. Most of the numerical computations performed in this work are based on this latter technique, using a stabilized $\mathbb{P}_1 - \mathbb{P}_1$ pair. Considering the discretization of the solid sub-problem, we denote with $\hat{V}_H^{\mathrm{s}}$ the internal, at least $\mathcal{C}^0$, finite element space approximation of $\hat{V}^{\mathrm{s}}$. For example, for the three dimensional elastodynamics equations, V_H^{s} represents the $\mathbb{P}_1$ finite element space; for the shell model, $\hat{V}_H^{\mathrm{s}}$ defines the MITC4 general shell element[1] space.

For the sake of generality, in the following, we adopt the notations

$$A_h^{\mathrm{f}}(\mathbf{u}_h, p_h; \boldsymbol{v}_h^{\mathrm{f}}, q_h) = F_h^{\mathrm{f}}(\boldsymbol{v}_h^{\mathrm{f}}), \tag{2.64}$$

$$A_H^{\mathrm{s}}(\hat{\boldsymbol{d}}_H; \hat{\boldsymbol{v}}_H^{\mathrm{s}}) = F_H^{\mathrm{s}}(\hat{\boldsymbol{v}}_H^{\mathrm{s}}), \tag{2.65}$$

to identify the semi-discretization in space of the variational forms

$$A^{\mathrm{f}}(\mathbf{u}, p; \boldsymbol{v}^{\mathrm{f}}, q) = F^{\mathrm{f}}(\boldsymbol{v}^{\mathrm{f}}),$$

$$A^{\mathrm{s}}(\hat{\boldsymbol{d}}; \hat{\boldsymbol{v}}^{\mathrm{s}}) = F^{\mathrm{s}}(\hat{\boldsymbol{v}}^{\mathrm{s}}),$$

whose symbols have been introduced in Section 2.4.2. The variables $(\mathbf{u}_h(t), p_h(t), \hat{\boldsymbol{d}}_H(t)) \in X_h^{\mathrm{f}} \times Q_h \times \hat{V}_H^{\mathrm{s}}$ are the finite element approximations of the velocity $\mathbf{u}$, of the pressure p and of the structure displacement $\hat{\boldsymbol{d}}$, respectively.

Space discretization of the coupling conditions in the ALE formulation. The space semi-discretization of the coupling conditions strictly depends on the conformity of the fluid and structure discretizations. The non-conformity of the discretizations could be related either to the choice of the finite elements spaces (*e.g.* $\mathbb{P}_2 - \mathbb{P}_1$ for the fluid, $\mathbb{P}_1$ for the structure) and/or to the matching of the fluid and structure meshes at the interface Σ (see Figure 2.3).

[1] The MITC4 finite element has five degrees of freedom per node: the three components of the displacement and the two parameters which define the variation of the unit vector. It is known to be reliable and effective in the two asymptotic states, membrane and bending, and is almost free of locking thanks to a particular interpolation strategy resorted to for the different components of the strain tensor. We refer to [Bat96, CB03, Vid08] for more details.

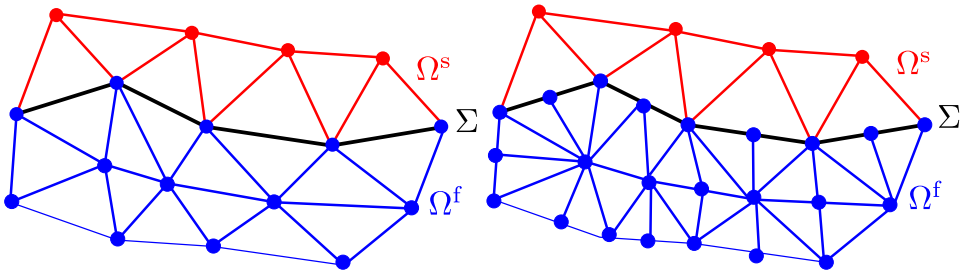

(a) matching grids (b) non-matching grids

Figure 2.3: Examples of matching and non-matching grids.

In the case of non-conforming discretizations, it is mandatory to introduce an interface matching operator $\pi_h : \hat{V}_H^s(\Sigma) \to \hat{X}_h^f(\Sigma)$, where $\hat{V}_H^s(\Sigma)$ (resp. $\hat{X}_h^f(\Sigma)$) stands for the trace finite element space associated with $\hat{V}_H^s$ (resp. $\hat{X}_h^f$). Then the fluid-structure problem (2.52)-(2.54) semi-discretized in space reads:
For all $(\boldsymbol{v}_h^f, q_h, \hat{\boldsymbol{v}}_H^s) \in V_{h,0}^f \times Q_h \times \hat{V}_H^s$ and $t \in \mathbb{R}^+$, find $(\mathbf{u}_h(t), p_h(t), \hat{\boldsymbol{d}}_H(t)) \in X_h^f \times Q_h \times \hat{V}_H^s$, satisfying $\mathbf{u}_h = \mathbf{w}_h$ on $\Sigma(t)$, $\mathbf{u}_h = \mathbf{u}_D$ on Γ_D^f, and such that

- Geometry sub-problem:

$$\hat{\boldsymbol{d}}_h^f = \mathrm{Ext}_h(\hat{\boldsymbol{d}}_{H|\Sigma}), \quad \hat{\mathbf{w}}_h = \partial_t \hat{\boldsymbol{d}}_h^f \quad \text{in} \quad \hat{\Omega}^f, \quad \Omega^f(t) = (\mathbf{I}_{\Omega^f} + \hat{\boldsymbol{d}}_h^f)(\hat{\Omega}^f), \tag{2.66}$$

- Fluid sub-problem:

$$A_h^f(\mathbf{u}_h, p_h; \boldsymbol{v}_h^f, q_h) = F_h^f(\boldsymbol{v}_h^f), \tag{2.67}$$

- Solid sub-problem:

$$A_H^s(\hat{\boldsymbol{d}}_H; \hat{\boldsymbol{v}}_H^s) = F_H^s(\hat{\boldsymbol{v}}_H^s) - \langle \mathcal{R}(\mathbf{u}_h, p_h), \mathcal{L}_h \boldsymbol{v}_H^s \rangle, \tag{2.68}$$

where the operator $\mathcal{L}_h : V_H^s(\Sigma) \to X_h^f$ stands for a given discrete lifting operator satisfying

$$\mathcal{L}_h(\mathbf{b}_H) = \pi_h(\mathbf{b}_H) \quad \text{on} \quad \Sigma. \tag{2.69}$$

Possible choices for $\mathcal{L}_h$ are discussed in Chapters 3 and 4. The operator π_h can be, for instance, the standard Lagrange interpolant (pointwise matching) or a projection based operator (see for example [FLLT98, GM98, AG09]). We will deal with the different types of matching operators in Chapter 3. In the remaining part of this chapter, we can assume for the sake of simplicity that the fluid and structure discretizations are conforming on the interface Σ (*i.e.* $\pi_h = \mathcal{I}_h$, being $\mathcal{I}_h$ the discrete identity operator).

Coupling conditions based on the Nitsche's method. In the semi-discrete problem (2.66)-(2.68) the coupling conditions are strongly imposed on the fluid-structure interface Σ. However, as already mentioned, the coupling conditions

could be also weakly imposed. A classical technique to impose in a weak sense the transmission conditions at the interface is the Lagrange multiplier approach presented in Section 2.4.3. Another approach is the so-called Nitsche's method. Introduced in 1971 to easily handle weakly Dirichlet boundary conditions without the use of Lagrange multipliers [Nit71], this technique has been later extended for the treatment of various interface problems (see [Han05] for a review). In the context of fluid-structure interaction important results are given in [HH03, HHS04, BF09].

The use of the Nitsche's method to enforce the transmission conditions in a weak sense leads to the following variational formulation of the coupled problem:
For all $(\boldsymbol{v}_h^{\mathrm{f}}, q_h, \hat{\boldsymbol{v}}_H^{\mathrm{s}}) \in V_h^{\mathrm{f}} \times Q_h \times \hat{V}_H^{\mathrm{s}}$ and $t \in \mathbb{R}^+$, find $(\mathbf{u}_h(t), p_h(t), \hat{\boldsymbol{d}}_H(t)) \in X_h^{\mathrm{f}} \times Q_h \times \hat{V}_H^{\mathrm{s}}$, satisfying $\mathbf{u}_h = \mathbf{u}_D$ on Γ_D^{f}, and such that

- Geometry sub-problem:

$$\hat{\boldsymbol{d}}_h^{\mathrm{f}} = \mathrm{Ext}_h(\hat{\boldsymbol{d}}_{H|\Sigma}), \quad \hat{\mathbf{w}}_h = \partial_t \hat{\boldsymbol{d}}_h^{\mathrm{f}} \quad \text{in} \quad \hat{\Omega}^{\mathrm{f}}, \quad \Omega^{\mathrm{f}}(t) = (\mathbf{I}_{\Omega^{\mathrm{f}}} + \hat{\boldsymbol{d}}_h^{\mathrm{f}})(\hat{\Omega}^{\mathrm{f}}), \tag{2.70}$$

- Fluid-structure sub-problem:

$$\begin{aligned} &A_h^{\mathrm{f}}(\mathbf{u}_h, p_h; \boldsymbol{v}_h^{\mathrm{f}}, q_h) + A_H^{\mathrm{s}}(\hat{\boldsymbol{d}}_H; \hat{\boldsymbol{v}}_H^{\mathrm{s}}) \\ &\underbrace{+\gamma \frac{\mu}{h} \int_{\Sigma(t)} (\mathbf{u}_h - \partial_t \boldsymbol{d}_H) \cdot (\boldsymbol{v}_h^{\mathrm{f}} - \boldsymbol{v}_H^{\mathrm{s}}) \, \mathrm{d}\boldsymbol{\gamma}}_{\mathcal{T}_1} \underbrace{- \int_{\Sigma(t)} \boldsymbol{\sigma}^{\mathrm{f}}(\mathbf{u}_h, p_h)\mathbf{n}^{\mathrm{f}} \cdot (\boldsymbol{v}_h^{\mathrm{f}} - \boldsymbol{v}_H^{\mathrm{s}}) \, \mathrm{d}\boldsymbol{\gamma}}_{\mathcal{T}_2} \\ &\underbrace{- \int_{\Sigma(t)} (\mathbf{u}_h - \partial_t \boldsymbol{d}_H) \cdot \boldsymbol{\sigma}^{\mathrm{f}}(\alpha \boldsymbol{v}_h^{\mathrm{f}}, -q_h)\mathbf{n}^{\mathrm{f}} \, \mathrm{d}\boldsymbol{\gamma}}_{\mathcal{T}_3} = F_h^{\mathrm{f}}(\boldsymbol{v}_h^{\mathrm{f}}) + F_H^{\mathrm{s}}(\hat{\boldsymbol{v}}_H^{\mathrm{s}}). \end{aligned} \tag{2.71}$$

Term $\mathcal{T}_1$ imposes the kinematic condition (2.30) at the interface, the positive dimensionless parameter γ is the so called *Nitsche's penalty parameter*, μ and h indicate the fluid viscosity and the fluid mesh size, respectively. Term $\mathcal{T}_2$ is a consistency term, added at the interface, involving normal loads across the interface (derived from condition (2.31)). Finally, term $\mathcal{T}_3$ is used to symmetrize the problem, the parameter α taking values in $\{-1, 1\}$. The variational formulation (2.71) is symmetric for $\alpha = 1$, non-symmetric for $\alpha = -1$.

Remark 2.8 *The Nitsche's method resembles a mesh-dependent penalty method, but with added consistency terms (term $\mathcal{T}_2$). Note that this formulation allows to deduce optimal order error estimates with preserved condition number for a quasi-uniform mesh. Pure penalty methods, in contrast, are not consistent, and optimal error estimates require degrading the condition number for higher polynomial approximation [BHS03].*

In view of the presentation of the partitioned procedures, it is finally useful to provide the fluid and structure sub-problems corresponding to the variational formulation (2.71):

- Fluid sub-problem:

$$A_h^{\mathrm{f}}(\mathbf{u}_h, p_h; \boldsymbol{v}_h^{\mathrm{f}}, q_h) + \gamma \frac{\mu}{h} \int_{\Sigma(t)} (\mathbf{u}_h - \partial_t \boldsymbol{d}_h) \cdot \boldsymbol{v}_h^{\mathrm{f}} \, \mathrm{d}\boldsymbol{\gamma} - \int_{\Sigma(t)} \boldsymbol{\sigma}^{\mathrm{f}}(\mathbf{u}_h, p_h)\mathbf{n}^{\mathrm{f}} \cdot \boldsymbol{v}_h^{\mathrm{f}} \, \mathrm{d}\boldsymbol{\gamma} - \int_{\Sigma(t)} (\mathbf{u}_h - \partial_t \boldsymbol{d}_H) \cdot \boldsymbol{\sigma}^{\mathrm{f}}(\alpha \boldsymbol{v}_h^{\mathrm{f}}, -q_h)\mathbf{n}^{\mathrm{f}} \, \mathrm{d}\boldsymbol{\gamma} = F_h^{\mathrm{f}}(\boldsymbol{v}_h^{\mathrm{f}}). \quad (2.72)$$

- Structure sub-problem:

$$A_H^{\mathrm{s}}(\hat{\boldsymbol{d}}_H; \hat{\boldsymbol{v}}_H^{\mathrm{s}}) + \gamma \frac{\mu}{h} \int_{\Sigma(t)} (\partial_t \boldsymbol{d}_h - \mathbf{u}_h) \cdot \boldsymbol{v}_H^{\mathrm{s}} \, \mathrm{d}\boldsymbol{\gamma} + \int_{\Sigma(t)} \boldsymbol{\sigma}^{\mathrm{f}}(\mathbf{u}_h, p_h)\mathbf{n}^{\mathrm{f}} \cdot \boldsymbol{v}_H^{\mathrm{s}} \, \mathrm{d}\boldsymbol{\gamma} = F_H^{\mathrm{s}}(\hat{\boldsymbol{v}}_H^{\mathrm{s}}). \quad (2.73)$$

Space discretization of the coupling conditions in the FD formulation. We now address the space discretization of the fluid-structure interaction problem in case of the Lagrange Multiplier/Fictitious Domain formulation. Figure 2.4 provides an example of the fluid and structure meshes for the mechanical system given in Figure 2.2. Note that in this case, the grids are non-conforming, the fluid mesh is fixed and the interface nodes coincide with the structure nodes.

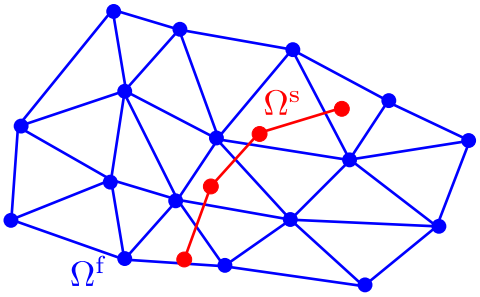

Figure 2.4: Example of non-conforming grids in the FD case.

The space semi-discrete formulation corresponding to the variational problem (2.60)-(2.62) reads:
For all $(\boldsymbol{v}_h^{\mathrm{f}}, q_h, \hat{\boldsymbol{v}}_H^{\mathrm{s}}, \boldsymbol{\mu}_h) \in V_h^{\mathrm{f}} \times Q_h \times \hat{V}_H^{\mathrm{s}} \times \Lambda_h$ and $t \in \mathbb{R}^+$, find $(\mathbf{u}_h(t), p_h(t), \hat{\boldsymbol{d}}_H(t), \boldsymbol{\lambda}_h(t)) \in X_h^{\mathrm{f}} \times Q_h \times \hat{V}_H^{\mathrm{s}} \times \Lambda_h$, satisfying $\mathbf{u}_h = \mathbf{u}_D$ on Γ_D^{f}, and such that

- Fluid sub-problem:

$$A_h^{\mathrm{f}}(\mathbf{u}_h, p_h; \boldsymbol{v}_h^{\mathrm{f}}, q_h) + \langle \boldsymbol{\lambda}_h, \boldsymbol{v}_h^{\mathrm{f}} \rangle_\Sigma = F_h^{\mathrm{f}}(\boldsymbol{v}_h^{\mathrm{f}}), \quad (2.74)$$

- Solid sub-problem:

$$A_H^{\mathrm{s}}(\hat{\boldsymbol{d}}_H; \hat{\boldsymbol{v}}_H^{\mathrm{s}}) - \langle \boldsymbol{\lambda}_h, \boldsymbol{v}_H^{\mathrm{s}} \rangle_\Sigma = F_H^{\mathrm{s}}(\hat{\boldsymbol{v}}_H^{\mathrm{s}}), \quad (2.75)$$

- Coupling condition:

$$\langle \boldsymbol{\mu}_h, \mathbf{u}_h \rangle_\Sigma = \langle \boldsymbol{\mu}_h, \partial_t \boldsymbol{d}_H \rangle_\Sigma. \tag{2.76}$$

The space Λ_h represents the approximation of the Lagrange multipliers space Λ defined in Section 2.4.3. Different choices for this space can be considered, for example the trace of the structure basis function or more general L^2 functions. In this work we make the following choice:

$$\Lambda_h = \left\{ \boldsymbol{\mu}_h \text{ measure on } \Sigma,\ \boldsymbol{\mu}_h = \sum_{i=1}^{N_\mathrm{s}} \boldsymbol{\mu}_i \delta(\mathbf{x}_i), \boldsymbol{\mu}_i \in \mathbb{R}^d \right\}, \tag{2.77}$$

where $(\mathbf{x}_i)_{i=1,\dots,N_\mathrm{s}}$ denotes structure nodes lying on the fluid-structure interface (which coincides with the whole structure for a thin solid) and $\delta(\mathbf{x}_i)$ the Dirac measure at point $\mathbf{x}_i$. Note that this approach is meaningful only after discretization. Moreover, for $\boldsymbol{\mu}_h \in \Lambda_h$ and $\boldsymbol{v}_h^\mathrm{f} \in X_h^\mathrm{f}$ the quantity

$$\langle \boldsymbol{\mu}_h, \boldsymbol{v}_h^\mathrm{f} \rangle_\Sigma = \sum_{i=1}^{N_\mathrm{s}} \boldsymbol{\mu}_i \boldsymbol{v}_h^\mathrm{f}(\mathbf{x}_i)$$

is well-defined as soon as $X_h^\mathrm{f} \subset (\mathcal{C}^0(\Omega^\mathrm{f}))^d$, which is the case with our choice of the fluid finite element space.

To better understand the consequences of the particular choice of the space Λ_h, it is useful to look at the algebraic counterpart of the coupling condition (2.76), which can be readily put in the following matrix form:

$$\mathrm{K_f U_f^k} = \mathrm{K_s U_s^k} \quad k = 1, ..., d. \tag{2.78}$$

The components of the vector $\mathrm{U_f^k}$ (resp. $\mathrm{U_s^k}$) are given by u_h^k (resp. $\partial_t d_H^k$) on the fluid (resp. structure) velocity finite element basis, and the matrices $\mathrm{K_f}$ and $\mathrm{K_s}$ are defined by:

$$\begin{aligned} [\mathrm{K_f}]_{ij} = &\quad \langle \delta(\mathbf{x}_i), v_j^\mathrm{f} \rangle = v_j^\mathrm{f}(\mathbf{x}_i), \\ [\mathrm{K_s}]_{ij} = &\quad \langle \delta(\mathbf{x}_i), v_j^\mathrm{s} \rangle = v_j^\mathrm{s}(\mathbf{x}_i) = \delta_{ij}. \end{aligned}$$

Recalling that for thin solids, the nodes on the structure coincide with the ones on the interface, we easily infer that $\mathrm{K_f}$ is a rectangular matrix representing the fluid-to-structure interpolation matrix, while $\mathrm{K_s}$ is the identity matrix. We refer to [FG09] for more details.

2.5.2 Semi-discretization in time

For the sake of simplicity, the semi-discretization in time of the FSI problem is addressed considering the coupled problem (2.33)-(2.35) in its strong form. Even though all the considerations made are suited also for the space-discrete finite element formulations presented. First the fluid and the structure sub-problems are considered. Later we take into account the different semi-discretizations in time of the coupling conditions, leading to different fluid-structure interaction couplings.

Time discretization of the fluid and solid sub-problems. Let $\tau \in (0, T]$ be the time-step size, being T the total physical time of the problem under analysis. We set $t^n = n\tau$, with $n = 1, ..., N$, where $N = T/\tau$. Moreover we also denote by $D_\tau X^{n+1} \stackrel{\text{def}}{=} (X^{n+1} - X^n)/\tau$ the first order backward difference in time and by $X^{n+\frac{1}{2}} \stackrel{\text{def}}{=} (X^{n+1} + X^n)/2$ the mid-point value approximation.

With regard to the fluid problem, in this work two different kinds of time discretization strategies are considered. The first approach is based on a standard Backward Discretization Formula of order 1 (implicit Euler scheme) for the Navier-Stokes equation (2.1):
Given $\mathbf{u}^n$, for $n > 0$ find the fluid velocity $\mathbf{u}^{n+1} = \mathbf{u}(\mathbf{x}, t^{n+1})$ and the pressure $p^{n+1} = p(\mathbf{x}, t^{n+1})$, such that

$$\begin{cases} \rho^{\mathrm{f}} \left(D_\tau \mathbf{u}^{n+1} + (\mathbf{u}^* \cdot \nabla)\mathbf{u}^{n+1} \right) - \operatorname{div} \boldsymbol{\sigma}^{\mathrm{f}}(\mathbf{u}^{n+1}, p^{n+1}) = \mathbf{f}^{n+1}, & \text{in} \quad \Omega^{\mathrm{f},n+1}, \\ \operatorname{div} \mathbf{u}^{n+1} = 0, & \text{in} \quad \Omega^{\mathrm{f},n+1}, \end{cases} \tag{2.79}$$

being $\mathbf{u}^*$ equal to or an approximation of $\mathbf{u}^{n+1}$ and $\Omega^{\mathrm{f},n+1}$ being an approximation of $\Omega^{\mathrm{f}}(t^{n+1})$. If $\mathbf{u}^* = \mathbf{u}^{n+1}$ the system is fully implicit and nonlinear, otherwise it can be linearized taking $\mathbf{u}^* = \mathbf{u}^n$ (1st order approximation of $\mathbf{u}^{n+1}$) or $\mathbf{u}^* = 2\mathbf{u}^n - \mathbf{u}^{n-1}$ (2nd order approximation of $\mathbf{u}^{n+1}$).

The second time-advancing scheme we consider is the well-known Chorin-Temam projection method [Cho68, Tem68, Cho69], which belongs to the class of the *fractional step schemes*. A fractional step scheme is a method which uses multiple calculation steps for each numerical time-step. Precisely, the Chorin-Temam projection method is a *predictor-corrector* fractional step scheme. Here we limit ourselves to present the original formulation of the scheme, however different variations exist (*e.g.* see [GMS06] for an overview).

The prediction step of the scheme is progressed in time to a mid-time-step position and consists of solving the momentum equation ignoring the pressure gradient term:

$$\rho^{\mathrm{f}} \left(\frac{\tilde{\mathbf{u}}^{n+1} - \mathbf{u}^n}{\tau} + (\mathbf{u}^* \cdot \nabla)\tilde{\mathbf{u}}^{n+1} \right) - \operatorname{div} \boldsymbol{\varepsilon}(\tilde{\mathbf{u}}^{n+1}) = \mathbf{f}^{n+1}, \quad \text{in} \quad \Omega^{\mathrm{f},n+1}. \tag{2.80}$$

The correction step is a *projection step*, that enforces the divergence free constraint to the velocity field:

$$\begin{cases} \rho^{\mathrm{f}} \left(\dfrac{\mathbf{u}^{n+1} - \tilde{\mathbf{u}}^{n+1}}{\tau} \right) + \nabla p^{n+1} = \mathbf{0}, & \text{in} \quad \Omega^{\mathrm{f},n+1}, \\ \operatorname{div} \mathbf{u}^{n+1} = 0, & \text{in} \quad \Omega^{\mathrm{f},n+1}. \end{cases} \tag{2.81}$$

The system is now fully updated to the new time.

Remark 2.9 *Note that the projection step entails the boundary condition*

$$\mathbf{u}^{n+1} \cdot \mathbf{n}^{\mathrm{f}} = \mathbf{u}_D \cdot \mathbf{n}^{\mathrm{f}} \quad \text{on} \quad \Gamma_D^{\mathrm{f}}, \tag{2.82}$$

instead of the standard Dirichlet boundary condition $(2.2)_1$. *We refer to [Gue96] for a discussion on the boundary conditions for the end-of-step velocity.*

The key advantage of the projection method is that the computations of the velocity and the pressure fields can be decoupled [GQ98a]. As a matter of fact, applying the divergence free constraint on $(2.81)_1$ we can rewrite the projection step, supplemented with (2.82), as a Poisson equation:

$$\Delta\, p^{n+1} = \frac{\operatorname{div} \tilde{\mathbf{u}}^{n+1}}{\tau}, \quad \text{in} \quad \Omega^{\mathrm{f},n+1}, \tag{2.83}$$

with the homogeneous Neumann boundary condition

$$\nabla p^{n+1} \cdot \mathbf{n}^{\mathrm{f}} = 0, \quad \text{on} \quad \Gamma_D^{\mathrm{f}},$$

instead of (2.82). The final velocity is updated using the relation

$$\mathbf{u}^{n+1} = \tilde{\mathbf{u}}^{n+1} - \frac{\tau}{\rho^{\mathrm{f}}} \nabla p^{n+1}. \tag{2.84}$$

In the following, we refer to (2.80)-(2.81) as the *pressure-correction formulation* of the Chorin-Temam method with a *pressure-Darcy* step and to (2.83)-(2.84) as the *pressure-Poisson* step. Notice also that in the pressure-Poisson formulation of the Chorin-Temam method the end-of-step velocity can be completely eliminated from the computation by replacing (2.84) in (2.80). Further details and references on the Chorin-Temam type schemes are given in Chapters 3 and 4.

With regard to the structure problem, the semi-discretization in time of the structure equations is based on the Newmark class of finite difference scheme. For a given second order ordinary differential equation

$$\ddot{y}(t) = \phi(t, y, \dot{y}), \quad 0 \le t \le T, \tag{2.85}$$

with initial conditions

$$y^0 = y_0, \quad \dot{y}^0 = z_0,$$

the Newmark method is based on the following approximation of (2.85):

$$\begin{cases} y^{n+1} = y^{n+1} + \tau z^n + \tau^2 \left[\beta \phi^{n+1} + \left(\dfrac{1}{2} - \beta \right) \phi^n \right] \\ z^{n+1} = z^{n+1} + \tau \left[\gamma \phi^{n+1} + (1-\gamma) \phi^n \right], \\ y(0) = y_0, \quad \dot{y}(0) = z_0, \end{cases} \tag{2.86}$$

where β and γ are positive parameters to be chosen [RT83]. For the elastodynamic problem, a standard choice is $\beta = \frac{1}{4}$ and $\gamma = \frac{1}{2}$ that corresponds to the well-known mid-point scheme. Therefore, the semi-discretization in time of the problem (2.5) reads:
Given $\hat{\boldsymbol{d}}^n$ and $\hat{\mathbf{u}}^{\mathrm{s},n}$, for $n > 0$ find the solid displacement $\hat{\boldsymbol{d}}^{n+1} = \hat{\boldsymbol{d}}(\hat{\mathbf{x}}, t^{n+1})$ and the velocity $\hat{\mathbf{u}}^{\mathrm{s},n+1} = \hat{\mathbf{u}}^{\mathrm{s}}(\hat{\mathbf{x}}, t^{n+1})$ such that

$$\begin{cases} \hat{\rho}_0^{\mathrm{s}} D_\tau \hat{\mathbf{u}}^{\mathrm{s},n+1} - \operatorname{div}_{\hat{\mathbf{x}}} \hat{\boldsymbol{\Pi}}(\hat{\boldsymbol{d}}^{n+\frac{1}{2}}) = \hat{\rho}_0^{\mathrm{s}} \hat{\mathbf{f}}^{\mathrm{s},n+\frac{1}{2}}, & \text{in} \quad \hat{\Omega}^{\mathrm{s}}, \\ D_\tau \hat{\boldsymbol{d}}^{n+1} = \hat{\mathbf{u}}^{\mathrm{s},n+\frac{1}{2}}, & \text{in} \quad \hat{\Omega}^{\mathrm{s}}. \end{cases} \tag{2.87}$$

Remark 2.10 *Other choices of the parameters are possible. In particular in Chapter 3, for the linearized elastodynamics equations (2.19) we set $\beta = 1$ and $\gamma = \frac{3}{2}$ that corresponds to the Leap-Frog scheme for the structure.*

Time discretization of the coupling conditions. A straightforward way to discretize in time the coupling conditions (2.35) is to enforce simultaneously all their discrete counterparts. Using (2.79) for the fluid and (2.87) for the structure, we have the following semi-discrete in time approximation of the FSI problem (2.33)-(2.35):
Given $(\mathbf{u}^n, \hat{\boldsymbol{d}}^n, \hat{\mathbf{u}}^{\mathrm{s},n})$, find the fluid velocity $\mathbf{u}^{n+1}$, the pressure p^{n+1}, the solid displacement $\hat{\boldsymbol{d}}^{n+1}$ and the solid velocity $\hat{\mathbf{u}}^{\mathrm{s},n+1}$ such that

- Fluid sub-problem:

$$\begin{cases} \rho^{\mathrm{f}} D_\tau \mathbf{u}^{n+1}_{|\mathcal{A}} + \rho^{\mathrm{f}}(\mathbf{u}^{n+1} - \mathbf{w}^{n+1}) \cdot \nabla \mathbf{u}^{n+1} - \mathrm{div}(\boldsymbol{\sigma}^{\mathrm{f}}(\mathbf{u}^{n+1}, p^{n+1})) = \mathbf{0}, & \text{in} \quad \Omega^{\mathrm{f},n+1}, \\ \mathrm{div}\, \mathbf{u}^{n+1} = 0, & \text{in} \quad \Omega^{\mathrm{f},n+1}, \\ \mathbf{u}^{n+1} = \mathbf{u}_D, & \text{on} \quad \Gamma^{\mathrm{f}}_D, \\ \boldsymbol{\sigma}^{\mathrm{f},n+1}\mathbf{n}^{\mathrm{f}} = \mathbf{g}, & \text{on} \quad \Gamma^{\mathrm{f}}_N, \end{cases} \tag{2.88}$$

- Solid sub-problem:

$$\begin{cases} \hat{\rho}^{\mathrm{s}}_0 D_\tau \hat{\mathbf{u}}^{\mathrm{s},n+1} - \mathrm{div}_{\hat{\mathbf{x}}}\, \hat{\boldsymbol{\Pi}}(\hat{\boldsymbol{d}}^{n+\frac{1}{2}}) = \hat{\rho}^{\mathrm{s}}_0 \hat{\mathbf{f}}^{\mathrm{s},n+\frac{1}{2}}, & \text{in} \quad \hat{\Omega}^{\mathrm{s}}, \\ D_\tau \hat{\boldsymbol{d}}^{n+1} = \hat{\mathbf{u}}^{\mathrm{s},n+\frac{1}{2}}, & \text{in} \quad \hat{\Omega}^{\mathrm{s}}, \\ \hat{\boldsymbol{d}}^{n+1} = \hat{\boldsymbol{d}}_D, & \text{on} \quad \hat{\Gamma}^{\mathrm{s}}_D, \\ \hat{\boldsymbol{\Pi}}^{n+\frac{1}{2}} \hat{\mathbf{n}}^{\mathrm{s}} = \hat{J}^{\mathrm{s}} || (\hat{\boldsymbol{F}}^{\mathrm{s}})^{-\mathrm{T}} \hat{\mathbf{n}}^{\mathrm{s}} || \hat{\mathbf{h}}, & \text{on} \quad \hat{\Gamma}^{\mathrm{s}}_N, \end{cases} \tag{2.89}$$

- Coupling conditions:

$$\begin{cases} \hat{\boldsymbol{d}}^{\mathrm{f},n+1} = \mathrm{Ext}(\hat{\boldsymbol{d}}^{n+1}_{|\Sigma}), \ \hat{\mathbf{w}}^{n+1} = D_\tau \hat{\boldsymbol{d}}^{\mathrm{f},n+1} \quad \text{in} \quad \hat{\Omega}^{\mathrm{f}}, \ \Omega^{\mathrm{f},n+1} = (\mathbf{I}_{\Omega^{\mathrm{f}}} + \hat{\boldsymbol{d}}^{\mathrm{f},n+1})(\hat{\Omega}^{\mathrm{f}}), \\ \mathbf{u}^{n+1} = \mathbf{w}^{n+1}, \quad \text{on} \quad \Sigma^{n+1}, \\ \hat{\boldsymbol{\Pi}}^{n+\frac{1}{2}} \hat{\mathbf{n}}^{\mathrm{s}} = \hat{J}^{\mathrm{f},n+1} \hat{\boldsymbol{\sigma}}^{\mathrm{f},n+1} (\hat{\boldsymbol{F}}^{\mathrm{f},n+1})^{-\mathrm{T}} \hat{\mathbf{n}}^{\mathrm{s}}, \quad \text{on} \quad \hat{\Sigma}. \end{cases} \tag{2.90}$$

Note that, at each time step, we end up with a highly nonlinear system. As a matter of fact, this is a fully implicit semi-discrete-in-time coupling where the nonlinearities of the fluid and of the solid are implicitly coupled to the geometrical nonlinearities within the fluid equations.

A lot of effort in the mathematical community has been made to reduce the complexity of the non-linear FSI coupling. In the next section a review of the most important achievements is given.

2.5.3 Partitioned schemes in FSI

The space and time discretization of the coupled problem plays a key role in the development of stable and efficient fluid-structure interaction algorithms.

Focusing in particular on the coupling conditions, a solution algorithm which enforces simultaneously their time-discrete counterpart is said to be *strongly* (or *implicitly*) coupled. For strongly coupled methods, it is possible to prove the discrete equivalent of the continuous energy balance (2.36). Therefore they are in general stable in the energy norm. *Monolithic* methods, which simultaneously solve the fluid and the structure problems in a unique solver, are strongly coupled. Opposite to the monolithic methods there are the so-called *partitioned* (or *segregated*) time-advancing procedures, where the fluid and the structure are solved with their own software. These algorithms consist of the evaluations of independent fluid and structure problems, coupled *via* transmission conditions in an iterative fashion. The partitioned procedures we consider in this work are based on a Dirichlet-Neumann heterogeneous domain decomposition strategy [QV99], where the fluid subproblem is supplemented with the Dirichlet boundary condition $(2.35)_2$, whereas the structure subproblem with the Neumann boundary conditions $(2.35)_3$. For these algorithms a master-slaves approach such as the one represented in Figure 2.5 can be devised.

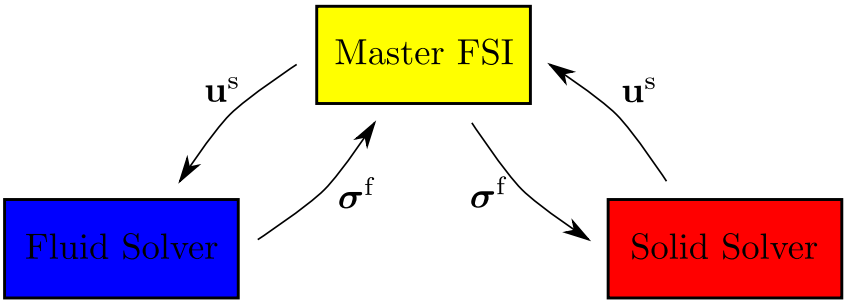

Figure 2.5: Master-slave approach for FSI algorithms.

Remark 2.11 *Other types of domain decomposition strategies can be considered* (e.g. *Robin-Robin coupling [NV08, BNV08]). In Chapter 4 we also deal with a Robin-Robin coupling, which is however derived from Dirichlet-Neumann coupling discretized in space with the Nitsche's method* (2.70)-(2.71).

A partitioned scheme can be either *weakly* or *strongly* coupled. On the one hand, a partitioned scheme is weakly (or *loosely*) coupled when the transmission conditions are not exactly satisfied at each time step, or in other words, when a spurious numerical power may appear on the fluid-structure interface. On the other hand, a partitioned scheme is strongly coupled when the transmission conditions are enforced with a high accuracy by means of sub-iterations performed at each time step between the two solvers. Nevertheless, partitioned procedures are often used to implement weakly coupled schemes. Among others, we mention [PFL95, FvdZG06] as examples of stable weakly coupled schemes in the field of aeroelasticity.

The development of stable loosely coupled algorithms in computational hemodynamics is however very challenging. A partial theoretical explanation of this fact is given in [CGN05], where a "toy FSI model" representing the interaction between a potential fluid and a linear elastic thin solid has been used to investigate the role of the *added-mass effect* in the stability of partitioned procedures. This effect takes into account the inertia added to the structure because of the interaction with the fluid. In [CGN05], the authors show that numerical difficulties in partitioned procedures can be experienced for increasing values of this inertial term, which has been proved to depend upon the density ratio ρ^s/ρ^f and the geometry of the domain. Here we limit ourselves to recall the main results stated, referring to [CGN05] for the details:

1. For a given geometry, numerical instabilities can be experienced in loosely coupled partitioned algorithms as soon as the density ratio ρ^s/ρ^f is lower than a certain threshold.

2. For a given geometry, an increase of sub-iterations can be experienced in strongly coupled partitioned algorithms as soon as the density ratio ρ^s/ρ^f decreases.

3. For a given density ratio, numerical instabilities can be experienced in loosely coupled partitioned algorithms as soon as the length of the domain is greater than a certain threshold.

4. For a given density ratio, an increase of sub-iterations can be experienced in strongly coupled partitioned algorithms as soon as the length of the domain increases.

In hemodynamics, the fluid and structure densities being of the same magnitude, the added-mass effect is non-negligible and numerical difficulties may appear with the use of partitioned schemes. Note that, this is not the case in aeroelasticity, where the structure density is much bigger than the fluid one.

In the following, the recent advances in the development of partitioned procedures for hemodynamics applications are reviewed. Depending on the type of fluid-structure coupling enforced, three groups of schemes can be identified: implicit schemes, that enforce strongly (with sub-iterations) the coupling conditions, semi-implicit schemes, in which only part of the transmission conditions is strongly coupled, and explicit schemes, where the coupling is weak. In this overview, we also present the algorithms of the partitioned schemes on which are based the results of the following chapters.

Implicit coupling schemes. Many works have been focused on the development of techniques capable of accelerating the convergence in strongly coupled partitioned schemes. A number of fixed point strategies have been proposed: in [LTM01] a steepest-descent algorithm is presented, an Aitken-like acceleration formula is used in [MWR99, MWR01] and transpiration boundary conditions are used in [DFF03] to

avoid the computation of the fluid matrices at each sub-iteration. In [RRLJ01], the authors propose to relax the fluid incompressibility constraint in order to accelerate the convergence of the fixed-point iterations. Further advances on the topic suggest the use of Newton-based methods for a fast convergence towards the solution of the coupled non-linear system. These methods require the evaluation of the Jacobian associated with the fluid-solid coupled state equations. Inexact Newton methods are addressed in [Tez01, MS02, MS03, Hei04] by using finite difference approximations of the Jacobian, in [Tez01, GV03, ZZJ+03, Hei04] by replacing the coupled tangent operator by a simpler linear operator and, applied to complex geometries in [GVF05]. Exact Newton algorithms, including differentiation with respect to the fluid domain, are introduced in [FM03, FM05]. Acceleration techniques using Krylov spaces have been proposed in [Hei04, MvBdB05]. More recently strongly coupled procedures based on a Robin-Robin coupling have also been investigated, among these we recall [BNV08] for fixed point iterative strategies and [BNV09] for Krylov methods.

The heterogeneous domain decomposition point of view adopted in [LTM01], and further developed in [DDQ04, DDFQ06, BNV08, FGGV08], offers an interesting unified presentation of all these partitioned strongly coupled schemes.

In this work a strongly coupled FSI algorithm has been used within the FD formulation for the numerical simulation of heart valves. The scheme, based on a fixed point algorithm with Aitken-like acceleration, has been proposed in [dSGB08]. Assuming that $\mathbf{u}_h^n$, $\hat{\boldsymbol{d}}_H^n$, $\hat{\mathbf{u}}_H^{\mathrm{s,n}}$ are given at time-step t^n, the time-stepping algorithm is as follow:

Algorithm 2.1 *A strongly coupled scheme with fixed point iterations.*

`Initialize` $\hat{\boldsymbol{d}}_{H,\Sigma}^0$ `(e.g.` $\hat{\boldsymbol{d}}_{H,\Sigma}^0 = \hat{\boldsymbol{d}}_{H,\Sigma}^n$`);`
`Do`

Step 1 : `(fluid sub-problem)`
`Find` $(\mathbf{u}_h^{k+1}, p_h^{k+1}, \boldsymbol{\lambda}_h^{k+1}) \in X_h^{\mathrm{f}} \times Q_h \times \Lambda_h$ `such that`

$$\begin{cases} A_{\tau,h}^{\mathrm{f}}(\mathbf{u}_h^{k+1}, p_h^{k+1}; \boldsymbol{v}_h^{\mathrm{f}}, q_h) & +\langle \boldsymbol{\lambda}_h^{k+1}, \boldsymbol{v}_h^{\mathrm{f}} \rangle_\Sigma = F_h^{\mathrm{f}}(\boldsymbol{v}_h^{\mathrm{f}}) \\ \langle \boldsymbol{\mu}_h, \mathbf{u}_h^{k+1} \rangle_\Sigma & = \langle \boldsymbol{\mu}_h, D_\tau \boldsymbol{d}_H^{k+1} \rangle_\Sigma \end{cases} \tag{2.91}$$

`for all` $(\boldsymbol{v}_h^{\mathrm{f}}, q_h, \boldsymbol{\mu}_h) \in V_h^{\mathrm{f}} \times Q_h \times \Lambda_h$`;`

Step 2 : `(solid sub-problem)`
`Find` $\tilde{\boldsymbol{d}}_H^{k+1} \in \hat{V}_H^{\mathrm{s}}$ `such that`

$$A_{\tau,H}^{\mathrm{s}}(\tilde{\boldsymbol{d}}_H^{k+1}; \hat{\boldsymbol{v}}_H^{\mathrm{s}}) = F_H^{\mathrm{s}}(\hat{\boldsymbol{v}}_H^{\mathrm{s}}) + \langle \boldsymbol{\lambda}_h^{k+1}, \boldsymbol{v}_H^{\mathrm{s}} \rangle_\Sigma, \tag{2.92}$$

`for all` $\hat{\boldsymbol{v}}_H^{\mathrm{s}} \in \hat{V}_H^{\mathrm{s}}$`;`

Step 3 : `(Aitken acceleration formula)`
`Correct the position of the interface:`

$$\hat{\boldsymbol{d}}_{H,\Sigma}^{k+1} = \omega^k \tilde{\boldsymbol{d}}_{H,\Sigma}^{k+1} + (1 - \omega^k) \hat{\boldsymbol{d}}_{H,\Sigma}^k$$

`with`

$$\omega^j = \frac{(\hat{\boldsymbol{d}}^k_{H,\Sigma} - \hat{\boldsymbol{d}}^{k-1}_{H,\Sigma}) \cdot (\hat{\boldsymbol{d}}^k_{H,\Sigma} - \tilde{\boldsymbol{d}}^{k+1}_{H,\Sigma} - \hat{\boldsymbol{d}}^{k-1}_{H,\Sigma} + \tilde{\boldsymbol{d}}^k_{H,\Sigma})}{|\hat{\boldsymbol{d}}^k_{H,\Sigma} - \tilde{\boldsymbol{d}}^{k+1}_{H,\Sigma} - \hat{\boldsymbol{d}}^{k-1}_{H,\Sigma} + \tilde{\boldsymbol{d}}^k_{H,\Sigma}|^2}; \tag{2.93}$$

`While` $\|\hat{\boldsymbol{d}}^{k+1}_{H,\Sigma} - \hat{\boldsymbol{d}}^k_{H,\Sigma}\| > \varepsilon$;

In the sub-iterations, $A^{\mathrm{f}}_{\tau,h}$ and $A^{\mathrm{s}}_{\tau,H}$ represent respectively the fully-discrete approximations of A^{f} and A^{s}, and $D_\tau X^k \stackrel{\text{def}}{=} (X^k - X^n)/\tau$.

Considering the numerical resolution of (2.91)-(2.93) a few remarks are in order:

- The fluid problem (2.91) defines a saddle-point problem in the unknowns $(\mathbf{u}_h, p_h)$ and $\boldsymbol{\lambda}_h$, that can be solved for example by penalization. We refer to [dS07, Chapter 4] for the details of the implementation.
- The Aitken formula requires at least two sub-iterations to be effectively applied. At the first sub-iteration a fixed relaxation parameter is commonly used.

Semi-implicit coupling schemes. The methods we introduce in this paragraph are *not* strongly coupled, in the sense that $(2.35)_2$ and $(2.35)_3$ are not exactly enforced, but exhibit very good stability properties in hemodynamics problems.

The first semi-implicit coupling scheme was presented in [FGG06, FGG07]. It basically relies upon two ideas. The first one is to couple implicitly the pressure stress to ensure stability (this is also suggested by the analysis made in [CGN05]). The remaining terms of the fluid equations – dissipation, convection and geometrical nonlinearities – are *explicitly* coupled to the structure. This drastically reduces the cost of the coupling without affecting too much the stability. The second idea relies upon the fact that this kind of implicit-explicit splitting can be conveniently performed using a Chorin-Temam projection scheme in the fluid: at each time step the projection sub-step (carried out in a known fluid domain) is strongly coupled with the structure, so accounting for the added-mass effect in an implicit way, while the expensive ALE-advection-viscous sub-step is explicitly, *i.e.* weakly, coupled. The main advantages of the resulting algorithm are: its simplicity of implementation and its efficiency compared to the methods presented in the previous section. Obviously, the main drawbacks are: first, it assumes the fluid to be solved with a projection scheme and, second, the energy is not perfectly balanced, at least from a theoretical viewpoint. In spite of that, theoretical and numerical evidence show that, for a wide range of physical and discrete parameters, the scheme is numerically stable.

Remark 2.12 *This idea can be generalised to other fractional step schemes. An extension to algebraic factorisation methods has been presented in [QQ07, BQQ08, Qua08].*

For the sake of clarity we present the time semi-discrete version of the algorithm. Assuming that $\Omega^{\mathrm{f},n}$, $\mathbf{u}^n$, $\hat{\boldsymbol{d}}^n$, $\hat{\mathbf{u}}^{\mathrm{s,n}}$ are known at time t^n, the computation of $\Omega^{\mathrm{f},n+1}$, $\mathbf{u}^{n+1}$, p^{n+1}, $\hat{\boldsymbol{d}}^{n+1}$ is done according to the following procedure:

Algorithm 2.2 *Semi-implicit coupling scheme based on the projection Chorin-Temam method.*

Step 1 : (update fluid domain)

$$\begin{aligned} \hat{\boldsymbol{d}}^{\mathrm{f},n+1} = \mathtt{Ext}(\hat{\boldsymbol{d}}^{n}_{|\hat{\Sigma}}), \quad \hat{\mathbf{w}} = D_\tau \hat{\boldsymbol{d}}^{\mathrm{f},n+1} \quad \mathtt{in} \quad \hat{\Omega}^{\mathrm{f}}, \\ \Omega^{\mathrm{f},n+1} = (\mathbf{I}_{\Omega^{\mathrm{f}}} + \hat{\boldsymbol{d}}^{\mathrm{f},n+1})(\hat{\Omega}^{\mathrm{f}}) \end{aligned} \tag{2.94}$$

Step 2 : (explicit viscous-structure coupling)

$$\begin{cases} \rho^{\mathrm{f}} \left. \dfrac{\tilde{\mathbf{u}}^{n+1} - \mathbf{u}^{n}}{\tau} \right|_{\mathcal{A}} + \rho^{\mathrm{f}} (\tilde{\mathbf{u}}^{n} - \mathbf{w}^{n+1}) \cdot \nabla \tilde{\mathbf{u}}^{n+1} \\ \qquad\qquad -2\mu \operatorname{div}(\boldsymbol{\varepsilon}(\tilde{\mathbf{u}}^{n+1})) = \mathbf{0}, \quad \mathtt{in} \quad \Omega^{\mathrm{f},n+1}, \\ \qquad\qquad \tilde{\mathbf{u}}^{n+1} = \mathbf{w}^{n+1}, \quad \mathtt{on} \quad \Sigma^{n+1}. \end{cases} \tag{2.95}$$

Step 3 : (implicit pressure-structure coupling)

– **Step 3.1** : (fluid projection sub-step)

$$\begin{cases} \rho^{\mathrm{f}} \dfrac{\mathbf{u}^{n+1} - \tilde{\mathbf{u}}^{n+1}}{\tau} + \nabla p^{n+1} = \mathbf{0}, \quad \mathtt{in} \quad \Omega^{\mathrm{f},n+1}, \\ \qquad \operatorname{div} \mathbf{u}^{n+1} = 0, \quad \mathtt{in} \quad \Omega^{\mathrm{f},n+1}, \\ \mathbf{u}^{n+1} \cdot \mathbf{n}^{\mathrm{f}} = \dfrac{\hat{\boldsymbol{d}}^{n+1} - \hat{\boldsymbol{d}}^{n}}{\tau} \cdot \mathbf{n}^{\mathrm{f}}, \quad \mathtt{on} \quad \Sigma^{n+1}. \end{cases} \tag{2.96}$$

– **Step 3.2** : (solid sub-step)

$$\begin{cases} \hat{\rho}^{\mathrm{s}}_0 \dfrac{\hat{\mathbf{u}}^{\mathrm{s},n+1} - \hat{\mathbf{u}}^{\mathrm{s},n}}{\tau} - \operatorname{div}_{\hat{\mathbf{x}}} \left(\dfrac{\hat{\boldsymbol{\Pi}}^{n+1} + \hat{\boldsymbol{\Pi}}^{n}}{2} \right) = \mathbf{0}, \quad \mathtt{in} \quad \hat{\Omega}^{\mathrm{s}}, \\ \qquad \dfrac{\hat{\boldsymbol{d}}^{n+1} - \hat{\boldsymbol{d}}^{n}}{\tau} = \dfrac{\hat{\mathbf{u}}^{\mathrm{s},n+1} + \hat{\mathbf{u}}^{\mathrm{s},n}}{2}, \quad \mathtt{in} \quad \hat{\Omega}^{\mathrm{s}}, \\ \hat{\boldsymbol{\Pi}}^{n+1} \cdot \hat{\mathbf{n}}^{\mathrm{s}} = \hat{J}^{\mathrm{f},n+1} (\boldsymbol{\sigma}^{\mathrm{f}} \ (\tilde{\mathbf{u}}^{n+1}, p^{n+1}) \circ \mathcal{A}^{n+1}) (\boldsymbol{F}^{\mathrm{f},n+1})^{-T} \cdot \hat{\mathbf{n}}^{\mathrm{s}}, \quad \mathtt{on} \quad \hat{\Sigma}. \end{cases} \tag{2.97}$$

Note that the steps 1 and 2 are performed only *once* per time-step. In a partitioned procedure, step 3 is solved by sub-iterating between steps 3.1 and 3.2 (using fixed-point or Newton iterations, for instance) since $\hat{\boldsymbol{d}}^{n+1}$ is required in 3.1 while p^{n+1} is required in 3.2. The two sub-problems of step 3 are therefore solved several times but contrarily to a fully coupled procedure, the part of the fluid solved during the inner iterations reduces to a simple Darcy-like problem. The efficiency of the scheme can be furthermore increased by replacing in step 3.1 the Darcy-like problem with the corresponding Poisson-like problem, see equation (2.83).

The stability properties of the scheme, analyzed in [FGG07] for a linearized FSI problem, are recalled in Chapter 3. In the same chapter the convergence of the scheme for the same simplified problem is also investigated. In Chapter 4, a

modification of the original semi-implicit scheme is presented and numerical simulations of an idealized abdominal aortic aneurism (AAA) are performed in the ALE framework.

In the FD framework, the scheme in its pressure-Darcy formulation has been presented in [dS07], however the corresponding algorithm in its pressure-Poisson formulation is still an active research point due to the difficulties introduced by the differentiation of the Dirac measure for the Langrange multiplier space (2.77).

Explicit coupling schemes. Weakly coupled schemes for FSI are very recent in the field of computational hemodynamics. As a matter of fact, the strong added-mass effect that characterize FSI problems in blood flows makes sequentially staggered schemes generally unstable.

Explicit coupling procedures, based on the use of a simplified structural model, have been recently reported in [NV08, GGC+09, GGCC09]. A stabilized explicit coupling scheme whose stability properties are independent of the added-mass effect has been proposed in [BF07, BF09]. The added-mass independence and the use of general mechanical laws for the structure make this scheme suitable for fully 3D FSI problems in blood flows. The key ingredients of the scheme are the following:

1. The coupling interface conditions are treated in a weak sense, using a formulation based on Nitsche's method.

2. The added-mass uniform stability is obtained by means of a time penalty term that gives an L^2-control on the fluid pressure fluctuations at the FSI interface.

Considering the space-discrete variational formulation (2.72)-(2.73) and assuming that $\Omega^{\mathrm{f},n}$, $\mathbf{u}_h^n$, p_h^n, $\tilde{\boldsymbol{d}}_H^n$, $\hat{\mathbf{u}}_H^{\mathrm{s,n}}$ are known at time t^n, the computation of $\Omega^{\mathrm{f},n+1}$, $\mathbf{u}^{n+1}$, p^{n+1}, $\hat{\boldsymbol{d}}^{n+1}$ is done according to the following explicit procedure:

Algorithm 2.3 *Stabilized explicit coupling scheme.*

Step 1: (solid sub-problem)
Find $\tilde{\boldsymbol{d}}_H^{k+1} \in \hat{V}_H^{\mathrm{s}}$ such that

$$A_{\tau,H}^{\mathrm{s}}(\hat{\boldsymbol{d}}_H^{n+1};\hat{\boldsymbol{v}}_H^{\mathrm{s}}) + \gamma\frac{\mu}{h}\int_{\Sigma^n} D_\tau \boldsymbol{d}_H^{n+1}\cdot\boldsymbol{v}_H^{\mathrm{s}}\,\mathrm{d}\boldsymbol{\gamma} = F_H^{\mathrm{s}}(\hat{\boldsymbol{v}}_H^{\mathrm{s}}) + \gamma\frac{\mu}{h}\int_{\Sigma^n}\mathbf{u}_h^n\cdot\boldsymbol{v}_H^{\mathrm{s}}\,\mathrm{d}\boldsymbol{\gamma} - \int_{\Sigma^n}\boldsymbol{\sigma}^{\mathrm{f}}(\mathbf{u}_h^n,p_h^n)\mathbf{n}^{\mathrm{f}}\cdot\boldsymbol{v}_H^{\mathrm{s}}\,\mathrm{d}\boldsymbol{\gamma} \quad (2.98)$$

for all $\hat{\boldsymbol{v}}_H^{\mathrm{s}} \in \hat{V}_H^{\mathrm{s}}$;
Step 2: (fluid sub-problem)

`Find` $(\mathbf{u}_h, p_h) \in X_h^{\mathrm{f}} \times Q_h$ `such that`

$$A_{\tau,h}^{\mathrm{f}}(\mathbf{u}_h^{n+1}, p_h^{n+1}; \boldsymbol{v}_h^{\mathrm{f}}, q_h) + \gamma \frac{\mu}{h} \int_{\Sigma^n} \mathbf{u}_h^{n+1} \cdot \boldsymbol{v}_h^{\mathrm{f}} \, \mathrm{d}\boldsymbol{\gamma}$$
$$- \int_{\Sigma^n} \mathbf{u}_h^{n+1} \cdot \boldsymbol{\sigma}^{\mathrm{f}}(\alpha \boldsymbol{v}_h^{\mathrm{f}}, -q_h)\mathbf{n}^{\mathrm{f}} \, \mathrm{d}\boldsymbol{\gamma} = F_h^{\mathrm{f}}(\boldsymbol{v}_h^{\mathrm{f}}) + \gamma \frac{\mu}{h} \int_{\Sigma^n} D_\tau \boldsymbol{d}_H^{n+1} \cdot \boldsymbol{v}_h^{\mathrm{f}} \, \mathrm{d}\boldsymbol{\gamma}$$
$$+ \int_{\Sigma^n} D_\tau \boldsymbol{d}_H^{n+1} \cdot \boldsymbol{\sigma}^{\mathrm{f}}(\alpha \boldsymbol{v}_h^{\mathrm{f}}, -q_h)\mathbf{n}^{\mathrm{f}} \, \mathrm{d}\boldsymbol{\gamma} + \int_{\Sigma^n} \boldsymbol{\sigma}^{\mathrm{f}}(\mathbf{u}_h^n, p_h^n)\mathbf{n}^{\mathrm{f}} \cdot \boldsymbol{v}_h^{\mathrm{f}} \, \mathrm{d}\boldsymbol{\gamma} \quad (2.99)$$

`for all` $(\boldsymbol{v}_h^{\mathrm{f}}, q_h) \in V_h^{\mathrm{f}} \times Q_h$;

Step 3 : `(update fluid domain)`

$$\hat{\boldsymbol{d}}_h^{\mathrm{f},n+1} = \mathtt{Ext}(\hat{\boldsymbol{d}}_{H|\hat{\Sigma}}^n), \quad \hat{\mathbf{w}}_h = D_\tau \hat{\boldsymbol{d}}_h^{\mathrm{f},n+1} \quad \mathtt{in} \quad \hat{\Omega}^{\mathrm{f}},$$
$$\Omega^{\mathrm{f},n+1} = (\mathbf{I}_{\Omega^{\mathrm{f}}} + \hat{\boldsymbol{d}}_h^{\mathrm{f},n+1})(\hat{\Omega}^{\mathrm{f}}); \quad (2.100)$$

Note that the method may suffer from a deterioration of the time accuracy, due to a weak consistency of the time penalty stabilization term, which rates as $O(\tau^{\frac{1}{2}})$. However, it is possible to recover optimal accuracy with a few defect-correction iterations (see [BF09, Algorithm 3]). For a linearized FSI problem, the scheme has been proved to be stable under the following condition

$$\gamma > 4(1+\alpha)^2 C_{\mathrm{ti}},$$

where C_{ti} is the constant associated with the following local trace-inverse inequality

$$\|\boldsymbol{v}_h\|_{0,\partial K}^2 \leq C_{\mathrm{ti}} h^{-1} \|\boldsymbol{v}_h\|_{0,K}^2, \quad \forall \boldsymbol{v}_h \in X_h^{\mathrm{f}}, \quad \forall K \in \mathcal{T}_h^{\mathrm{f}} \quad (2.101)$$

We refer to [BF09] for the details of the stability analysis.

2.6 Conclusion

In this chapter, the mathematical modeling and the numerical resolution of the coupled fluid-structure interaction problem have been addressed. For the mathematical modeling, the equations governing the fluid and the structure have been presented. For the numerical resolution, we focused on partitioned procedures, which allow the use of different solvers for the fluid and structure problems. Three different groups of partitioned scheme have been presented and for each one a review of the most recent advances has been given. We finally remark that the notation introduced here for the fluid and structure problem is used also in the following chapters. The only simplification concerns the superscript $\hat{\cdot}$, for the Lagrangian or ALE field, which is omitted when there is no ambiguity.

Part I

A projection semi-implicit coupling for fluid-structure interaction problems: analysis and numerics

Chapter 3

Convergence analysis of a semi-implicit coupling scheme for fluid-structure interaction problems

M. Astorino and C. Grandmont. *Convergence analysis of a semi-implicit coupling scheme for fluid-structure interaction problems.* INRIA Research Report RR-6996, accepted for publication in Numerische Mathematik.

Contents

3.1 Introduction

In the previous chapter we briefly presented various partitioned procedures for the numerical resolution of fluid-structure problems involving an incompressible viscous fluid and a flexible structure when the so-called added-mass effect is strong [CGN05, FWR06]. In literature, a great variety of partitioned strategies have been proposed to solve this kind of problems. In Section 2.5.3, they have been classified in three groups of coupling schemes: *implicit* (or *strongly coupled*), *semi-implicit* and *explicit*.

A number of works are devoted to the numerical analysis of FSI coupling schemes [Gra98, GM00, Tak02, DGHL03], among them we refer in particular to [LTM00], where the convergence of an implicit time-dependent linearized FSI problem has been studied. There, optimal error estimates are derived for the case of non-matching finite element approximations at the interface.

This chapter is devoted to the convergence analysis of the projection semi-implicit algorithm proposed in [FGG07], where the non-incremental Chorin-Temam projection scheme is used to obtain a conditionally stable method (see [FGG07, Theorem 1]). The analysis is carried out for a linear fluid-structure problem, where the fluid is described by the Stokes equations, the structure by the classical linear elastodynamics equations (linearized elasticity, plate or shell models) and all changes of geometry are neglected. The fluid and structure equations are fully discretized in space and time. For the space discretization, finite element approximations with a non-conforming matching at the interface are considered. For the time discretization, the non-incremental Chorin-Temam projection scheme is used for the fluid and the Leap-Frog scheme for the structure (see Remark 2.10). The coupling conditions at the interface are first order in time approximations and are treated in a *semi-implicit* way.

Remark 3.1 *The use of the Leap-Frog scheme for the structure is dictated by the fact that the conditional stability of the coupling scheme is proved with this time-advancing scheme. From a theoretical point of view, the proof of the stability with the Newmark scheme is still open, even if computationally it is known to lead to stable algorithms.*

The algorithm raises interesting theoretical and numerical problems concerning its accuracy in time. Our aim is to better understand what kind of time accuracy could be expected. It is clear that the scheme will be at most first order. However, there are two main reasons for which it could be of order less than one. First, it is well-known that the non-incremental Chorin-Temam scheme, in a pure hydrodynamic problem, has a reduced time accuracy. The following error estimates were indeed proved (see [BC07, EG04, GQ98a, GQ98b, Ran91] for more details):

$$\begin{aligned} ||\mathbf{u}(t^n) - \mathbf{u}_h^n||_{l^\infty(L^2(\Omega^f))} + ||\mathbf{u}(t^n) - \widetilde{\mathbf{u}}_h^n||_{l^\infty(L^2(\Omega^f))} &\leq c(h^{k+1} + \tau), \\ ||\mathbf{u}(t^n) - \widetilde{\mathbf{u}}_h^n||_{l^\infty(H^1(\Omega^f))} + ||p(t^n) - p_h^n||_{l^\infty(L^2(\Omega^f))} &\leq c(h^k + \sqrt{\tau}), \end{aligned} \tag{3.1}$$

where k is the finite element order (we refer to Section 2.5.2 for the notation used). How the accuracy of the fluid scheme acts on the one of the coupled scheme must then be studied. Second, the *semi-implicit* treatment of the coupling conditions at the fluid-structure interface may also contribute to a modification of the convergence order. Therefore, we aim at investigating through a theoretical analysis and by means of some numerical experiments if and how the convergence rate of the projection semi-implicit algorithm is affected.

The chapter is organized as follows. In Section 3.2 the linear coupled fluid-structure problem is introduced in a differential form. Initial and boundary conditions are given both for the Stokes and the elastodynamic equations. Subsequently the variational formulation is presented. In Section 3.3 we briefly recall the projection semi-implicit scheme proposed in [FGG07], paying special attention to the interface matching operator between the fluid and the structure. A non-conforming space discretization of the coupled domain is considered and two possible matching

operators are analyzed: a pointwise matching and an integral one. The introduction of a matching operator comes from the fact that, for the time being, the stability analysis of the semi-implicit scheme is proved in [FGG07] under stability conditions that involve different mesh sizes for the fluid and the structure. In Section 3.4, we build appropriate finite element approximations of the continuous velocity, pressure and displacement. In Section 3.5, we state the main result and we detail the error analysis of the numerical scheme. A discussion on the optimality in space of the error estimates depending on the structure model, on the interface matching operator and on the polynomial degree of the fluid approximation is also presented. Numerical experiments that confirm the theoretical result are given in Section 3.6. There, the time accuracy of the analyzed semi-implicit coupling scheme is compared to the ones of two other FSI algorithms with respect to an analytical solution. Finally, the last section is devoted to concluding remarks.

3.2 Problem setting

3.2.1 Hypotheses and notations

In order to carry out the analysis we consider a simplified fluid-structure interaction model where a low Reynolds regime is assumed and where the fluid-structure interface undergoes infinitesimal displacements. The fluid might then be simply described by the Stokes equations in a fixed domain $\Omega^{\mathrm{f}} \subset \mathbb{R}^d$, $d = 2, 3$. For the structure we also consider a linear behavior, described either by the classical linearized elastodynamics equations or by equations based on linear beam/plate/shell models. The reference domain of the solid is denoted by $\Omega^{\mathrm{s}} \subset \mathbb{R}^d$. It will be either a domain or a surface of $\mathbb{R}^d$ (in this latter case the elastic domain is identified by its mid-surface). We still denote by $\Sigma \stackrel{\text{def}}{=} \partial\Omega^{\mathrm{s}} \cap \partial\Omega^{\mathrm{f}}$ the fluid-structure interface. When the structure is described by beam/shell model we have $\overline{\Omega^{\mathrm{s}}} = \Sigma$, see Figure 3.1. We indicate by Γ_D^{f} (resp. Γ_D^{s}) the fluid (resp. structure) boundary which doesn't belong to the fluid-structure interface. Namely $\Gamma_D^{\mathrm{f}} = \partial\Omega^{\mathrm{f}} \backslash \overline{\Sigma}$ (resp. $\Gamma_D^{\mathrm{s}} = \partial\Omega^{\mathrm{s}} \backslash \overline{\Sigma}$).

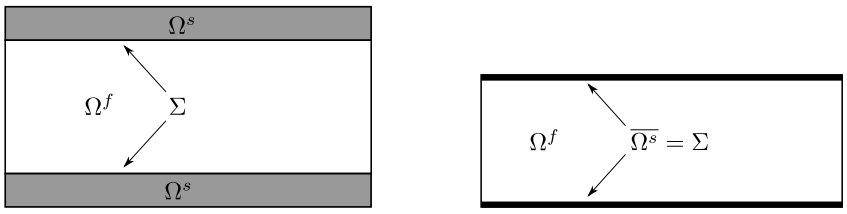

(a) Case $\overline{\Omega^{\mathrm{s}}} \neq \Sigma$ (b) Case $\overline{\Omega^{\mathrm{s}}} = \Sigma$

Figure 3.1: Examples of geometric configurations.

When dealing with a d-dimensional structure, our fluid-structure problem reads as follows:
Find the fluid velocity $\mathbf{u} : \Omega^{\mathrm{f}} \times \mathbb{R}^+ \to \mathbb{R}^d$, the fluid pressure $p : \Omega^{\mathrm{f}} \times \mathbb{R}^+ \to \mathbb{R}$ and the structure displacement $\boldsymbol{d} : \Omega^{\mathrm{s}} \times \mathbb{R}^+ \to \mathbb{R}^d$ such that

$$\begin{cases} \rho^{\mathrm{f}}\partial_t \mathbf{u} - \nabla\cdot\boldsymbol{\sigma}^{\mathrm{f}}(\mathbf{u},p) = \mathbf{0} & \text{in} \quad \Omega^{\mathrm{f}}, \\ \nabla\cdot\mathbf{u} = 0 & \text{in} \quad \Omega^{\mathrm{f}}, \\ \mathbf{u} = \mathbf{0} & \text{on} \quad \Gamma^{\mathrm{f}}_D, \\ \rho^{\mathrm{s}}\partial_{tt}\boldsymbol{d} - \nabla\cdot\boldsymbol{\sigma}^{\mathrm{s}}(\boldsymbol{d}) = \mathbf{0} & \text{in} \quad \Omega^{\mathrm{s}}, \\ \boldsymbol{d} = \mathbf{0} & \text{on} \quad \Gamma^{\mathrm{s}}_D, \end{cases} \tag{3.2}$$

with the interface coupling conditions

$$\begin{cases} \mathbf{u} = \partial_t \boldsymbol{d} & \text{on} \quad \Sigma, \\ \boldsymbol{\sigma}^{\mathrm{s}}(\boldsymbol{d})\mathbf{n}^{\mathrm{s}} = -\boldsymbol{\sigma}^{\mathrm{f}}(\mathbf{u},p)\mathbf{n}^{\mathrm{f}} & \text{on} \quad \Sigma. \end{cases} \tag{3.3}$$

The coupled problem (3.2)-(3.3) is finally completed by the initial conditions

$$\mathbf{u}(0) = \mathbf{u}_0, \ \boldsymbol{d}(0) = \boldsymbol{d}_0, \ \partial_t \boldsymbol{d}(0) = \boldsymbol{d}_1. \tag{3.4}$$

Before going any further in the analysis, a few remarks are in order:

- For the sake of simplicity, we choose to consider homogeneous Dirichlet boundary conditions on Γ^{f}_D and Γ^{s}_D and no external forces on the coupled system. Nonetheless, the performed convergence analysis could be easily extended to a case where more general assumptions on boundary conditions hold and external forces are considered.
- When the structure motion is described by a beam, shell or membrane model the coupling condition is the kinematic condition (equality of the velocities) and instead of condition $(3.3)_2$, the load applied by the fluid on the elastic media appears in the right-hand side of the structure equation. Nevertheless, the variational formulation of both problems takes the very same form.

3.2.2 Variational formulation

For the variational setting, we consider the usual Sobolev spaces introduced in Section 2.4.1, and the functional spaces X^{f}, V^{f}, V^{f}_0 and V^{s} of Section 2.4.2. Note that for the structures considered, $V^{\mathrm{s}} \subseteq \left\{\boldsymbol{v}^{\mathrm{s}} \in [H^1(\Omega^{\mathrm{s}})]^d : \boldsymbol{v}^{\mathrm{s}} = \mathbf{0} \text{ on } \Gamma^{\mathrm{s}}_D\right\}$. In the particular case of linearized elasticity the equality holds, that is

$$V^{\mathrm{s}} = \left\{\boldsymbol{v}^{\mathrm{s}} \in [H^1(\Omega^{\mathrm{s}})]^d : \quad \boldsymbol{v}^{\mathrm{s}} = \mathbf{0} \quad \text{on} \quad \Gamma^{\mathrm{s}}_D\right\}.$$

We also recall that the space-time dependence of the unknowns is occasionally omitted throughout this work, *i.e.*

$$\mathbf{u} = \mathbf{u}(t) = \mathbf{u}(\mathbf{x},t), \qquad p = p(t) = p(\mathbf{x},t) \quad \text{and} \quad \boldsymbol{d} = \boldsymbol{d}(t) = \boldsymbol{d}(\mathbf{x},t).$$

A first weak formulation for the problem (3.2)-(3.3) can be derived by multiplying equations $(3.2)_1$ and $(3.2)_4$ by a test function $\boldsymbol{v} \in [H^1_0(\Omega^{\mathrm{f}} \cup \Omega^{\mathrm{s}} \cup \Sigma)]^d$ such that

$\boldsymbol{v}_{|\Omega^s} \in V^s$. Performing an integration by parts and using the interface condition $(3.3)_2$ we have

$$\begin{aligned}\rho^s(\partial_{tt}\boldsymbol{d},\boldsymbol{v})_{\Omega^s} + a^s(\boldsymbol{d},\boldsymbol{v}) + \rho^f\big(\partial_t\mathbf{u},\boldsymbol{v}\big)_{\Omega^f} + 2\mu\big(\boldsymbol{\varepsilon}(\mathbf{u}),\boldsymbol{\varepsilon}(\boldsymbol{v})\big)_{\Omega^f} \\ - \big(p,\nabla\cdot\boldsymbol{v}\big)_{\Omega^f} + \big(q,\nabla\cdot\mathbf{u}\big)_{\Omega^f} = 0, \\ \forall(\boldsymbol{v},q) \in [H_0^1(\Omega^f\cup\Omega^s\cup\Sigma)]^d \times L^2(\Omega^f),\ \boldsymbol{v}_{|\Omega^s} \in V^s, \quad (3.5)\end{aligned}$$

where $a^s(\cdot,\cdot)$ denotes the bilinear form associated with the structure part. We will assume that $a^s(\cdot,\cdot)$ defines a scalar product on V^s and that exists $r \geq 1$ such that

$$a^s(\boldsymbol{v},\boldsymbol{v}) \geq C\|\boldsymbol{v}\|^2_{r,\Omega^s}, \quad \forall \boldsymbol{v} \in V^s. \tag{3.6}$$

Typically, r will be equal to 1 or 2. In the case of linearized elasticity, $a^s(\cdot,\cdot)$ writes

$$a^s(\boldsymbol{d},\boldsymbol{v}) = \big(\boldsymbol{\sigma}^s(\boldsymbol{d}),\boldsymbol{\varepsilon}(\boldsymbol{v})\big)_{\Omega^s},$$

and it is coercive in $H^1_{0,\Gamma^s_D}(\Omega^s)$ (thus $r=1$) thanks to Korn's inequality [Cia88].

In (3.5), a global test function $\boldsymbol{v} \in [H_0^1(\Omega^f\cup\Omega^s\cup\Sigma)]^d$ is used. Nonetheless, we could also have independent test functions that are not necessary equal at the interface Σ of the two sub-domains. In this case, a more general variational formulation of (3.2)-(3.3) can be written by introducing the Lagrange multipliers $\boldsymbol{\lambda}$ such that $(\mathbf{u},\boldsymbol{d},p,\boldsymbol{\lambda})$ satisfy

$$\begin{aligned}\rho^s(\partial_{tt}\boldsymbol{d},\boldsymbol{v}^s)_{\Omega^s} + a^s(\boldsymbol{d},\boldsymbol{v}^s) + \rho^f\big(\partial_t\mathbf{u},\boldsymbol{v}^f\big)_{\Omega^f} + 2\mu\big(\boldsymbol{\varepsilon}(\mathbf{u}),\boldsymbol{\varepsilon}(\boldsymbol{v}^f)\big)_{\Omega^f} \\ - \big(p,\nabla\cdot\boldsymbol{v}^f\big)_{\Omega^f} + \big(q,\nabla\cdot\mathbf{u}\big)_{\Omega^f} + \langle\boldsymbol{\lambda},\boldsymbol{v}^s-\boldsymbol{v}^f\rangle_\Sigma = 0, \\ \forall(\boldsymbol{v}^s,\boldsymbol{v}^f,q) \in V^s\times V^f\times Q. \quad (3.7)\end{aligned}$$

Here, the operator $\langle\cdot,\cdot\rangle_\Sigma$ denotes the duality product between $[(H^{1/2}_{00}(\Sigma))']^d$ and $[H^{1/2}_{00}(\Sigma)]^d$. The space $[H^{1/2}_{00}(\Sigma)]^d$ is a subspace of $[H^{1/2}(\Sigma)]^d$ with a strictly finer topology, such that, if we extend by zero on $\partial\Omega^f$ (resp. $\partial\Omega^s$) any $\boldsymbol{v} \in [H^{1/2}_{00}(\Sigma)]^d$, then the extension belongs to $[H^{1/2}(\partial\Omega^f)]^d$ (resp. $[H^{1/2}(\partial\Omega^s)]^d$). For a proof of the existence of the Lagrange multipliers $\boldsymbol{\lambda}$ we refer to [LTM00]. Note also that in (3.7) we still assume the coupling condition $(3.3)_1$ to be satisfied.

This last formulation will be used in our analysis. As a matter of fact, since we consider non-conforming finite element approximations, the discrete test functions are not equal at the interface but satisfy only a weak matching.

Note that any regular enough solution of such a coupled fluid-structure system

satisfies an energy equality that writes

$$\underbrace{\frac{\rho^{\mathrm{f}}}{2}\int_{\Omega^{\mathrm{f}}}|\mathbf{u}|^2}_{\text{Fluid kinetic energy}} + \underbrace{2\mu\int_{\Omega^{\mathrm{f}}}|\boldsymbol{\varepsilon}(\mathbf{u})|^2}_{\text{Dissipation within the fluid}} + \underbrace{\frac{\rho^{\mathrm{s}}}{2}\int_{\Omega^{\mathrm{s}}}|\partial_t \boldsymbol{d}|^2}_{\text{Structure kinetic energy}} + \underbrace{\frac{1}{2}a^{\mathrm{s}}(\boldsymbol{d},\boldsymbol{d})}_{\text{Structure mechanical energy}} = \frac{\rho^{\mathrm{f}}}{2}\int_{\Omega^{\mathrm{f}}}|\mathbf{u}_0|^2 + \frac{\rho^{\mathrm{s}}}{2}\int_{\Omega^{\mathrm{s}}}|\boldsymbol{d}_1|^2 + \frac{1}{2}a^{\mathrm{s}}(\boldsymbol{d}_0,\boldsymbol{d}_0).$$

For the well-posedness of the linear fluid-structure interaction problem we refer to [DGHL03, LTM00, Lio69], and, in all that follows, we suppose that its solution is smooth enough.

Remark 3.2 *We recall that for the coupled problem (3.2)-(3.3) different resolution strategies have been developed: from monolithic approaches, to partitioned procedures (see Section 2.5.3 for a review). The semi-implicit fluid-structure interaction scheme we analyze is based on a Dirichlet–Neumann partitioned procedure. In this framework, the variational formulation (3.5) is equivalently rewritten in the following way:*
For all $(\boldsymbol{v}^{\mathrm{f}}, q) \in V_0^{\mathrm{f}} \times Q$ *and* $\boldsymbol{v}^{\mathrm{s}} \in V^{\mathrm{s}}$, *find* $(\mathbf{u}, p, \boldsymbol{d}) \in V^{\mathrm{f}} \times Q \times V^{\mathrm{s}}$ *such that*

$$\begin{cases} \rho^{\mathrm{f}}\big(\partial_t \mathbf{u}, \boldsymbol{v}^{\mathrm{f}}\big)_{\Omega^{\mathrm{f}}} + 2\mu\big(\boldsymbol{\varepsilon}(\mathbf{u}), \boldsymbol{\varepsilon}(\boldsymbol{v}^{\mathrm{f}})\big)_{\Omega^{\mathrm{f}}} - \big(p, \nabla\cdot\boldsymbol{v}^{\mathrm{f}}\big)_{\Omega^{\mathrm{f}}} + \big(q, \nabla\cdot\mathbf{u}\big)_{\Omega^{\mathrm{f}}} = 0, \\ \mathbf{u} = \partial_t \boldsymbol{d}, \quad \text{on} \quad \Sigma, \\ \rho^{\mathrm{s}}(\partial_{tt}\boldsymbol{d}, \boldsymbol{v}^{\mathrm{s}})_{\Omega^{\mathrm{s}}} + a^{\mathrm{s}}(\boldsymbol{d}, \boldsymbol{v}^{\mathrm{s}}) = -\left\langle \mathcal{R}(\mathbf{u}, p), \mathcal{L}(\boldsymbol{v}^{\mathrm{s}})\right\rangle. \end{cases} \tag{3.8}$$

The operator $\mathcal{L}$ *represents a continuous extension operator from* V^{s} *into the space* V^{f}, *while* $\left\langle \mathcal{R}(\mathbf{u}, p), \boldsymbol{v}^{\mathrm{f}}\right\rangle$ *is defined by*

$$\left\langle \mathcal{R}(\mathbf{u}, p), \boldsymbol{v}^{\mathrm{f}}\right\rangle \overset{\text{def}}{=} \rho^{\mathrm{f}}\big(\partial_t \mathbf{u}, \boldsymbol{v}^{\mathrm{f}}\big)_{\Omega^{\mathrm{f}}} + 2\mu\big(\boldsymbol{\varepsilon}(\mathbf{u}), \boldsymbol{\varepsilon}(\boldsymbol{v}^{\mathrm{f}})\big)_{\Omega^{\mathrm{f}}} - \big(p, \nabla\cdot\boldsymbol{v}^{\mathrm{f}}\big)_{\Omega^{\mathrm{f}}}, \quad \forall \boldsymbol{v}^{\mathrm{f}} \in V^{\mathrm{f}},$$

and it represents the fluid interface load on the structure.

Note that, since $\left\langle \mathcal{R}(\mathbf{u}, p), \boldsymbol{v}^{\mathrm{f}}\right\rangle$ *depends only on the trace of* $\boldsymbol{v}^{\mathrm{s}}$ *at the interface and not on the choice of* $\mathcal{L}$, *it can be easily proved the equivalence between (3.5) and (3.8) thanks to the following decomposition*

$$[H_0^1(\Omega^{\mathrm{f}} \cup \Omega^{\mathrm{s}} \cup \Sigma)]^d = V_D \oplus V_N,$$

where

$$V_D = \left\{ \boldsymbol{v} \in [H_0^1(\Omega^{\mathrm{f}} \cup \Omega^{\mathrm{s}} \cup \Sigma)]^d : \boldsymbol{v}_{|\Omega^{\mathrm{s}}} = \boldsymbol{v}^{\mathrm{f}} \in V_0^{\mathrm{f}} \quad \textit{and} \quad \boldsymbol{v}_{|\Omega^{\mathrm{s}}} = \mathbf{0} \right\},$$

$$V_N = \left\{ \boldsymbol{v} \in [H_0^1(\Omega^{\mathrm{f}} \cup \Omega^{\mathrm{s}} \cup \Sigma)]^d : \boldsymbol{v}_{|\Omega^{\mathrm{s}}} = \boldsymbol{v}^{\mathrm{s}} \in V^{\mathrm{s}} \quad \textit{and} \quad \exists\ \mathcal{L} \quad \textit{s.t.} \quad \boldsymbol{v}_{|\Omega^{\mathrm{f}}} = \mathcal{L}(\boldsymbol{v}^{\mathrm{s}}) \right\}.$$

3.3 Semi-implicit projection scheme

3.3.1 Time semi-discrete scheme

For the sake of clarity, we recall here the semi-implicit coupling scheme (2.94)-(2.97) with the Leap-Frog scheme for the structure. Let $D_{\tau\tau}X^{n+1} \stackrel{\text{def}}{=} (X^{n+1} - 2X^n + X^{n-1})/\tau^2$, assuming that $\tilde{\mathbf{u}}^n$, $\mathbf{u}^n$, p^n, $\boldsymbol{d}^n$ and $\boldsymbol{d}^{n-1}$ are known at time $t^n = n\tau$, the semi-implicit projection scheme for the linear problem (3.2)-(3.3) reads

Algorithm 3.1 *Semi-implicit coupling scheme based on the projection Chorin-Temam method*

Step 1 : (explicit viscous-structure coupling)

$$\begin{cases} \rho^{\mathrm{f}} \dfrac{\tilde{\mathbf{u}}^{n+1} - \mathbf{u}^n}{\tau} - 2\mu \mathtt{div}\,(\boldsymbol{\varepsilon}(\tilde{\mathbf{u}}^{n+1})) = \mathbf{0}, \quad \mathtt{in} \quad \Omega^{\mathrm{f}}, \\ \tilde{\mathbf{u}}^{n+1} = D_\tau \boldsymbol{d}^n, \quad \mathtt{on} \quad \Sigma. \end{cases} \tag{3.9}$$

Step 2 : (implicit pressure-structure coupling)

– **Step 2.1** : (fluid projection sub-step)

$$\begin{cases} \rho^{\mathrm{f}} \dfrac{\mathbf{u}^{n+1} - \tilde{\mathbf{u}}^{n+1}}{\tau} + \nabla p^{n+1} = \mathbf{0}, \quad \mathtt{in} \quad \Omega^{\mathrm{f}}, \\ \mathtt{div}\,\mathbf{u}^{n+1} = 0, \quad \mathtt{in} \quad \Omega^{\mathrm{f}}, \\ \mathbf{u}^{n+1} \cdot \mathbf{n}^{\mathrm{f}} = D_\tau \boldsymbol{d}^{n+1} \cdot \mathbf{n}^{\mathrm{f}}, \quad \mathtt{on} \quad \Sigma. \end{cases} \tag{3.10}$$

– **Step 2.2** : (solid sub-step)

$$\begin{cases} \rho^{\mathrm{s}} D_{\tau\tau} \boldsymbol{d}^{n+1} - \mathtt{div}\,\boldsymbol{\sigma}^{\mathrm{s}}(\boldsymbol{d}^{n+1}) = \mathbf{0}, \quad \mathtt{in} \quad \Omega^s, \\ \boldsymbol{\sigma}^{\mathrm{s}}(\boldsymbol{d}^{n+1})\mathbf{n}^{\mathrm{s}} = \boldsymbol{\sigma}^{\mathrm{f}}(\tilde{\mathbf{u}}^{n+1}, p^{n+1})\mathbf{n}^{\mathrm{s}}, \quad \mathtt{on} \quad \Sigma. \end{cases} \tag{3.11}$$

Note that, for the first step, the kinematic condition verified by $\tilde{\mathbf{u}}^{n+1}$ is explicit, whereas, for the second step, the one verified by $\mathbf{u}^{n+1}$ is implicit. The stress applied by the fluid on the structure is split in two parts: the pressure part computed through an implicit procedure and the viscous part computed through an explicit one.

In order to introduce the corresponding variational formulation of (3.9)-(3.11) let us define the spaces

$$Y^{\mathrm{f}} \stackrel{\text{def}}{=} \left\{ \boldsymbol{v}^{\mathrm{f}} \in [L^2(\Omega^{\mathrm{f}})]^d \,:\, \nabla \cdot \boldsymbol{v}^{\mathrm{f}} \in L^2(\Omega^{\mathrm{f}}),\, \boldsymbol{v}^{\mathrm{f}} \cdot \mathbf{n}^{\mathrm{f}} = 0 \quad \text{on } \Gamma_D^{\mathrm{f}} \right\},$$

and

$$Y_0^{\mathrm{f}} \stackrel{\text{def}}{=} \left\{ \boldsymbol{v}^{\mathrm{f}} \in Y^{\mathrm{f}} : \boldsymbol{v}^{\mathrm{f}} \cdot \mathbf{n}^{\mathrm{f}} = 0 \quad \text{on} \quad \Sigma \right\}.$$

Assuming that $\tilde{\mathbf{u}}^n$, $\mathbf{u}^n$, $\boldsymbol{d}^n$ and $\boldsymbol{d}^{n-1}$ are known at time $t^n = n\tau$, the time semi-discrete variational formulation writes:

Algorithm 3.2 *Variational time semi-discrete semi-implicit coupling scheme.*

Step 1 : (explicit viscous-structure coupling)
Find $\tilde{\mathbf{u}}^{n+1} \in V^{\mathrm{f}}$ such that:

$$\begin{cases} \dfrac{\rho^{\mathrm{f}}}{\tau}\big(\tilde{\mathbf{u}}^{n+1} - \mathbf{u}^{n}, \tilde{\boldsymbol{v}}^{\mathrm{f}}\big)_{\Omega^{\mathrm{f}}} + 2\mu\big(\boldsymbol{\varepsilon}(\tilde{\mathbf{u}}^{n+1}), \boldsymbol{\varepsilon}(\tilde{\boldsymbol{v}}^{\mathrm{f}})\big)_{\Omega^{\mathrm{f}}} = 0, \quad \forall \tilde{\boldsymbol{v}}^{\mathrm{f}} \in V_0^{\mathrm{f}}, \\ \tilde{\mathbf{u}}^{n+1} = D_\tau \boldsymbol{d}^{n}, \quad \text{on} \quad \Sigma; \end{cases} \tag{3.12}$$

Step 2 : (implicit pressure-structure coupling)

- **Step 2.1** : (fluid projection sub-step)
  Find $(\mathbf{u}^{n+1}, p^{n+1}) \in Y^{\mathrm{f}} \times Q$ such that:

$$\begin{cases} \dfrac{\rho^{\mathrm{f}}}{\tau}\big(\mathbf{u}^{n+1} - \tilde{\mathbf{u}}^{n+1}, \boldsymbol{v}^{\mathrm{f}}\big)_{\Omega^{\mathrm{f}}} - \big(p^{n+1}, \nabla \cdot \boldsymbol{v}^{\mathrm{f}}\big)_{\Omega^{\mathrm{f}}} + \big(q, \nabla \cdot \mathbf{u}^{n+1}\big)_{\Omega^{\mathrm{f}}} = 0, \\ \forall (\boldsymbol{v}^{\mathrm{f}}, q) \in Y_0^{\mathrm{f}} \times Q, \\ \mathbf{u}^{n+1} \cdot \mathbf{n}^{\mathrm{f}} = D_\tau \boldsymbol{d}^{n+1} \cdot \mathbf{n}^{\mathrm{f}}, \quad \text{on} \quad \Sigma; \end{cases} \tag{3.13}$$

- **Step 2.2** : (solid sub-step)
  Find $\boldsymbol{d}^{n+1} \in V^{\mathrm{s}}$ such that:

$$\begin{aligned} \rho^{\mathrm{s}}\big(D_{\tau\tau}\boldsymbol{d}^{n+1}, \boldsymbol{v}^{\mathrm{s}}\big)_{\Omega^{\mathrm{s}}} + a^{\mathrm{s}}(\boldsymbol{d}^{n+1}, \boldsymbol{v}^{\mathrm{s}}) = &- \big\langle \mathcal{R}_\mu(\tilde{\mathbf{u}}^{n+1}), \mathcal{L}(\boldsymbol{v}^{\mathrm{s}}) \big\rangle \\ &- \big\langle \mathcal{R}_p(\mathbf{u}^{n+1}, p^{n+1}), \mathcal{L}(\boldsymbol{v}^{\mathrm{s}}) \big\rangle, \quad \forall \boldsymbol{v}^{\mathrm{s}} \in V^{\mathrm{s}}; \end{aligned} \tag{3.14}$$

In (3.14) the fluid residuals $\mathcal{R}_\mu$ and $\mathcal{R}_p$ are defined by

$$\begin{aligned} \big\langle \mathcal{R}_\mu(\tilde{\mathbf{u}}^{n+1}), \tilde{\boldsymbol{v}}^{\mathrm{f}} \big\rangle &\overset{\text{def}}{=} \frac{\rho^{\mathrm{f}}}{\tau}\big(\tilde{\mathbf{u}}^{n+1} - \mathbf{u}^{n}, \tilde{\boldsymbol{v}}^{\mathrm{f}}\big)_{\Omega^{\mathrm{f}}} + 2\mu\big(\boldsymbol{\varepsilon}(\tilde{\mathbf{u}}^{n+1}), \boldsymbol{\varepsilon}(\tilde{\boldsymbol{v}}^{\mathrm{f}})\big)_{\Omega^{\mathrm{f}}}, \\ \big\langle \mathcal{R}_p(\mathbf{u}^{n+1}, p^{n+1}), \boldsymbol{v}^{\mathrm{f}} \big\rangle &\overset{\text{def}}{=} \frac{\rho^{\mathrm{f}}}{\tau}\big(\mathbf{u}^{n+1} - \tilde{\mathbf{u}}^{n+1}, \boldsymbol{v}^{\mathrm{f}}\big)_{\Omega^{\mathrm{f}}} - \big(p^{n+1}, \nabla \cdot \boldsymbol{v}^{\mathrm{f}}\big)_{\Omega^{\mathrm{f}}}, \end{aligned}$$

for all $\tilde{\boldsymbol{v}}^{\mathrm{f}}, \boldsymbol{v}^{\mathrm{f}} \in V^{\mathrm{f}}$. In this scheme the residual $\mathcal{R}$ is split in two terms, $\mathcal{R}_\mu$ and $\mathcal{R}_p$, one associated with the viscous step, the other with the projection step.

3.3.2 Fully discrete scheme

For the space discretization we consider the finite element spaces introduced in Section 2.5.1, namely X_h^{f}, V_h^{f}, $V_{h,0}^{\mathrm{f}}$, Q_h and V_H^{s}. We assume that X_h^{f} satisfies:

$$\Big\{ \boldsymbol{v}_h \in \mathcal{C}^0(\overline{\Omega^{\mathrm{f}}}), \boldsymbol{v}_{h|K} \in \mathbb{P}_k, \forall K \in \mathcal{T}_h^{\mathrm{f}} \Big\} \subset X_h^{\mathrm{f}}, \text{ with } k \geq 1, \tag{3.15}$$

where $\mathbb{P}_k$, $k \geq 0$, is the space of polynomials of degree less than or equal to k. Moreover, the spaces V_h^{f} and Q_h are chosen in such a way that every couple $(\boldsymbol{v}_h, q_h)$ in $V_h^{\mathrm{f}} \times Q_h$ satisfies the LBB condition [Bre74, BF91]. We refer to [DGHL03] where, assuming that $\big(V_h^{\mathrm{f}} \cap H_0^1(\Omega^{\mathrm{f}})\big) \times \big(Q_h \cap L_0^2(\Omega^{\mathrm{f}})\big)$ satisfies the LBB, it is proved that it is also the case for $V_h^{\mathrm{f}} \times Q_h$. Here, the space $L_0^2(\Omega^{\mathrm{f}})$ denotes the subspace of

$L^2(\Omega^{\mathrm{f}})$ of zero-average functions in Ω^{f}. We also suppose that the space Y^{f} (resp. Y_0^{f}) is approximated by Y_h^{f} (resp. $Y_{h,0}^{\mathrm{f}}$) such that $V_h^{\mathrm{f}} \subset Y_h^{\mathrm{f}}$. For a discussion on the possible choices of approximation spaces for the projection method we refer to [GQ98a]. Furthermore, we denote by $V_H^{\mathrm{s}}(\Sigma)$ and $V_h^{\mathrm{f}}(\Sigma)$ the finite element trace spaces associated with V_H^{s} and V_h^{f}, respectively. Note that $V_H^{\mathrm{s}}(\Sigma)$ is equal to V_H^{s} whenever $\Omega^{\mathrm{s}} \subset \mathbb{R}^{d-1}$. Finally, $\pi_h : V_H^{\mathrm{s}}(\Sigma) \to V_h^{\mathrm{f}}(\Sigma)$ stands for a given interface matching operator. For instance, π_h can be a linear interpolation operator associated with the fluid finite element (nodal-wise matching) or a projection based operator (see [BMP93]). Therefore, the fully discrete problem writes as follows:

Algorithm 3.3 *Fully discrete semi-implicit coupling scheme.*

Step 1 : `(explicit viscous-structure coupling)`
`Find` $\tilde{\mathbf{u}}_h^{n+1} \in V_h^{\mathrm{f}}$ `such that:`

$$\begin{cases} \dfrac{\rho^{\mathrm{f}}}{\tau}\big(\tilde{\mathbf{u}}_h^{n+1} - \mathbf{u}^n, \tilde{\boldsymbol{v}}_h^{\mathrm{f}}\big)_{\Omega^{\mathrm{f}}} + 2\mu\big(\boldsymbol{\varepsilon}(\tilde{\mathbf{u}}_h^{n+1}), \boldsymbol{\varepsilon}(\tilde{\boldsymbol{v}}_h^{\mathrm{f}})\big)_{\Omega^{\mathrm{f}}} = 0, \quad \forall \tilde{\boldsymbol{v}}_h^{\mathrm{f}} \in V_{h,0}^{\mathrm{f}}, \\ \tilde{\mathbf{u}}_h^{n+1} = \pi_h\left(D_\tau \boldsymbol{d}_H^n\right), \quad \texttt{on} \quad \Sigma; \end{cases} \tag{3.16}$$

Step 2 : `(implicit pressure-structure coupling)`

- **Step 2.1** : `(fluid projection sub-step)`
  `Find` $(\mathbf{u}_h^{n+1}, p_h^{n+1}) \in Y_h^{\mathrm{f}} \times Q_h$ `such that:`

$$\begin{cases} \dfrac{\rho^{\mathrm{f}}}{\tau}\big(\mathbf{u}_h^{n+1} - \tilde{\mathbf{u}}_h^{n+1}, \boldsymbol{v}_h^{\mathrm{f}}\big)_{\Omega^{\mathrm{f}}} - \big(p_h^{n+1}, \nabla \cdot \boldsymbol{v}_h^{\mathrm{f}}\big)_{\Omega^{\mathrm{f}}} + \big(q_h, \nabla \cdot \mathbf{u}_h^{n+1}\big)_{\Omega^{\mathrm{f}}} = 0, \\ \forall (\boldsymbol{v}_h^{\mathrm{f}}, q_h) \in Y_{h,0}^{\mathrm{f}} \times Q_h, \\ \mathbf{u}_h^{n+1} \cdot \mathbf{n}^{\mathrm{f}} = \pi_h\left(D_\tau \boldsymbol{d}_H^{n+1}\right) \cdot \mathbf{n}^{\mathrm{f}}, \quad \texttt{on} \quad \Sigma; \end{cases} \tag{3.17}$$

- **Step 2.2** : `(solid sub-step)`
  `Find` $\boldsymbol{d}_H^{n+1} \in V_H^{\mathrm{s}}$ `such that:`

$$\begin{aligned} \rho^{\mathrm{s}}\big(D_{\tau\tau}\boldsymbol{d}_H^{n+1}, \boldsymbol{v}_H^{\mathrm{s}}\big)_{\Omega^{\mathrm{s}}} + a^{\mathrm{s}}(\boldsymbol{d}_H^{n+1}, \boldsymbol{v}_H^{\mathrm{s}}) = &- \left\langle \mathcal{R}_\mu(\tilde{\mathbf{u}}_h^{n+1}), \mathcal{L}_h(\boldsymbol{v}_H^{\mathrm{s}}) \right\rangle \\ &- \left\langle \mathcal{R}_p(\mathbf{u}_h^{n+1}, p_h^{n+1}), \mathcal{L}_h(\boldsymbol{v}_h^{\mathrm{s}}) \right\rangle, \quad \forall \boldsymbol{v}_h^{\mathrm{s}} \in V_h^{\mathrm{s}}; \end{aligned} \tag{3.18}$$

Here, $\mathcal{L}_h : V_H^{\mathrm{s}}(\Sigma) \to V_h^{\mathrm{f}}$ stands for any given discrete continuous lifting operator satisfying

$$\mathcal{L}_h(\boldsymbol{b}_H) = \pi_h(\boldsymbol{b}_H), \quad \text{on} \quad \Sigma. \tag{3.19}$$

There are several reasons for introducing non-conforming finite elements at the interface. On the one hand, the fluid-structure problem could involve different type of operators (take, for instance, Stokes coupled with a plate) for which the finite element discretization may lead to non-conforming finite elements at the interface even for matching grids. On the other hand, from a technical point of view, the stability of this semi-implicit scheme (3.16)-(3.18) is known under sufficient conditions obtained by using different mesh sizes:

Theorem 3.1 *Assume that the interface operator* $\pi_h : V_H^{\mathrm{s}}(\Sigma) \longrightarrow V_h^{\mathrm{f}}(\Sigma)$ *is* L^2*-stable on* $V_H^{\mathrm{s}}(\Sigma)$*. Then, there exists a constant* $C > 0$*, independent of the physical and discretization parameters, such that under the condition*

$$\rho^{\mathrm{s}} \geq C \left(\rho^{\mathrm{f}} \frac{h}{H^\alpha} + \frac{\mu\tau}{hH^\alpha} \right), \quad \textit{with} \quad \alpha \overset{\mathrm{def}}{=} \begin{cases} 0, & \textit{if} \quad \overline{\Omega^{\mathrm{s}}} = \Sigma, \\ 1, & \textit{if} \quad \overline{\Omega^{\mathrm{s}}} \neq \Sigma, \end{cases} \tag{3.20}$$

the semi-implicit coupling scheme is stable in the energy-norm.

Considering (3.20), it is worth noticing that:

- The stability of the scheme is enhanced by decreasing τ. Moreover, the sufficient condition (3.20) can be satisfied by reducing the ratios $\frac{h}{H^\alpha}$ and $\frac{\delta t}{hH^\alpha}$. The latter might be thought as a CFL-like condition.

- The assumption on the L^2-stability of the interface matching operator is satisfied by the standard finite element interpolation operator, for example, whenever the fluid interface triangulation is a sub-triangulation of the solid interface triangulation. This includes, in particular, the case of interface matching meshes. By construction, a mortar based matching operator also fulfils that assumption [BMP93].

- In the case $\overline{\Omega^{\mathrm{s}}} = \Sigma$, *i.e.* $\alpha = 0$, condition (3.20) becomes independent of the solid mesh size H. In particular, we may set $H = h$, and stabilize the scheme by simply reducing h (and τ).

- In the case $\overline{\Omega^{\mathrm{s}}} \neq \Sigma$, *i.e.* $\alpha = 1$, the stability of the scheme can be ensured provided that the fluid mesh size h is small enough compared to the structure mesh size H. Numerical simulations performed in $2D$ and $3D$, with $h = H$, showed however that this condition seems to be not necessary, when dealing with a reasonable range of physical parameters.

- The scheme is added-mass dependent. As a matter of fact the stability condition (3.20) still depends on the fluid-solid density ratio. In Chapter 4, where the Dirichlet boundary conditions of the explicit step is replaced with a specific Robin boundary condition (derived from the Nitsche's method), this dependency does not appear.

3.3.3 Interface matching operators

We now give the definitions as well as some properties of two possible matching operators: a pointwise matching and an integral one.

Pointwise matching. Let $\pi_h : \mathcal{C}^0(\overline{\Sigma}) \to V_h^{\mathrm{f}}(\Sigma)$ be the standard finite element interpolation operator associated with the fluid part. As in Theorem 3.1, we assume that

$$\pi_h \text{ is } L^2\text{-stable and } H_0^1\text{-stable in } V_H^{\mathrm{s}}(\Sigma). \tag{3.21}$$

Moreover, we suppose it satisfies the following approximation property:

$$\|\pi_h(\boldsymbol{b}_H) - \boldsymbol{b}_H\|_{0,\Sigma} \leq Ch^l \|\boldsymbol{b}_H\|_{l,\Sigma}, \ \forall \boldsymbol{b}_H \in V_H^{\mathrm{s}}(\Sigma), \tag{3.22}$$

$\forall\ 0 \leq l \leq k+1,$ such that $V^{\mathrm{s}}(\Sigma) \subset H^l(\Sigma)$.
In (3.22), $V^{\mathrm{s}}(\Sigma)$ denotes the space of trace functions of V^{s} on the interface Σ. Note that since we assume that V^{s} is continuously embedded in $H^r(\Omega^{\mathrm{s}})$, then $l \leq r - \frac{\alpha}{2}$ with

$$\alpha \stackrel{\text{def}}{=} \begin{cases} 0, & \text{if} \quad \overline{\Omega^{\mathrm{s}}} = \Sigma, \\ 1, & \text{if} \quad \overline{\Omega^{\mathrm{s}}} \neq \Sigma. \end{cases} \tag{3.23}$$

The property (3.21) holds true, for instance, when the fluid interface mesh is a sub-triangulation of the solid interface mesh, namely, for all $K \in \mathcal{T}_h^{\mathrm{f}}$ with $|K \cap \Sigma| \neq 0$ there exists $K' \in \mathcal{T}_H^{\mathrm{s}}$ such that

$$K \cap \Sigma \subset K' \cap \Sigma.$$

We refer to [FGG07, Appendix A] for a proof of the L^2-stability. In a similar way one can prove that the finite element interpolation operator is H_0^1-stable on $V_H^{\mathrm{s}}(\Sigma)$. Under the same assumption on the interface meshes, estimate (3.22) can be proved by introducing the Clement operator that is known to verify (3.22) (see [CL91]) and by using (3.21) for the finite element interpolation operator π_h.

Remark 3.3 *Note that if we consider the Clement operator instead of the standard finite element interpolation operator then properties* (3.21) *and* (3.22) *hold with no additional assumption on the interface mesh [CL91].*

Mortar matching. In the case of a mortar matching, the operator $\pi_h : L^2(\Sigma) \to V_h^{\mathrm{f}}(\Sigma)$ is defined as follows:

$$\int_\Sigma (\boldsymbol{b} - \pi_h(\boldsymbol{b})) \cdot \boldsymbol{\phi}_h = 0, \forall \boldsymbol{\phi}_h \in \tilde{V}_h^{\mathrm{f}}(\Sigma), \tag{3.24}$$

where $\tilde{V}_h^{\mathrm{f}}(\Sigma)$ is a subspace of $X_h^{\mathrm{f}}(\Sigma)$ such that

$$\left\{ \boldsymbol{v}_h \in \mathcal{C}^0(\overline{\Sigma}), \boldsymbol{v}_{h|K} \in \mathbb{P}_{k-1}, \forall K \in \mathcal{T}_h^{\mathrm{f}} \text{ with } |K \cap \Sigma| \neq 0 \right\} \subset \tilde{V}_h^{\mathrm{f}}(\Sigma), \text{ with } k \geq 1.$$

We will moreover assume that $\tilde{V}_h^{\mathrm{f}}(\Sigma)$ has good approximation properties. More precisely, let $\tilde{\pi}_h$ be the L^2 orthogonal projection operator on $\tilde{V}_h^{\mathrm{f}}(\Sigma)$, then $\forall\ 0 \leq \tau \leq 1, \forall \boldsymbol{v} \in H^\tau(\Sigma)$

$$\|\tilde{\pi}_h(\boldsymbol{v}) - \boldsymbol{v}\|_{0,\Sigma} + h^{-\frac{1}{2}} \|\tilde{\pi}_h(\boldsymbol{v}) - \boldsymbol{v}\|_{(H_{00}^{\frac{1}{2}}(\Sigma))'} \leq Ch^\tau \|\boldsymbol{v}\|_{\tau,\Sigma}. \tag{3.25}$$

The proof of this property, in the two-dimensional case, can be found in [BMP93, BMP94]. Moreover, we require that the mortar operator π_h verifies the following stability properties:

$$\|\pi_h(\boldsymbol{v})\|_{0,\Sigma} \leq C\|\boldsymbol{v}\|_{0,\Sigma}, \quad \forall \boldsymbol{v} \in H_0^1(\Sigma), \tag{3.26}$$

$$\|\pi_h(\boldsymbol{v})\|_{H_0^1(\Sigma)} \leq C\|\boldsymbol{v}\|_{H_0^1(\Sigma)}, \quad \forall \boldsymbol{v} \in H_0^1(\Sigma), \tag{3.27}$$

and

$$\|\pi_h(\boldsymbol{v})\|_{H_{00}^{\frac{1}{2}}(\Sigma)} \leq C\|\boldsymbol{v}\|_{H_{00}^{\frac{1}{2}}(\Sigma)}, \quad \forall \boldsymbol{v} \in H_{00}^{\frac{1}{2}}(\Sigma). \tag{3.28}$$

Finally, the following error estimate is assumed to hold true, $\forall\ \frac{1}{2} \leq \lambda \leq k+1$

$$\forall \boldsymbol{v} \in H^\lambda(\Sigma) \cap H_{00}^{\frac{1}{2}}(\Sigma), \quad \|\pi_h(\boldsymbol{v}) - \boldsymbol{v}\|_{H_{00}^{\frac{1}{2}}(\Sigma)} \leq Ch^{\lambda-\frac{1}{2}}\|\boldsymbol{v}\|_{\lambda,\Sigma}. \tag{3.29}$$

The proof of (3.26)-(3.29) can be found in [BB99] for the two-dimensional case. Examples of three-dimensional finite element spaces verifying the same inequalities can be found in [BBM97]. Note that these properties imply that $\tilde{V}_h^{\mathrm{f}}(\Sigma)$ is a good approximation of the space $(H_{00}^{\frac{1}{2}}(\Sigma))'$.

3.4 Construction of the finite element approximations

In this section, we build an appropriate finite element approximation of the exact solution $(\mathbf{u}, p, \boldsymbol{d})$ defined in Section 3.2, that verifies at the interface the space-discrete counterpart of the time-discrete coupling condition $\mathbf{u}(t^{n+1}) = D_\tau \boldsymbol{d}(t^{n+1})$, where $D_\tau X(t^{n+1}) \stackrel{\text{def}}{=} (X(t^{n+1}) - X(t^n))/\tau$. A space and a time discretization errors are consequently introduced. In [LTM00], a quite similar construction is made. There, the authors first build approximations of the fluid and structure displacements that match at the interface at each time and then they build velocity approximations satisfying an implicit condition at the interface. Here instead we directly build the approximations of the fluid velocity $\mathbf{u}_h(t) \in V_h^{\mathrm{f}}$ and of the structure displacement $\boldsymbol{d}_H(t) \in V_H^{\mathrm{s}}$ such that

$$\mathbf{u}_h(t^i) = \pi_h\big(D_\tau \boldsymbol{d}_H(t^i)\big), \quad \forall i \text{ s.t. } t^i \leq T. \tag{3.30}$$

Let us define $(P_h^{\mathrm{f}}(\mathbf{u})(t), P_h^{\mathrm{f}}(p)(t), P_H^{\mathrm{s}}(\boldsymbol{d})(t))$ as follows:

$$\begin{cases} 2\mu\left(\boldsymbol{\varepsilon}(P_h^{\mathrm{f}}(\mathbf{u})(t)), \boldsymbol{\varepsilon}(\boldsymbol{v}_h)\right)_{\Omega^{\mathrm{f}}} + \left(P_h^{\mathrm{f}}(p)(t), \nabla\cdot\boldsymbol{v}_h\right)_{\Omega^{\mathrm{f}}} = \\ \qquad\qquad 2\mu\left(\boldsymbol{\varepsilon}(\mathbf{u})(t), \boldsymbol{\varepsilon}(\boldsymbol{v}_h)\right)_{\Omega^{\mathrm{f}}} + \left(p(t), \nabla\cdot\boldsymbol{v}_h\right)_{\Omega^{\mathrm{f}}}, \quad \forall \boldsymbol{v}_h \in V_h^{\mathrm{f}}, \\ \left(q_h, \nabla\cdot P_h^{\mathrm{f}}(\mathbf{u})(t)\right)_{\Omega^{\mathrm{f}}} = 0, \quad \forall q_h \in Q_h, \end{cases}$$

$$a^{\mathrm{s}}(P_H^{\mathrm{s}}(\boldsymbol{d})(t), \boldsymbol{v}_H) = a^{\mathrm{s}}(\boldsymbol{d}(t), \boldsymbol{v}_H), \forall \boldsymbol{v}_H \in V_H^{\mathrm{s}}.$$

In a standard way (see [BF91, CL91]), these finite element functions satisfy the following error estimates:

$$\|P_h^{\mathrm{f}}(\mathbf{u})(t) - \mathbf{u}(t)\|_{1,\Omega^{\mathrm{f}}} + \|P_h^{\mathrm{f}}(p)(t) - p(t)\|_{0,\Omega^{\mathrm{f}}} \leq \inf_{\boldsymbol{v}_h \in V_h^{\mathrm{f}}} \|\mathbf{u}(t) - \boldsymbol{v}_h\|_{1,\Omega^{\mathrm{f}}} + \inf_{q_h \in Q_h} \|p(t) - q_h\|_{0,\Omega^{\mathrm{f}}}, \tag{3.31}$$

$$\|P_H^{\mathrm{s}}(\boldsymbol{d})(t) - \boldsymbol{d}(t)\|_{V^{\mathrm{s}}} \leq \inf_{\boldsymbol{v}_H \in V_H^{\mathrm{s}}} \|\boldsymbol{d}(t) - \boldsymbol{v}_H\|_{V^{\mathrm{s}}}. \tag{3.32}$$

We now build corrections of $(P_h^{\rm f}(\mathbf{u}), P_h^{\rm s}(\boldsymbol{d}))$ such that (3.30) is satisfied and $(\nabla\cdot\mathbf{u}_h, q_h)_{\Omega^{\rm f}} = 0$, $\forall q_h \in Q_h$. These two conditions imply that

$$\int_\Sigma \pi_h\big(D_\tau \boldsymbol{d}_H(t^i)\big)\cdot\mathbf{n} = 0.$$

Nevertheless, $\int_\Sigma \pi_h\big(D_\tau P_H^{\rm s}(\boldsymbol{d})(t^i)\big)\cdot\mathbf{n} \neq 0$. Consequently, we add a correction $\boldsymbol{c}_H(t)$ to $P_H^{\rm s}(\boldsymbol{d})$ so that $\int_\Sigma \pi_h\big(P_H^{\rm s}(\boldsymbol{d})(t) + \boldsymbol{c}_H(t)\big)\cdot\mathbf{n}$ is equal to a given time independent constant. Let $\mathbf{u}_H^{\rm s} \in V_H^{\rm s}$ be an approximation of $\mathbf{u}^{\rm s} \in V^{\rm s}$ such that $\int_\Sigma \mathbf{u}^{\rm s}\cdot\mathbf{n} \neq 0$. Then, for h and H sufficiently small $\int_\Sigma \pi_h(\mathbf{u}_H^{\rm s})\cdot\mathbf{n} \neq 0$. We set

$$\boldsymbol{d}_H(t) = P_H^{\rm s}(\boldsymbol{d})(t) + \boldsymbol{c}_H(t) = P_H^{\rm s}(\boldsymbol{d})(t) - \frac{\displaystyle\int_\Sigma \Big(\pi_h\big(P_H^{\rm s}(\boldsymbol{d})(t)\big) - \boldsymbol{d}_0\Big)\cdot\mathbf{n}}{\displaystyle\int_\Sigma \pi_h(\mathbf{u}_H^{\rm s})\cdot\mathbf{n}}\mathbf{u}_H^{\rm s}.$$

and this definition yields $\int_\Sigma \pi_h(\boldsymbol{d}_H(t))\cdot\mathbf{n} = \int_\Sigma \boldsymbol{d}_0\cdot\mathbf{n}, \forall t$.

Next, we build a correction of $P_h^{\rm f}(\mathbf{u})(t)$, denoted $\boldsymbol{z}_h(t)$, affine in time and such that satisfies

$$P_h^{\rm f}(\mathbf{u})(t^i) + \boldsymbol{z}_h(t^i) = \pi_h\big(D_\tau \boldsymbol{d}_H(t^i)\big)\cdot\mathbf{n}, \quad \text{on} \quad \Sigma,$$

and

$$(\nabla\cdot\boldsymbol{z}_h, q_h)_{\Omega^{\rm f}} = 0, \quad \forall q_h \in Q_h.$$

This can be done by solving the discrete Stokes problem:
Find $(\boldsymbol{z}_h(t^i), \mu_h(t^i)) \in V_h^{\rm f} \times \big(Q_h \cap L_0^2(\Omega^{\rm f})\big)$ such that

$$\left\{\begin{array}{lcll} 2\mu\left(\boldsymbol{\varepsilon}(\boldsymbol{z}_h(t^i)), \boldsymbol{\varepsilon}(\boldsymbol{v}_h)\right)_{\Omega^{\rm f}} + \left(\mu_h(t^i), \nabla\cdot\boldsymbol{v}_h\right)_{\Omega^{\rm f}} & = & 0, & \forall \boldsymbol{v}_h \in V_{h,0}^{\rm f}, \\ \left(q_h, \nabla\cdot\boldsymbol{z}_h(t^i)\right)_{\Omega^{\rm f}} & = & 0 & , \forall q_h \in Q_h \cap L_0^2(\Omega^{\rm f}), \end{array}\right.$$

with

$$\boldsymbol{z}_h(t^i) = \pi_h\big(D_\tau \boldsymbol{d}_H(t^i)\big)\cdot\mathbf{n} - P_h^{\rm f}(\mathbf{u})(t^i), \text{ on } \Sigma.$$

This problem is well-posed and the couple $(\boldsymbol{z}_h(t^i), \mu_h(t^i))$ verifies

$$\|\boldsymbol{z}_h(t^i)\|_{1,\Omega^{\rm f}} + \|\mu_h(t^i)\|_{0,\Omega^{\rm f}} \leq C\left\|\pi_h\big(D_\tau \boldsymbol{d}_H(t^i)\big) - P_h^{\rm f}(\mathbf{u})(t^i)\right\|_{H_{00}^{\frac{1}{2}}(\Sigma)}. \tag{3.33}$$

Finally, the affine-in-time velocity and pressure are defined by

$$\begin{aligned} \mathbf{u}_h(t^i) &= P_h^{\rm f}(\mathbf{u})(t^i) + \boldsymbol{z}_h(t^i), \\ p_h(t^i) &= P_h^{\rm f}(p)(t^i) + \mu_h(t^i). \end{aligned}$$

We now verify that the considered velocity, pressure and displacement are good approximations of $(\mathbf{u}, p, \boldsymbol{d})$ in $V^{\rm f} \times Q \times V^{\rm s}$. Thus, the correction terms $(\boldsymbol{z}_h, \mu_h, \boldsymbol{c}_H)$ have to be estimated. Clearly, an error in time as well as an error due to the incompatible matching at the interface are expected.

Considering

$$\boldsymbol{c}_H(t) = -\int_\Sigma \big(\pi_h\big(P_H^{\mathrm{s}}(\boldsymbol{d})(t)\big)\cdot\mathbf{n} - \boldsymbol{d}_0\cdot\mathbf{n}\big)\overline{\mathbf{u}}_H^{\mathrm{s}},$$

with $\overline{\mathbf{u}}_H^{\mathrm{s}} = \dfrac{\mathbf{u}_H^{\mathrm{s}}}{\int_\Sigma \pi_h(\mathbf{u}_H^{\mathrm{s}})\cdot\mathbf{n}}$, and recalling that $\displaystyle\int_\Sigma \boldsymbol{d}(t)\cdot\mathbf{n} = \int_\Sigma \boldsymbol{d}_0\cdot\mathbf{n}\ \forall t$, we have

$$\boldsymbol{c}_H(t) = -\int_\Sigma \big(\pi_h\big(P_H^{\mathrm{s}}(\boldsymbol{d})(t)\big)\cdot\mathbf{n} - \boldsymbol{d}(t)\cdot\mathbf{n}\big)\overline{\mathbf{u}}_H^{\mathrm{s}}. \tag{3.34}$$

Two cases have to be studied.

Pointwise matching. If π_h is a pointwise matching operator, then for $\boldsymbol{c}_H(t)$ the following decomposition holds

$$\boldsymbol{c}_H(t) = -\int_\Sigma \big(\pi_h(P_H^{\mathrm{s}}(\boldsymbol{d})(t)) - P_H^{\mathrm{s}}(\boldsymbol{d})(t)\big)\cdot\mathbf{n}\ \overline{\mathbf{u}}_H^{\mathrm{s}} + \int_\Sigma \big(P_H^{\mathrm{s}}(\boldsymbol{d})(t) - \boldsymbol{d}(t)\big)\cdot\mathbf{n}\ \overline{\mathbf{u}}_H^{\mathrm{s}}.$$

Consequently, we obtain

$$\|\boldsymbol{c}_H(t)\|_{V^{\mathrm{s}}} \le C\big(\|\pi_h(P_H^{\mathrm{s}}(\boldsymbol{d})(t)) - P_H^{\mathrm{s}}(\boldsymbol{d})(t)\|_{0,\Sigma} + \|\boldsymbol{d}(t) - P_H^{\mathrm{s}}(\boldsymbol{d})(t)\|_{0,\Sigma}\big).$$

To estimate the first term we use the assumption (3.22), for the second term we recall (3.32). Thus,

$$\|\boldsymbol{c}_H(t)\|_{V^{\mathrm{s}}} \le C\big(h^l\big\|P_H^{\mathrm{s}}(\boldsymbol{d})(t)\big\|_{l,\Sigma} + \inf_{\boldsymbol{v}_H\in V_H^{\mathrm{s}}}\big\|\boldsymbol{d}(t) - \boldsymbol{v}_H\big\|_{V^{\mathrm{s}}}\big),$$

for all $0 \le l \le k+1$ such that $V^{\mathrm{s}}(\Sigma)$ is continuously embedded in $H^l(\Sigma)$. In particular, $l \le \min(r - \frac{\alpha}{2}, k+1)$, where α is defined by (3.23) and r is such that V^{s} is continuously embedded in $H^r(\Omega^{\mathrm{s}})$. Finally, the definition of $P_H^{\mathrm{s}}(\boldsymbol{d})$, for $l \le r - \frac{\alpha}{2}$, gives

$$\|P_H^{\mathrm{s}}(\boldsymbol{d})\|_{l,\Sigma} \le C\|P_H^{\mathrm{s}}(\boldsymbol{d})\|_{r,\Omega^{\mathrm{s}}} \le C\|P_H^{\mathrm{s}}(\boldsymbol{d})\|_{V^{\mathrm{s}}} \le C\|\boldsymbol{d}\|_{V^{\mathrm{s}}},$$

which yields

$$\|\boldsymbol{c}_H(t)\|_{V^{\mathrm{s}}} \le C\left(h^l\|\boldsymbol{d}(t)\|_{V^{\mathrm{s}}} + \inf_{\boldsymbol{v}_H\in V_H^{\mathrm{s}}}\|\boldsymbol{d}(t) - \boldsymbol{v}_H\|_{V^{\mathrm{s}}}\right).$$

Mortar matching. If π_h is a mortar matching operator, then for $\boldsymbol{c}_H(t)$ the following decomposition holds

$$\begin{aligned}\boldsymbol{c}_H(t) &= -\int_\Sigma \left(\pi_h\big(P_H^{\mathrm{s}}(\boldsymbol{d})(t)\big)\cdot\mathbf{n} - \boldsymbol{d}(t)\cdot\mathbf{n}\right)\overline{\mathbf{u}}_H^{\mathrm{s}}\\ &= -\left(\int_\Sigma \pi_h\big(P_H^{\mathrm{s}}(\boldsymbol{d})(t) - \boldsymbol{d}(t)\big)\cdot\mathbf{n}\right)\overline{\mathbf{u}}_H^{\mathrm{s}} + \int_\Sigma \left(\pi_h\big(\boldsymbol{d}(t)\big)\cdot\mathbf{n} - \boldsymbol{d}(t)\cdot\mathbf{n}\right)\overline{\mathbf{u}}_H^{\mathrm{s}},\end{aligned}$$

as a result,

$$\|\boldsymbol{c}_H(t)\|_{V^{\mathrm{s}}} \le C\left(\big\|\pi_h\big(P_H^{\mathrm{s}}(\boldsymbol{d})(t) - \boldsymbol{d}(t)\big)\big\|_{0,\Sigma} + \left|\int_\Sigma (\pi_h(\boldsymbol{d}(t)) - \boldsymbol{d}(t))\cdot\mathbf{n}\right|\right).$$

Since the mortar matching operator is stable in the L^2-norm, see (3.26), we obtain

$$\|\boldsymbol{c}_H(t)\|_{V^{\mathrm{s}}} \leq C\bigg(\|P_H^{\mathrm{s}}(\boldsymbol{d})(t) - \boldsymbol{d}(t)\|_{0,\Sigma} + \bigg| \int_\Sigma (\pi_h(\boldsymbol{d}(t)) - \boldsymbol{d}(t)) \cdot \mathbf{n} \bigg| \bigg).$$

The first term of this inequality is estimated as in (3.32). For the second term, we take advantage of the definition of the operator to get

$$\int_\Sigma \big(\pi_h(\boldsymbol{d}(t)) - \boldsymbol{d}(t)\big) \cdot \mathbf{n} = \int_\Sigma \big(\pi_h(\boldsymbol{d}(t)) - \boldsymbol{d}(t)\big) \cdot \big(\mathbf{n} - \tilde{\pi}_h(\mathbf{n})\big),$$

therefore

$$\bigg| \int_\Sigma \big(\pi_h(\boldsymbol{d}(t)) - \boldsymbol{d}(t)\big) \cdot \mathbf{n} \bigg| \leq C \big\|\pi_h(\boldsymbol{d}(t)) - \boldsymbol{d}(t)\big\|_{H_{00}^{\frac{1}{2}}(\Sigma)} \big\|\mathbf{n} - \tilde{\pi}_h(\mathbf{n})\big\|_{(H_{00}^{\frac{1}{2}}(\Sigma))'}.$$

From the assumptions (3.25) and (3.29) made respectively on $\tilde{\pi}_h$ and π_h we finally obtain

$$\bigg| \int_\Sigma (\pi_h(\boldsymbol{d}(t)) - \boldsymbol{d}(t)) \cdot \mathbf{n} \bigg| \leq C h^\lambda \|\boldsymbol{d}(t)\|_{\lambda,\Sigma}, \quad \forall\, \frac{1}{2} \leq \lambda \leq k+1.$$

To summarize, in both cases we have

$$\|\boldsymbol{c}_H(t)\|_{V^{\mathrm{s}}} \leq C\bigg(h^l \|\boldsymbol{d}(t)\|_{V^{\mathrm{s}}} + \inf_{\boldsymbol{v}_H \in V_H^{\mathrm{s}}} \|\boldsymbol{d}(t) - \boldsymbol{v}_H\|_{V^{\mathrm{s}}} \bigg),$$

where,

$$l \leq \min\left(r - \frac{\alpha}{2}, k+1\right), \tag{3.35}$$

for a **pointwise matching operator**, while

$$\frac{1}{2} \leq l \leq k+1, \tag{3.36}$$

for the **mortar matching operator**.

Hence, the difference between the continuous displacement $\boldsymbol{d}$ and its finite element approximation $\boldsymbol{d}_H$ in V^{s} can be estimated by the best approximation of $\boldsymbol{d}$ in V_H^{s} and a term measuring the error due to the non-conforming matching at the interface:

$$\big\|\boldsymbol{d}(t) - \boldsymbol{d}_H(t)\big\|_{V^{\mathrm{s}}} \leq C\bigg(h^l \|\boldsymbol{d}(t)\|_{V^{\mathrm{s}}} + \inf_{\boldsymbol{v}_H \in V_H^{\mathrm{s}}} \|\boldsymbol{d}(t) - \boldsymbol{v}_H\|_{V^{\mathrm{s}}} \bigg), \tag{3.37}$$

where l is subject to the same restrictions as above, *i.e.* (3.35) and (3.36) for an interpolation and an integral matching operator, respectively.

Now we consider fluid velocity and the estimate $\big\|\mathbf{u}(t^i) - \mathbf{u}_h(t^i)\big\|_{1,\Omega^{\mathrm{f}}}$. To this end, we have to estimate $\big\|\boldsymbol{z}(t^i)\big\|_{1,\Omega^{\mathrm{f}}}$. By definition of $\boldsymbol{z}_h$ and remembering (3.33),

$$\|\boldsymbol{z}_h(t^i)\|_{1,\Omega^{\mathrm{f}}} \leq C \Big\|\pi_h\big(D_\tau \boldsymbol{d}_H(t^i)\big) - P_h^{\mathrm{f}}(\mathbf{u})(t^i)\Big\|_{H_{00}^{\frac{1}{2}}(\Sigma)}. \tag{3.38}$$

But thanks to the assumption of $H_{00}^{1/2}$-stability of π_h (see (3.21) and (3.28)) and to the fact that $\pi_h(\boldsymbol{v}_h) = \boldsymbol{v}_h,\ \forall \boldsymbol{v}_h \in V_h^{\mathrm{f}}(\Sigma)$

$$\|\boldsymbol{z}_h(t^i)\|_{1,\Omega^{\mathrm{f}}} \quad \leq \quad C \left\| D_\tau \boldsymbol{d}_H(t^i) - P_h^{\mathrm{f}}(\mathbf{u})(t^i) \right\|_{H_{00}^{\frac{1}{2}}(\Sigma)}.$$

Note that we have used the $H_{00}^{1/2}$-stability of π_h not only on $V_H^{\mathrm{s}}(\Sigma)$ but also on the space of functions that writes as a sum of functions of $V_H^{\mathrm{s}}(\Sigma)$ and of $V_h^{\mathrm{f}}(\Sigma)$. It is clear the mortar finite element operator verifies this property. Concerning the finite element interpolation operator at the interface, this is stable on every spaces whose $\mathcal{C}^0$ functions are polynomial on $K \in \mathcal{T}_h^{\mathrm{f}}$ with $|K \cap \Sigma| \neq 0$. The needed stability property is then verified for instance when the fluid interface mesh is a sub-triangulation of the solid interface mesh. As a result,

$$\begin{aligned}
\|\boldsymbol{z}_h(t^i)\|_{1,\Omega^{\mathrm{f}}} \quad \leq \quad & C \Big(\left\| D_\tau \boldsymbol{d}_H(t^i) - \partial_t \boldsymbol{d}_H(t^i) \right\|_{H_{00}^{\frac{1}{2}}(\Sigma)} + \left\| \partial_t \boldsymbol{d}_H(t^i) - \partial_t \boldsymbol{d}(t^i) \right\|_{H_{00}^{\frac{1}{2}}(\Sigma)} \\
& + \left\| \partial_t \boldsymbol{d}(t^i) - P_h^{\mathrm{f}}(\mathbf{u})(t^i) \right\|_{H_{00}^{\frac{1}{2}}(\Sigma)} \Big) \\
\leq \quad & C \Big(\left\| D_\tau \boldsymbol{d}_H(t^i) - \partial_t \boldsymbol{d}_H(t^i) \right\|_{H_{00}^{\frac{1}{2}}(\Sigma)} + \left\| P_H^{\mathrm{s}}(\partial_t \boldsymbol{d})(t^i) - \partial_t \boldsymbol{d}(t^i) \right\|_{H_{00}^{\frac{1}{2}}(\Sigma)} \\
& + \left\| \partial_t \boldsymbol{c}_H(t^i) \right\|_{H_{00}^{\frac{1}{2}}(\Sigma)} + \left\| \mathbf{u}(t^i) - P_h^{\mathrm{f}}(\mathbf{u})(t^i) \right\|_{H_{00}^{\frac{1}{2}}(\Sigma)} \Big) \\
\leq \quad & C \Big(\inf_{\boldsymbol{v}_H \in V_H^{\mathrm{s}}} \left\| \partial_t \boldsymbol{d}(t^i) - \boldsymbol{v}_H \right\|_{V^{\mathrm{s}}} + \inf_{\boldsymbol{v}_h \in V_h^{\mathrm{f}}} \left\| \mathbf{u}(t^i) - \boldsymbol{v}_h \right\|_{V^{\mathrm{f}}} \\
& + \left\| D_\tau \boldsymbol{d}_H(t^i) - \partial_t \boldsymbol{d}_H(t^i) \right\|_{H_{00}^{\frac{1}{2}}(\Sigma)} + \left\| \partial_t \boldsymbol{c}_H(t^i) \right\|_{H_{00}^{\frac{1}{2}}(\Sigma)} \Big).
\end{aligned}$$

We have therefore to estimate $\left\| D_\tau \boldsymbol{d}_H(t^i) - \partial_t \boldsymbol{d}_H(t^i) \right\|_{H_{00}^{\frac{1}{2}}(\Sigma)}$ and $\|\partial_t \boldsymbol{c}_H(t^i)\|_{H_{00}^{\frac{1}{2}}(\Sigma)}$. Recalling the definition of $\boldsymbol{d}_H$, it is easy to see that

$$\begin{aligned}
\left\| D_\tau \boldsymbol{d}_H(t^i) - \partial_t \boldsymbol{d}_H(t^i) \right\|_{H_{00}^{\frac{1}{2}}(\Sigma)} \leq & \left\| D_\tau \big(P_H^{\mathrm{s}}(\boldsymbol{d})(t^i) \big) - P_H^{\mathrm{s}}(\partial_t \boldsymbol{d})(t^i) \right\|_{H_{00}^{\frac{1}{2}}(\Sigma)} \\
& + \left\| D_\tau \boldsymbol{c}_H(t^i) - \partial_t \boldsymbol{c}_H(t^i) \right\|_{H_{00}^{\frac{1}{2}}(\Sigma)}.
\end{aligned}$$

But

$$D_\tau \boldsymbol{c}_H(t^i) - \partial_t \boldsymbol{c}_H(t^i) = - \left(\int_\Sigma \pi_h \left(D_\tau \big(P_H^{\mathrm{s}}(\boldsymbol{d})(t^i) \big) - P_H^{\mathrm{s}}(\partial_t \boldsymbol{d})(t^i) \big) \cdot \mathbf{n} \right) \overline{\mathbf{u}}_H^{\mathrm{s}},$$

which yields

$$\left\| D_\tau \boldsymbol{c}_H(t^i) - \partial_t \boldsymbol{c}_H(t^i) \right\|_{H_{00}^{1/2}(\Sigma)} \leq C\tau \|\boldsymbol{d}\|_{W^{2,\infty}(0,T;V^{\mathrm{s}})},$$

and thus, for the definition of P_H^{s},

$$\left\| D_\tau \boldsymbol{d}_H(t^i) - \partial_t \boldsymbol{d}_H(t^i) \right\|_{H_{00}^{\frac{1}{2}}(\Sigma)} \leq C\tau \|\boldsymbol{d}\|_{W^{2,\infty}(0,T;V^{\mathrm{s}})}.$$

Moreover, as for the estimate of $\|\boldsymbol{c}_H\|_{H^{\frac{1}{2}}_{00}(\Sigma)}$, we have

$$\|\partial_t \boldsymbol{c}_H(t^i)\|_{H^{\frac{1}{2}}_{00}(\Sigma)} \leq C\|\partial_t \boldsymbol{c}_H(t^i)\|_{V^{\mathrm{s}}} \leq C\left(h^l\|\partial_t \boldsymbol{d}(t^i)\|_{V^{\mathrm{s}}} + \inf_{\boldsymbol{v}_H \in V^{\mathrm{s}}_H} \|\partial_t \boldsymbol{d}(t^i) - \boldsymbol{v}_H\|_{V^{\mathrm{s}}}\right).$$

with l verifying either (3.35) in the interpolation case or (3.36) in the mortar case. Therefore,

$$\begin{aligned}\left\|\boldsymbol{z}_h(t^i)\right\|_{1,\Omega^{\mathrm{f}}} \leq C\Bigg(\tau\left\|\boldsymbol{d}\right\|_{W^{2,\infty}(0,T;V^{\mathrm{s}})} + \inf_{\boldsymbol{v}_H \in V^{\mathrm{s}}_H} \left\|\partial_t \boldsymbol{d}(t^i) - \boldsymbol{v}_H\right\|_{V^{\mathrm{s}}} \\ + \inf_{\boldsymbol{v}_h \in V^{\mathrm{f}}_h} \left\|\mathbf{u}(t^i) - \boldsymbol{v}_h\right\|_{V^{\mathrm{f}}} + Ch^l\left\|\partial_t \boldsymbol{d}(t^i)\right\|_{V^{\mathrm{s}}}\Bigg)\end{aligned}$$

and

$$\begin{aligned}\left\|\mathbf{u}(t^i) - \mathbf{u}_h(t^i)\right\|_{1,\Omega^{\mathrm{f}}} \leq C\Bigg(\tau\left\|\boldsymbol{d}\right\|_{W^{2,\infty}(0,T;V^{\mathrm{s}})} + \inf_{\boldsymbol{v}_H \in V^{\mathrm{s}}_H} \left\|\partial_t \boldsymbol{d}(t^i) - \boldsymbol{v}_H\right\|_{V^{\mathrm{s}}} \\ + \inf_{\boldsymbol{v}_h \in V^{\mathrm{f}}_h} \left\|\mathbf{u}(t^i) - \boldsymbol{v}_h\right\|_{1,\Omega^{\mathrm{f}}} + \inf_{q_h \in Q_h} \left\|p(t^i) - q_h\right\|_{0,\Omega^{\mathrm{f}}} + h^l\left\|\partial_t \boldsymbol{d}(t^i)\right\|_{V^{\mathrm{s}}}\Bigg). \quad (3.39)\end{aligned}$$

Finally, for the pressure we have exactly the same estimate, namely,

$$\begin{aligned}\left\|p(t^i) - p_h(t^i)\right\|_{1,\Omega^{\mathrm{f}}} \leq C\Bigg(\tau\left\|\boldsymbol{d}\right\|_{W^{2,\infty}(0,T;V^{\mathrm{s}})} + \inf_{\boldsymbol{v}_H \in V^{\mathrm{s}}_H} \left\|\partial_t \boldsymbol{d}(t^i) - \boldsymbol{v}_H\right\|_{V^{\mathrm{s}}} \\ + \inf_{\boldsymbol{v}_h \in V^{\mathrm{f}}_h} \left\|\mathbf{u}(t^i) - \boldsymbol{v}_h\right\|_{1,\Omega^{\mathrm{f}}} + \inf_{q_h \in Q_h} \left\|p(t^i) - q_h\right\|_{0,\Omega^{\mathrm{f}}} + h^l\left\|\partial_t \boldsymbol{d}(t^i)\right\|_{H^l(\Sigma)}\Bigg). \quad (3.40)\end{aligned}$$

Again, l verifies either (3.35) in the interpolation case or (3.36) in the mortar case. Notice that the finite element approximations built depend on the type of matching operator π_h (pointwise or mortar). As a consequence, we can easily expect that also the error estimate depends on the type of matching operator. A discussion on the optimality in space of the error estimate is given in the next section.

3.5 Main result and error analysis

Here we focus on the error analysis of the projection semi-implicit scheme for the velocity unknowns. The analysis is performed assuming homogeneous Dirichlet conditions on the fluid velocity and on the structure displacement. As observed for example in [GQ98b], different boundary conditions could be used, provided we have at hand proper assumptions and regularity estimates. In the following, for the sake of conciseness, we indicate the errors associated with the fluid velocities and with the structure displacement as

$$e_h^k \stackrel{\text{def}}{=} \mathbf{u}_h^k - \mathbf{u}_h(t^k), \quad \tilde{e}_h^k \stackrel{\text{def}}{=} \tilde{\mathbf{u}}_h^k - \mathbf{u}_h(t^k), \quad e_H^k \stackrel{\text{def}}{=} \boldsymbol{d}_H^k - \boldsymbol{d}_H(t^k).$$

Theorem 3.2 *Assume that hypothesis (3.21)-(3.22) (resp. (3.25)-(3.29)) are satisfied when π_h is a finite element interpolation (resp. mortar) operator at the interface. Under the stability condition of the semi-implicit scheme,* i.e.

$$\rho^{\mathrm{s}} \geq C\left(\rho^{\mathrm{f}}\frac{h}{H^{\alpha}} + \frac{\mu\tau}{hH^{\alpha}}\right), \quad \textit{with} \quad \alpha = \begin{cases} 0, & \textit{if} \quad \overline{\Omega^{\mathrm{s}}} = \Sigma, \\ 1, & \textit{if} \quad \overline{\Omega^{\mathrm{s}}} \neq \Sigma, \end{cases}$$

and if the solution of the coupled problem (3.2)-(3.3) is smooth enough in space and time, then the discrete solution of (3.12)-(3.14) satisfies the following error estimate

$$\frac{\rho^{\mathrm{f}}}{2}\|e_h^{n+1}\|_{0,\Omega^{\mathrm{f}}}^2 + \frac{\rho^{\mathrm{s}}}{2}\left\|D_\tau e_H^{n+1}\right\|_{0,\Omega^{\mathrm{s}}}^2 + \frac{1}{4}a^{\mathrm{s}}(e_H^{n+1}, e_H^{n+1}) + \sum_{n=0}^{N}\mu\tau\|\boldsymbol{\varepsilon}(\tilde{e}_h^{n+1})\|_{0,\Omega^{\mathrm{f}}}^2 \leq C\tau + Ch^{2k} + CH^{2m} + Ch^{2l}, \quad (3.41)$$

where C denotes a strictly positive constant independent of h, H and τ. Here m depends on the choice of the finite element approximation space associated with the structure part and, for $\boldsymbol{v}^{\mathrm{s}}$ smooth enough, is such that

$$\inf_{\boldsymbol{v}_H \in V_H^{\mathrm{s}}} \|\boldsymbol{v}^{\mathrm{s}} - \boldsymbol{v}_H\|_{V^{\mathrm{s}}} \leq CH^m;$$

while l depends on the choice of the operator π_h, that is,

- $l \leq \min\left(r - \frac{\alpha}{2}, k+1\right)$ *for the pointwise-type operator,*
- $\frac{1}{2} \leq l \leq k$ *for the mortar-type operator.*

Before giving a proof of the previous theorem, a few remarks are in order. Considering the accuracy in time, the fluid-structure interaction scheme has globally a convergence order of $\sqrt{\tau}$. As observed in the proof, this is due to the use of the non-incremental Chorin-Temam projection scheme in the fluid problem (which is known to satisfy (3.1) for the hydrodynamic problem) and to the semi-implicit coupling at the interface. Moreover, the optimality of the error estimate is strictly dependent on the interface operator used. As a matter of fact, the mortar matching gives, in any case, optimal error estimate, whereas the finite element interpolation operator leads to an optimal error bound only in specific cases, depending on the structure model and on the degree of the polynomial approximation for the fluid. For instance, if we consider a membrane, then $r = 1$ and $\alpha = 0$ and the error estimate is optimal for $k = 1$. Table 3.1 summarizes the different cases.

Proof. For the sake of clarity, due to its complexity, the proof is split in several parts. Each one focuses on a particular point of the error estimate.

Part 1. The first step to obtain the error estimate (3.41) is to derive the equations verified by the errors e_h^k, $\tilde{e}_h^k$ and e_H^k.

π_h	d-dimensional structure ($r=1,\ \alpha=1$)	(d-1)-dimensional structure: 2^{nd} order oper. ($r=1,\ \alpha=0$)	(d-1)-dimensional structure: 4^{th} order oper. ($r=2,\ \alpha=0$)
Interpolation	non optimal	$k=1$ optimal	$k\leq 2$ optimal
Mortar	optimal $\forall k$	optimal $\forall k$	optimal $\forall k$

Table 3.1: Optimality of the error estimates depending on the structure model, the matching operator and the polynomial degree of the approximation of the fluid.

Let us consider the fluid equation associated with the coupled problem (3.7). Choosing $(\boldsymbol{v}^{\mathrm{f}}, q, \boldsymbol{v}^{\mathrm{s}}) = (\boldsymbol{v}_h^{\mathrm{f}}, q_h, 0)$, with $(\boldsymbol{v}^{\mathrm{f}}, q) \in V_{h,0}^{\mathrm{f}} \times Q_h$, in (3.7) and recalling the definition of the finite element approximation $(\mathbf{u}_h(t^{n+1}), p_h(t^{n+1}))$ of $(\mathbf{u}(t^{n+1}), p(t^{n+1}))$, we obtain

$$\rho^{\mathrm{f}}\big(D_\tau \mathbf{u}_h(t^{n+1}), \boldsymbol{v}_h^{\mathrm{f}}\big)_{\Omega^{\mathrm{f}}} + 2\mu\big(\boldsymbol{\varepsilon}(\mathbf{u}_h(t^{n+1})), \boldsymbol{\varepsilon}(\boldsymbol{v}_h^{\mathrm{f}})\big)_{\Omega^{\mathrm{f}}} - \big(p_h(t^{n+1}), \nabla\cdot \boldsymbol{v}_h^{\mathrm{f}}\big)_{\Omega^{\mathrm{f}}} + \big(q_h, \nabla\cdot \mathbf{u}_h(t^{n+1})\big)_{\Omega^{\mathrm{f}}} = \rho^{\mathrm{f}}\big(D_\tau \mathbf{u}_h(t^{n+1}) - \partial_t \mathbf{u}(t^{n+1}), \boldsymbol{v}_h^{\mathrm{f}}\big)_{\Omega^{\mathrm{f}}}. \quad (3.42)$$

Similarly, for the structure part, thanks to the definition of the finite element approximation $\boldsymbol{d}_H(t^{n+1})$ of $\boldsymbol{d}(t^{n+1})$ and choosing, in the variational formulation (3.7), $(\boldsymbol{v}^{\mathrm{f}}, q, \boldsymbol{v}^{\mathrm{s}}) = (\mathcal{L}_h(\boldsymbol{v}_H^{\mathrm{s}}), 0, \boldsymbol{v}_H^{\mathrm{s}})$, such that $\boldsymbol{v}_H^{\mathrm{s}} \in V_H^{\mathrm{s}}$, we have

$$\begin{aligned}
&\rho^{\mathrm{s}}\big(D_{\tau\tau}\boldsymbol{d}_H(t^{n+1}), \boldsymbol{v}_H^{\mathrm{s}}\big)_{\Omega^{\mathrm{s}}} + a^{\mathrm{s}}\big(\boldsymbol{d}_H(t^{n+1}), \boldsymbol{v}_H^{\mathrm{s}}\big) \\
&\quad = \rho^{\mathrm{s}}\left(D_{\tau\tau}\boldsymbol{d}_H(t^{n+1}) - \partial_{tt}\boldsymbol{d}(t^{n+1}), \boldsymbol{v}_H^{\mathrm{s}}\right)_{\Omega^{\mathrm{s}}} - \left\langle \mathcal{R}(\mathbf{u}(t^{n+1}), p(t^{n+1})), \mathcal{L}_h(\boldsymbol{v}_H^{s})\right\rangle \\
&\qquad + a^{\mathrm{s}}(\boldsymbol{d}_H(t^{n+1}) - \boldsymbol{d}(t^{n+1}), \boldsymbol{v}_H^{\mathrm{s}}) + \left\langle \boldsymbol{\lambda}(t^{n+1}), \boldsymbol{v}_H^{\mathrm{s}} - \pi_h(\boldsymbol{v}_H^{\mathrm{s}})\right\rangle_{\Sigma}. \quad (3.43)
\end{aligned}$$

The two equations are satisfied for all $t^{n+1} \leq T$. The last two terms on the right-hand side of (3.43) are respectively due to the introduction of the finite element approximation and to the non-conforming finite element discretization at the interface. The discrete lifting operator $\mathcal{L}_h : V_H^{\mathrm{s}}(\Sigma) \to V_h^{\mathrm{f}}$ verifies

$$\mathcal{L}_h(\boldsymbol{v}_H^{\mathrm{s}}) = \pi_h(\boldsymbol{v}_H^{\mathrm{s}}), \qquad \text{on} \qquad \Sigma.$$

The lifting $\mathcal{L}_h$ is chosen to be equal to $r_h \circ \pi_h$, where r_h is a continuous linear lifting from $V_h^{\mathrm{f}}(\Sigma)$ onto V_h^{f} (for example defined through a discrete Poisson problem), such that

$$\|r_h(\boldsymbol{v}_h^{\mathrm{f}})\|_{1,\Omega^{\mathrm{f}}} \leq C\|\boldsymbol{v}_h^{\mathrm{f}}\|_{H_{00}^{\frac{1}{2}}(\Sigma)},\ \forall \boldsymbol{v}_h^{\mathrm{f}} \in V_h^{\mathrm{f}}(\Sigma). \quad (3.44)$$

Here the constant C does not depend on the space discretization. As a result, $\mathcal{L}_h$ satisfies

$$\|\mathcal{L}_h(\boldsymbol{v}_H^{\mathrm{s}})\|_{1,\Omega^{\mathrm{f}}} \leq C\|\pi_h(\boldsymbol{v}_H^{\mathrm{s}})\|_{H_{00}^{\frac{1}{2}}(\Sigma)},\ \forall \boldsymbol{v}_H^{\mathrm{s}} \in V_H^{\mathrm{s}}(\Sigma). \quad (3.45)$$

Subtracting equation (3.42) from $(3.16)_1$, we get the error equation associated with the first step of the semi-implicit scheme:

$$\frac{\rho^{\mathrm{f}}}{\tau}\big(\tilde{e}_h^{n+1}-e_h^n,\tilde{\boldsymbol{v}}_h^{\mathrm{f}}\big)_{\Omega^{\mathrm{f}}}+2\mu\big(\boldsymbol{\varepsilon}(\tilde{e}_h^{n+1}),\boldsymbol{\varepsilon}(\tilde{\boldsymbol{v}}_h^{\mathrm{f}})\big)_{\Omega^{\mathrm{f}}}+\big(p_h(t^{n+1}),\nabla\cdot\tilde{\boldsymbol{v}}_h^{\mathrm{f}}\big)_{\Omega^{\mathrm{f}}}$$
$$-\big(q_h,\nabla\cdot\mathbf{u}_h(t^{n+1})\big)_{\Omega^{\mathrm{f}}}=\rho^{\mathrm{f}}\big(\partial_t\mathbf{u}(t^{n+1})-D_\tau\mathbf{u}_h(t^{n+1}),\tilde{\boldsymbol{v}}_h^{\mathrm{f}}\big)_{\Omega^{\mathrm{f}}},$$
$$\forall(\tilde{\boldsymbol{v}}_h^{\mathrm{f}},q_h)\in V_{h,0}^{\mathrm{f}}\times Q_h. \quad (3.46)$$

The error equation associated with the fluid part of the second step can be obtained by rewriting (3.17) in the following form:

$$\frac{\rho^{\mathrm{f}}}{\tau}\big(e_h^{n+1}-\tilde{e}_h^{n+1},\boldsymbol{v}_h^{\mathrm{f}}\big)_{\Omega^{\mathrm{f}}}-\big(p_h^{n+1},\nabla\cdot\boldsymbol{v}_h^{\mathrm{f}}\big)_{\Omega^{\mathrm{f}}}+\big(q_h,\nabla\cdot e_h^{n+1}\big)_{\Omega^{\mathrm{f}}}+\big(q_h,\nabla\cdot\mathbf{u}_h(t^{n+1})\big)_{\Omega^{\mathrm{f}}}=0,$$
$$\forall(\boldsymbol{v}_h^{\mathrm{f}},q_h)\in Y_{h,0}^{\mathrm{f}}\times Q_h. \quad (3.47)$$

Finally, for the structure part, subtracting equation (3.43) from (3.18) leads to

$$\rho^{\mathrm{s}}\big(D_{\tau\tau}e_H^{n+1},\boldsymbol{v}_H^{\mathrm{s}}\big)_{\Omega^{\mathrm{s}}}+a^{\mathrm{s}}(e_H^{n+1},\boldsymbol{v}_H^{\mathrm{s}})=\rho^{\mathrm{s}}\big(\partial_{tt}\boldsymbol{d}(t^{n+1})-D_{\tau\tau}\boldsymbol{d}_H(t^{n+1}),\boldsymbol{v}_H^{\mathrm{s}}\big)_{\Omega^{\mathrm{s}}}$$
$$+\mathcal{T}_h^{n+1}-a^{\mathrm{s}}(\boldsymbol{d}_H(t^{n+1})-\boldsymbol{d}(t^{n+1}),\boldsymbol{v}_H^{\mathrm{s}})-\big\langle\boldsymbol{\lambda}(t^{n+1}),\boldsymbol{v}_H^{\mathrm{s}}-\pi_h(\boldsymbol{v}_H^{\mathrm{s}})\big\rangle_\Sigma,$$
$$\forall\boldsymbol{v}_H^{\mathrm{s}}\in V_H^{\mathrm{s}}, \quad (3.48)$$

where

$$\begin{aligned}
\mathcal{T}_h^{n+1} &\overset{\mathrm{def}}{=} \big\langle\mathcal{R}(\mathbf{u}(t^{n+1}),p(t^{n+1})),\mathcal{L}_h(\boldsymbol{v}_H^s)\big\rangle-\big\langle\mathcal{R}_\mu(\tilde{\mathbf{u}}_h^{n+1}),\mathcal{L}_h(\boldsymbol{v}_H^s)\big\rangle\\
&\quad-\big\langle\mathcal{R}_p(\mathbf{u}_h^{n+1},p_h^{n+1}),\mathcal{L}_h(\boldsymbol{v}_H^s)\big\rangle\\
&= \rho^{\mathrm{f}}\big(\partial_t\mathbf{u}(t^{n+1}),\mathcal{L}_h(\boldsymbol{v}_H^{\mathrm{s}})\big)_{\Omega^{\mathrm{f}}}+2\mu\big(\boldsymbol{\varepsilon}(\mathbf{u}(t^{n+1})),\boldsymbol{\varepsilon}(\mathcal{L}_h(\boldsymbol{v}_H^{\mathrm{s}}))\big)_{\Omega^{\mathrm{f}}}\\
&\quad-\big(p(t^{n+1}),\nabla\cdot\mathcal{L}_h(\boldsymbol{v}_H^{\mathrm{s}})\big)_{\Omega^{\mathrm{f}}}-\frac{\rho^{\mathrm{f}}}{\tau}\big(\tilde{\mathbf{u}}_h^{n+1}-\mathbf{u}_h^n,\mathcal{L}_h(\boldsymbol{v}_H^{\mathrm{s}})\big)_{\Omega^{\mathrm{f}}}\\
&\quad-2\mu\big(\boldsymbol{\varepsilon}(\tilde{\mathbf{u}}_h^{n+1}),\boldsymbol{\varepsilon}(\mathcal{L}_h(\boldsymbol{v}_H^{\mathrm{s}}))\big)_{\Omega^{\mathrm{f}}}-\frac{\rho^{\mathrm{f}}}{\tau}\big(\mathbf{u}_h^{n+1}-\tilde{\mathbf{u}}_h^{n+1},\mathcal{L}_h(\boldsymbol{v}_H^{\mathrm{s}})\big)_{\Omega^{\mathrm{f}}}\\
&\quad+\big(p_h^{n+1},\nabla\cdot\mathcal{L}_h(\boldsymbol{v}_H^{\mathrm{s}})\big)_{\Omega^{\mathrm{f}}}\\
&= \rho^{\mathrm{f}}\left(\partial_t\mathbf{u}(t^{n+1})-D_\tau\mathbf{u}_h(t^{n+1}),\mathcal{L}_h(\boldsymbol{v}_H^{\mathrm{s}})\right)_{\Omega^{\mathrm{f}}}-\rho^{\mathrm{f}}\left(D_\tau e_h^{n+1},\mathcal{L}_h(\boldsymbol{v}_H^{\mathrm{s}})\right)_{\Omega^{\mathrm{f}}}\\
&\quad-2\mu\big(\boldsymbol{\varepsilon}(\tilde{e}_h^{n+1}),\boldsymbol{\varepsilon}(\mathcal{L}_h(\boldsymbol{v}_H^{\mathrm{s}}))\big)_{\Omega^{\mathrm{f}}}+2\mu\big(\boldsymbol{\varepsilon}(\mathbf{u}(t^{n+1})-\mathbf{u}_h(t^{n+1})),\boldsymbol{\varepsilon}(\mathcal{L}_h(\boldsymbol{v}_H^{\mathrm{s}}))\big)_{\Omega^{\mathrm{f}}}\\
&\quad+\big(p_h^{n+1}-p(t^{n+1}),\nabla\cdot\mathcal{L}_h(\boldsymbol{v}_H^{\mathrm{s}})\big)_{\Omega^{\mathrm{f}}}.
\end{aligned}$$

Part 2. We now sum (3.46), (3.47) and (3.48) and test them using the following test functions:

$$\boldsymbol{v}_H^{\mathrm{s}}=e_H^{n+1}-e_H^n,\quad \boldsymbol{v}_h^{\mathrm{f}}=\tau\left(e_h^{n+1}-\mathcal{L}_h\left(D_\tau e_H^{n+1}\right)\right),\quad q_h=0,$$
$$\tilde{\boldsymbol{v}}_h^{\mathrm{f}}=\tau\Big(\tilde{e}_h^{n+1}-\mathcal{L}_h\left(D_\tau e_H^{n+1}\right)+\mathcal{L}_h'\big(D_\tau e_H^{n+1}-D_\tau e_H^n\big)$$
$$+\mathcal{L}_h'\left(D_\tau\boldsymbol{d}_H(t^{n+1})-D_\tau\boldsymbol{d}_H(t^n)\right)\Big),$$

where $\mathcal{L}'_h$ is a second discrete lifting operator, satisfying $\mathcal{L}'_h(\boldsymbol{v}_H) = \pi_h(\boldsymbol{v}^{\mathrm{s}}_H)$ on Σ. It is defined as in [FGG07] by:

$$\mathcal{L}'_h(\boldsymbol{b}_H) \stackrel{\text{def}}{=} \sum_{i=1, x^i_h \in \Sigma}^{N_h} \pi_h(\boldsymbol{b}_H)(x^i_h)\phi^i_h,$$

with $\{x^i_h\}_{i=1}^{N_h}$, $\{\phi^i_h\}_{i=1}^{N_h}$ the sets of nodes and shape functions of V^{f}_h. We distinguish the latter from $\mathcal{L}_h$ since the two have different properties. This new lifting satisfies the following lemma (proved in [FGG07])

Lemma 3.1 *If the interface operator π_h is stable in the L^2-norm on $V^{\mathrm{s}}_H(\Sigma)$, then there exists a constant $C > 0$, depending only on the local mesh geometry and on the polynomial order, such that:*

$$\begin{aligned} \|\mathcal{L}'_h(\boldsymbol{b}_H)\|^2_{0,\Omega^{\mathrm{f}}} &\leq \frac{Ch}{H^\alpha}\|\boldsymbol{b}_H\|^2_{0,\Omega^{\mathrm{s}}}, \\ \|\nabla\mathcal{L}'_h(\boldsymbol{b}_H)\|^2_{0,\Omega^{\mathrm{f}}} &\leq \frac{C}{hH^\alpha}\|\boldsymbol{b}_H\|^2_{0,\Omega^{\mathrm{s}}}, \end{aligned} \tag{3.49}$$

for all $\boldsymbol{b}_H \in V^{\mathrm{s}}_H$, and α given by (3.23).

Remark 3.4 *The last two terms in the definition of the test function $\tilde{\boldsymbol{v}}^{\mathrm{f}}_h$ represent an appropriate correction, added because $\tilde{\mathbf{u}}^{n+1}_h$ is equal to the structure velocity at the previous time-step at the interface (explicit coupling). This guarantees the admissibility of the test functions.*

After some direct simplifications, we have

$$\begin{aligned} \rho^{\mathrm{f}}\left(\tilde{e}^{n+1}_h - e^n_h, \tilde{e}^{n+1}_h\right)_{\Omega^{\mathrm{f}}} + 2\mu\tau\|\boldsymbol{\varepsilon}(\tilde{e}^{n+1}_h)\|^2_{0,\Omega^{\mathrm{f}}} + \rho^{\mathrm{f}}\left(e^{n+1}_h - \tilde{e}^{n+1}_h, e^{n+1}_h\right)_{\Omega^{\mathrm{f}}} \\ +\rho^{\mathrm{s}}\left(D_{\tau\tau}e^{n+1}_H, e^{n+1}_H - e^n_H\right)_{\Omega^{\mathrm{s}}} + a^{\mathrm{s}}(e^{n+1}_H, e^{n+1}_H - e^n_H) \\ +\mathcal{P}^{n+1}_h + \mathcal{C}^{n+1}_h + \mathcal{S}^{n+1}_h = \mathcal{D}^{n+1}_h + \mathcal{A}^{n+1}_h. \end{aligned} \tag{3.50}$$

In the left-hand side $\mathcal{P}^{n+1}_h$, $\mathcal{C}^{n+1}_h$ and $\mathcal{S}^{n+1}_h$ are respectively defined by

$$\begin{aligned} \mathcal{P}^{n+1}_h \stackrel{\text{def}}{=}\ & \tau\left(p_h(t^{n+1}), \nabla\cdot(\tilde{e}^{n+1}_h - e^{n+1}_h)\right)_{\Omega^{\mathrm{f}}} \\ & +\tau\left(p_h(t^{n+1}), \nabla\cdot\mathcal{L}'_h\left(D_\tau e^{n+1}_H - D_\tau e^n_H\right)\right)_{\Omega^{\mathrm{f}}} \\ & +\tau\left(p_h(t^{n+1}), \nabla\cdot\mathcal{L}'_h\left(D_\tau \boldsymbol{d}_H(t^{n+1}) - D_\tau \boldsymbol{d}_H(t^n)\right)\right)_{\Omega^{\mathrm{f}}}, \end{aligned} \tag{3.51}$$

$$\begin{aligned} \mathcal{C}^{n+1}_h \stackrel{\text{def}}{=}\ & \rho^{\mathrm{f}}\left(\tilde{e}^{n+1}_h - e^n_h, \mathcal{L}'_h\left(D_\tau \boldsymbol{d}_H(t^{n+1}) - D_\tau \boldsymbol{d}_H(t^n)\right)\right)_{\Omega^{\mathrm{f}}} \\ & +2\mu\tau\left(\boldsymbol{\varepsilon}(\tilde{e}^{n+1}_h), \boldsymbol{\varepsilon}\left(\mathcal{L}'_h\left(D_\tau \boldsymbol{d}_H(t^{n+1}) - D_\tau \boldsymbol{d}_H(t^n)\right)\right)\right)_{\Omega^{\mathrm{f}}}, \end{aligned} \tag{3.52}$$

$$\begin{aligned} \mathcal{S}^{n+1}_h \stackrel{\text{def}}{=}\ & \rho^{\mathrm{f}}\left(\tilde{e}^{n+1}_h - e^n_h, \mathcal{L}'_h\left(D_\tau e^{n+1}_H - D_\tau e^n_H\right)\right)_{\Omega^{\mathrm{f}}} \\ & +2\mu\tau\left(\boldsymbol{\varepsilon}(\tilde{e}^{n+1}_h), \boldsymbol{\varepsilon}\left(\mathcal{L}'_h\left(D_\tau e^{n+1}_H - D_\tau e^n_H\right)\right)\right)_{\Omega^{\mathrm{f}}}. \end{aligned} \tag{3.53}$$

The term $\mathcal{P}_h^{n+1}$ regroups all the parts related to the pressure $p_h(t^{n+1})$. In $\mathcal{C}_h^{n+1}$ we put the terms associated with the semi-implicit coupling (see the following remark for more details), while in $\mathcal{S}_h^{n+1}$ there are the ones that will be controlled by means of the stability condition (3.20).

Remark 3.5 *The discrete fluid velocities, $\tilde{\mathbf{u}}_h^{n+1}$ and $\mathbf{u}_h^{n+1}$, verify respectively an explicit and an implicit interface condition, while the finite element approximation of the continuous solution $\mathbf{u}$ is based only on the implicit one. This difference generate terms like the ones in (3.52). Note also that the last term in (3.51) is of the same kind. In the same way, analogous terms would appear using a finite element approximation of $\mathbf{u}$ satisfying an explicit coupling condition instead of the implicit one.*

Considering the right-hand side, in $\mathcal{D}_h^{n+1}$ we include terms in which a time consistency error has to be estimated, that is

$$\begin{aligned}\mathcal{D}_h^{n+1} \stackrel{\text{def}}{=}\ & \rho^{\mathrm{f}}\tau\left(\partial_t\mathbf{u}(t^{n+1}) - D_\tau\mathbf{u}_h(t^{n+1}), \tilde{e}_h^{n+1}\right)_{\Omega^{\mathrm{f}}} \\ & +\rho^{\mathrm{f}}\tau\left(\partial_t\mathbf{u}(t^{n+1}) - D_\tau\mathbf{u}_h(t^{n+1}), \mathcal{L}_h'\left(D_\tau e_H^{n+1} - D_\tau e_H^n\right)\right)_{\Omega^{\mathrm{f}}} \\ & +\rho^{\mathrm{f}}\tau\left(\partial_t\mathbf{u}(t^{n+1}) - D_\tau\mathbf{u}_h(t^{n+1}), \mathcal{L}_h'\left(D_\tau\boldsymbol{d}_H(t^{n+1}) - D_\tau\boldsymbol{d}_H(t^n)\right)\right)_{\Omega^{\mathrm{f}}} \\ & +\rho^{\mathrm{s}}\left(\partial_{tt}\boldsymbol{d}(t^{n+1}) - D_{\tau\tau}\boldsymbol{d}_H(t^{n+1}), e_H^{n+1} - e_H^n\right)_{\Omega^{\mathrm{s}}}. \end{aligned} \tag{3.54}$$

Finally, $\mathcal{A}_h^{n+1}$ regroups terms in which a space consistency error has to be estimated (depending on the finite element approximation of the continuous solution we built):

$$\begin{aligned}\mathcal{A}_h^{n+1} \stackrel{\text{def}}{=}\ & -a^{\mathrm{s}}(\boldsymbol{d}_H(t^{n+1}) - \boldsymbol{d}(t^{n+1}), e_H^{n+1} - e_H^n) \\ & -\left\langle\boldsymbol{\lambda}(t^{n+1}), e_H^{n+1} - e_H^n - \pi_h(e_H^{n+1} - e_H^n)\right\rangle_\Sigma \\ & +2\mu\big(\boldsymbol{\varepsilon}(\mathbf{u}(t^{n+1}) - \mathbf{u}_h(t^{n+1})), \boldsymbol{\varepsilon}(\mathcal{L}_h(e_H^{n+1} - e_H^n))\big)_{\Omega^{\mathrm{f}}} \\ & +\tau\big(p_h(t^{n+1}) - p(t^{n+1}), \nabla\cdot\mathcal{L}_h(D_\tau e_H^{n+1})\big)_{\Omega^{\mathrm{f}}}. \end{aligned} \tag{3.55}$$

In (3.50), most of the terms involving the continuous lifting $\mathcal{L}_h$ cancel each other except for the two appearing in $\mathcal{A}_h^{n+1}$. The cancellation is due to the fact that they are linked to the energy balance of the system at the interface.

Next, we set

$$\begin{aligned}\mathcal{E}_h^{n+1} \stackrel{\text{def}}{=}\ & \rho^{\mathrm{f}}\left(\tilde{e}_h^{n+1} - e_h^n, \tilde{e}_h^{n+1}\right)_{\Omega^{\mathrm{f}}} + 2\mu\tau\|\boldsymbol{\varepsilon}(\tilde{e}_h^{n+1})\|_{0,\Omega^{\mathrm{f}}}^2 + \rho^{\mathrm{f}}\left(e_h^{n+1} - \tilde{e}_h^{n+1}, e_h^{n+1}\right)_{\Omega^{\mathrm{f}}} \\ & +\rho^{\mathrm{s}}\left(D_{\tau\tau}e_H^{n+1}, e_H^{n+1} - e_H^n\right)_{\Omega^{\mathrm{s}}} + a^{\mathrm{s}}(e_H^{n+1}, e_H^{n+1} - e_H^n). \end{aligned} \tag{3.56}$$

In $\mathcal{E}_h^{n+1}$ we collect all the terms associated with the energy of the system. Using the identity $(a-b,a) = \frac{1}{2}\|a\|^2 - \frac{1}{2}\|b\|^2 + \frac{1}{2}\|a-b\|^2$, the bi-linearity and the symmetry of $a^{\mathrm{s}}(\cdot,\cdot)$ and introducing the quantity

$$\tilde{E}^{n+1} \stackrel{\text{def}}{=} \frac{\rho^{\mathrm{f}}}{2}\|e_h^{n+1}\|_{0,\Omega^{\mathrm{f}}}^2 + \frac{\rho^{\mathrm{s}}}{2}\left\|D_\tau e_H^{n+1}\right\|_{0,\Omega^{\mathrm{s}}}^2 + \frac{1}{2}a^{\mathrm{s}}(e_H^{n+1}, e_H^{n+1}),$$

we have

$$\begin{aligned}
\mathcal{E}_h^{n+1} &= \frac{\rho^{\mathrm{f}}}{2}\left[\left\|e_h^{n+1}\right\|_{0,\Omega^{\mathrm{f}}}^2 - \left\|e_h^{n}\right\|_{0,\Omega^{\mathrm{f}}}^2 + \left\|\tilde{e}_h^{n+1} - e_h^{n}\right\|_{0,\Omega^{\mathrm{f}}}^2 + \left\|e_h^{n+1} - \tilde{e}_h^{n+1}\right\|_{0,\Omega^{\mathrm{f}}}^2\right] \\
&\quad + \frac{\rho^{\mathrm{s}}}{2}\left[\left\|D_\tau e_H^{n+1}\right\|_{0,\Omega^{\mathrm{s}}}^2 - \left\|D_\tau e_H^{n}\right\|_{0,\Omega^{\mathrm{s}}}^2 + \left\|D_\tau e_H^{n+1} - D_\tau e_H^{n}\right\|_{0,\Omega^{\mathrm{s}}}^2\right] \\
&\quad + \frac{1}{2}\left[a^{\mathrm{s}}(e_H^{n+1}, e_H^{n+1}) - a^{\mathrm{s}}(e_H^{n}, e_H^{n}) + a^{\mathrm{s}}(e_H^{n+1} - e_H^{n}, e_H^{n+1} - e_H^{n})\right] \\
&\quad + 2\mu\tau\left\|\boldsymbol{\varepsilon}(\tilde{e}_h^{n+1})\right\|_{0,\Omega^{\mathrm{f}}}^2 \\
&= \tilde{E}^{n+1} - \tilde{E}^{n} + \frac{\rho^{\mathrm{f}}}{2}\left[\|\tilde{e}_h^{n+1} - e_h^{n}\|_{0,\Omega^{\mathrm{f}}}^2 + \|e_h^{n+1} - e_h^{n}\|_{0,\Omega^{\mathrm{f}}}^2\right] \\
&\quad + 2\mu\tau\left\|\boldsymbol{\varepsilon}(\tilde{e}_h^{n+1})\right\|_{0,\Omega^{\mathrm{f}}}^2 + \frac{\rho^{\mathrm{s}}}{2}\left\|D_\tau e_H^{n+1} - D_\tau e_H^{n}\right\|_{0,\Omega^{\mathrm{s}}}^2 \\
&\quad + \frac{1}{2}a^{\mathrm{s}}(e_H^{n+1} - e_H^{n}, e_H^{n+1} - e_H^{n}).
\end{aligned} \tag{3.57}$$

Using the equality (3.57) in (3.50) and reordering the different terms, we get

$$\begin{aligned}
\tilde{E}^{n+1} &+ \frac{\rho^{\mathrm{f}}}{2}\left[\|\tilde{e}_h^{n+1} - e_h^{n}\|_{0,\Omega^{\mathrm{f}}}^2 + \|e_h^{n+1} - \tilde{e}_h^{n+1}\|_{0,\Omega^{\mathrm{f}}}^2\right] + 2\mu\tau\left\|\boldsymbol{\varepsilon}(\tilde{e}_h^{n+1})\right\|_{0,\Omega^{\mathrm{f}}}^2 \\
&+ \frac{\rho^{\mathrm{s}}}{2}\left\|D_\tau e_H^{n+1} - D_\tau e_H^{n}\right\|_{0,\Omega^{\mathrm{s}}}^2 + \frac{1}{2}a^{\mathrm{s}}(e_H^{n+1} - e_H^{n}, e_H^{n+1} - e_H^{n}) \\
&= \tilde{E}^{n} - \mathcal{P}_h^{n+1} - \mathcal{C}_h^{n+1} - \mathcal{S}_h^{n+1} + \mathcal{D}_h^{n+1} + \mathcal{A}_h^{n+1}.
\end{aligned} \tag{3.58}$$

Part 3. We now give an upper bound for each term in the right-hand side of (3.58). In the following we frequently make use of the classical Young's inequality

$$ab \leq \frac{\gamma}{2}a^2 + \frac{1}{2\gamma}b^2 \quad \forall \gamma > 0,$$

that is simply replaced by

$$ab \leq \frac{\gamma}{2}a^2 + Cb^2, \tag{3.59}$$

or by

$$ab \leq C(a^2 + b^2), \tag{3.60}$$

whenever the definition of the constant γ for one (or both) of the terms doesn't play a key role in the convergence analysis. The quantity C represents a positive constant.

Let us consider $\mathcal{P}_h^{n+1}$. First we integrate by parts all its terms:

$$\begin{aligned}
-\mathcal{P}_h^{n+1} &= \tau\left(\nabla p_h(t^{n+1}), \tilde{e}_h^{n+1} - e_h^{n+1}\right)_{\Omega^{\mathrm{f}}} \\
&\quad + \tau\left(\nabla p_h(t^{n+1}), \mathcal{L}_h'\left(D_\tau e_H^{n+1} - D_\tau e_H^{n}\right)\right)_{\Omega^{\mathrm{f}}} \\
&\quad + \tau\left(\nabla p_h(t^{n+1}), \mathcal{L}_h'\left(D_\tau \boldsymbol{d}_H(t^{n+1}) - D_\tau \boldsymbol{d}_H(t^{n})\right)\right)_{\Omega^{\mathrm{f}}};
\end{aligned} \tag{3.61}$$

note that in the (3.61) no extra boundary terms were introduced since

$$\left(e_h^{n+1} - \tilde{e}_h^{n+1}\right)\cdot \mathbf{n}|_{\Sigma} = \pi_h\left(D_\tau \boldsymbol{d}_H^{n+1} - D_\tau \boldsymbol{d}_H^{n}\right)\cdot \mathbf{n}|_{\Sigma}.$$

Then, the Young's inequality and the properties (3.49) of $\mathcal{L}'_h$ yield

$$-\mathcal{P}_h^{n+1} \leq \frac{\gamma_1\rho^{\mathrm{f}}}{2}\|e_h^{n+1}-\tilde{e}_h^{n+1}\|_{0,\Omega^{\mathrm{f}}}^2+\frac{Ch\rho^{\mathrm{f}}}{H^\alpha}\left\|D_\tau e_H^{n+1}-D_\tau e_H^n\right\|_{0,\Omega^{\mathrm{s}}}^2 + \frac{Ch\rho^{\mathrm{f}}}{H^\alpha}\left\|D_\tau \boldsymbol{d}_H(t^{n+1})-D_\tau \boldsymbol{d}_H(t^n)\right\|_{0,\Omega^{\mathrm{s}}}^2+\frac{C\tau^2}{\rho^{\mathrm{f}}}\|\nabla p_h(t^{n+1})\|_{0,\Omega^{\mathrm{f}}}^2. \quad (3.62)$$

In a similar way, for $\mathcal{C}_h^{n+1}$ and $\mathcal{S}_h^{n+1}$, defined respectively by (3.52) and (3.53), using (3.59) and the properties (3.49) of $\mathcal{L}'_h$, we get

$$-\mathcal{C}_h^{n+1} \leq \frac{\gamma_2\rho^{\mathrm{f}}}{2}\|\tilde{e}_h^{n+1}-e_h^n\|_{0,\Omega^{\mathrm{f}}}^2+\gamma_3\mu\tau\|\boldsymbol{\varepsilon}(\tilde{e}_h^{n+1})\|_{0,\Omega^{\mathrm{f}}}^2 + C\left(\frac{h\rho^{\mathrm{f}}}{H^\alpha}+\frac{\mu\tau}{hH^\alpha}\right)\left\|D_\tau \boldsymbol{d}_H(t^{n+1})-D_\tau \boldsymbol{d}_H(t^n)\right\|_{0,\Omega^{\mathrm{s}}}^2, \quad (3.63)$$

$$-\mathcal{S}_h^{n+1} \leq \frac{\gamma_1\rho^{\mathrm{f}}}{2}\|e_h^{n+1}-\tilde{e}_h^{n+1}\|_{0,\Omega^{\mathrm{f}}}^2+\gamma_3\mu\tau\|\boldsymbol{\varepsilon}(\tilde{e}_h^{n+1})\|_{0,\Omega^{\mathrm{f}}}^2 + C\left(\frac{h\rho^{\mathrm{f}}}{H^\alpha}+\frac{\mu\tau}{hH^\alpha}\right)\left\|D_\tau e_H^{n+1}-D_\tau e_H^n\right\|_{0,\Omega^{\mathrm{s}}}^2. \quad (3.64)$$

For $\mathcal{D}_h^{n+1}$, defined by (3.54), we rewrite the first term as

$$\rho^{\mathrm{f}}\tau\left(\partial_t\mathbf{u}(t^{n+1})-D_\tau\mathbf{u}_h(t^{n+1}),\tilde{e}_h^{n+1}\right)_{\Omega^{\mathrm{f}}} = \rho^{\mathrm{f}}\tau\left(\partial_t\mathbf{u}(t^{n+1})-D_\tau\mathbf{u}_h(t^{n+1}),\tilde{e}_h^{n+1}-e_h^{n+1}\right)_{\Omega^{\mathrm{f}}} + \rho^{\mathrm{f}}\tau\left(\partial_t\mathbf{u}(t^{n+1})-D_\tau\mathbf{u}_h(t^{n+1}),e_h^{n+1}\right)_{\Omega^{\mathrm{f}}}, \quad (3.65)$$

then, the use of (3.60) and of the properties (3.49) yields after some rearrangement

$$\mathcal{D}_h^{n+1} \leq C\rho^{\mathrm{f}}\tau(\|\tilde{e}_h^{n+1}-e_h^{n+1}\|_{0,\Omega^{\mathrm{f}}}^2+\|e_h^{n+1}\|_{0,\Omega^{\mathrm{f}}}^2)+\frac{Ch\rho^{\mathrm{f}}\tau}{H^\alpha}\left\|D_\tau e_H^{n+1}-D_\tau e_H^n\right\|_{0,\Omega^{\mathrm{s}}}^2 + \frac{Ch\rho^{\mathrm{f}}\tau}{H^\alpha}\left\|D_\tau \boldsymbol{d}_H(t^{n+1})-D_\tau \boldsymbol{d}_H(t^n)\right\|_{0,\Omega^{\mathrm{s}}}^2+C\rho^{\mathrm{s}}\tau\left\|D_\tau e_H^{n+1}\right\|_{0,\Omega^{\mathrm{s}}}^2 + C\rho^{\mathrm{f}}\tau\left\|\partial_t\mathbf{u}(t^{n+1})-D_\tau\mathbf{u}_h(t^{n+1})\right\|_{0,\Omega^{\mathrm{f}}}^2 + C\rho^{\mathrm{s}}\tau\left\|\partial_{tt}\boldsymbol{d}(t^{n+1})-D_{\tau\tau}\boldsymbol{d}_H(t^{n+1})\right\|_{0,\Omega^{\mathrm{s}}}^2. \quad (3.66)$$

Remark 3.6 *Instead of rewriting the first term as in (3.65), another possibility is to apply first the Young's inequality (3.60) and then control $\|\tilde{e}_h^{n+1}\|_{0,\Omega^{\mathrm{f}}}^2$ with the Korn's inequality.*

Before estimating the four terms of $\mathcal{A}_h^{n+1}$, we first apply to the error equation (3.58) the estimates (3.62), (3.63), (3.64) and (3.66), respectively obtained for $\mathcal{P}_h^{n+1}$, $\mathcal{C}_h^{n+1}$,

$\mathcal{S}_h^{n+1}$ and $\mathcal{D}_h^{n+1}$. Then, summing over n (from 0 to N, being N a positive integer such that $(N+1)\tau \leq T$) and rearranging the different terms, we obtain

$$
\begin{aligned}
\tilde{E}^{N+1} \;+\; & \frac{\rho^{\mathrm{f}}}{2}\sum_{n=0}^{N}[(1-\gamma_2)\|\tilde{e}_h^{n+1}-e_h^n\|_{0,\Omega^{\mathrm{f}}}^2+(1-2\gamma_1)\|e_h^{n+1}-\tilde{e}_h^{n+1}\|_{0,\Omega^{\mathrm{f}}}^2] \\
+\; & \sum_{n=0}^{N} 2\mu\tau\,(1-\gamma_3)\,\|\boldsymbol{\varepsilon}(\tilde{e}_h^{n+1})\|_{0,\Omega^{\mathrm{f}}}^2+\frac{1}{2}\sum_{n=0}^{N} a^{\mathrm{s}}(e_H^{n+1}-e_H^n,e_H^{n+1}-e_H^n) \\
+\; & \sum_{n=0}^{N}\left(\frac{\rho^{\mathrm{s}}}{2}-\frac{Ch\rho^{\mathrm{f}}}{H^\alpha}-\frac{C\mu\tau}{hH^\alpha}\right)\left\|D_\tau e_H^{n+1}-D_\tau e_H^n\right\|_{0,\Omega^{\mathrm{s}}}^2 \\
\leq\; & \tilde{E}^0+\sum_{n=0}^{N} C\left(\frac{h\rho^{\mathrm{f}}}{H^\alpha}+\frac{\mu\tau}{hH^\alpha}\right)\left\|D_\tau \boldsymbol{d}_H(t^{n+1})-D_\tau \boldsymbol{d}_H(t^n)\right\|_{0,\Omega^{\mathrm{s}}}^2 \\
& +\sum_{n=0}^{N}\frac{C\tau^2}{\rho^{\mathrm{f}}}\|\nabla p_h(t^{n+1})\|_{0,\Omega^{\mathrm{f}}}^2+\sum_{n=0}^{N} C\frac{h\rho^{\mathrm{f}}\tau}{H^\alpha}\left\|D_\tau \boldsymbol{d}_H(t^{n+1})-D_\tau \boldsymbol{d}_H(t^n)\right\|_{0,\Omega^{\mathrm{s}}}^2 \\
& +\sum_{n=0}^{N} C\rho^{\mathrm{f}}\tau(\|\tilde{e}_h^{n+1}-e_h^{n+1}\|_{0,\Omega^{\mathrm{f}}}^2+\|e_h^{n+1}\|_{0,\Omega^{\mathrm{f}}}^2) \\
& +\sum_{n=0}^{N} C\rho^{\mathrm{s}}\tau\left\|D_\tau e_H^{n+1}\right\|_{0,\Omega^{\mathrm{s}}}^2+\sum_{n=0}^{N}\frac{Ch\rho^{\mathrm{f}}\tau}{H^\alpha}\left\|D_\tau e_H^{n+1}-D_\tau e_H^n\right\|_{0,\Omega^{\mathrm{s}}}^2 \\
& +\sum_{n=0}^{N} C\rho^{\mathrm{f}}\tau\left\|\partial_t \mathbf{u}(t^{n+1})-D_{\tau\tau}\mathbf{u}_h(t^{n+1})\right\|_{0,\Omega^{\mathrm{f}}}^2 \\
& +\sum_{n=0}^{N} C\rho^{\mathrm{s}}\tau\left\|\partial_{tt}\boldsymbol{d}(t^{n+1})-D_{\tau\tau}\boldsymbol{d}_H(t^{n+1})\right\|_{0,\Omega^{\mathrm{s}}}^2+\sum_{n=0}^{N}\mathcal{A}_h^{n+1}. \qquad (3.67)
\end{aligned}
$$

Remark 3.7 *We note, in particular, that the second and fourth term in the right-hand side are separated intentionally. Indeed, as observed in the following, the second one induces a lower convergence rate in time for the semi-implicit scheme, while the fourth one doesn't.*

For the sake of clarity, in the following we will redefine $\sum_{n=0}^{N}\mathcal{A}_h^{n+1}$ as $\sum_{i=1}^{4} T_i^N$, where T_i^N for $1 \leq i \leq 4$ are introduced and analyzed below. We set

$$
T_1^N \stackrel{\text{def}}{=} -\sum_{n=0}^{N} a^{\mathrm{s}}(\boldsymbol{d}_H(t^{n+1})-\boldsymbol{d}(t^{n+1}),e_H^{n+1}-e_H^n),
$$

$$
T_2^N \stackrel{\text{def}}{=} -\sum_{n=0}^{N}\left\langle \boldsymbol{\lambda}(t^{n+1}),e_H^{n+1}-e_H^n-\pi_h(e_H^{n+1}-e_H^n)\right\rangle_{\Sigma},
$$

$$
T_3^N \stackrel{\text{def}}{=} \sum_{n=0}^{N} 2\mu(\boldsymbol{\varepsilon}(\mathbf{u}(t^{n+1})-\mathbf{u}_h(t^{n+1})),\boldsymbol{\varepsilon}(\mathcal{L}_h(e_H^{n+1}-e_H^n)))_{\Omega^{\mathrm{f}}},
$$

and

$$T_4^N \stackrel{\text{def}}{=} \sum_{n=0}^{N} \left(p_h(t^{n+1}) - p(t^{n+1}), \nabla \cdot \mathcal{L}_h\left(e_H^{n+1} - e_H^n\right)\right)_{\Omega^{\mathrm{f}}}.$$

Considering the term $T_1^N = -\sum_{n=0}^{N} a^{\mathrm{s}}(\boldsymbol{d}_H(t^{n+1}) - \boldsymbol{d}(t^{n+1}), e_H^{n+1} - e_H^n)$ we have

$$\begin{aligned} T_1^N &= -\sum_{n=1}^{N+1} a^{\mathrm{s}}(\boldsymbol{d}_H(t^n) - \boldsymbol{d}(t^n), e_H^n) + \sum_{n=0}^{N} a^{\mathrm{s}}(\boldsymbol{d}_H(t^{n+1}) - \boldsymbol{d}(t^{n+1}), e_H^n) \\ &= \sum_{n=1}^{N} a^{\mathrm{s}}((\boldsymbol{d}_H(t^{n+1}) - \boldsymbol{d}(t^{n+1})) - (\boldsymbol{d}_H(t^n) - \boldsymbol{d}(t^n)), e_H^n) \\ &\quad -a^{\mathrm{s}}(\boldsymbol{d}_H(t^{N+1}) - \boldsymbol{d}(t^{N+1}), e_H^{N+1}) + a^{\mathrm{s}}(\boldsymbol{d}_H(t^1) - \boldsymbol{d}(t^1), e_H^0) \end{aligned}$$

Choosing $\boldsymbol{d}_H(t^0) = \boldsymbol{d}_H^0$ (*i.e.* $e_H^0 = 0$) and using the continuity of $a^{\mathrm{s}}(\cdot,\cdot)$ we get

$$\begin{aligned} |T_1^N| \leq & \sum_{n=1}^{N} C\tau \left(\left\| \frac{\boldsymbol{d}_H(t^{n+1}) - \boldsymbol{d}(t^{n+1})}{\tau} - \frac{\boldsymbol{d}_H(t^n) - \boldsymbol{d}(t^n)}{\tau} \right\|_{V^{\mathrm{s}}}^2 + a^{\mathrm{s}}(e_H^n, e_H^n) \right) \\ & + C \left\| \boldsymbol{d}_H(t^{N+1}) - \boldsymbol{d}(t^{N+1}) \right\|_{V^{\mathrm{s}}}^2 + \frac{\gamma_4}{2} a^{\mathrm{s}}(e_H^{N+1}, e_H^{N+1}). \end{aligned}$$

By a Taylor expansion, since we assume that the continuous solution is smooth enough, T_1^N can be bounded by

$$\begin{aligned} |T_1^N| \leq & \sum_{n=1}^{N} C\tau \left(\left\| \partial_t \boldsymbol{d}(t^{n+1}) - D_\tau \boldsymbol{d}_H(t^{n+1}) \right\|_{V^{\mathrm{s}}}^2 + a^{\mathrm{s}}(e_H^n, e_H^n) \right) \\ & + C \left\| \boldsymbol{d}_H(t^{N+1}) - \boldsymbol{d}(t^{N+1}) \right\|_{V^{\mathrm{s}}}^2 + \frac{\gamma_4}{2} a^{\mathrm{s}}(e_H^{N+1}, e_H^{N+1}) + C\tau^2. \quad (3.68) \end{aligned}$$

Before going on, we observe that the quantity $\left\| \boldsymbol{d}_H(t^{N+1}) - \boldsymbol{d}(t^{N+1}) \right\|_{V^{\mathrm{s}}}^2$ can be estimated by means of estimate (3.37). Notice also that the Taylor formula and the fact that $e_H^0 = 0$ are still used for the remaining estimates of T_i^N, $\forall\ 2 \leq i \leq 4$; but their notification is omitted for the sake of conciseness.

The term $T_2^N = -\sum_{n=0}^{N} \left\langle \boldsymbol{\lambda}(t^{n+1}), e_H^{n+1} - e_H^n - \pi_h(e_H^{n+1} - e_H^n) \right\rangle_\Sigma$, representing the consistency error associated with the non-conforming matching at the interface, can be rewritten as

$$\begin{aligned} T_2^N &= -\sum_{n=1}^{N+1} \left\langle \boldsymbol{\lambda}(t^n), e_H^n - \pi_h(e_H^n) \right\rangle_\Sigma + \sum_{n=0}^{N} \left\langle \boldsymbol{\lambda}(t^{n+1}), e_H^n - \pi_h(e_H^n) \right\rangle_\Sigma \\ &= -\sum_{n=1}^{N} \left\langle \boldsymbol{\lambda}(t^{n+1}) - \boldsymbol{\lambda}(t^n), e_H^n - \pi_h(e_H^n) \right\rangle_\Sigma \\ &\quad -\left\langle \boldsymbol{\lambda}(t^{N+1}), e_H^{N+1} - \pi_h(e_H^{N+1}) \right\rangle_\Sigma + \left\langle \boldsymbol{\lambda}(t^1), e_H^0 - \pi_h(e_H^0) \right\rangle_\Sigma. \end{aligned}$$

Depending on the choice of the operator π_h we have different kind of estimates. If

π_h is a **mortar-type operator**, using property (3.24) we have

$$\begin{aligned} T_2^N &= -\sum_{n=1}^{N} \tau \left\langle \frac{\boldsymbol{\lambda}(t^{n+1}) - \tilde{\pi}_h(\boldsymbol{\lambda}(t^{n+1}))}{\tau} - \frac{\boldsymbol{\lambda}(t^n) - \tilde{\pi}_h(\boldsymbol{\lambda}(t^n))}{\tau}, e_H^n - \pi_h(e_H^n) \right\rangle_\Sigma \\ &\quad -\left\langle \boldsymbol{\lambda}(t^{N+1}) - \tilde{\pi}_h(\boldsymbol{\lambda}(t^{N+1})), e_H^{N+1} - \pi_h(e_H^{N+1}) \right\rangle_\Sigma \\ &\quad +\left\langle \boldsymbol{\lambda}(t^1) - \tilde{\pi}_h(\boldsymbol{\lambda}(t^1)), e_H^0 - \pi_h(e_H^0) \right\rangle_\Sigma, \end{aligned}$$

where $\tilde{\pi}_h(\boldsymbol{\lambda}(t^i)) \in \tilde{V}_h^{\mathrm{f}}(\Sigma)$ denotes the L^2 orthogonal projection of $\boldsymbol{\lambda}(t^i)$ on $V_h^{\mathrm{f}}(\Sigma)$. First we estimate $|T_2^N|$ as

$$\begin{aligned} |T_2^N| &\leq \sum_{n=1}^{N} C\tau \left(\left\| \left(\mathcal{I} - \tilde{\pi}_h\right) \left(D_\tau \boldsymbol{\lambda}(t^{n+1})\right) \right\|^2_{(H_{00}^{\frac{1}{2}}(\Sigma))'} + \left\| e_H^n - \pi_h(e_H^n) \right\|^2_{H_{00}^{\frac{1}{2}}(\Sigma)} \right) \\ &\quad + C \left\| \left(\mathcal{I} - \tilde{\pi}_h\right) \left(\boldsymbol{\lambda}(t^{N+1})\right) \right\|^2_{(H_{00}^{\frac{1}{2}}(\Sigma))'} + \frac{\gamma_4}{2} \left\| e_H^{N+1} - \pi_h(e_H^{N+1}) \right\|^2_{H_{00}^{\frac{1}{2}}(\Sigma)}. \end{aligned}$$

Then, the $H_{00}^{\frac{1}{2}}(\Sigma)$-stability of π_h, see (3.28), and the coercivity of $a_s(\cdot,\cdot)$ on $H^1_{0,\Gamma_d^{\mathrm{s}}}(\Omega^{\mathrm{s}})$ yield

$$\left\| e_H^n - \pi_h(e_H^n) \right\|^2_{H_{00}^{\frac{1}{2}}(\Sigma)} \leq C \left\| e_H^n \right\|^2_{H_{00}^{\frac{1}{2}}(\Sigma)} \leq C \left\| e_H^n \right\|^2_{1,\Omega^{\mathrm{s}}} \leq a_s(e_H^n, e_H^n).$$

Therefore $|T_2^N|$ can be controlled by

$$\begin{aligned} |T_2^N| &\leq \sum_{n=1}^{N} C\tau \left(\left\| \left(\mathcal{I} - \tilde{\pi}_h\right) \left(D_\tau \boldsymbol{\lambda}(t^{n+1})\right) \right\|^2_{(H_{00}^{\frac{1}{2}}(\Sigma))'} + a^{\mathrm{s}}(e_H^n, e_H^n) \right) \\ &\quad + C \left\| \left(\mathcal{I} - \tilde{\pi}_h\right) \left(\boldsymbol{\lambda}(t^{N+1})\right) \right\|^2_{(H_{00}^{\frac{1}{2}}(\Sigma))'} + \frac{\gamma_4}{2} a^{\mathrm{s}}(e_H^{N+1}, e_H^{N+1}) \\ &\leq \sum_{n=1}^{N} C\tau \left(\left\| \left(\mathcal{I} - \tilde{\pi}_h\right) \left(\partial_t \boldsymbol{\lambda}(t^{n+1})\right) \right\|^2_{(H_{00}^{\frac{1}{2}}(\Sigma))'} + a^{\mathrm{s}}(e_H^n, e_H^n) \right) \\ &\quad + C \left\| \left(\mathcal{I} - \tilde{\pi}_h\right) \left(\boldsymbol{\lambda}(t^{N+1})\right) \right\|^2_{(H_{00}^{\frac{1}{2}}(\Sigma))'} + \frac{\gamma_4}{2} a^{\mathrm{s}}(e_H^{N+1}, e_H^{N+1}) + C\tau^2. \end{aligned}$$

To estimate the quantity $\left\| \left(\mathcal{I} - \tilde{\pi}_h\right) \left(\boldsymbol{\lambda}(t^{N+1})\right) \right\|_{(H_{00}^{\frac{1}{2}}(\Sigma))'}$ (as well as $\left\| \left(\mathcal{I} - \tilde{\pi}_h\right) \left(\partial_t \boldsymbol{\lambda}(t^{n+1})\right) \right\|_{(H_{00}^{\frac{1}{2}}(\Sigma))'}$) we make use of (3.25) and of the standard finite element estimate on $\{\boldsymbol{v}_h \in \mathcal{C}^0(\overline{\Sigma}), \boldsymbol{v}_{h|K} \in \mathbb{P}_{k-1}, \forall K \in \mathcal{T}_h^{\mathrm{f}} \text{ with } |K \cap \Sigma| \neq 0\} \subset \tilde{V}_h^{\mathrm{f}}(\Sigma)$,

$$\begin{aligned} &\left\| \left(\mathcal{I} - \tilde{\pi}_h\right) \left(\boldsymbol{\lambda}(t^i)\right) \right\|_{(H_{00}^{\frac{1}{2}}(\Sigma))'} = \left\| \boldsymbol{\lambda}(t^i) - \tilde{\boldsymbol{\lambda}}_h(t^i) - \tilde{\pi}_h(\boldsymbol{\lambda}(t^i) - \tilde{\boldsymbol{\lambda}}_h(t^i)) \right\|_{(H_{00}^{\frac{1}{2}}(\Sigma))'} \\ &\leq C h^{\frac{1}{2}} \left\| \boldsymbol{\lambda}(t^i) - \tilde{\boldsymbol{\lambda}}_h(t^i) \right\|_{0,\Sigma} \leq C h^l \left\| \boldsymbol{\lambda}(t^i) \right\|_{l-\frac{1}{2},\Sigma}, \quad \forall\, \frac{1}{2} \leq l \leq k, \quad \forall \tilde{\boldsymbol{\lambda}}_h \in \tilde{V}_h^{\mathrm{f}}(\Sigma). \end{aligned}$$

We note, in particular, that $\tilde{V}_h^{\mathrm{f}}(\Sigma)$ has good approximations properties for $(H_{00}^{\frac{1}{2}}(\Sigma))'$. Therefore, in the mortar case, T_2^N can be controlled by

$$|T_2^N| \leq \sum_{n=1}^{N} C\tau a^{\mathrm{s}}(e_H^n, e_H^n) + \frac{\gamma_4}{2} a^{\mathrm{s}}(e_H^{N+1}, e_H^{N+1}) + C\tau^2 + Ch^{2l}, \quad \forall\, \frac{1}{2} \leq l \leq k. \tag{3.69}$$

Whereas, if π_h is a **finite element interpolation operator**, we can conclude that

$$\begin{aligned}
|T_2^N| &\leq \sum_{n=1}^{N} C\tau\|e_H^n - \pi_h(e_H^n)\|_{0,\Sigma} + C\|e_H^{N+1} - \pi_h(e_H^{N+1})\|_{0,\Sigma} \\
&\leq \sum_{n=1}^{N} C\tau h^l \|e_H^n\|_{l,\Sigma} + Ch^l\|e_H^{N+1}\|_{l,\Sigma} \\
&\leq \sum_{n=1}^{N} C\tau\|e_H^n\|_{l,\Sigma}^2 + C\|e_H^{N+1}\|_{l,\Sigma}^2 + Ch^{2l}, \quad \text{with} \quad l \leq \min\left(r - \frac{\alpha}{2}, k+1\right),
\end{aligned}$$

where we have used the approximation property (3.22). Finally, the inequality

$$\|\boldsymbol{v}\|_{l,\Sigma} \leq C\|\boldsymbol{v}\|_{l+\frac{\alpha}{2},\Omega^{\mathrm{s}}} \leq C\|\boldsymbol{v}\|_{r,\Omega^{\mathrm{s}}}, \ \forall \boldsymbol{v} \in H^r(\Omega^{\mathrm{s}}),$$

and the coercivity of $a^{\mathrm{s}}(\cdot,\cdot)$ in $V^{\mathrm{s}} \subset H^r(\Omega^{\mathrm{s}})$ lead to

$$|T_2^N| \leq \sum_{n=1}^{N} C\tau a^{\mathrm{s}}(e_H^n, e_H^n) + \frac{\gamma_4}{2} a^{\mathrm{s}}(e_H^{N+1}, e_H^{N+1}) + Ch^{2l} \tag{3.70}$$

with $l \leq \min\left(r - \frac{\alpha}{2}, k+1\right)$.

Like the previous terms,

$$\begin{aligned}
T_3^N =& \sum_{n=0}^{N} 2\mu(\boldsymbol{\varepsilon}(\mathbf{u}(t^{n+1}) - \mathbf{u}_h(t^{n+1})), \boldsymbol{\varepsilon}(\mathcal{L}_h(e_H^{n+1} - e_H^n)))_{\Omega^{\mathrm{f}}} \\
=& \sum_{n=1}^{N+1} 2\mu\big(\boldsymbol{\varepsilon}(\mathbf{u}(t^n) - \mathbf{u}_h(t^n)), \boldsymbol{\varepsilon}(\mathcal{L}_h(e_H^n))\big)_{\Omega^{\mathrm{f}}} \\
& - \sum_{n=0}^{N} 2\mu\big(\boldsymbol{\varepsilon}(\mathbf{u}(t^{n+1}) - \mathbf{u}_h(t^{n+1})), \boldsymbol{\varepsilon}(\mathcal{L}_h(e_H^n))\big)_{\Omega^{\mathrm{f}}}
\end{aligned}$$

is first rewritten as

$$\begin{aligned}
T_3^N =& \sum_{n=1}^{N} 2\mu\tau \left(\boldsymbol{\varepsilon}\left(D_\tau \mathbf{u}(t^{n+1})\right) - \boldsymbol{\varepsilon}\left(D_\tau \mathbf{u}_h(t^{n+1})\right), \boldsymbol{\varepsilon}(\mathcal{L}_h(e_H^n))\right)_{\Omega^{\mathrm{f}}} \\
& + 2\mu\big(\boldsymbol{\varepsilon}(\mathbf{u}(t^{N+1}) - \mathbf{u}_h(t^{N+1})), \boldsymbol{\varepsilon}(\mathcal{L}_h(e_H^{N+1}))\big)_{\Omega^{\mathrm{f}}} \\
& - 2\mu(\boldsymbol{\varepsilon}(\mathbf{u}(t^1) - \mathbf{u}_h(t^1)), \boldsymbol{\varepsilon}(\mathcal{L}_h(e_H^0)))_{\Omega^{\mathrm{f}}},
\end{aligned}$$

and then bounded by

$$\begin{aligned}
|T_3^N| \leq & \sum_{n=1}^{N} C\tau \left(\mu^2 \left\|\boldsymbol{\varepsilon}\left(\partial_t \mathbf{u}(t^{n+1}) - D_\tau \mathbf{u}_h(t^{n+1})\right)\right\|_{0,\Omega^{\mathrm{f}}}^2 + \left\|\boldsymbol{\varepsilon}\big(\mathcal{L}_h(e_H^n)\big)\right\|_{0,\Omega^{\mathrm{f}}}^2\right) \\
& + C\mu^2 \left\|\boldsymbol{\varepsilon}\big(\mathbf{u}(t^{N+1}) - \mathbf{u}_h(t^{N+1})\big)\right\|_{0,\Omega^{\mathrm{f}}}^2 + C\left\|\boldsymbol{\varepsilon}\big(\mathcal{L}_h(e_H^{N+1})\big)\right\|_{0,\Omega^{\mathrm{f}}}^2 + C\tau^2.
\end{aligned}$$

The definition of $\mathcal{L}_h$, the inequality (3.45) and the stability properties of π_h (see (3.21) in the finite element interpolation operator case or (3.28) in the mortar case) yield

$$\left\|\boldsymbol{\varepsilon}(\mathcal{L}_h(e_H^n))\right\|_{0,\Omega^{\mathrm{f}}}^2 \leq C\left\|\pi_h(e_H^n)\right\|_{H_{00}^{\frac{1}{2}}(\Sigma)}^2 \leq C\left\|e_H^n\right\|_{H_{00}^{\frac{1}{2}}(\Sigma)}^2 \leq Ca^{\mathrm{s}}(e_H^n, e_H^n) \quad \forall n \geq 0,$$

that gives

$$\begin{aligned} |T_3^N| \;\leq\; & \sum_{n=1}^{N} C\tau\left(\mu^2\left\|\boldsymbol{\varepsilon}\left(\partial_t\mathbf{u}(t^{n+1}) - D_\tau\mathbf{u}_h(t^{n+1})\right)\right\|_{0,\Omega^{\mathrm{f}}}^2 + a^{\mathrm{s}}(e_H^n, e_H^n)\right) \\ & + C\mu^2\left\|\mathbf{u}(t^{N+1}) - \mathbf{u}_h(t^{N+1})\right\|_{1,\Omega^{\mathrm{f}}}^2 + \frac{\gamma_4}{2}a^{\mathrm{s}}(e_H^{N+1}, e_H^{N+1}) + C\tau^2. \end{aligned} \tag{3.71}$$

Note that here $\left\|\mathbf{u}(t^{N+1}) - \mathbf{u}_h(t^{N+1})\right\|_{1,\Omega^{\mathrm{f}}}^2$ can be estimated as in (3.39).

Finally, for

$$\begin{aligned} T_4^N &\stackrel{\text{def}}{=} \sum_{n=0}^{N}\left(p_h(t^{n+1}) - p(t^{n+1}), \nabla\cdot\mathcal{L}_h\left(e_H^{n+1} - e_H^n\right)\right)_{\Omega^{\mathrm{f}}} \\ &= \sum_{n=1}^{N+1}\left(p_h(t^n) - p(t^n), \nabla\cdot\mathcal{L}_h(e_H^n)\right)_{\Omega^{\mathrm{f}}} \\ &\quad - \sum_{n=0}^{N+1}\left(p_h(t^{n+1}) - p(t^{n+1}), \nabla\cdot\mathcal{L}_h(e_H^n)\right)_{\Omega^{\mathrm{f}}} \\ &= \sum_{n=1}^{N}\tau\left(D_\tau p_h(t^{n+1}) - D_\tau p(t^{n+1}), \nabla\cdot(\mathcal{L}_h(e_H^n))\right)_{\Omega^{\mathrm{f}}} \\ &\quad + \left(p_h(t^{N+1}) - p(t^{N+1}), \nabla\cdot(\mathcal{L}_h(e_H^{N+1}))\right)_{\Omega^{\mathrm{f}}} \\ &\quad - \left(p_h(t^1) - p(t^1)), \nabla\cdot(\mathcal{L}_h(e_H^0))\right)_{\Omega^{\mathrm{f}}} \end{aligned}$$

we have that

$$\begin{aligned} |T_4^N| \;\leq\; & \sum_{n=1}^{N} C\tau\left(\left\|\partial_t p(t^{n+1}) - D_\tau p_h(t^{n+1})\right\|_{0,\Omega^{\mathrm{f}}}^2 + a^{\mathrm{s}}(e_H^n, e_H^n)\right) \\ & + C\left\|p(t^{N+1}) - p_h(t^{N+1})\right\|_{0,\Omega^{\mathrm{f}}}^2 + \frac{\gamma_4}{2}a^{\mathrm{s}}(e_H^{N+1}, e_H^{N+1}) + C\tau^2, \end{aligned} \tag{3.72}$$

where, as for T_3^N, we have used the fact that

$$\left\|\nabla\cdot(\mathcal{L}_h(e_H^n))\right\|_{0,\Omega^{\mathrm{f}}}^2 \leq Ca^{\mathrm{s}}(e_H^n, e_H^n) \quad \forall n \geq 0.$$

Note moreover that the quantity $\left\|p(t^{N+1}) - p_h(t^{N+1})\right\|_{0,\Omega^{\mathrm{f}}}^2$ verifies estimate (3.40).

Part 4. We finally replace in (3.67) the terms T_i^N, for $1 \leq i \leq 4$, by the corresponding bounds (3.68), (3.69) (or (3.70) depending on the type of matching operator at

the interface), (3.71) and (3.72), and we set $\gamma_1 = \frac{1}{4}$, $\gamma_2 = \gamma_3 = \frac{1}{2}$ and $\gamma_4 = \frac{1}{8}$. After some rearrangements, we obtain

$$\begin{aligned}
E^{N+1} \;+\; & \frac{\rho^{\mathrm{f}}}{4}\sum_{n=0}^{N}[\|\tilde{e}_h^{n+1}-e_h^n\|_{0,\Omega^{\mathrm{f}}}^2+\|e_h^{n+1}-\tilde{e}_h^{n+1}\|_{0,\Omega^{\mathrm{f}}}^2] \\
+\; & \sum_{n=0}^{N}\mu\tau\|\boldsymbol{\varepsilon}(\tilde{e}_h^{n+1})\|_{0,\Omega^{\mathrm{f}}}^2+\frac{1}{2}\sum_{n=0}^{N}a^{\mathrm{s}}(e_H^{n+1}-e_H^n,e_H^{n+1}-e_H^n) \\
+\; & \sum_{n=0}^{N}\left(\frac{\rho^{\mathrm{s}}}{2}-\frac{Ch\rho^{\mathrm{f}}}{H^\alpha}-\frac{C\mu\delta t}{hH^\alpha}\right)\left\|D_\tau e_H^{n+1}-D_\tau e_H^n\right\|_{0,\Omega^{\mathrm{s}}}^2 \\
\leq\; & \sum_{n=0}^{N}C\rho^{\mathrm{f}}\tau(\|\tilde{e}_h^{n+1}-e_h^{n+1}\|_{0,\Omega^{\mathrm{f}}}^2+\|e_h^{n+1}\|_{0,\Omega^{\mathrm{f}}}^2) \\
& +\sum_{n=0}^{N}C\rho^{\mathrm{s}}\delta t\left\|D_\tau e_H^{n+1}\right\|_{0,\Omega^{\mathrm{s}}}^2+\sum_{n=0}^{N}\frac{Ch\rho^{\mathrm{f}}\delta t}{H^\alpha}\left\|D_\tau e_H^{n+1}-D_\tau e_H^n\right\|_{0,\Omega^{\mathrm{s}}}^2 \\
& +\sum_{n=1}^{N}C\delta t a^{\mathrm{s}}(e_H^n,e_N^n)+\mathcal{I}+\mathcal{H}+\mathcal{T}+C\tau^2+Ch^{2l}, \qquad (3.73)
\end{aligned}$$

where

$$E^{n+1}\stackrel{\text{def}}{=}\frac{\rho^{\mathrm{f}}}{2}\|e_h^{n+1}\|_{0,\Omega^{\mathrm{f}}}^2+\frac{\rho^{\mathrm{s}}}{2}\left\|D_\tau e_H^{n+1}\right\|_{0,\Omega^{\mathrm{s}}}^2+\frac{1}{4}a^{\mathrm{s}}(e_H^{n+1},e_H^{n+1}).$$

Here, $\mathcal{T}$ contains the terms that cause a reduction of the convergence rate in time, $\mathcal{H}$ the ones that introduce a time consistency error, while $\mathcal{I}$ regroups the remaining terms, associated with the space discretization errors. More precisely

$$\begin{aligned}
\mathcal{I}\stackrel{\text{def}}{=} C\left\|\boldsymbol{d}_H(t^{N+1})-\boldsymbol{d}(t^{N+1})\right\|_{V^{\mathrm{s}}}^2+C\mu^2\left\|\mathbf{u}(t^{N+1})-\mathbf{u}_h(t^{N+1})\right\|_{1,\Omega^{\mathrm{f}}}^2 \\
+C\left\|p(t^{N+1})-p_h(t^{N+1})\right\|_{0,\Omega^{\mathrm{f}}}^2.
\end{aligned}$$

Using (3.37), (3.39) and (3.40), $\mathcal{I}$ can be bounded by

$$\mathcal{I} \;\leq\; C\delta t^2+Ch^{2k}+CH^{2m}+Ch^{2l}. \qquad (3.74)$$

In (3.74), k and m represent (and will represent in all that follows) the finite element order respectively for the fluid and the structure part, while $l \leq \min\left(r-\frac{\alpha}{2}, k+1\right)$ (resp. $\frac{1}{2} \leq l \leq k+1$) for a finite element interpolation (resp. mortar) matching operator at the interface.

$\mathcal{H}$ regroups some of the terms coming from the estimates of $\mathcal{D}_h^{n+1}$ and of T_1^N,

T_3^N, T_4^N, and is equal to

$$\begin{aligned}\mathcal{H} \overset{\text{def}}{=} & \sum_{n=0}^{N} C\frac{h\rho^{\mathrm{f}}\tau}{H^{\alpha}}\left\|D_\tau \boldsymbol{d}_H(t^{n+1}) - D_\tau \boldsymbol{d}_H(t^n)\right\|_{0,\Omega^{\mathrm{s}}}^2 \\ & + \sum_{n=0}^{N} C\rho^{\mathrm{f}}\tau\left\|\partial_t \mathbf{u}(t^{n+1}) - D_\tau \mathbf{u}_h(t^{n+1})\right\|_{0,\Omega^{\mathrm{f}}}^2 \\ & + \sum_{n=0}^{N} C\rho^{\mathrm{s}}\tau\left\|\partial_{tt} \boldsymbol{d}(t^{n+1}) - D_{\tau\tau} \boldsymbol{d}_H(t^{n+1})\right\|_{0,\Omega^{\mathrm{s}}}^2 \\ & + \sum_{n=1}^{N} C\tau\left\|\partial_t \boldsymbol{d}(t^{n+1}) - D_\tau \boldsymbol{d}_H(t^{n+1})\right\|_{V^{\mathrm{s}}}^2 \\ & + \sum_{n=1}^{N} C\tau\mu^2\left\|\boldsymbol{\varepsilon}\left(\partial_t \mathbf{u}(t^{n+1}) - D_\tau \mathbf{u}_h(t^{n+1})\right)\right\|_{0,\Omega^{\mathrm{f}}}^2 \\ & + \sum_{n=1}^{N} C\tau\left\|\partial_t p(t^{n+1}) - D_\tau p_h(t^{n+1})\right\|_{0,\Omega^{\mathrm{f}}}^2 .\end{aligned}$$

The first term is bounded by

$$\sum_{n=0}^{N} C\frac{h\rho^{\mathrm{f}}\tau}{H^{\alpha}}\left\|D_\tau \boldsymbol{d}_H(t^{n+1}) - D_\tau \boldsymbol{d}_H(t^n)\right\|_{0,\Omega^{\mathrm{s}}}^2 \leq C\frac{h\rho^{\mathrm{f}}}{H^{\alpha}}\tau^2, \tag{3.75}$$

using the fact that

$$\begin{aligned}&\left\|D_\tau \boldsymbol{d}_H(t^{n+1}) - D_\tau \boldsymbol{d}_H(t^n)\right\|_{0,\Omega^{\mathrm{s}}}^2 \\ &\quad \leq C\left(\left\|D_\tau \boldsymbol{d}_H(t^{n+1}) - \partial_t \boldsymbol{d}_H(t^n)\right\|_{0,\Omega^{\mathrm{s}}}^2 + \left\|\partial_t \boldsymbol{d}_H(t^n) - D_\tau \boldsymbol{d}_H(t^n)\right\|_{0,\Omega^{\mathrm{s}}}^2\right) \\ &\quad \leq C\tau^2.\end{aligned} \tag{3.76}$$

In order to control the remaining time consistency errors, we follow the same steps as in the derivation of (3.37), (3.39) and (3.40), using the definitions of the different correction terms $(\boldsymbol{z}_h, \mu_h, \boldsymbol{c}_H)$. For example, considering $\left\|\partial_t \mathbf{u}(t^{n+1}) - D_\tau \mathbf{u}_h(t^{n+1})\right\|_{0,\Omega^{\mathrm{f}}}^2$ we have

$$\begin{aligned}\left\|\partial_t \mathbf{u}(t^{n+1}) - D_\tau \mathbf{u}_h(t^{n+1})\right\|_{0,\Omega^{\mathrm{f}}}^2 &= \left\|\partial_t \mathbf{u}(t^{n+1}) - D_\tau P_h^{\mathrm{f}}(\mathbf{u})(t^{n+1}) - D_\tau \boldsymbol{z}_h(t^{n+1})\right\|_{0,\Omega^{\mathrm{f}}}^2 \\ &\leq C\left\|\partial_t \mathbf{u}(t^{n+1}) - P_h^{\mathrm{f}}(\partial_t \mathbf{u})(t^{n+1})\right\|_{0,\Omega^{\mathrm{f}}}^2 + C\left\|D_\tau \boldsymbol{z}_h(t^{n+1})\right\|_{0,\Omega^{\mathrm{f}}}^2 + C\tau^2.\end{aligned}$$

The first term can be estimated by remembering the definition of P_h^{f}:

$$\left\|\partial_t \mathbf{u}(t^{n+1}) - P_h^{\mathrm{f}}(\partial_t \mathbf{u})(t^{n+1})\right\|_{0,\Omega^{\mathrm{f}}}^2 \leq C\inf_{\boldsymbol{v}_h \in V_h^{\mathrm{f}}}\left\|\partial_t \mathbf{u}(t^{n+1}) - \boldsymbol{v}_h\right\|_{V^{\mathrm{f}}}^2.$$

For the second term, recalling the definition of the correction term $\boldsymbol{z}_h$, it is easy to see that

$$\left\|D_\tau \boldsymbol{z}_h(t^{n+1})\right\|_{0,\Omega^{\mathrm{f}}}^2 \leq C\left\|\pi_h\left(D_{\tau\tau} \boldsymbol{d}_H(t^{n+1})\right) - P_h^{\mathrm{f}}\left(D_\tau \mathbf{u}(t^{n+1})\right)\right\|_{H_{00}^{\frac{1}{2}}(\Sigma)}^2 .$$

Thus the $H^{\frac{1}{2}}_{00}$-stability of π_h and the fact that $\pi_h(\boldsymbol{v}_h) = \boldsymbol{v}_h,\ \forall \boldsymbol{v}_h \in V^{\mathrm{f}}_h(\Sigma)$, lead to

$$\left\|D_\tau \boldsymbol{z}_h(t^{n+1})\right\|^2_{0,\Omega^{\mathrm{f}}} \leq C \left\|D_{\tau\tau}\boldsymbol{d}_H(t^{n+1}) - P^{\mathrm{f}}_h\left(D_\tau \mathbf{u}(t^{n+1})\right)\right\|^2_{H^{\frac{1}{2}}_{00}(\Sigma)}.$$

The upper bound is now estimated following the same arguments used for the estimate of $\boldsymbol{z}_h$. In particular, by taking into account the fact that $\partial_t \mathbf{u}(t) = \partial_{tt}\boldsymbol{d}(t)$ at the interface, we get

$$\begin{aligned}\left\|D_\tau \boldsymbol{z}_h(t^{n+1})\right\|^2_{0,\Omega^{\mathrm{f}}} \leq C\Bigg(&\tau^2 \left\|\boldsymbol{d}\right\|^2_{W^{3,\infty}(0,T;V^{\mathrm{s}})} + \inf_{\boldsymbol{v}_H \in V^{\mathrm{s}}_H} \left\|\partial_{tt}\boldsymbol{d}(t^i) - \boldsymbol{v}_H\right\|^2_{V^{\mathrm{s}}} \\ &+ \inf_{\boldsymbol{v}_h \in V^{\mathrm{f}}_h} \left\|\partial_t \mathbf{u}(t^i) - \boldsymbol{v}_h\right\|^2_{V^{\mathrm{f}}} + Ch^{2l}\left\|\partial_{tt}\boldsymbol{d}(t^i)\right\|^2_{V^{\mathrm{s}}}\Bigg),\end{aligned}$$

with $\frac{1}{2} \leq l \leq k+1$ for the mortar case and $l \leq \min\left(r - \frac{\alpha}{2}, k+1\right)$ for the interpolation case. Therefore, with our particular choice of the finite element approximation spaces, the quantity $\left\|\partial_t \mathbf{u}(t^{n+1}) - D_\tau \mathbf{u}_h(t^{n+1})\right\|^2_{0,\Omega^{\mathrm{f}}}$ is controlled by

$$\begin{aligned}\left\|\partial_t \mathbf{u}(t^{n+1}) - D_\tau \mathbf{u}_h(t^{n+1})\right\|^2_{0,\Omega^{\mathrm{f}}} \leq\ & C\Bigg(\tau^2 \left\|\boldsymbol{d}\right\|^2_{W^{3,\infty}(0,T;V^{\mathrm{s}})} + \inf_{\boldsymbol{v}_H \in V^{\mathrm{s}}_H} \left\|\partial_{tt}\boldsymbol{d}(t^i) - \boldsymbol{v}_H\right\|^2_{V^{\mathrm{s}}} \\ &+ \inf_{\boldsymbol{v}_h \in V^{\mathrm{f}}_h} \left\|\partial_t \mathbf{u}(t^i) - \boldsymbol{v}_h\right\|^2_{V^{\mathrm{f}}} + Ch^{2l}\left\|\partial_{tt}\boldsymbol{d}(t^i)\right\|^2_{V^{\mathrm{s}}}\Bigg) \\ \leq\ & C\tau^2 + Ch^{2k} + CH^{2m} + Ch^{2l}. \qquad (3.77)\end{aligned}$$

All the other terms of $\mathcal{H}$ can be bounded in a similar manner, consequently, using (3.75):

$$\mathcal{H} \leq C\tau^2 + Ch^{2k} + CH^{2m} + Ch^{2l} + C\frac{h\rho^{\mathrm{f}}}{H^\alpha}\tau^2.$$

Finally, the stability conditions (3.20) imply:

$$\mathcal{H} \leq C\tau^2 + Ch^{2k} + CH^{2m} + Ch^{2l}. \qquad (3.78)$$

Let us now consider

$$\begin{aligned}\mathcal{T} \stackrel{\mathrm{def}}{=} \sum_{n=0}^{N} C\left(\frac{h\rho^{\mathrm{f}}}{H^\alpha} + \frac{\mu\delta t}{hH^\alpha}\right)\left\|D_\tau \boldsymbol{d}_H(t^{n+1}) - D_\tau \boldsymbol{d}_H(t^n)\right\|^2_{0,\Omega^{\mathrm{s}}} \\ + \sum_{n=0}^{N} \frac{C\tau^2}{\rho^{\mathrm{f}}}\|\nabla p_h(t^{n+1})\|^2_{0,\Omega^{\mathrm{f}}}. \qquad (3.79)\end{aligned}$$

Using (3.76), $\mathcal{T}$ can be bounded by

$$\mathcal{T} \leq C\left(\frac{h\rho^{\mathrm{f}}}{H^\alpha} + \frac{\mu\delta t}{hH^\alpha} + 1\right)\tau. \qquad (3.80)$$

By applying the stability conditions (3.20), $\mathcal{T}$ can be bounded by $C\tau$, which leads to a time error estimate of order $\sqrt{\tau}$.

Remark 3.8 *Note that the reduction of the convergence rate in time is due to two different contributions. The first part, associated with the term* $\left\|D_\tau \boldsymbol{d}_H(t^{n+1}) - D_\tau \boldsymbol{d}_H(t^n)\right\|^2_{0,\Omega^s}$, *comes intrinsically from the semi-implicit coupling (see Remark 3.5). The second part, associated with the term* $\|\nabla p_h(t^{n+1})\|^2_{0,\Omega^f}$, *comes from the non-incremental Chorin-Temam scheme. It is well-known that this scheme has a reduced time accuracy in a pure hydrodynamic problem. Nevertheless, we must observe that, for the non-incremental Chorin-Temam scheme, the reduced time accuracy affects the fluid pressure in the* $L^\infty(0,T;L^2(\Omega^f))$ *norm and the fluid velocity error in the* $L^\infty(0,T;H^1(\Omega^f))$ *norm (see for example [Hor97]). Here we also obtain a reduced time accuracy for the fluid velocity error in the* $L^\infty(0,T;L^2(\Omega^f))$ *norm. This may be due to the way we have derived our error estimate as well as to the fact that the reduced time accuracy observed for the pressure and for the fluid velocity affects the whole fluid-structure scheme.*

Remark 3.9 *Note finally that, if in (3.80) we don't apply the stability condition, in some particular case (e.g.* $\alpha = 0$*) the convergence rate in time of the first term of* $\mathcal{T}$ *could be slightly better than* τ.

Consequently, from estimate (3.73) and using (3.74), (3.78) and (3.80), we obtain

$$
\begin{aligned}
E^{N+1} \;+\; & \frac{\rho^f}{4}\sum_{n=0}^{N}[\|\tilde{e}_h^{n+1} - e_h^n\|^2_{0,\Omega^f} + \|e_h^{n+1} - \tilde{e}_h^{n+1}\|^2_{0,\Omega^f}] \\
+\; & \sum_{n=0}^{N}\mu\tau\|\boldsymbol{\varepsilon}(\tilde{e}_h^{n+1})\|^2_{0,\Omega^f} + \frac{1}{2}\sum_{n=0}^{N}a^s(e_H^{n+1}-e_H^n, e_H^{n+1}-e_H^n) \\
+\; & \sum_{n=0}^{N}\left(\frac{\rho^s}{2} - \frac{Ch\rho^f}{H^\alpha} - \frac{C\mu\delta t}{hH^\alpha}\right)\left\|D_\tau e_H^{n+1} - D_\tau e_H^n\right\|^2_{0,\Omega^s} \\
\leq\; & \sum_{n=0}^{N}C\rho^f\tau(\|\tilde{e}_h^{n+1} - e_h^{n+1}\|^2_{0,\Omega^f} + \|e_h^{n+1}\|^2_{0,\Omega^f}) \\
& + \sum_{n=0}^{N}C\rho^s\delta t\left\|D_\tau e_H^{n+1}\right\|^2_{0,\Omega^s} + \sum_{n=0}^{N}\frac{Ch\rho^f\delta t}{H^\alpha}\left\|D_\tau e_H^{n+1} - D_\tau e_H^n\right\|^2_{0,\Omega^s} \\
& + \sum_{n=1}^{N}C\delta t a^s(e_H^n, e_N^n) + C\tau + Ch^{2k} + H^{2m} + Ch^{2l},
\end{aligned}
\tag{3.81}
$$

where $\frac{1}{2} \leq l \leq k$ for the mortar case and $l \leq \min\left(r - \frac{\alpha}{2}, k+1\right)$ for the interpolation case. Note that we can restrict ourselves to $l \leq k$ for both matching operators since r is typically equal to 1 or 2.

The analysis is concluded applying a discrete version of the Gronwall's inequality. Here, for the sake of completeness, we recall only the result, referring to [HR90] for a proof of it.

Lemma 3.2 *Let δ, g^0, a^n, b^n, c^n and γ_n be a sequence of non negative numbers for integers $n \geq 0$ so that*

$$a^n + \delta \sum_{j=0}^{n} b^j \leq \delta \sum_{j=0}^{n} \gamma_j a^j + \delta \sum_{j=0}^{n} c^j + g^0$$

Assume that $\gamma_j \delta < 1$ for all j, and set $\sigma_j = (1 - \gamma_j \delta)^{-1}$. Then,for all $n \geq 0$.

$$a^n + \delta \sum_{j=0}^{n} b^j \leq \exp\left(\delta \sum_{j=0}^{n} \sigma_j \gamma_j\right) \left[\delta \sum_{j=0}^{n} c^j + g^0\right].$$

Assuming that the stability condition (3.20) holds true, the discrete Gronwall's lemma yields

$$E^{N+1} + \frac{\rho^{\mathrm{f}}}{4} \sum_{n=0}^{N} \left[\|\tilde{e}_h^{n+1} - e_h^n\|_{0,\Omega^{\mathrm{f}}}^2 + \|e_h^{n+1} - \tilde{e}_h^{n+1}\|_{0,\Omega^{\mathrm{f}}}^2\right] + \sum_{n=0}^{N} \mu\tau \|\boldsymbol{\varepsilon}(\tilde{e}_h^{n+1})\|_{0,\Omega^{\mathrm{f}}}^2$$
$$+ \frac{1}{2} \sum_{n=0}^{N} a^{\mathrm{s}}(e_H^{n+1} - e_H^n, e_H^{n+1} - e_H^n) + \sum_{n=0}^{N} \left(\frac{\rho^{\mathrm{s}}}{2} - \frac{Ch\rho^{\mathrm{f}}}{H^\alpha} - \frac{C\mu\delta t}{hH^\alpha}\right) \left\|D_\tau e_H^{n+1} - D_\tau e_H^n\right\|_{0,\Omega^{\mathrm{s}}}^2$$
$$\leq C\tau + Ch^{2k} + CH^{2m} + Ch^{2l}, \quad (3.82)$$

that concludes the derivation of error estimate (3.41). $\diamond$

3.6 Numerical experiments

In this section we investigate numerically the order of convergence in time of the semi-implicit coupling scheme. Some computational results that confirm the previous analysis are given. Moreover, the realized numerical experiments give a deeper insight into the accuracy of the scheme that could be useful for further improvements of the theoretical analysis.

First the two-dimensional test case used in all the test is introduced. Later, the convergence rate of the semi-implicit scheme (3.12)-(3.14) is evaluated and compared to the one of other FSI algorithms. All the computations are performed with FreeFem++ [Hec].

The test case. A two-dimensional test case consisting of the following analytical solution over the domains $\Omega^{\mathrm{f}} = [0,1] \times [0,1]$ and $\Omega^{\mathrm{s}} = [0,1] \times [1,1.25]$ (Figure 3.2) is considered:

$$\begin{cases} u_x = \cos(x+t)\sin(y+t) + \sin(x+t)\cos(y+t), \\ u_y = -\sin(x+t)\cos(y+t) - \cos(x+t)\sin(y+t), \\ p = 2\mu(\sin(x+t)\sin(y+t) - \cos(x+t)\cos(y+t)) + 2L_2\cos(x+t)\sin(y+t), \\ d_x = \sin(x+t)\sin(y+t), \\ d_y = \cos(x+t)\cos(y+t), \end{cases} \quad (3.83)$$

where L_2 stands for the second Lamé constant of solid. For the fluid, the physical parameters are $\rho^{\mathrm{f}} = 1.0$ g/cm^3, $\mu = 0.013$ poise. For the solid, we have $\rho^{\mathrm{s}} = 1.9$ g/cm^3, the Lamé constant $L_2 = 3$ dyne/cm^2, and the Poisson's ratio $\nu = 0.3$.

External boundary conditions, initial conditions and body forces, for the fluid and the structure, are chosen in order to ensure that the coupled system (3.2)-(3.3) is satisfied by the exact solution (3.83). In particular, considering Figure 3.2, Dirichlet and Neumann boundary conditions are respectively imposed on Γ^{d} and Γ^{n}.

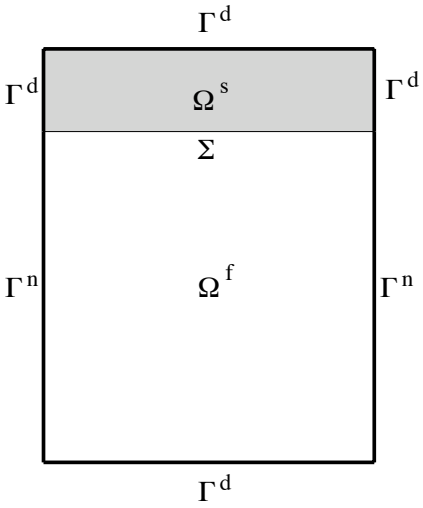

Figure 3.2: Computational domain.

For all the numerical simulations, we adopt a conforming matching between the fluid and the structure without any consequence on the stability of the scheme (see Section 3.3). A uniform space discretization step $h = 0.05$ cm is used. For the fluid, we choose Taylor-Hood finite element, while for the structure, $\mathbb{P}_2$ finite elements are used in order to guarantee a small space discretization error. For the time discretization, a sequence of decreasing time-steps ($\tau = 5 \cdot 10^{-2}, 2.5 \cdot 10^{-2}, 1.25 \cdot 10^{-2}, 6.25 \cdot 10^{-3}, 3.125 \cdot 10^{-3}$s) is considered for the comparison of the numerical solutions with the exact one (3.83).

Three different FSI algorithms are compared: the semi-implicit scheme (3.12)-(3.14), a fully implicit scheme where the Stokes equations are solved as a mixed problem in the velocity and pressure unknowns, and a modified version of the semi-implicit scheme where we replace the non-incremental Chorin-Temam method with its incremental version (see for instance [GQ98b]). The latter is given by:

Algorithm 3.4 *Semi-implicit coupling scheme based on the incremental projection Chorin-Temam method*

Step 1 : `(explicit viscous-structure coupling)`

$$\begin{cases} \rho^{\mathrm{f}} \dfrac{\tilde{\mathbf{u}}^{n+1} - \mathbf{u}^n}{\tau} - 2\mu \mathtt{div}\,(\boldsymbol{\varepsilon}(\tilde{\mathbf{u}}^{n+1})) + \nabla p^n = \mathbf{0}, \quad \mathtt{in} \quad \Omega^{\mathrm{f}}, \\ \tilde{\mathbf{u}}^{n+1} = D_\tau \boldsymbol{d}^n, \quad \mathtt{on} \quad \Sigma. \end{cases}$$

Step 2 : (implicit pressure-structure coupling)

- **Step 2.1** : (fluid projection sub-step)

$$\begin{cases} \rho^{\mathrm{f}} \dfrac{\mathbf{u}^{n+1} - \tilde{\mathbf{u}}^{n+1}}{\tau} + \nabla(p^{n+1} - p^n) = \mathbf{0}, \quad \texttt{in} \quad \Omega^{\mathrm{f}}, \\ \texttt{div}\, \mathbf{u}^{n+1} = 0, \quad \texttt{in} \quad \Omega^{\mathrm{f}}, \\ \mathbf{u}^{n+1} \cdot \mathbf{n}^{\mathrm{f}} = D_\tau \boldsymbol{d}^{n+1} \cdot \mathbf{n}^{\mathrm{f}}, \quad \texttt{on} \quad \Sigma. \end{cases}$$

- **Step 2.2** : (solid sub-step)

$$\begin{cases} \rho^{\mathrm{s}} D_{\tau\tau} \boldsymbol{d}^{n+1} - \texttt{div}\, \boldsymbol{\sigma}^{\mathrm{s}}(\boldsymbol{d}^{n+1}) = \mathbf{0}, \quad \texttt{in} \quad \Omega^s, \\ \boldsymbol{\sigma}^{\mathrm{s}}(\boldsymbol{d}^{n+1}) \cdot \mathbf{n}^{\mathrm{s}} = \boldsymbol{\sigma}^{\mathrm{f}}(\tilde{\mathbf{u}}^{n+1}, p^{n+1}) \cdot \mathbf{n}^{\mathrm{s}}, \quad \texttt{on} \quad \Sigma. \end{cases}$$

For both of the semi-implicit schemes, the fluid part of the projection step has been rewritten as a Poisson problem for the pressure (see [GQ98a, ACF09] for more details). For the sake of conciseness, in the following, we address the previous schemes respectively as: non-incremental semi-implicit scheme, fully implicit scheme and incremental semi-implicit scheme.

The errors, between the numerical solutions and the exact one, are computed with respect to the norms $l^\infty(t_0, T, L^2(\Omega^{\mathrm{f}}))$, for $\mathbf{u}$ and p, $l^\infty(t_0, T, L^2(\Omega^{\mathrm{s}}))$, for the structure velocity $\mathbf{u}^{\mathrm{s}} \overset{\text{def}}{=} \partial_t \boldsymbol{d}$, and $l^\infty(t_0, T, H^1(\Omega^{\mathrm{s}}))$, for $\boldsymbol{d}$, with $t_0 = 0.5$ and $T = 1$. They are presented in Figure 3.3 and reported in logarithmic scale as a function of τ: in red for the non-incremental semi-implicit algorithm, in green for the incremental one and in blue for the fully implicit scheme.

Non-incremental semi-implicit scheme *versus* fully implicit scheme. Let us first consider the time discretization error of the two algorithms. From Figure 3.3, it can be easily observed that for a given time-step the discretization error is smaller in the fully implicit scheme than in the non-incremental semi-implicit scheme. As we will see later, this difference is mainly due to the use of the non-incremental Chorin-Temam scheme in the fluid problem.

For the convergence in time, as expected, the fully implicit scheme is first order accurate in time for velocity, pressure and displacement. Instead, for the semi-implicit one, we observe a lower convergence rate if compared to the implicit scheme. We can therefore confirm also from a numerical point of view that the scheme (3.12)-(3.14) has a convergence rate globally lower than one. In detail, it is important to note that a small reduction of convergence is experienced for the fluid pressure and for the structure unknowns, but not for the fluid velocity. The latter is indeed still linear in time. Therefore, at least in this test case, it seems that the velocity error with respect to the norm $l^\infty(t_0, T, L^2(\Omega^{\mathrm{f}}))$ isn't affected by a reduced convergence rate.

Remark 3.10 *It is worth noticing that the test case proposed is only one of the many different analyzed and in none of them we have observed a reduction in the velocity accuracy in the* $l^\infty(t_0, T, L^2(\Omega^{\mathrm{f}}))$ *norm.*

The convergence in time of the velocity unknowns therefore remains an open problem for the semi-implicit scheme. Possible improvements can be done either in the choice of the test case, or in a *non trivial* improvement of our theoretical result, that aims at decoupling the analysis of the velocity error from the one of the pressure and displacement errors, in order to retrieve its linear convergence rate.

Non-incremental semi-implicit scheme *versus* incremental semi-implicit scheme. Here the convergence in time of the semi-implicit scheme is investigated by comparing the non-incremental version of the semi-implicit scheme with the incremental one. It is well-known that, for pure Stokes and Navier-Stokes problems, the incremental version of the Chorin-Temam scheme has better accuracy properties than the original one (see for example [EG04, GMS06, GQ98a, GQ98b] and references therein). A linear convergence in time is retrieved for velocities and pressure (for a proof we refer to [GQ98a, She92]):

$$\begin{aligned} ||\mathbf{u}(t^n) - \mathbf{u}_h^n||_{l^\infty(L^2(\Omega^f))} + ||\mathbf{u}(t^n) - \widetilde{\mathbf{u}}_h^n||_{l^\infty(L^2(\Omega^f))} &\leq c(h^{k+1} + \tau), \\ ||\mathbf{u}(t^n) - \widetilde{\mathbf{u}}_h^n||_{l^\infty(H^1(\Omega^f))} + ||p(t^n) - p_h^n||_{l^\infty(L^2(\Omega^f))} &\leq c(h^k + \tau). \end{aligned}$$

A direct comparison between the numerical results of the two schemes, Figure 3.3, clearly shows that the choice of the fractional step method for the fluid problem changes the accuracy in time of the whole fluid-structure interaction procedure. In detail, the non-incremental Chorin-Temam method induces a numerical dissipation on the coupled problem and modifies the convergence in time of the structure problem. With the incremental semi-implicit scheme a linear convergence rate in the fluid-structure problem seems to be retrieved.

Incremental semi-implicit scheme *versus* fully implicit scheme. Through this last comparison we stress once more the efficiency of the semi-implicit algorithm proposed in [FGG07] and, in particular here, of its incremental version. Indeed, the latter is computationally cheaper than the fully implicit algorithm but it guarantees the same convergence order and similar discretization errors in time (see Figure 3.3). Finally we note that the semi-implicit coupling does not seem to affect the convergence of the incremental scheme. A deeper investigation of this last point will be addressed in future works both from a theoretical and numerical point of view.

Before concluding, some more remarks are in order:

- The choice of the test case and of the physical and numerical parameters has been accurately set in order to satisfy the stability condition (3.20) and to stress the effects of a convergence rate lower than one in the non-incremental semi-implicit scheme. As a matter of fact, depending on the exact solution considered or on the parameters chosen, a linear convergence rate could be observed for some of (or even all) the unknowns.

- Numerically, the convergence rates of the fluid velocity and of the structure unknowns seem to be slightly better than the ones theoretically predicted in

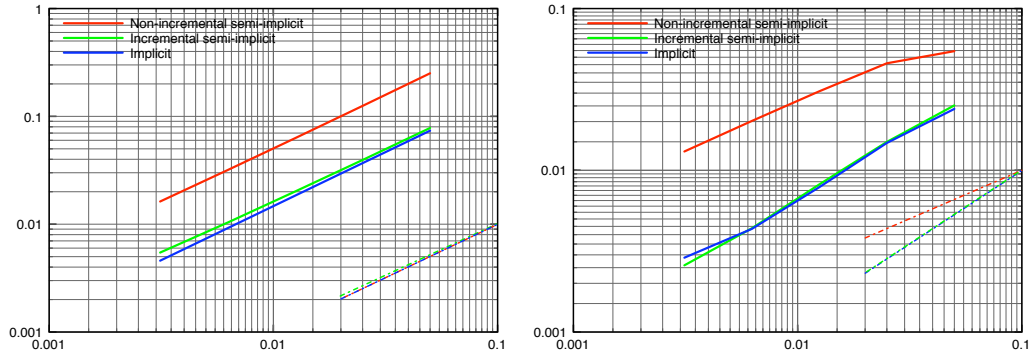

(a) $\max_{t_0 \le t \le T} \|\mathbf{u}_{\text{ex}} - \mathbf{u}_h\|_0$

(b) $\max_{t_0 \le t \le T} \|p_{\text{ex}} - p_h\|_0$

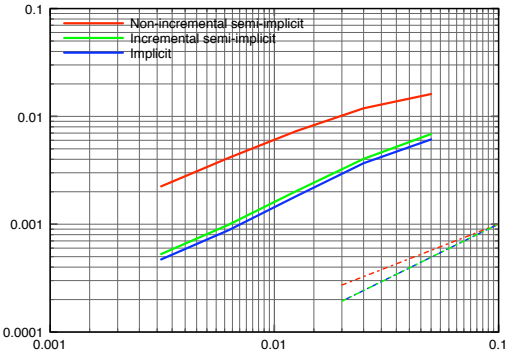

(c) $\max_{t_0 \le t \le T} \|\boldsymbol{d}_{\text{ex}} - \boldsymbol{d}_H\|_1$

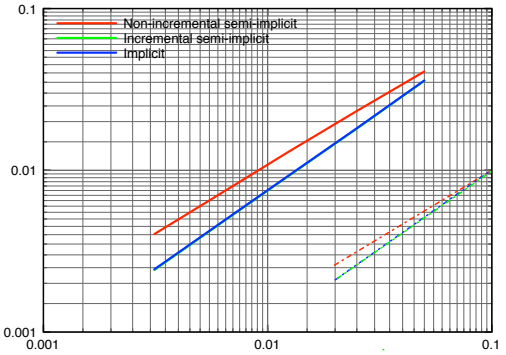

(d) $\max_{t_0 \le t \le T} \|\mathbf{u}^{\text{s}}_{\text{ex}} - \mathbf{u}^{\text{s}}_H\|_0$

Figure 3.3: Convergence of the different FSI algorithms to the exact solution, for velocities, pressure and displacement. In red the non-incremental version of the semi-implicit scheme, in green the incremental one, while in blue the fully implicit scheme. Dashed lines are used to compare the slopes of the represented curves.

(3.41). A similar discrepancy between theoretical and numerical results can be observed, in a pure fluid problem, for the estimate $(3.1)_2$ (see [Hor97, GMS06]).

3.7 Conclusion

In this chapter we have analyzed from a theoretical and numerical viewpoint the semi-implicit scheme presented in [FGG07]. The convergence of the scheme has been proved using a non-conforming space discretization of the two domains. The Leap-Frog scheme is used for the discretization in time of the structure problem. The cases of a pointwise and a mortar matching operator have been considered.

We proved that the projection semi-implicit coupling scheme proposed in [FGG07] is at least $\sqrt{\tau}$ accurate in time. We supported the theoretical result with a numerical test where a small reduction of the convergence rate for pressure and displacement is observed. However, the effects of the coupling scheme on the fluid velocity remain an open question since no accuracy reduction has been experienced. Finally the use of the incremental version of the Chorin-Temam method in the fluid-structure interaction scheme actually improves the global accuracy and a linear convergence rate in time is retrieved for all the unknowns.

Chapter 4

A Robin based semi-implicit coupling in fluid-structure interaction

M. Astorino, F. Chouly and M.A. Fernández. *An added-mass free semi-implicit coupling scheme for fluid-structure interaction.* C. R. Math. Acad. Sci. Paris, Vol. 347, Num. 1-2, 2009, pp. 99-104.

M. Astorino, F. Chouly and M.A. Fernández. *Robin based semi-implicit coupling in fluid-structure interaction: stability analysis and numerics.* SIAM J. Sci. Comput., Vol. 31, Num. 6, pp. 4041-4065, 2009.

Contents

4.1 Introduction

In the previous chapter, the convergence properties of the semi-implicit coupling method reported in [FGG06, FGG07] have been analyzed. For this scheme we know that computational cost and numerical stability are balanced by performing an explicit-implicit splitting, based on the use of the Chorin-Temam's projection scheme within the fluid [Cho69, Tem68, GMS06]. At each time-step, the projection sub-step is implicitly coupled with the structure, whereas the viscous sub-step, taking into account the convective-viscous effects and the geometrical non-linearities, is treated explicitly.

Although the theoretical and numerical results, reported in [FGG07], showed that the resulting algorithm drastically improves the stability properties of conventional explicit coupling and the efficiency of implicit coupling, the original semi-implicit coupling scheme has two limitations. On the one hand, though much less sensitive to the added-mass effect than the standard explicit coupling, numerical evidence (see Section 4.5) shows that the stability still depends on the fluid-solid density ratio. As a matter of fact, in the linear case, stability is obtained (see Theorem 3.1) under a condition of the type:

$$\rho^{\mathrm{s}}/\rho^{\mathrm{f}} \geq C\left[1+\mu\tau/(\rho^{\mathrm{f}}h^2)\right]. \tag{4.1}$$

On the other hand, from the theoretical point of view, a dissipative time-discretization is required within the structure in order to prove stability (see Remark 3.1).

In the present chapter, we propose a semi-implicit coupling scheme that circumvents the above mentioned inconveniences. The stability properties of the new scheme are independent of the added-mass effect and allow for conservative time-stepping within the structure. The key idea consists of treating the explicit part of the coupling in a weak sense, by using a specific Robin coupling derived from Nitsche's interface method (see *e.g.* [BHS03, HHS04, BF07, BF09]).

The remainder of the chapter is organized as follows. In Section 4.2, we briefly recall the preliminary notions associated with the problem under analysis. For some of them we will refer to the previous chapters. The proposed Robin based semi-implicit coupling is detailed in Section 4.3. Section 4.4 is devoted to the stability analysis. We show that the linearized version of the algorithm is stable (in the energy norm) irrespectively of the added-mass effect and of the numerical dissipation within the structure. Numerical experiments, in two and three space dimensions, are carried out in Section 4.5, illustrating the theoretical results. Finally, some concluding remarks are given in Section 4.6.

4.2 Preliminaries

The coupled FSI problem. The problem we analyze models the mechanical interaction between a viscous incompressible fluid and an elastic structure. The fluid and the solid are respectively described by Navier-Stokes problem (in its ALE formulation) and by the three-dimensional elastodynamics equations (in the Lagrangian formulation). The resulting non-linear coupled problem is defined by the set of equations (2.33)-(2.35). For this problem, the following boundary conditions for the fluid and the structure are assumed in this chapter:

$$\begin{cases} \boldsymbol{\sigma}^{\mathrm{f}}(\mathbf{u},p)\mathbf{n}^{\mathrm{f}} = -\bar{p}\mathbf{n}^{\mathrm{f}} & \text{on} \quad \Gamma^{\mathrm{in-out}} = \partial\Omega^{\mathrm{f}}\backslash\Sigma, \\ \boldsymbol{d} = \mathbf{0} & \text{on} \quad \Gamma^{\mathrm{s}}_D, \\ \boldsymbol{\Pi}(\boldsymbol{d})\mathbf{n}^{\mathrm{s}} = \mathbf{0} & \text{on} \quad \Gamma^{\mathrm{s}}_N. \end{cases}$$

Time semi-discretization. We now propose to semi-discretize in time the nonlinear coupled problem (2.33)-(2.35) using the framework of the semi-implicit coupling scheme introduced in [FGG06, FGG07]. The scheme has been already given in Algorithm 2.2, p. 52, in its pressure-correction formulation. Nonetheless, since in the sequel the velocity-correction version of the scheme will be mainly used, here we recall the algorithm in its (non-incremental) velocity-correction version (see *e.g.* [GMS06, Section 4.1]). For the sake of completeness, other variants will also be discussed in Section 4.3.3.

Algorithm 4.1 *Semi-implicit coupling scheme based on the projection Chorin-Temam method in its velocity-correction formulation.*

Step 1 : `(update fluid domain)`

$$\begin{aligned} &\boldsymbol{d}^{\mathrm{f},n+1} = \mathrm{Ext}(\boldsymbol{d}^n|_\Sigma), \quad \mathbf{w}^{n+1} = D_\tau \boldsymbol{d}^{\mathrm{f},n+1} \quad \texttt{in} \quad \Omega^{\mathrm{f}}, \\ &\Omega^{\mathrm{f},n+1} = (\mathbf{I}_{\Omega^{\mathrm{f}}} + \boldsymbol{d}^{\mathrm{f},n+1})(\Omega^{\mathrm{f}}). \end{aligned} \tag{4.2}$$

Step 2 : `(implicit pressure-structure coupling)`

– **Step 2.1** : `(fluid projection sub-step)`

$$\begin{cases} \dfrac{\rho^{\mathrm{f}}}{\tau}\left(\mathbf{u}^{n+1} - \tilde{\mathbf{u}}^n\right) + \nabla p^{n+1} = 0 & \texttt{in} \quad \Omega^{\mathrm{f},n}, \\ \nabla \cdot \mathbf{u}^{n+1} = 0 & \texttt{in} \quad \Omega^{\mathrm{f},n}, \\ p^{n+1} = \bar{p} & \texttt{on} \quad \Gamma^{\mathrm{in-out}}, \\ \mathbf{u}^{n+1} \cdot \mathbf{n}^{\mathrm{f}} = D_\tau \boldsymbol{d}^{n+1} \cdot \mathbf{n}^{\mathrm{f}} & \texttt{on} \quad \Sigma^n. \end{cases} \tag{4.3}$$

– **Step 2.2** : `(solid sub-step)`

$$\begin{cases} \rho^{\mathrm{s}} D_\tau \dot{\boldsymbol{d}}^{n+1} - \nabla \cdot \boldsymbol{\Pi}(\boldsymbol{d}^{n+\frac{1}{2}}) = \mathbf{0} & \texttt{in} \quad \Omega^{\mathrm{s}}, \\ D_\tau \boldsymbol{d}^{n+1} = \dot{\boldsymbol{d}}^{n+\frac{1}{2}} & \texttt{in} \quad \Omega^{\mathrm{s}}, \\ \boldsymbol{d}^{n+1} = \mathbf{0} & \texttt{on} \quad \Gamma^{\mathrm{s}}_D, \\ \boldsymbol{\Pi}(\boldsymbol{d}^{n+\frac{1}{2}})\mathbf{n}^{\mathrm{s}} = \mathbf{0} & \texttt{on} \quad \Gamma^{\mathrm{s}}_N, \\ \boldsymbol{\Pi}(\boldsymbol{d}^{n+\frac{1}{2}})\mathbf{n}^{\mathrm{s}} = -J^{\mathrm{f},n+1}\boldsymbol{\sigma}^{\mathrm{f}}(\tilde{\mathbf{u}}^n, p^{n+1})(\boldsymbol{F}^{\mathrm{f},n+1})^{-\mathrm{T}}\mathbf{n}^{\mathrm{f}} & \texttt{on} \quad \Sigma. \end{cases} \tag{4.4}$$

Step 3 : `(explicit viscous-structure coupling)`

$$\begin{cases} \rho^{\mathrm{f}} \dfrac{\tilde{\mathbf{u}}^{n+1} - \mathbf{u}^n}{\tau}\Big|_{\mathcal{A}} + \rho^{\mathrm{f}}(\mathbf{u}^{n+1} - \mathbf{w}^{n+1}) \cdot \nabla \tilde{\mathbf{u}}^{n+1} - 2\mu \nabla \cdot \boldsymbol{\varepsilon}(\tilde{\mathbf{u}}^{n+1}) = \mathbf{0} & \texttt{in} \quad \Omega^{\mathrm{f},n+1}, \\ 2\mu\boldsymbol{\varepsilon}(\tilde{\mathbf{u}}^{n+1})\mathbf{n}^{\mathrm{f}} = \mathbf{0} & \texttt{on} \quad \Gamma^{\mathrm{in-out}}, \\ \tilde{\mathbf{u}}^{n+1} = D_\tau \boldsymbol{d}^{n+1} & \texttt{on} \quad \Sigma^{n+1}. \end{cases} \tag{4.5}$$

4.3 Robin based semi-implicit coupling

The main contribution of this chapter concerns the discretization in space of (4.3)-(4.5), more precisely, how condition $(4.5)_3$ is enforced at the discrete level. In [FGG07] this condition is treated in a strong fashion. In order to enhance stability, here we consider a different point of view. We propose to treat weakly the explicit *viscous coupling* (4.4)-(4.5), using a Robin-Robin coupling derived from Nitsche's penalty method (see Section 2.5.1 and [Nit71, BHS03, BF07]).

4.3.1 The coupling scheme

In what follows, we consider as usual the functional spaces introduced in Section 2.4.2, and the corresponding finite element spaces. Nonetheless, with abuse of notation, we suppose that Q_h^{f} (resp. $Q_{\Gamma,h}^{\mathrm{f}}$) is an internal continuous Lagrange finite element approximation of $H^1(\Omega^{\mathrm{f}})$ (resp. $H^1_{\Gamma^{\mathrm{in-out}}}(\Omega^{\mathrm{f}})$) and that $X_{h,0}^{\mathrm{f}}$ is an internal continuous Lagrange finite element approximation of $[H^1_{\Sigma}(\Omega^{\mathrm{f}})]^d$. We assume all these spaces properly defined in the ALE framework. In view of the stability analysis of the scheme, we shall introduce also the following standard discrete trace-inverse inequality (see *e.g.* [Tho06]):

$$||\boldsymbol{v}_h^{\mathrm{f}}||^2_{0,\partial K} \leq C_{\mathrm{ti}} h^{-1} ||\boldsymbol{v}_h^{\mathrm{f}}||^2_{0,K} \quad \forall \boldsymbol{v}_h^{\mathrm{f}} \in X_h^{\mathrm{f}} \tag{4.6}$$

for all $K \in \mathcal{T}_h^{\mathrm{f}}$, and with $C_{\mathrm{ti}} > 0$ a constant independent of the discretization parameter h (but that might depend on the polynomial order). Since the fluid and solid space discretizations do not necessarily match at the interface Σ, we consider an interface matching operator $\pi_h : V_H^{\mathrm{s}}(\Sigma) \to X_h^{\mathrm{f}}(\Sigma)$, where $V_H^{\mathrm{s}}(\Sigma)$ (resp. $X_h^{\mathrm{f}}(\Sigma)$) stands for the trace finite element space associated with V_H^{s} (resp. X_h^{f}). As already presented in Chapter 3, the operator π_h can be, for instance, the standard Lagrange interpolant (nodal-wise matching) or a projection based operator (see also [FLLT98, GM98]).

Starting from (4.2)-(4.5), our Robin based fully-discrete semi-implicit coupling scheme reads as follows:

Algorithm 4.2 *Robin based semi-implicit coupling scheme (pressure-Darcy formulation).*

Step 1 : `(update fluid domain)`

$$\begin{aligned} &\boldsymbol{d}_h^{\mathrm{f},n+1} = \mathrm{Ext}_h(\boldsymbol{d}_H^n|_{\Sigma}), \quad \mathbf{w}_h^{n+1} = D_\tau \boldsymbol{d}_h^{\mathrm{f},n+1} \quad \texttt{in} \quad \Omega^{\mathrm{f}}, \\ &\Omega^{\mathrm{f},n+1} = (\mathbf{I}_{\Omega^{\mathrm{f}}} + \boldsymbol{d}_h^{\mathrm{f},n+1})(\Omega^{\mathrm{f}}). \end{aligned} \tag{4.7}$$

Step 2 : `(implicit pressure-structure coupling)`

– **Step 2.1** : `(fluid projection sub-step)`

Find $(\mathbf{u}_h^{n+1}, p_h^{n+1}) \in X_h^{\mathrm{f}} \times Q_h^{\mathrm{f}}$ such that

$$\begin{cases} \dfrac{\rho^{\mathrm{f}}}{\tau}\left(\mathbf{u}_h^{n+1} - \widetilde{\mathbf{u}}_h^{n}, \boldsymbol{v}_h^{\mathrm{f}}\right)_{\Omega^{\mathrm{f},n}} - \left(p_h^{n+1}, \nabla\cdot \boldsymbol{v}_h^{\mathrm{f}}\right)_{\Omega^{\mathrm{f},n}} + \left(\nabla\cdot \mathbf{u}_h^{n+1}, q_h\right)_{\Omega^{\mathrm{f},n}} \\ \qquad\qquad = -\left(\bar{p}\mathbf{n}^{\mathrm{f}}, \boldsymbol{v}_h^{\mathrm{f}}\right)_{\Gamma^{\mathrm{in-out}}}, \\ \mathbf{u}_h^{n+1} = \pi_h(D_\tau \boldsymbol{d}_H^{n+1}) \quad \text{on} \quad \Sigma^n \end{cases} \tag{4.8}$$

for all $(\boldsymbol{v}_h^{\mathrm{f}}, q_h) \in X_{h,0}^{\mathrm{f}} \times Q_h^{\mathrm{f}}$.

– **Step 2.2** : (solid sub-step)

Find $(\boldsymbol{d}_H^{n+1}, \dot{\boldsymbol{d}}_H^{n+1}) \in [V_H^{\mathrm{s}}]^2$ such that

$$A_{\tau,H}^{\mathrm{s}}\left(\boldsymbol{d}_H^{n+1}, \dot{\boldsymbol{d}}_H^{n+1}; \boldsymbol{v}_H^{\mathrm{s}}, \dot{\boldsymbol{v}}_H^{\mathrm{s}}\right) + \frac{\gamma\mu}{h}(D_\tau \boldsymbol{d}_H^{n+1}, \boldsymbol{v}_H^{\mathrm{s}})_{\Sigma^{n+1}} = \frac{\gamma\mu}{h}(\widetilde{\mathbf{u}}_h^{n}, \boldsymbol{v}_H^{\mathrm{s}})_{\Sigma^{n+1}} - (2\mu\boldsymbol{\varepsilon}(\widetilde{\mathbf{u}}_h^{n})\mathbf{n}^{\mathrm{f}}, \boldsymbol{v}_H^{\mathrm{s}})_{\Sigma^{n+1}} + \left(p_h^{n+1}\mathbf{n}^{\mathrm{f}}, \boldsymbol{v}_H^{\mathrm{s}}\right)_{\Sigma^{n+1}} \tag{4.9}$$

for all $\boldsymbol{v}_H^{\mathrm{s}}, \dot{\boldsymbol{v}}_H^{\mathrm{s}} \in V_H^{\mathrm{s}}$.

Step 3 : (explicit viscous-structure coupling)

Find $\widetilde{\mathbf{u}}_h^{n+1} \in X_h^{\mathrm{f}}$ such that

$$\widetilde{A}_{\tau,h}^{\mathrm{f}}(\widetilde{\mathbf{u}}_h^{n+1}, \widetilde{\boldsymbol{v}}_h^{\mathrm{f}}) + \frac{\gamma\mu}{h}(\widetilde{\mathbf{u}}_h^{n+1}, \widetilde{\boldsymbol{v}}_h^{\mathrm{f}})_{\Sigma^{n+1}} = \frac{\gamma\mu}{h}(D_\tau \boldsymbol{d}_H^{n+1}, \widetilde{\boldsymbol{v}}_h^{\mathrm{f}})_{\Sigma^{n+1}} + \left(2\mu\boldsymbol{\varepsilon}(\widetilde{\mathbf{u}}_h^{n})\mathbf{n}^{\mathrm{f}}, \widetilde{\boldsymbol{v}}_h^{\mathrm{f}}\right)_{\Sigma^{n+1}} \tag{4.10}$$

for all $\widetilde{\boldsymbol{v}}_h^{\mathrm{f}} \in X_h^{\mathrm{f}}$.

In the previous algorithm, Ext_h stands for a discrete counterpart of Ext. The solid mass and stiffness contribution, $A_{\tau,H}^{\mathrm{s}}\left(\boldsymbol{d}_H^{n+1}, \dot{\boldsymbol{d}}_H^{n+1}; \boldsymbol{v}_H^{\mathrm{s}}, \dot{\boldsymbol{v}}_H^{\mathrm{s}}\right)$, is given by

$$A_{\tau,H}^{\mathrm{s}}\left(\boldsymbol{d}_H^{n+1}, \dot{\boldsymbol{d}}_H^{n+1}; \boldsymbol{v}_H^{\mathrm{s}}, \dot{\boldsymbol{v}}_H^{\mathrm{s}}\right) \overset{\mathrm{def}}{=} \rho^{s}\left(D_\tau \dot{\boldsymbol{d}}_H^{n+1}, \boldsymbol{v}_H^{\mathrm{s}}\right)_{\Omega^{\mathrm{s}}} + \left(\boldsymbol{\Pi}(\boldsymbol{d}_H^{n+\frac{1}{2}}), \nabla \boldsymbol{v}_H^{\mathrm{s}}\right)_{\Omega^{\mathrm{s}}} + \rho^{\mathrm{s}}\left(\dot{\boldsymbol{d}}_H^{n+\frac{1}{2}} - D_\tau \boldsymbol{d}_H^{n+1}, \dot{\boldsymbol{v}}_H^{\mathrm{s}}\right)_{\Omega^{\mathrm{s}}},$$

while, for the fluid, $\widetilde{A}_{\tau,h}^{\mathrm{f}}(\widetilde{\mathbf{u}}_h^{n+1}, \widetilde{\boldsymbol{v}}_h^{\mathrm{f}})$ is defined as

$$\begin{aligned} \widetilde{A}_{\tau,h}^{\mathrm{f}}(\widetilde{\mathbf{u}}_h^{n+1}, \widetilde{\boldsymbol{v}}_h^{\mathrm{f}}) \overset{\mathrm{def}}{=} & \frac{\rho^{\mathrm{f}}}{\tau}\left(\widetilde{\mathbf{u}}_h^{n+1}, \widetilde{\boldsymbol{v}}_h^{\mathrm{f}}\right)_{\Omega^{\mathrm{f},n+1}} - \frac{\rho^{\mathrm{f}}}{\tau}\left(\mathbf{u}_h^{n+1}, \widetilde{\boldsymbol{v}}_h^{\mathrm{f}}\right)_{\Omega^{\mathrm{f},n}} + \frac{\rho^{\mathrm{f}}}{2}\left((\nabla\cdot\widetilde{\mathbf{u}}_h^{n})\widetilde{\mathbf{u}}_h^{n+1}, \widetilde{\boldsymbol{v}}_h^{\mathrm{f}}\right)_{\Omega^{\mathrm{f},n+1}} \\ & - \rho^{\mathrm{f}}\left((\nabla\cdot\mathbf{w}_h^{n+1})\widetilde{\mathbf{u}}_h^{n+1}, \widetilde{\boldsymbol{v}}_h^{\mathrm{f}}\right)_{\Omega^{\mathrm{f},n+1}} + \rho^{\mathrm{f}}\left((\widetilde{\mathbf{u}}_h^{n} - \mathbf{w}_h^{n+1})\cdot\nabla\widetilde{\mathbf{u}}_h^{n+1}, \widetilde{\boldsymbol{v}}_h^{\mathrm{f}}\right)_{\Omega^{\mathrm{f},n+1}} \\ & + \left(2\mu\boldsymbol{\varepsilon}(\widetilde{\mathbf{u}}_h^{n+1}), \boldsymbol{\varepsilon}(\widetilde{\boldsymbol{v}}_h^{\mathrm{f}})\right)_{\Omega^{\mathrm{f},n+1}}. \end{aligned} \tag{4.11}$$

Finally, $\gamma > 0$ is a dimensionless parameter. Some remarks are now in order.

Remark 4.1 *In Algorithm 4.2, the kinematic condition* $(4.3)_4$ *is strongly imposed (as in [FGG07]). However, now the coupling between the solid* (4.4) *and viscous* (4.5) *sub-steps is weakly enforced.*

Remark 4.2 *Note that, in (4.8), we impose* $\mathbf{u}_h^{n+1} = \pi_h(D_\tau \boldsymbol{d}_H^{n+1})$ *on* Σ^n *(instead of* $(4.3)_4$*) which is also optimal in the framework of finite element approximations (see [Gue96]).*

The interface weak coupling between steps (4.9) and (4.10) differs from the commonly used Nitsche's interface formulations (see *e.g.* [BHS03, HHS04, BF09, ACF09]). In particular, the interface mortaring in (4.10) does not contain the classical Nitsche's symmetrizing term

$$-\big(\widetilde{\mathbf{u}}_h^{n+1} - D_\tau \boldsymbol{d}_H^{n+1}, 2\mu\boldsymbol{\varepsilon}(\widetilde{\boldsymbol{v}}_h^{\mathrm{f}})\mathbf{n}^{\mathrm{f}}\big)_{\Sigma^{n+1}}.$$

Note that this simplification does not compromise symmetry, since (as in [BF09, ACF09]) the Nitsche's consistency term

$$-\big(2\mu\boldsymbol{\varepsilon}(\widetilde{\mathbf{u}}_h^{n})\mathbf{n}^{\mathrm{f}}, \widetilde{\boldsymbol{v}}_h^{\mathrm{f}} - \boldsymbol{v}_H^{\mathrm{s}}\big)_{\Sigma^{n+1}},$$

is evaluated at the previous time-step.

A major consequence of the previous observation is that the space continuous counterpart of the coupling between sub-steps (4.9) and (4.10) can be formally written as

$$\left.\begin{aligned} \frac{\gamma\mu}{h} D_\tau \boldsymbol{d}^{n+1} + \boldsymbol{\sigma}^{\mathrm{s}}(\boldsymbol{d}^{n+\frac{1}{2}})\mathbf{n}^{\mathrm{s}} &= \frac{\gamma\mu}{h}\tilde{\mathbf{u}}^{n} - 2\mu\boldsymbol{\varepsilon}(\tilde{\mathbf{u}}^{n})\mathbf{n}^{\mathrm{f}} + p^{n+1}\mathbf{n}^{\mathrm{f}} \\ \frac{\gamma\mu}{h}\tilde{\mathbf{u}}^{n+1} + 2\mu\boldsymbol{\varepsilon}(\tilde{\mathbf{u}}^{n+1})\mathbf{n}^{\mathrm{f}} &= \frac{\gamma\mu}{h} D_\tau \boldsymbol{d}^{n+1} + 2\mu\boldsymbol{\varepsilon}(\tilde{\mathbf{u}}^{n})\mathbf{n}^{\mathrm{f}} \end{aligned}\right\} \quad \text{on} \quad \Sigma^{n+1}, \tag{4.12}$$

which corresponds to an explicit Robin-Robin coupling between sub-steps (4.9) and (4.10). Note that the scaling $\gamma\mu/h$ of the Robin parameter, appearing in (4.12), coincides with the scaling of the original Nitsche's penalty method (see *e.g.* [Nit71, BHS03, BF07, BF09]), which is based on optimal convergence and energy arguments. However, it drastically differs from the heuristic Robin-Robin scaling proposed in [BNV08], based on simplified models and which aims at accelerating partitioned iterative solution methods within a fully implicit coupling framework.

4.3.2 Pressure load computation

In (4.9), the pressure contribution of the fluid load at the interface $\big(p_h^{n+1}\mathbf{n}^{\mathrm{f}}, \boldsymbol{v}_H^{\mathrm{s}}\big)_{\Sigma^{n+1}}$ is computed as a face-wise integral. This approach is referred in the numerical experiments as FWI (Face-Wise Integral). Nevertheless, the theoretical stability analysis (carried out in Section 4.4) calls for the standard residual based approximation of the pressure interface integral:

$$\begin{aligned} \big\langle \mathcal{R}(\mathbf{u}_h^{n+1}, \tilde{\mathbf{u}}_h^{n}, p_h^{n+1}), \mathcal{L}_h(\boldsymbol{v}_H^{\mathrm{s}})\big\rangle \overset{\text{def}}{=} & \frac{\rho^{\mathrm{f}}}{\tau}\big(\mathbf{u}_h^{n+1} - \tilde{\mathbf{u}}_h^{n}, \mathcal{L}_h(\boldsymbol{v}_H^{\mathrm{s}})\big)_{\Omega^{\mathrm{f},n+1}} \\ & - \big(p_h^{n+1}, \nabla\cdot(\mathcal{L}_h(\boldsymbol{v}_H^{\mathrm{s}}))\big)_{\Omega^{\mathrm{f},n+1}}, \end{aligned} \tag{4.13}$$

with $\mathcal{L}_h \overset{\text{def}}{=} \mathcal{L}_h^{\mathrm{f}} \circ \pi_h$ and $\mathcal{L}_h^{\mathrm{f}} : X_h^{\mathrm{f}}(\Sigma) \to X_h^{\mathrm{f}}$ is a given discrete fluid lifting operator such that

$$\mathcal{L}_h^{\mathrm{f}}(\boldsymbol{v}_h^{\mathrm{f}}) = \begin{cases} \boldsymbol{v}_h^{\mathrm{f}} & \text{on} \quad \Sigma, \\ \mathbf{0} & \text{on} \quad \Gamma^{\mathrm{in-out}}. \end{cases}$$

Moreover, for the stability analysis reported in Section 4.4.3, we shall assume that the following continuity estimate holds

$$\|\mathcal{L}_h^{\mathrm{f}}(\boldsymbol{v}_h^{\mathrm{f}})\|_{0,\Omega^{\mathrm{f}}}^2 \leq C_{\mathcal{L}} h \|\boldsymbol{v}_h^{\mathrm{f}}\|_{0,\Sigma}^2, \tag{4.14}$$

with $C_{\mathcal{L}} > 0$ a constant depending only on the fluid polynomial order and the mesh regularity. Let us emphasize that (4.14) holds for the discrete lifting operator commonly used in practice (see *e.g.* [FLLT98, FGG07]).

In the numerical experiments, the method resulting from replacing in (4.9) the interface integral $\left(p_h^{n+1}\mathbf{n}^{\mathrm{f}}, \boldsymbol{v}_H^{\mathrm{s}}\right)_{\Sigma^{n+1}}$ by $\left\langle \mathcal{R}(\mathbf{u}_h^{n+1}, \tilde{\mathbf{u}}_h^n, p_h^{n+1}), \mathcal{L}_h(\boldsymbol{v}_H^{\mathrm{s}}) \right\rangle$ will be indicated as VR (Variational-Residual).

4.3.3 Variants

We now discuss a couple of variants of the semi-implicit coupling scheme (4.7)-(4.10).

Pressure-Poisson formulation. As usual, instead of the pressure-Darcy formulation (4.8), the intermediate velocity $\mathbf{u}_h^{n+1}$ can be eliminated by rewriting the projection step as a pressure-Poisson equation (with a Neumann condition on the interface). Thus, (4.8) becomes

$$\begin{cases} \dfrac{\tau}{\rho^{\mathrm{f}}} \left(\nabla p_h^{n+1}, \nabla q_h\right)_{\Omega^{\mathrm{f},n}} = -\left(\nabla \cdot \widetilde{\mathbf{u}}_h^n, q_h\right)_{\Omega^{\mathrm{f},n}} - \left((\pi_h(D_\tau \boldsymbol{d}_H^{n+1}) - \widetilde{\mathbf{u}}_h^n) \cdot \mathbf{n}^{\mathrm{f}}, q_h \right)_{\Sigma^n}, \\ \qquad\qquad p_h^{n+1} = \bar{p} \quad \text{on} \quad \Gamma^{\mathrm{in-out}} \end{cases} \tag{4.15}$$

for all $q_h \in Q_{\Gamma,h}^{\mathrm{f}}$, and the intermediate velocity $\widetilde{\mathbf{u}}_h^n - \dfrac{\tau}{\rho^{\mathrm{f}}} \nabla p_h^{n+1}$ replaces $\mathbf{u}_h^{n+1}$ in (4.11).

Note that, due to the hybrid treatment of the kinematic conditions $(4.3)_4$ and $(4.5)_3$ (see Remark 4.1), the interface integral in $(4.15)_1$ couples two different kinds of interface mortaring: one based on the (solid-to-fluid) matching operator π_h and the other on the viscous Robin coupling. Thus, as suggested by the theoretical stability analysis carried out in Section 4.4.3, this hybrid mortaring requires a specific integration of the interface terms in (4.9) and (4.10). More precisely, (4.9) has to be replaced by

$$\begin{cases} A_{\tau,H}^{\mathrm{s}}\left(\boldsymbol{d}_H^{n+1}, \dot{\boldsymbol{d}}_H^{n+1}; \boldsymbol{v}_H^{\mathrm{s}}, \dot{\boldsymbol{v}}_H^{\mathrm{s}}\right) + \dfrac{\gamma\mu}{h}\left(\pi_h(D_\tau \boldsymbol{d}_H^{n+1}) - \widetilde{\mathbf{u}}_h^n, \pi_h(\boldsymbol{v}_H^{\mathrm{s}})\right)_{\Sigma^{n+1}} \\ \qquad\qquad = -\left(2\mu\boldsymbol{\varepsilon}(\widetilde{\mathbf{u}}_h^n)\mathbf{n}^{\mathrm{f}}, \pi_h(\boldsymbol{v}_H^{\mathrm{s}})\right)_{\Sigma^{n+1}} + \left(p_h^{n+1}\mathbf{n}^{\mathrm{f}}, \boldsymbol{v}_H^{\mathrm{s}}\right)_{\Sigma^{n+1}} \end{cases} \tag{4.16}$$

for all $\boldsymbol{v}_H^{\mathrm{s}}, \dot{\boldsymbol{v}}_H^{\mathrm{s}} \in V_H^{\mathrm{s}}$, and (4.10) by

$$\widetilde{A}_{\tau,h}^{\mathrm{f}}\left(\widetilde{\mathbf{u}}_h^{n+1}, \widetilde{\boldsymbol{v}}_h^{\mathrm{f}}\right) + \frac{\gamma\mu}{h}\left(\widetilde{\mathbf{u}}_h^{n+1} - \pi_h(D_\tau \boldsymbol{d}_H^{n+1}), \widetilde{\boldsymbol{v}}_h^{\mathrm{f}}\right)_{\Sigma^{n+1}} = \left(2\mu\boldsymbol{\varepsilon}(\widetilde{\mathbf{u}}_h^n)\mathbf{n}^{\mathrm{f}}, \widetilde{\boldsymbol{v}}_h^{\mathrm{f}}\right)_{\Sigma^{n+1}} \tag{4.17}$$

for all $\widetilde{\boldsymbol{v}}_h^{\mathrm{f}} \in X_h^{\mathrm{f}}$.

Note that the modifications (4.16) and (4.17) are only suggested when dealing with non-matching fluid-solid discretizations and when using the pressure-Poisson version of the Chorin-Temam scheme.

Remark 4.3 *In the pressure-Poisson version of Algorithm 4.2 combined with a VR based pressure load computation, the intermediate velocity* $\mathbf{u}_h^{n+1} \in X_h^{\mathrm{f}}$*, required by* (4.13)*, is the solution of*

$$\frac{\rho^f}{\tau}\big(\mathbf{u}_h^{n+1} - \tilde{\mathbf{u}}_h^n, \boldsymbol{v}_h^{\mathrm{f}}\big)_{\Omega^{\mathrm{f},n}} = -\big(\nabla p_h^{n+1}, \boldsymbol{v}_h^{\mathrm{f}}\big)_{\Omega^{\mathrm{f},n}},$$
$$\mathbf{u}_h^{n+1} = \pi_h(D_\tau \boldsymbol{d}_H^{n+1}) \quad on \quad \Sigma^n$$

for all $\boldsymbol{v}_h^{\mathrm{f}} \in X_{h,0}^{\mathrm{f}}$.

Pressure-correction formulation. In Algorithm 4.2 we have used the velocity-correction version of the Chorin-Temam projection scheme. However, as in [FGG07], we could also have considered the original (non-incremental) pressure-correction version (see *e.g.* [GMS06, Section 3.1]) by switching the explicit and implicit steps (see Remark 4.7): $\mathbf{u}_h^{n+1}$ has to be replaced by $\mathbf{u}_h^n$ in $\widetilde{A}_{\tau,h}^{\mathrm{f}}\big(\widetilde{\mathbf{u}}_h^{n+1}, \widetilde{\boldsymbol{v}}_h^{\mathrm{f}}\big)$, step (4.10) by

$$\widetilde{A}_{\tau,h}^{\mathrm{f}}\big(\widetilde{\mathbf{u}}_h^{n+1}, \widetilde{\boldsymbol{v}}_h^{\mathrm{f}}\big) + \frac{\gamma\mu}{h}\big(\widetilde{\mathbf{u}}_h^{n+1}, \widetilde{\boldsymbol{v}}_h^{\mathrm{f}}\big)_{\Sigma^{n+1}} = \frac{\gamma\mu}{h}\big(D_\tau \boldsymbol{d}_H^n, \widetilde{\boldsymbol{v}}_h^{\mathrm{f}}\big)_{\Sigma^{n+1}} + \big(2\mu\boldsymbol{\varepsilon}(\widetilde{\mathbf{u}}_h^n)\mathbf{n}^{\mathrm{f}}, \widetilde{\boldsymbol{v}}_h^{\mathrm{f}}\big)_{\Sigma^{n+1}} \tag{4.18}$$

for all $\widetilde{\boldsymbol{v}}_h^{\mathrm{f}} \in X_h^{\mathrm{f}}$, step (4.8) by

$$\begin{cases} \dfrac{\rho^{\mathrm{f}}}{\tau}\left(\mathbf{u}_h^{n+1} - \widetilde{\mathbf{u}}_h^{n+1}, \boldsymbol{v}_h^{\mathrm{f}}\right)_{\Omega^{\mathrm{f},n+1}} - \left(p_h^{n+1}, \nabla\cdot\boldsymbol{v}_h^{\mathrm{f}}\right)_{\Omega^{\mathrm{f},n+1}} + \left(\nabla\cdot\mathbf{u}_h^{n+1}, q_h\right)_{\Omega^{\mathrm{f},n+1}} \\ \qquad\qquad = -\left(\bar{p}\mathbf{n}^{\mathrm{f}}, \boldsymbol{v}_h^{\mathrm{f}}\right)_{\Gamma^{\mathrm{in-out}}}, \\ \mathbf{u}_h^{n+1} = \pi_h(D_\tau \boldsymbol{d}_H^{n+1}) \quad \text{on} \quad \Sigma^{n+1} \end{cases} \tag{4.19}$$

for all $(\boldsymbol{v}_h^{\mathrm{f}}, q_h) \in X_{h,0}^{\mathrm{f}} \times Q_h^{\mathrm{f}}$, and finally step (4.9) becomes

$$A_{\tau,H}^{\mathrm{s}}\big(\boldsymbol{d}_H^{n+1}, \dot{\boldsymbol{d}}_H^{n+1}; \boldsymbol{v}_H^{\mathrm{s}}, \dot{\boldsymbol{v}}_H^{\mathrm{s}}\big) + \frac{\gamma\mu}{h}(D_\tau \boldsymbol{d}_H^{n+1}, \boldsymbol{v}_H^{\mathrm{s}})_{\Sigma^{n+1}} = \frac{\gamma\mu}{h}(\widetilde{\mathbf{u}}_h^{n+1}, \boldsymbol{v}_H^{\mathrm{s}})_{\Sigma^{n+1}}$$
$$- (2\mu\boldsymbol{\varepsilon}(\widetilde{\mathbf{u}}_h^n)\mathbf{n}^{\mathrm{f}}, \boldsymbol{v}_H^{\mathrm{s}})_{\Sigma^{n+1}} + \big(p_h^{n+1}\mathbf{n}^{\mathrm{f}}, \boldsymbol{v}_H^{\mathrm{s}}\big)_{\Sigma^{n+1}} \tag{4.20}$$

for all $\boldsymbol{v}_H^{\mathrm{s}}, \dot{\boldsymbol{v}}_H^{\mathrm{s}} \in V_H^{\mathrm{s}}$.

Remark 4.4 *The extension of our approach to the semi-implicit coupling framework reported in [QQ07, BQQ08] is not straightforward. Note that our Robin based semi-implicit coupling fully exploits the splitting* (4.3)-(4.5) *induced by the Chorin-Temam scheme, which allows a hybrid treatment of the kinematic coupling conditions* $(4.3)_4$ *and* $(4.5)_3$*. However, in [QQ07, BQQ08] the splitting is performed directly on the fully discrete linearized system, by using appropriate inexact LU factorizations, with a predefined treatment of the kinematic coupling.*

4.4 Stability analysis

In this section, the stability analysis of our Robin based semi-implicit coupling is carried out on a linearized version of the FSI problem considered. Both the pressure-Darcy and pressure-Poisson formulations are analyzed.

4.4.1 A simplified model problem

As in Chapter 3, the fluid is described by the Stokes equations in a fixed domain $\Omega^{\mathrm{f}} \subset \mathbb{R}^d$, $d = 2, 3$. For the structure, we consider the classical linear elastodynamics equations, in the solid domain $\Omega^{\mathrm{s}} \subset \mathbb{R}^d$. We still denote by $\Sigma \overset{\text{def}}{=} \partial\Omega^{\mathrm{s}} \cap \partial\Omega^{\mathrm{f}}$ the fluid-structure interface. Then, our linearized fluid-structure problem reads as follows: Find the fluid velocity $\mathbf{u} : \Omega^{\mathrm{f}} \times \mathbb{R}^+ \to \mathbb{R}^d$, the fluid pressure $p : \Omega^{\mathrm{f}} \times \mathbb{R}^+ \to \mathbb{R}$ and the structure displacement $\boldsymbol{d} : \Omega^{\mathrm{s}} \times \mathbb{R}^+ \to \mathbb{R}^d$ such that:

$$
\begin{cases}
\rho^{\mathrm{f}} \partial_t \mathbf{u} - \nabla \cdot \boldsymbol{\sigma}^{\mathrm{f}}(\mathbf{u}, p) = \mathbf{0} & \text{in} \quad \Omega^{\mathrm{f}}, \\
\nabla \cdot \mathbf{u} = 0 & \text{in} \quad \Omega^{\mathrm{f}}, \\
\boldsymbol{\sigma}^{\mathrm{f}}(\mathbf{u}, p)\mathbf{n}^{\mathrm{f}} = -\bar{p}\mathbf{n}^{\mathrm{f}} & \text{on} \quad \Gamma^{\mathrm{in-out}}, \\
\rho^{\mathrm{s}} \partial_{tt} \boldsymbol{d} - \nabla \cdot \boldsymbol{\sigma}^{\mathrm{s}}(\boldsymbol{d}) = \mathbf{0} & \text{in} \quad \Omega^{\mathrm{s}}, \\
\boldsymbol{d} = \mathbf{0} & \text{on} \quad \Gamma^{\mathrm{s}}_D, \\
\boldsymbol{\sigma}^{\mathrm{s}}(\boldsymbol{d})\mathbf{n}^{\mathrm{s}} = \mathbf{0} & \text{on} \quad \Gamma^{\mathrm{s}}_N, \\
\mathbf{u} = \partial_t \boldsymbol{d} & \text{on} \quad \Sigma, \\
\boldsymbol{\sigma}^{\mathrm{s}}(\boldsymbol{d})\mathbf{n}^{\mathrm{s}} = -\boldsymbol{\sigma}^{\mathrm{f}}(\mathbf{u}, p)\mathbf{n}^{\mathrm{f}} & \text{on} \quad \Sigma.
\end{cases}
\tag{4.21}
$$

System (4.21), though simplified, contains the key features of more complex fluid-structure problems involving an incompressible fluid, with respect to the stability of the coupling schemes (see *e.g.* [CGN05, FGG07, BF09]).

4.4.2 Semi-implicit coupling with pressure-Darcy formulation

Algorithm 4.2 applied to the linearized problem (4.21) yields:

Algorithm 4.3 *Robin based semi-implicit coupling scheme (pressure-Darcy formulation) for the linearized problem.*

- `Implicit step (pressure-solid coupling):`
  `Find` $(\mathbf{u}_h^{n+1}, p_h^{n+1}, \boldsymbol{d}_H^{n+1}, \dot{\boldsymbol{d}}_H^{n+1}) \in X_h^{\mathrm{f}} \times Q_h^{\mathrm{f}} \times [V_H^{\mathrm{s}}]^2$ `such that`

$$
\begin{cases}
\dfrac{\rho^{\mathrm{f}}}{\tau}\left(\mathbf{u}_h^{n+1} - \tilde{\mathbf{u}}_h^n, \boldsymbol{v}_h^{\mathrm{f}}\right)_{\Omega^{\mathrm{f}}} - \left(p_h^{n+1}, \nabla \cdot \boldsymbol{v}_h^{\mathrm{f}}\right)_{\Omega^{\mathrm{f}}} + \left(q_h, \nabla \cdot \mathbf{u}_h^{n+1}\right)_{\Omega^{\mathrm{f}}} \\
\qquad = -\left(\bar{p}\boldsymbol{v}_h^{\mathrm{f}}, \mathbf{n}^{\mathrm{f}}\right)_{\Gamma^{\mathrm{in-out}}} \quad \forall (\boldsymbol{v}_h^{\mathrm{f}}, q_h) \in X_{0,h}^{\mathrm{f}} \times Q_h^{\mathrm{f}}, \\
\qquad \mathbf{u}_h^{n+1} = \pi_h(D_\tau \boldsymbol{d}_H^{n+1}) \quad \text{on} \quad \Sigma.
\end{cases}
\tag{4.22}
$$

$$
\begin{cases}
\dfrac{\rho^{\mathrm{s}}}{\tau}\left(\dot{\boldsymbol{d}}_H^{n+1} - \dot{\boldsymbol{d}}_H^n, \boldsymbol{v}_H^{\mathrm{s}}\right)_{\Omega^{\mathrm{s}}} + a^{\mathrm{s}}\left(\boldsymbol{d}_H^{n+\frac{1}{2}}, \boldsymbol{v}_H^{\mathrm{s}}\right) + \dfrac{\gamma\mu}{h}\left(D_\tau \boldsymbol{d}_H^{n+1} - \tilde{\mathbf{u}}_h^n, \boldsymbol{v}_H^{\mathrm{s}}\right)_\Sigma \\
= -2\mu\left(\boldsymbol{\varepsilon}(\tilde{\mathbf{u}}_h^n)\mathbf{n}^{\mathrm{f}}, \boldsymbol{v}_H^{\mathrm{s}}\right)_\Sigma - \left\langle \mathcal{R}(\mathbf{u}_h^{n+1}, \tilde{\mathbf{u}}_h^n, p_h^{n+1}), \mathcal{L}_h(\boldsymbol{v}_H^{\mathrm{s}}) \right\rangle, \quad \forall \boldsymbol{v}_H^{\mathrm{s}} \in V_H^{\mathrm{s}}, \\
\qquad D_\tau \boldsymbol{d}_H^{n+1} = \dot{\boldsymbol{d}}_H^{n+\frac{1}{2}}, \quad \text{in} \quad \Omega^{\mathrm{s}}.
\end{cases}
\tag{4.23}
$$

- `Explicit step (viscous-solid coupling):`
  `Find` $\tilde{\mathbf{u}}_h^{n+1} \in X_h^{\mathrm{f}}$ `such that`

$$\left\{ \begin{aligned} &\frac{\rho^{\mathrm{f}}}{\tau}\big(\tilde{\mathbf{u}}_h^{n+1} - \mathbf{u}_h^{n+1}, \tilde{\boldsymbol{v}}_h^{\mathrm{f}}\big)_{\Omega^{\mathrm{f}}} + 2\mu\big(\boldsymbol{\varepsilon}(\tilde{\mathbf{u}}_h^{n+1}), \boldsymbol{\varepsilon}(\tilde{\boldsymbol{v}}_h^{\mathrm{f}})\big)_{\Omega^{\mathrm{f}}} + \frac{\gamma\mu}{h}\big(\tilde{\mathbf{u}}_h^{n+1} - D_\tau \boldsymbol{d}_H^{n+1}, \tilde{\boldsymbol{v}}_h^{\mathrm{f}}\big)_{\Sigma} \\ &\qquad\qquad = 2\mu\big(\boldsymbol{\varepsilon}(\tilde{\mathbf{u}}_h^{n})\mathbf{n}^{\mathrm{f}}, \tilde{\boldsymbol{v}}_h^{\mathrm{f}}\big)_{\Sigma} \quad \forall \tilde{\boldsymbol{v}}_h^{\mathrm{f}} \in X_h^{\mathrm{f}}. \end{aligned} \right. \tag{4.24}$$

In (4.23), $a^{\mathrm{s}}(\cdot,\cdot)$ stands for the solid stiffness symmetric bilinear form. Note that we have considered a VR (Variational-Residual) based approximation of the pressure stresses at the interface, which in this case is given by:

$$\big\langle \mathcal{R}(\mathbf{u}_h^{n+1}, \tilde{\mathbf{u}}_h^{n}, p_h^{n+1}), \mathcal{L}_h(\boldsymbol{v}_H^{\mathrm{s}}) \big\rangle \overset{\text{def}}{=} \frac{\rho^{\mathrm{f}}}{\tau}\big(\mathbf{u}_h^{n+1} - \tilde{\mathbf{u}}_h^{n}, \mathcal{L}_h(\boldsymbol{v}_H^{\mathrm{s}})\big)_{\Omega^{\mathrm{f}}} - \big(p_h^{n+1}, \nabla\cdot(\mathcal{L}_h(\boldsymbol{v}_H^{\mathrm{s}}))\big)_{\Omega^{\mathrm{f}}}$$

for all $\boldsymbol{v}_H^{\mathrm{s}} \in V_H^{\mathrm{s}}$.

Energy based stability analysis. We now show that the semi-implicit scheme (4.22)-(4.24) is conditionally stable irrespectively of the added-mass effect.

Let us define the energy of the discrete coupled system, at time $t_n \overset{\text{def}}{=} n\tau$, as:

$$E^n = \frac{\rho^{\mathrm{f}}}{2}\|\tilde{\mathbf{u}}_h^n\|_{0,\Omega^{\mathrm{f}}}^2 + \frac{\rho^{\mathrm{s}}}{2}\|\dot{\boldsymbol{d}}_H^n\|_{0,\Omega^{\mathrm{s}}}^2 + \frac{1}{2}a^{\mathrm{s}}(\boldsymbol{d}_H^n, \boldsymbol{d}_H^n).$$

Theorem 4.1 *Assume that the system is isolated,* i.e. $\bar{p} = 0$ *on* $\Gamma^{\mathrm{in-out}}$*, and let* $\big\{(\tilde{\mathbf{u}}_h^n, \mathbf{u}_h^n, p_h^n, \boldsymbol{d}_H^n, \dot{\boldsymbol{d}}_H^n)\big\}_{n\geq 0}$ *be solution of* (4.22)-(4.24)*. Then, the following discrete energy estimate holds:*

$$E^n + \mu\tau\sum_{m=0}^{n-1}\|\boldsymbol{\varepsilon}(\tilde{\mathbf{u}}_h^{m+1})\|_{0,\Omega^{\mathrm{f}}}^2 + (\gamma - 2C_{\mathrm{ti}})\frac{\mu\tau}{2h}\sum_{m=0}^{n}\|\tilde{\mathbf{u}}_h^{m+1} - D_\tau \boldsymbol{d}_H^{m+1}\|_{0,\Sigma}^2 + \frac{\gamma\mu\tau}{2h}\|\tilde{\mathbf{u}}_h^n\|_{0,\Sigma}^2 \\ \leq E^0 + \mu\tau\|\boldsymbol{\varepsilon}(\tilde{\mathbf{u}}_h^0)\|_{0,\Omega^{\mathrm{f}}}^2 + \frac{\gamma\mu\tau}{2h}\|\tilde{\mathbf{u}}_h^0\|_{0,\Sigma}^2. \tag{4.25}$$

Therefore, the semi-implicit coupling scheme (4.22)-(4.24) *is stable, in the energy-norm, under the conditions:*

$$\gamma \geq 2C_{\mathrm{ti}}, \quad \gamma\mu\tau = \mathcal{O}(h). \tag{4.26}$$

Proof. We proceed by testing equations (4.22)-(4.24) with

$$\boldsymbol{v}_h^{\mathrm{f}} = \tau(\mathbf{u}_h^{n+1} - \mathcal{L}_h(D_\tau \boldsymbol{d}_H^{n+1})), \quad q_h = \tau p_h^{n+1}, \quad \boldsymbol{v}_H^{\mathrm{s}} = \tau D_\tau \boldsymbol{d}_H^{n+1}, \quad \tilde{\boldsymbol{v}}_h^{\mathrm{f}} = \tau\tilde{\mathbf{u}}_h^{n+1},$$

which are all admissible test functions. Therefore, using the identity $(a-b,a) = \frac{1}{2}\|a\|^2 - \frac{1}{2}\|b\|^2 + \frac{1}{2}\|a-b\|^2$, from (4.22) we get

$$\frac{\rho^{\mathrm{f}}}{2}\Big[\|\mathbf{u}_h^{n+1}\|_{0,\Omega^{\mathrm{f}}}^2 - \|\tilde{\mathbf{u}}_h^{n}\|_{0,\Omega^{\mathrm{f}}}^2\Big] - \tau\big\langle \mathcal{R}(\mathbf{u}_h^{n+1}, \tilde{\mathbf{u}}_h^{n}, p_h^{n+1}), \mathcal{L}_h(D_\tau \boldsymbol{d}_H^{n+1})\big\rangle \leq 0.$$

Similarly, from (4.23) we obtain

$$\frac{\rho^{\mathrm{s}}}{2}\left[\|\dot{\boldsymbol{d}}_H^{n+1}\|_{0,\Omega^{\mathrm{s}}}^2-\|\dot{\boldsymbol{d}}_H^{n}\|_{0,\Omega^{\mathrm{s}}}^2\right]+\frac{1}{2}\left[a^{\mathrm{s}}(\boldsymbol{d}_H^{n+1},\boldsymbol{d}_H^{n+1})-a^{\mathrm{s}}(\boldsymbol{d}_H^{n},\boldsymbol{d}_H^{n})\right]$$
$$+2\mu\tau\big(\boldsymbol{\varepsilon}(\tilde{\mathbf{u}}_h^n)\mathbf{n}^{\mathrm{f}},D_\tau\boldsymbol{d}_H^{n+1}\big)_\Sigma+\frac{\gamma\mu\tau}{h}\big(D_\tau\boldsymbol{d}_H^{n+1}-\tilde{\mathbf{u}}_h^n,D_\tau\boldsymbol{d}_H^{n+1}\big)_\Sigma$$
$$+\tau\left\langle\mathcal{R}(\mathbf{u}_h^{n+1},\tilde{\mathbf{u}}_h^n,p_h^{n+1}),\mathcal{L}_h(D_\tau\boldsymbol{d}_H^{n+1})\right\rangle=0,\quad(4.27)$$

and (4.24) yields

$$\frac{\rho^{\mathrm{f}}}{2}\left[\|\tilde{\mathbf{u}}_h^{n+1}\|_{0,\Omega^{\mathrm{f}}}^2-\|\mathbf{u}_h^{n+1}\|_{0,\Omega^{\mathrm{f}}}^2\right]+2\mu\tau\|\boldsymbol{\varepsilon}(\tilde{\mathbf{u}}_h^{n+1})\|_{0,\Omega^{\mathrm{f}}}^2-2\mu\tau\big(\boldsymbol{\varepsilon}(\tilde{\mathbf{u}}_h^n)\mathbf{n}^{\mathrm{f}},\tilde{\mathbf{u}}_h^{n+1}\big)_\Sigma$$
$$+\frac{\gamma\mu\tau}{h}\big(\tilde{\mathbf{u}}_h^{n+1}-D_\tau\boldsymbol{d}_H^{n+1},\tilde{\mathbf{u}}_h^{n+1}\big)_\Sigma\le 0.$$

By summation of these three inequalities, we obtain

$$E^{n+1}-E^n+2\mu\tau\|\boldsymbol{\varepsilon}(\tilde{\mathbf{u}}_h^{n+1})\|_{0,\Omega^{\mathrm{f}}}\underbrace{-2\mu\tau\big(\boldsymbol{\varepsilon}(\tilde{\mathbf{u}}_h^n)\mathbf{n}^{\mathrm{f}},\tilde{\mathbf{u}}_h^{n+1}-D_\tau\boldsymbol{d}_H^{n+1}\big)_\Sigma}_{\mathcal{T}_2}$$
$$+\underbrace{\frac{\gamma\mu\tau}{h}\Big[\big(D_\tau\boldsymbol{d}_H^{n+1}-\tilde{\mathbf{u}}_h^n,D_\tau\boldsymbol{d}_H^{n+1}\big)_\Sigma+\big(\tilde{\mathbf{u}}_h^{n+1}-D_\tau\boldsymbol{d}_H^{n+1},\tilde{\mathbf{u}}_h^{n+1}\big)_\Sigma\Big]}_{\mathcal{T}_1}\le 0.\quad(4.28)$$

We now estimate terms $\mathcal{T}_1$ and $\mathcal{T}_2$ separately.

We first consider term $\mathcal{T}_1$ by noting that

$$\mathcal{T}_1=\frac{\gamma\mu\tau}{h}\left[\|\tilde{\mathbf{u}}_h^{n+1}-D_\tau\boldsymbol{d}_H^{n+1}\|_{0,\Sigma}^2+\big(\tilde{\mathbf{u}}_h^{n+1}-\tilde{\mathbf{u}}_h^n,D_\tau\boldsymbol{d}_H^{n+1}\big)_\Sigma\right].\quad(4.29)$$

As in [BF09], the last term in (4.29) can be treated as follows

$$\begin{aligned}\big(\tilde{\mathbf{u}}_h^{n+1}-\tilde{\mathbf{u}}_h^n,D_\tau\boldsymbol{d}_H^{n+1}\big)_\Sigma=&\big(\tilde{\mathbf{u}}_h^{n+1}-\tilde{\mathbf{u}}_h^n,D_\tau\boldsymbol{d}_H^{n+1}-\tilde{\mathbf{u}}_h^{n+1}\big)_\Sigma+\big(\tilde{\mathbf{u}}_h^{n+1}-\tilde{\mathbf{u}}_h^n,\tilde{\mathbf{u}}_h^{n+1}\big)_\Sigma\\ \ge&-\frac{1}{2}\|\tilde{\mathbf{u}}_h^{n+1}-\tilde{\mathbf{u}}_h^n\|_{0,\Sigma}^2-\frac{1}{2}\|D_\tau\boldsymbol{d}_H^{n+1}-\tilde{\mathbf{u}}_h^{n+1}\|_{0,\Sigma}^2\\ &+\frac{1}{2}\|\tilde{\mathbf{u}}_h^{n+1}\|_{0,\Sigma}^2-\frac{1}{2}\|\tilde{\mathbf{u}}_h^{n}\|_{0,\Sigma}^2+\frac{1}{2}\|\tilde{\mathbf{u}}_h^{n+1}-\tilde{\mathbf{u}}_h^{n}\|_{0,\Sigma}^2\\ \ge&\frac{1}{2}\big(\|\tilde{\mathbf{u}}_h^{n+1}\|_{0,\Sigma}^2-\|\tilde{\mathbf{u}}_h^{n}\|_{0,\Sigma}^2-\|\tilde{\mathbf{u}}_h^{n+1}-D_\tau\boldsymbol{d}_H^{n+1}\|_{0,\Sigma}^2\big),\end{aligned}$$

which leads to the bound

$$\mathcal{T}_1\ge\frac{\gamma\mu\tau}{2h}\big[\|\tilde{\mathbf{u}}_h^{n+1}-D_\tau\boldsymbol{d}_H^{n+1}\|_{0,\Sigma}^2+\|\tilde{\mathbf{u}}_h^{n+1}\|_{0,\Sigma}^2-\|\tilde{\mathbf{u}}_h^{n}\|_{0,\Sigma}^2\big].\quad(4.30)$$

For term $\mathcal{T}_2$, by combining the Cauchy-Schwarz and Young inequalities with (4.6) we get

$$\mathcal{T}_2\ge-\mu\tau\|\boldsymbol{\varepsilon}(\tilde{\mathbf{u}}_h^n)\|_{0,\Omega^{\mathrm{f}}}^2-\frac{\mu\tau C_{\mathrm{ti}}}{h}\|\tilde{\mathbf{u}}_h^{n+1}-D_\tau\boldsymbol{d}_H^{n+1}\|_{0,\Sigma}^2.\quad(4.31)$$

Finally, we recover (4.25) by inserting (4.30) and (4.31) into (4.28), replacing n by m and summing over $m=0,\dots,n-1$. This completes the proof. ⋄

Remark 4.5 *Since the stability condition of Theorem 4.1 does not depend neither on the fluid-solid density ratio nor on the geometry of the domain, the semi-implicit coupling scheme (4.22)-(4.24) remains stable irrespectively of the added-mass effect. This was not the case of the original semi-implicit scheme reported in [FGG07] (see condition (4.1)). Moreover, because of the natural interface dissipation of the Robin coupling, diffusive time marching in the structure is no longer needed to prove stability. As a matter of fact, here we have considered a conservative scheme (see the energy equation (4.27)). We emphasize that this was not the case for the original semi-implicit scheme (see [FGG07, Remarks 3,4]).*

Remark 4.6 *The extra dissipative interface term $\gamma\mu\tau/(2h)\|\tilde{\mathbf{u}}_h^n\|_{0,\Sigma}^2$ in (4.25) and the CFL-like condition $\gamma\mu\tau = \mathcal{O}(h)$ arise also in the Nitsche based stabilized explicit coupling reported in [BF09]. On the contrary, here we do not need to stabilize pressure fluctuations, that is, to introduce a weakly consistent artificial compressibility at the interface. Indeed, due to the implicit treatment of the pressure-solid coupling, no artificial pressure power appears in the energy estimate (4.28).*

Remark 4.7 *One can prove a similar energy estimate for the non-incremental pressure-correction version of algorithm (4.22)-(4.24). Indeed, under the same assumptions as in Theorem 4.1, there holds*

$$E^n + \mu\tau \sum_{m=0}^{n-1} \|\boldsymbol{\varepsilon}(\tilde{\mathbf{u}}_h^{m+1})\|_{0,\Omega^{\mathrm{f}}}^2 + (\gamma - 2C_{\mathrm{ti}})\frac{\mu\tau}{2h}\sum_{m=0}^{n} \|\tilde{\mathbf{u}}_h^{m+1} - D_\tau \boldsymbol{d}_H^{m+1}\|_{0,\Sigma}^2 + \frac{\gamma\mu\tau}{2h}\|D_\tau \boldsymbol{d}_H^n\|_{0,\Sigma}^2 \leq E^0 + \mu\tau\|\boldsymbol{\varepsilon}(\tilde{\mathbf{u}}_h^0)\|_{0,\Omega^{\mathrm{f}}}^2 + \frac{\gamma\mu\tau}{2h}\|D_\tau \boldsymbol{d}_H^0\|_{0,\Sigma}^2.$$

Note that, in this case, the extra numerical dissipation (mentioned in the previous remark) appears in the solid-side, that is $\gamma\mu\tau/(2h)\|D_\tau \boldsymbol{d}_H^n\|_{0,\Sigma}^2$.

Remark 4.8 *The energy estimate (4.25) holds irrespectively of the inf-sup compatibility of the discrete velocity/pressure pair (it does not provide pressure stability). However, in practice (see Section 4.5), this pair needs to be appropriately chosen so that the projection step (4.22) is well-posed.*

4.4.3 Semi-implicit coupling with pressure-Poisson formulation

The pressure-Poisson version of Algorithm 4.2 (see Section 4.3.3) applied to the model problem (4.21) reads:

Algorithm 4.4 *Robin based semi-implicit coupling scheme (pressure-Poisson formulation) for the linearized problem.*

- `Implicit step (pressure-solid coupling):`

Find $(p_h^{n+1}, \mathbf{u}_h^{n+1}, \boldsymbol{d}_H^{n+1}, \dot{\boldsymbol{d}}_H^{n+1}) \in Q_h^{\mathrm{f}} \times X_h^{\mathrm{f}} \times [V_H^{\mathrm{s}}]^2$ such that

$$\begin{cases} (\nabla p_h^{n+1}, \nabla q_h)_{\Omega^{\mathrm{f}}} = -\dfrac{\rho^{\mathrm{f}}}{\tau}(\nabla \cdot \tilde{\mathbf{u}}_h^n, q_h)_{\Omega^{\mathrm{f}}} \\ \qquad\qquad\qquad -\dfrac{\rho^{\mathrm{f}}}{\tau}\big((\pi_h(D_\tau \boldsymbol{d}_H^{n+1}) - \tilde{\mathbf{u}}_h^n)\cdot \mathbf{n}^{\mathrm{f}}, q_h\big)_\Sigma \quad \forall q_h \in Q_{\Gamma,h}^{\mathrm{f}}, \\ \qquad\qquad\qquad\qquad\qquad p_h^{n+1} = \bar{p} \quad \text{on} \quad \Gamma^{\mathrm{in-out}}. \end{cases} \tag{4.32}$$

$$\begin{cases} \dfrac{\rho^{\mathrm{f}}}{\tau}\big(\mathbf{u}_h^{n+1} - \tilde{\mathbf{u}}_h^n, \boldsymbol{v}_h^{\mathrm{f}}\big)_{\Omega^{\mathrm{f}}} + \big(\nabla p_h^{n+1}, \boldsymbol{v}_h^{\mathrm{f}}\big)_{\Omega^{\mathrm{f}}} = 0 \quad \forall \boldsymbol{v}_h^{\mathrm{f}} \in X_{h,0}^{\mathrm{f}}, \\ \qquad\qquad\qquad \mathbf{u}_h^{n+1} = \pi_h(D_\tau \boldsymbol{d}_H^{n+1}) \quad \text{on} \quad \Sigma. \end{cases} \tag{4.33}$$

$$\begin{cases} \dfrac{\rho^{\mathrm{s}}}{\tau}\big(\dot{\boldsymbol{d}}_H^{n+1} - \dot{\boldsymbol{d}}_H^n, \boldsymbol{v}_H^{\mathrm{s}}\big)_{\Omega^{\mathrm{s}}} + a^{\mathrm{s}}\big(\boldsymbol{d}_H^{n+\frac{1}{2}}, \boldsymbol{v}_H^{\mathrm{s}}\big) + \dfrac{\gamma\mu}{h}\big(\pi_h(D_\tau \boldsymbol{d}_H^{n+1}) - \tilde{\mathbf{u}}_h^n, \pi_h(\boldsymbol{v}_H^{\mathrm{s}})\big)_\Sigma \\ \qquad = -2\mu\big(\boldsymbol{\varepsilon}(\tilde{\mathbf{u}}_h^n)\mathbf{n}^{\mathrm{s}}, \pi_h(\boldsymbol{v}_H^{\mathrm{s}})\big)_\Sigma - \big\langle \mathcal{R}(\mathbf{u}_h^{n+1}, \tilde{\mathbf{u}}_h^n, p_h^{n+1}), \mathcal{L}_h(\boldsymbol{v}_H^s)\big\rangle \quad \forall \boldsymbol{v}_H^{\mathrm{s}} \in V_H^{\mathrm{s}}, \\ \qquad\qquad\qquad D_\tau \boldsymbol{d}_H^{n+1} = \dot{\boldsymbol{d}}_H^{n+\frac{1}{2}} \quad \text{in} \quad \Omega^{\mathrm{s}}. \end{cases} \tag{4.34}$$

- Explicit step (viscous-solid coupling):
  Find $\tilde{\mathbf{u}}_h^{n+1} \in X_h^{\mathrm{f}}$ such that

$$\begin{cases} \dfrac{\rho^{\mathrm{f}}}{\tau}\big(\tilde{\mathbf{u}}_h^{n+1} - \mathbf{u}_h^{n+1}, \tilde{\boldsymbol{v}}_h^{\mathrm{f}}\big)_{\Omega^{\mathrm{f}}} + 2\mu\big(\boldsymbol{\varepsilon}(\tilde{\mathbf{u}}_h^{n+1}), \boldsymbol{\varepsilon}(\tilde{\boldsymbol{v}}_h^{\mathrm{f}})\big)_{\Omega^{\mathrm{f}}} + \dfrac{\gamma\mu}{h}\big(\tilde{\mathbf{u}}_h^{n+1} - \pi_h(D_\tau \boldsymbol{d}_H^{n+1}), \tilde{\boldsymbol{v}}_h^{\mathrm{f}}\big)_\Sigma \\ \qquad\qquad = 2\mu\big(\boldsymbol{\varepsilon}(\tilde{\mathbf{u}}_h^n)\mathbf{n}^{\mathrm{f}}, \tilde{\boldsymbol{v}}_h^{\mathrm{f}}\big)_\Sigma \quad \forall \tilde{\boldsymbol{v}}_h^{\mathrm{f}} \in X_h^{\mathrm{f}}. \end{cases} \tag{4.35}$$

Energy based stability analysis We now provide an energy based estimate for the semi-implicit scheme (4.32)-(4.35) involving a pressure-Poisson equation.

In the analysis below, we shall make use of the following result, allowing to reformulate (4.32)-(4.33) as the Darcy-like problem, but with a modified continuity equation.

Lemma 4.1 *Assume that (4.32)-(4.33) holds. Then*

$$-(q_h, \nabla \cdot \mathbf{u}_h^{n+1})_{\Omega^{\mathrm{f}}} = \frac{\tau}{\rho^{\mathrm{f}}}(\nabla q_h, \Pi_h^\perp(\nabla p_h^{n+1}))_{\Omega^{\mathrm{f}}} - (\nabla q_h, \Pi_h^\perp(\tilde{\mathbf{u}}_h^n - \mathcal{L}_h(D_\tau \boldsymbol{d}_H^{n+1})))_{\Omega^{\mathrm{f}}}$$

for all $q_h \in Q_{\Gamma,h}^{\mathrm{f}}$. Here, $\Pi_h : L^2(\Omega^{\mathrm{f}}) \to X_{h,0}^{\mathrm{f}}$ stands for the L^2-projection operator into $X_{h,0}^{\mathrm{f}}$, and $\Pi_h^\perp \overset{\text{def}}{=} I - \Pi_h$ for the corresponding orthogonal projection.

Proof. The main idea consists in adapting, to the non-homogeneous case, a well-known property of the Chorin-Temam scheme with a pressure-Poisson equation (see *e.g.* [BC07, Page 550]).

From $(4.33)_1$, we have that

$$\big(\mathbf{u}_h^{n+1} - \mathcal{L}_h(D_\tau \boldsymbol{d}_H^{n+1}), \boldsymbol{v}_h^{\mathrm{f}}\big)_{\Omega^{\mathrm{f}}} = \big(\tilde{\mathbf{u}}_h^n - \mathcal{L}_h(D_\tau \boldsymbol{d}_H^{n+1}) - \frac{\tau}{\rho^{\mathrm{f}}}\nabla p_h^{n+1}, \boldsymbol{v}_h^{\mathrm{f}}\big)_{\Omega^{\mathrm{f}}} \qquad \forall \boldsymbol{v}_h^{\mathrm{f}} \in X_{h,0}^{\mathrm{f}}. \tag{4.36}$$

In addition, with the coupling condition $(4.33)_2$, it follows that $(\mathbf{u}_h^{n+1} - \mathcal{L}_h(D_\tau \boldsymbol{d}_H^{n+1})) \in X_{h,0}^{\mathrm{f}}$, and therefore (4.36) reduces to

$$\mathbf{u}_h^{n+1} - \mathcal{L}_h(D_\tau \boldsymbol{d}_H^{n+1}) = \Pi_h \left(\tilde{\mathbf{u}}_h^n - \mathcal{L}_h(D_\tau \boldsymbol{d}_H^{n+1}) - \frac{\tau}{\rho^{\mathrm{f}}} \nabla p_h^{n+1} \right),$$

or, equivalently,

$$\tilde{\mathbf{u}}_h^n = \mathbf{u}_h^{n+1} + \Pi_h^{\perp} \left(\tilde{\mathbf{u}}_h^n - \mathcal{L}_h(D_\tau \boldsymbol{d}_H^{n+1}) \right) + \frac{\tau}{\rho^{\mathrm{f}}} \Pi_h \left(\nabla p_h^{n+1} \right). \tag{4.37}$$

On the other hand, integrating by parts in $(4.32)_1$ and inserting (4.37) in the resulting expression yields

$$\begin{aligned}
(\nabla p_h^{n+1}, \nabla q_h)_{\Omega^{\mathrm{f}}} =& \frac{\rho^{\mathrm{f}}}{\tau} (\tilde{\mathbf{u}}_h^n, \nabla q_h)_{\Omega^{\mathrm{f}}} - \frac{\rho^{\mathrm{f}}}{\tau} (\tilde{\mathbf{u}}_h^n \cdot \mathbf{n}^{\mathrm{f}}, q_h)_{\Sigma} - \frac{\rho^{\mathrm{f}}}{\tau} \big((\pi_h(D_\tau \boldsymbol{d}_H^{n+1}) - \tilde{\mathbf{u}}_h^n) \cdot \mathbf{n}^{\mathrm{f}}, q_h \big)_{\Sigma} \\
=& \frac{\rho^{\mathrm{f}}}{\tau} (\tilde{\mathbf{u}}_h^n, \nabla q_h)_{\Omega^{\mathrm{f}}} - \frac{\rho^{\mathrm{f}}}{\tau} (\pi_h(D_\tau \boldsymbol{d}_H^{n+1}) \cdot \mathbf{n}^{\mathrm{f}}, q_h)_{\Sigma} \\
=& \frac{\rho^{\mathrm{f}}}{\tau} (\mathbf{u}_h^{n+1}, \nabla q_h)_{\Omega^{\mathrm{f}}} + \frac{\rho^{\mathrm{f}}}{\tau} \big(\Pi_h^{\perp} \left(\tilde{\mathbf{u}}_h^n - \mathcal{L}_h(D_\tau \boldsymbol{d}_H^{n+1}) \right), \nabla q_h \big)_{\Omega^{\mathrm{f}}} \\
& + (\Pi_h \left(\nabla p_h^{n+1} \right), \nabla q_h)_{\Omega^{\mathrm{f}}} - \frac{\rho^{\mathrm{f}}}{\tau} \big(\pi_h(D_\tau \boldsymbol{d}_H^{n+1}) \cdot \mathbf{n}^{\mathrm{f}}, q_h \big)_{\Sigma},
\end{aligned}$$

for all $q_h \in Q_{\Gamma,h}^{\mathrm{f}}$. Finally, reintegrating by parts and using the interface coupling condition $(4.33)_2$, we get

$$\begin{aligned}
(\nabla p_h^{n+1}, \nabla q_h)_{\Omega^{\mathrm{f}}} =& \frac{\rho^{\mathrm{f}}}{\tau} (\mathbf{u}_h^{n+1} \cdot \mathbf{n}^{\mathrm{f}}, q_h)_{\Sigma} - \frac{\rho^{\mathrm{f}}}{\tau} (\nabla \cdot \mathbf{u}_h^{n+1}, q_h)_{\Omega^{\mathrm{f}}} \\
& + \frac{\rho^{\mathrm{f}}}{\tau} (\Pi_h^{\perp} \left(\tilde{\mathbf{u}}_h^n - \mathcal{L}_h(D_\tau \boldsymbol{d}_H^{n+1}) \right), \nabla q_h)_{\Omega^{\mathrm{f}}} \\
& + (\Pi_h \left(\nabla p_h^{n+1} \right), \nabla q_h)_{\Omega^{\mathrm{f}}} - \frac{\rho^{\mathrm{f}}}{\tau} \big(\pi_h(D_\tau \boldsymbol{d}_H^{n+1}) \cdot \mathbf{n}^{\mathrm{f}}, q_h \big)_{\Sigma} \\
=& - \frac{\rho^{\mathrm{f}}}{\tau} (\nabla \cdot \mathbf{u}_h^{n+1}, q_h)_{\Omega^{\mathrm{f}}} + \frac{\rho^{\mathrm{f}}}{\tau} (\Pi_h^{\perp} (\tilde{\mathbf{u}}_h^n - \mathcal{L}_h(D_\tau \boldsymbol{d}_H^{n+1})), \nabla q_h)_{\Omega^{\mathrm{f}}} \\
& + (\Pi_h (\nabla p_h^{n+1}), \nabla q_h)_{\Omega^{\mathrm{f}}},
\end{aligned}$$

which completes the proof. $\diamond$

We now state the main result of this section, which provides the conditional stability of the coupling scheme (4.32)-(4.35).

Theorem 4.2 *Assume that* (4.14) *holds and that the system is isolated,* i.e. $\bar{p} = 0$ *on* $\Gamma^{\mathrm{in-out}}$. *Let* $\left\{ (\tilde{\mathbf{u}}_h^n, \mathbf{u}_h^n, p_h^n, \boldsymbol{d}_H^n, \dot{\boldsymbol{d}}_H^n) \right\}_{n \geq 0}$ *be solution of* (4.32)-(4.35). *Then, the*

following discrete energy estimate holds:

$$E^n + \mu\tau \sum_{m=0}^{n-1} \|\boldsymbol{\varepsilon}(\tilde{\mathbf{u}}_h^{m+1})\|_{0,\Omega^{\mathrm{f}}}^2 + \frac{\tau^2}{2\rho^{\mathrm{f}}} \sum_{m=0}^{n-1} ||\Pi_h^{\perp}(\nabla p_h^{m+1})||_{0,\Omega^{\mathrm{f}}}^2 + \frac{\mu\tau}{4h}\left(\gamma - 4C_{\mathrm{ti}} - \frac{4C_{\mathcal{L}}\rho^{\mathrm{f}}h^2}{\mu\tau}\right) \sum_{m=0}^{n-1} \|\tilde{\mathbf{u}}_h^{m+1} - \pi_h(D_\tau \boldsymbol{d}_H^{m+1})\|_{0,\Sigma}^2 + \frac{\gamma\mu\tau}{2h}\|\tilde{\mathbf{u}}_h^n\|_{0,\Sigma}^2 + \frac{\mu\tau}{6h}\left(\gamma - \frac{6C_{\mathcal{L}}\rho^{\mathrm{f}}h^2}{\mu\tau}\right) \sum_{m=0}^{n-1} \|\tilde{\mathbf{u}}_h^{m+1} - \tilde{\mathbf{u}}_h^m\|_{0,\Sigma}^2 \leq E^0 + \mu\tau\|\boldsymbol{\varepsilon}(\tilde{\mathbf{u}}_h^0)\|_{0,\Omega^{\mathrm{f}}}^2 + \frac{\gamma\mu\tau}{2h}\|\tilde{\mathbf{u}}_h^0\|_{0,\Sigma}^2. \quad (4.38)$$

Thus, the semi-implicit coupling scheme (4.32)-(4.35) is stable, in the energy norm, under the conditions:

$$\gamma \geq 8C_{\mathrm{ti}}, \quad \gamma\mu\tau = \mathcal{O}(h), \quad \gamma\mu\tau \geq 8\rho^{\mathrm{f}}C_{\mathcal{L}}h^2. \quad (4.39)$$

Proof. As in Theorem 4.1, we take in (4.32)-(4.35)

$$\boldsymbol{v}_h^{\mathrm{f}} = \tau(\mathbf{u}_h^{n+1} - \mathcal{L}_h(D_\tau \boldsymbol{d}_H^{n+1})), \quad q_h = \tau p_h^{n+1}, \quad \boldsymbol{v}_H^{\mathrm{s}} = \tau D_\tau \boldsymbol{d}_H^{n+1}, \quad \tilde{\boldsymbol{v}}_h^{\mathrm{f}} = \tau\tilde{\mathbf{u}}_h^{n+1}$$

and we sum the resulting expressions to obtain

$$E^{n+1} - E^n + 2\mu\tau\|\boldsymbol{\varepsilon}(\tilde{\mathbf{u}}_h^{n+1})\|_{0,\Omega^{\mathrm{f}}}^2 \underbrace{-2\mu\tau\big(\boldsymbol{\varepsilon}(\tilde{\mathbf{u}}_h^n)\mathbf{n}^{\mathrm{f}}, \tilde{\mathbf{u}}_h^{n+1} - \pi_h(D_\tau \boldsymbol{d}_H^{n+1})\big)_\Sigma}_{\mathcal{T}_2} + \underbrace{\frac{\gamma\mu\tau}{h}\big[\big(\pi_h(D_\tau \boldsymbol{d}_H^{n+1}) - \tilde{\mathbf{u}}_h^n, \pi_h(D_\tau \boldsymbol{d}_H^{n+1})\big)_\Sigma + \big(\tilde{\mathbf{u}}_h^{n+1} - \pi_h(D_\tau \boldsymbol{d}_H^{n+1}), \tilde{\mathbf{u}}_h^{n+1}\big)_\Sigma\big]}_{\mathcal{T}_1} \underbrace{-\tau(p_h^{n+1}, \nabla\cdot\mathbf{u}_h^{n+1})_{\Omega^{\mathrm{f}}}}_{\mathcal{T}_3} \leq 0. \quad (4.40)$$

Terms $\mathcal{T}_1$ and $\mathcal{T}_2$ can be bounded using arguments similar to those used in the proof of Theorem 4.1. Nevertheless, the new term $\mathcal{T}_3$ requires a specific treatment of term $\mathcal{T}_1$ as we shall see below.

Let consider first term $\mathcal{T}_3$. Using Lemma 4.1, the L^2-orthogonality of Π_h and the Cauchy-Schwarz inequality, we have that

$$\begin{aligned}\mathcal{T}_3 =& \frac{\tau^2}{\rho^{\mathrm{f}}}(\nabla p_h^{n+1}, \Pi_h^{\perp}(\nabla p_h^{n+1}))_{\Omega^{\mathrm{f}}} - \tau(\nabla p_h^{n+1}, \Pi_h^{\perp}(\tilde{\mathbf{u}}_h^n - \mathcal{L}_h(D_\tau \boldsymbol{d}_H^{n+1})))_{\Omega^{\mathrm{f}}} \\ =& \frac{\tau^2}{\rho^{\mathrm{f}}}\|\Pi_h^{\perp}(\nabla p_h^{n+1})\|_{0,\Omega^{\mathrm{f}}}^2 - \tau(\Pi_h^{\perp}(\nabla p_h^{n+1}), \Pi_h^{\perp}(\tilde{\mathbf{u}}_h^n - \mathcal{L}_h(D_\tau \boldsymbol{d}_H^{n+1})))_{\Omega^{\mathrm{f}}} \\ \geq& \frac{\tau^2}{2\rho^{\mathrm{f}}}\|\Pi_h^{\perp}(\nabla p_h^{n+1})\|_{0,\Omega^{\mathrm{f}}}^2 - \frac{\rho^{\mathrm{f}}}{2}\|\Pi_h^{\perp}(\tilde{\mathbf{u}}_h^n - \mathcal{L}_h(D_\tau \boldsymbol{d}_H^{n+1}))\|_{0,\Omega^{\mathrm{f}}}^2. \end{aligned} \quad (4.41)$$

In order to bound the last term, we note that

$$\tilde{\mathbf{u}}_h^n - \mathcal{L}_h(D_\tau \boldsymbol{d}_H^{n+1}) = \tilde{\mathbf{u}}_h^n - \mathcal{L}_h^{\mathrm{f}}(\tilde{\mathbf{u}}_h^n) + \mathcal{L}_h^{\mathrm{f}}(\tilde{\mathbf{u}}_h^n) - \mathcal{L}_h^{\mathrm{f}}\big(\pi_h(D_\tau \boldsymbol{d}_H^{n+1})\big),$$

and since $\tilde{\mathbf{u}}_h^n - \mathcal{L}_h^{\mathrm{f}}(\tilde{\mathbf{u}}_h^n) \in X_{h,0}^{\mathrm{f}}$ (by construction), we have that

$$\|\Pi_h^{\perp}(\tilde{\mathbf{u}}_h^n - \mathcal{L}_h(D_\tau \boldsymbol{d}_H^{n+1}))\|_{0,\Omega^{\mathrm{f}}}^2 = \|\Pi_h^{\perp}\mathcal{L}_h^{\mathrm{f}}(\tilde{\mathbf{u}}_h^n - \pi_h(D_\tau \boldsymbol{d}_H^{n+1}))\|_{0,\Omega^{\mathrm{f}}}^2. \tag{4.42}$$

On the other hand, using the L^2-continuity estimate (4.14), it follows that

$$\begin{aligned}\|\Pi_h^{\perp}\mathcal{L}_h^{\mathrm{f}}(\tilde{\mathbf{u}}_h^n - \pi_h(D_\tau \boldsymbol{d}_H^{n+1}))\|_{0,\Omega^{\mathrm{f}}}^2 \leq & \|\mathcal{L}_h^{\mathrm{f}}(\tilde{\mathbf{u}}_h^n - \pi_h(D_\tau \boldsymbol{d}_H^{n+1}))\|_{0,\Omega^{\mathrm{f}}}^2 \\ \leq & C_{\mathcal{L}} h \|\tilde{\mathbf{u}}_h^n - \pi_h(D_\tau \boldsymbol{d}_H^{n+1})\|_{0,\Sigma}^2 \\ \leq & 2C_{\mathcal{L}} h \big(\|\tilde{\mathbf{u}}_h^n - \tilde{\mathbf{u}}_h^{n+1}\|_{0,\Sigma}^2 \\ & + \|\tilde{\mathbf{u}}_h^{n+1} - \pi_h(D_\tau \boldsymbol{d}_H^{n+1})\|_{0,\Sigma}^2\big).\end{aligned} \tag{4.43}$$

In summary, from (4.41)-(4.43), we conclude that

$$\mathcal{T}_3 \geq \frac{\tau^2}{2\rho^{\mathrm{f}}}\|\Pi_h^{\perp}(\nabla p_h^{n+1})\|_{0,\Omega^{\mathrm{f}}}^2 - C_{\mathcal{L}}\rho^{\mathrm{f}} h\big(\|\tilde{\mathbf{u}}_h^n - \tilde{\mathbf{u}}_h^{n+1}\|_{0,\Sigma}^2 + \|\tilde{\mathbf{u}}_h^{n+1} - \pi_h(D_\tau \boldsymbol{d}_H^{n+1})\|_{0,\Sigma}^2\big). \tag{4.44}$$

The first term in the last inequality corresponds to the well-known enhanced pressure stability of the Chorin-Temam scheme in a pressure-Poisson formulation. The last term will be controlled using the natural numerical dissipation provided by term $\mathcal{T}_1$.

As in the proof of Theorem 4.1, we have

$$\mathcal{T}_1 = \frac{\gamma\mu\tau}{h}\left[\|\tilde{\mathbf{u}}_h^{n+1} - \pi_h(D_\tau \boldsymbol{d}_H^{n+1})\|_{0,\Sigma}^2 + \big(\tilde{\mathbf{u}}_h^{n+1} - \tilde{\mathbf{u}}_h^n, \pi_h(D_\tau \boldsymbol{d}_H^{n+1})\big)_\Sigma\right], \tag{4.45}$$

and, using Young's inequality,

$$\begin{aligned}\big(\tilde{\mathbf{u}}_h^{n+1} - \tilde{\mathbf{u}}_h^n, \pi_h(D_\tau \boldsymbol{d}_H^{n+1})\big)_\Sigma = & \big(\tilde{\mathbf{u}}_h^{n+1} - \tilde{\mathbf{u}}_h^n, \pi_h(D_\tau \boldsymbol{d}_H^{n+1}) - \tilde{\mathbf{u}}_h^{n+1}\big)_\Sigma + \big(\tilde{\mathbf{u}}_h^{n+1} - \tilde{\mathbf{u}}_h^n, \tilde{\mathbf{u}}_h^{n+1}\big)_\Sigma \\ \geq & -\frac{1}{2\varepsilon}\|\tilde{\mathbf{u}}_h^{n+1} - \tilde{\mathbf{u}}_h^n\|_{0,\Sigma}^2 - \frac{\varepsilon}{2}\|\pi_h(D_\tau \boldsymbol{d}_H^{n+1}) - \tilde{\mathbf{u}}_h^{n+1}\|_{0,\Sigma}^2 \\ & + \frac{1}{2}\|\tilde{\mathbf{u}}_h^{n+1}\|_{0,\Sigma}^2 - \frac{1}{2}\|\tilde{\mathbf{u}}_h^n\|_{0,\Sigma}^2 + \frac{1}{2}\|\tilde{\mathbf{u}}_h^{n+1} - \tilde{\mathbf{u}}_h^n\|_{0,\Sigma}^2 \\ \geq & -\frac{\varepsilon}{2}\|\pi_h(D_\tau \boldsymbol{d}_H^{n+1}) - \tilde{\mathbf{u}}_h^{n+1}\|_{0,\Sigma}^2 + \left(\frac{1}{2} - \frac{1}{2\varepsilon}\right)\|\tilde{\mathbf{u}}_h^{n+1} - \tilde{\mathbf{u}}_h^n\|_{0,\Sigma}^2 \\ & + \frac{1}{2}\|\tilde{\mathbf{u}}_h^{n+1}\|_{0,\Sigma}^2 - \frac{1}{2}\|\tilde{\mathbf{u}}_h^n\|_{0,\Sigma}^2,\end{aligned} \tag{4.46}$$

with $\varepsilon > 0$ arbitrary. Therefore, chosing $\varepsilon = \frac{3}{2}$ in (4.46) and inserting the resulting estimate in (4.45) yields

$$\mathcal{T}_1 \geq \frac{\gamma\mu\tau}{h}\left[\frac{1}{4}\|\tilde{\mathbf{u}}_h^{n+1} - \pi_h(D_\tau \boldsymbol{d}_H^{n+1})\|_{0,\Sigma}^2 + \frac{1}{6}\|\tilde{\mathbf{u}}_h^{n+1} - \tilde{\mathbf{u}}_h^n\|_{0,\Sigma}^2 + \frac{1}{2}\|\tilde{\mathbf{u}}_h^{n+1}\|_{0,\Sigma}^2 - \frac{1}{2}\|\tilde{\mathbf{u}}_h^n\|_{0,\Sigma}^2\right]. \tag{4.47}$$

On the other hand, similarly to (4.31), we have

$$\mathcal{T}_2 \geq -\mu\tau\|\boldsymbol{\varepsilon}(\tilde{\mathbf{u}}_h^n)\|_{0,\Omega^{\mathrm{f}}}^2 - \frac{\mu\tau C_{\mathrm{ti}}}{h}\|\tilde{\mathbf{u}}_h^{n+1} - \pi_h(D_\tau \boldsymbol{d}_H^{n+1})\|_{0,\Sigma}^2. \tag{4.48}$$

Finally, by inserting in (4.40) the estimates (4.44), (4.47) and (4.48), changing n by m and summing over $m = 0, \ldots, n-1$, we obtain (4.38), which completes the proof. $\diamond$

Remark 4.9 *The stability condition* (4.39)*, for the pressure-Poisson formulation, is stronger than condition* (4.26)*, for the pressure-Darcy formulation. Note that* (4.39) *enforces a restriction on the rate with which* h *and* τ *go to zero, namely,* $h^2 = O(\tau)$*. It is interesting to observe that this restriction arises also in the case of equal order velocity-pressure approximations of the Chorin-Temam scheme (for a pure fluid problem) with a pressure-Poisson equation (see* e.g. *[BC07, Assumption 8]). Obviously, condition* $h^2 = O(\tau)$ *is compatible with* $\gamma\tau\mu = O(h)$*.*

Remark 4.10 *Although* (4.39) *depends on the physical parameters* ρ^{f} *and* μ*, the scheme is still stable irrespectively of the amount of added-mass effect. Finally, we remark that the considered numerical experiments showed that this dependence does not affect the stability of the scheme.*

4.5 Numerical experiments

In order to illustrate the stability and accuracy properties of the coupling schemes, different numerical experiments are discussed. In Section 4.5.1 we report two different numerical tests involving the Stokes-linear elasticity coupling (4.21) in 2D. The non-linear case (2.33)-(2.35), with more realistic 3D geometries, is considered in Section 4.5.2.

4.5.1 Two-dimensional test cases

We have considered both the pressure-Poisson and pressure-Darcy formulations of our scheme, in its velocity-correction version, with a FWI-based pressure stress computation. The implicit part of the coupling has been solved using Aitken's accelerated fixed-point iterations (see *e.g.* [MWR01]). The numerical computations have been carried out with Freefem++ [Hec].

An analytical test case. We approximate an analytical solution of the Stokes-linear elasticity coupling:

$$\begin{cases} p(x,y) = [-2L_2\cos(\pi t)/\pi - 2\mu\sin(\pi t)]\sin(x)\sin(y), \\ \mathbf{u}(x,y) = \big(-\sin(\pi t)\cos(x)\sin(y), \sin(\pi t)\sin(x)\cos(y)\big), \\ \boldsymbol{d}(x,y) = \big(\cos(\pi t)\cos(x)\sin(y)/\pi, -\cos(\pi t)\sin(x)\cos(y)/\pi\big), \end{cases}$$

where L_2 stands for the second Lamé constant of the solid. The fluid and solid domains, reported in Figure 4.1 (left), are given by $\Omega^{\mathrm{f}} = [0,\pi]\times[0,\pi]$ and $\Omega^{\mathrm{s}} = [0,\pi]\times[\pi,1.25\pi]$. Initial conditions, external boundary conditions and the body forces, both for the fluid and the structure, are chosen in order to satisfy the exact solution. In particular, Dirichlet and Neumann boundary conditions are respectively imposed on Γ^{d} and Γ^{n} for both the problems. The physical parameters are $\rho^{\mathrm{f}} = 1.0$ g/cm^3, $\mu = 4$ poise, $\rho^{\mathrm{s}} = 2.15$ g/cm^3, the elastic modulus $E = 1$ dyn/cm^2, and the Poisson's ratio $\nu = 0.3$.

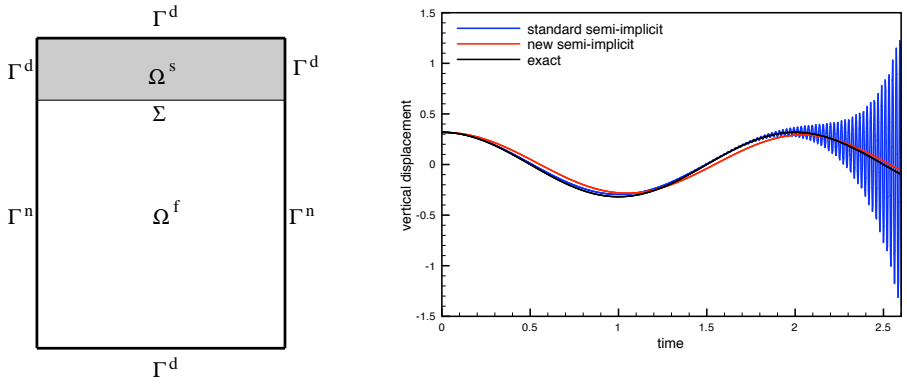

Figure 4.1: Left: Computational domain. Right: Comparison of the semi-implicit and the Robin based semi-implicit coupling schemes (interface mid-point vertical displacement).

The pressure-Poisson version of Algorithm 4.2 and the original semi-implicit coupling [FGG07] are tested using $\mathbb{P}_1$ finite elements and matching fluid-solid interface meshes. The penalty parameter γ has been fixed to 10. The mesh size is $h = \pi/20$ and the time-step is $\tau = 2.5 \cdot 10^{-3}$ s. Strong instabilities are observed for the original semi-implicit coupling scheme, see Figure 4.1 (right). On the contrary, our Robin based semi-implicit coupling scheme is stable and predicts the behavior of the exact solution.

Pressure wave propagation in a compliant vessel. We consider the 2D test case already used in [BF09, Section 6.1]. The fluid domain is given by $\Omega^{\mathrm{f}} \overset{\mathrm{def}}{=} [0,5] \times [0,0.5]$ and the solid domain by $\Omega^{\mathrm{s}} \overset{\mathrm{def}}{=} [0,5] \times [0.5,0.6]$. At $x = 0$, we impose a pressure of value $P = 10^4$ dyn/cm^2, during $5 \cdot 10^{-3}$ s. Zero pressure is enforced at $x = 5$. A symmetry condition is applied on the lower wall $y = 0$. The structure is clamped on $x = 0$ and $x = 5$, with zero traction applied on $y = 0.6$. The fluid physical parameters are given by $\rho^{\mathrm{f}} = 1.0$ g/cm^3, $\mu = 10$ poise. For the solid, we have $\rho^{\mathrm{s}} = 1.2 \cdot 10^{-2}$ g/cm^3, the elastic modulus $E = 3 \cdot 10^8$ dyn/cm^2, and the Poisson's ratio $\nu = 0.3$. Note that these values (high viscosity and small solid density) have been chosen so that the stability condition (4.1), for the original semi-implicit coupling scheme, is expected not to be satisfied. For the fluid, we use the Taylor-Hood finite element and for the structure a standard $\mathbb{P}_1$-continuous discretization with mesh size $h = 0.1$. The fluid and solid quantities in $(4.22)_2$ are matched using as operator π_h the $\mathbb{P}_2$-Lagrange interpolant implemented in Freefem++ [Hec, Section 6.5]. The time-step size is $\tau = 10^{-4}$ s and the penalty parameter γ is still set to 10.

A comparison between our Robin based semi-implicit coupling, in its pressure-Darcy version, an implicit coupling and the original semi-implicit coupling [FGG07] is given in Figure 4.2. Strong numerical instabilities are observed for the latter strategy. However, Algorithm 4.2 provides a stable numerical solution which accurately

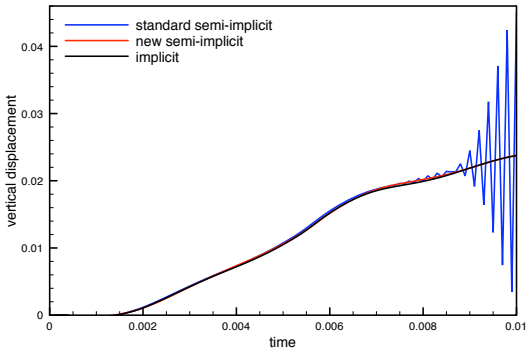

Figure 4.2: Comparison of the semi-implicit and Robin based semi-implicit coupling schemes: interface mid-point vertical displacement.

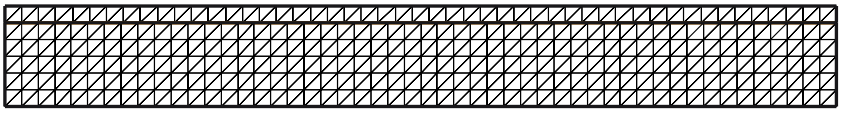

(a)

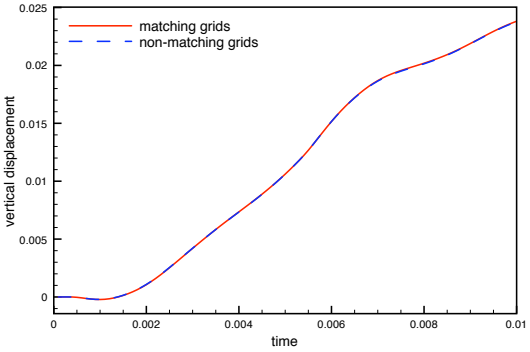

(b)

Figure 4.3: Top: Non-matching computational fluid-structure meshes. Bottom: Comparison between matching and non-matching meshes for the Robin based semi-implicit coupling scheme.

predicts the results of the fully implicit coupling. Simulations have been also carried out with the pressure-Poisson version of the algorithm, with the same results as in pressure-Darcy version.

In order to illustrate the capabilities of the scheme to deal with non-matching interface grids, the same problem has been solved using the meshes given in Figure 4.3.a. A comparison of the solutions of the matching and non-matching cases is reported in Figure 4.3.b. As expected, no instabilities are observed and the two solutions are almost undistinguishable.

4.5.2 Three-dimensional test cases

Here we have considered the pressure-Poisson version of Algorithm 4.2, using $\mathbb{P}_1/\mathbb{P}_1$-continuous finite elements for the fluid space discretization and $\mathbb{P}_1$-continuous finite elements for the solid. The fluid and solid meshes match at the interface and the penalty parameter γ is fixed to 50.

The implicit coupling step is solved using a partitioned Dirichlet-Neumann interface Newton-GMRES algorithm, as in [FGG07]. Comparisons are made with a reference solution obtained with a fully implicit scheme (solved through a partitioned Dirichlet-Neumann interface Newton-GMRES algorithm, see *e.g.* [FM05]). The LifeV[1] finite element library has been used for the numerical computations.

Pressure wave progation in a straight cylindrical vessel. In order to investigate the properties of the algorithm in its non-linear version we considered the three-dimensional benchmark proposed in [FGNQ01] (see also [FQV09, Chapter 12]). The fluid domain is a straight tube of radius 0.5 cm and of length 5 cm. The fluid is governed by the incompressible Navier-Stokes equations in ALE formulation. The vessel wall has a thickness of 0.1 cm and is clamped at its extremities. Here, we assume that the vessel displacement is governed by the laws of linear elasticity. The physical parameters for the fluid have been chosen as $\rho^{\mathrm{f}} = 1$ g/cm^3 and $\mu = 0.035$ poise. For the solid we have $\rho^{\mathrm{s}} = 1.2$ g/cm^3, Young modulus $E = 3 \cdot 10^6$ dyn/cm^2 and Poisson's ratio $\nu = 0.3$. The overall system is initially at rest and, during the first $5 \cdot 10^{-3}$ seconds, an over pressure of $1.3332 \cdot 10^4$ dyn/cm^2 is imposed on the inlet boundary. Simulations are carried out on 400 time-steps of size $\tau = 10^{-4}$ seconds.

Figure 4.4 shows the fluid pressure and the solid deformation at different time instants. A stable pressure wave propagation is observed, both for the standard and the new semi-implicit schemes. Moreover, the maximum displacement has been computed and compared to a reference simulation obtained with a full implicit coupling scheme. The results are displayed in Figure 4.5. Both the standard and the Robin based semi-implicit coupling schemes provide a stable prediction that compares well to the reference implicit solution.

Table 4.5.2 shows the computational time of the different methods, for 400 time-steps. Standard and Robin based semi-implicit coupling schemes are comparable in terms of computation time, and are more than 6 times faster than the traditional implicit coupling. As a result, the good computational performance of the original semi-implicit scheme is conserved by our Robin based scheme. Note finally that in the version FWI, the algorithm is twice as fast as in the version VR. This difference is mainly due to the fact that the implementation of the VR algorithm has not been optimized yet.

A physiological test case. We consider now the numerical fluid-structure simulations reported in [SFCLT05] using *in vitro* aneurysm geometries. The fluid computational domain is the idealized abdominal aortic aneurysm given in Figure 4.6.a.

[1] WWW.LIFEV.ORG

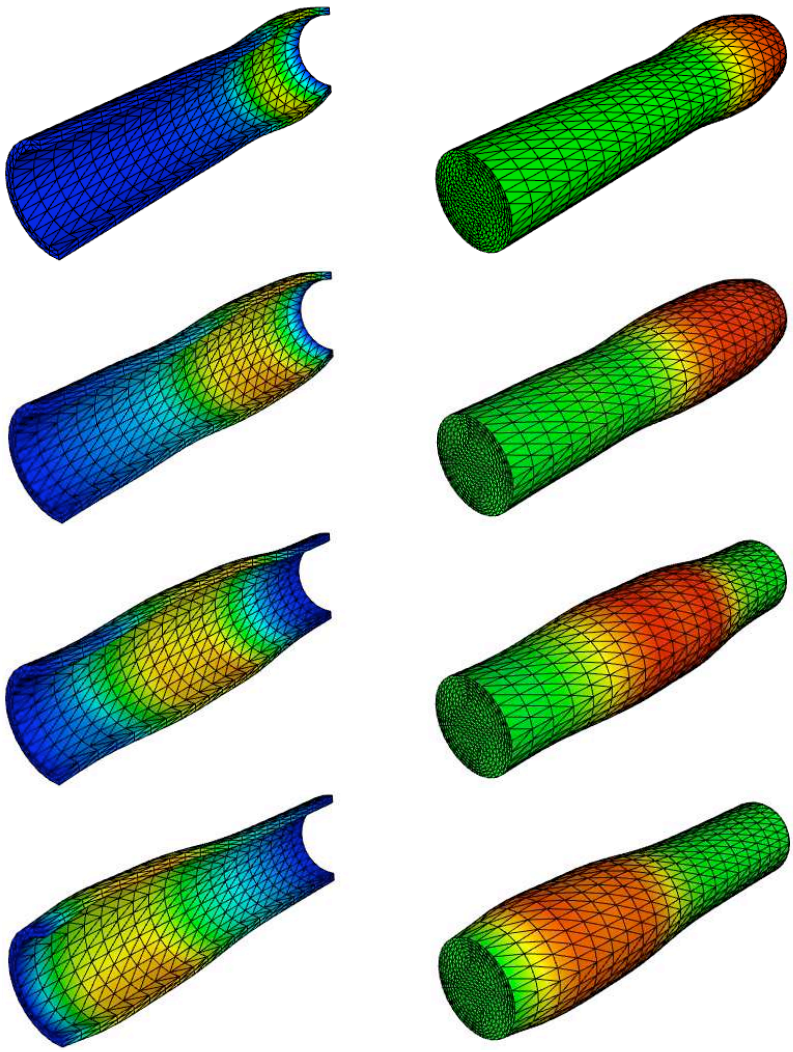

Figure 4.4: Robin based semi-implicit coupling: snapshots of the - exaggerated - solid deformation and of the pressure at different time instants ($t = 0.0025$, 0.005, 0.0075 and 0.01 seconds).

Algorithm	CPU Time
Implicit	13.1
Standard semi-implicit (VR/FWI)	1.9/0.9
New semi-implicit (VR/FWI)	2.0/1.0

Table 4.1: Elapsed CPU Time (dimensionless)

We refer to [SFCLT05, SSCL06] for the details. The whole compliant wall has a uniform thickness of 0.17 cm and length of 22.95 cm.

The physical parameters are given by $E = 6 \cdot 10^6\,\mathrm{dyn/cm^2}$, $\nu = 0.3$, $\rho^s = 1.2\,\mathrm{g/cm^3}$, $\mu = 0.035\,\mathrm{poise}$ and $\rho^f = 1\,\mathrm{g/cm^2}$. Initially, the fluid is at rest. An in-

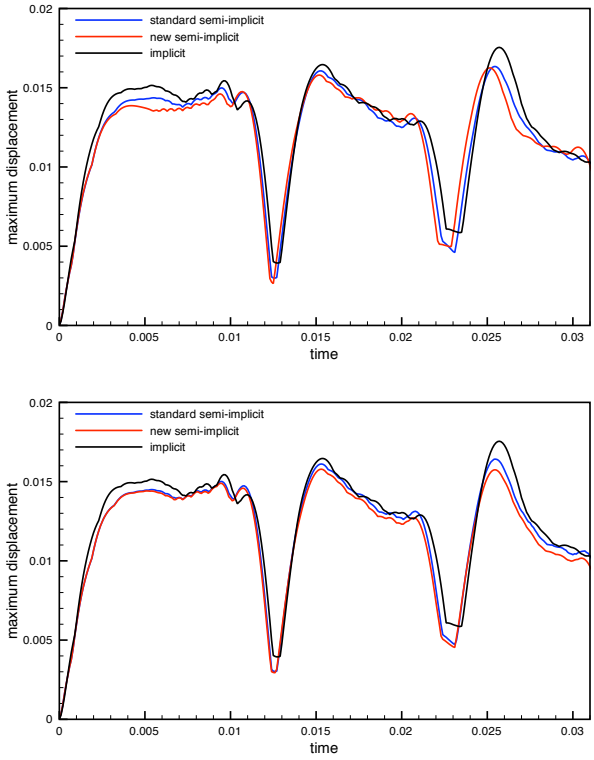

Figure 4.5: Comparison of the implicit, standard semi-implicit and Robin based semi-implicit coupling schemes: maximal displacement of the structure. Top: VR. Bottom: FWI.

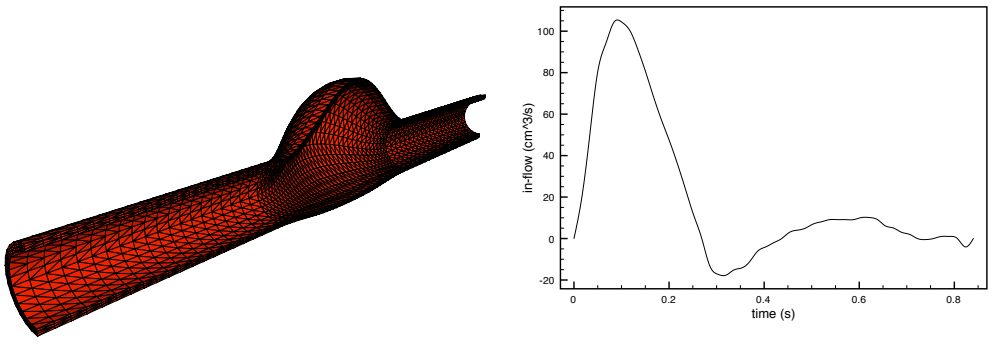

(a) (b)

Figure 4.6: Left: Aneurysm geometry. Right: In-flow rate data.

flow rate corresponding to a cardiac cycle, see Figure 4.6.b, is imposed on the inlet boundary. A resistive-like boundary condition is prescribed on the outlet boundary, the value of the resistance being $R = 600\,\mathrm{dyn{\cdot}s/cm^5}$. We have simulated 1000 time-steps of size $\tau = 1.68 \cdot 10^{-3}\,\mathrm{s}$, which corresponds to two cardiac cycles.

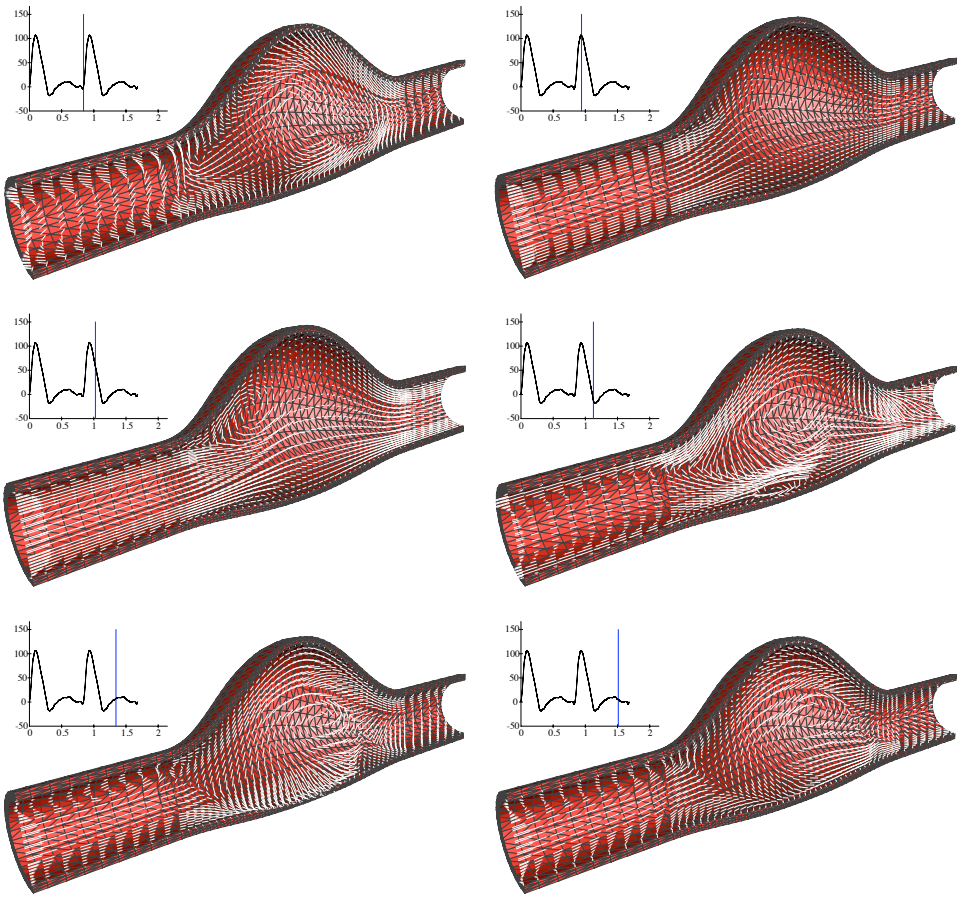

Figure 4.7: Robin based semi-implicit coupling: snapshots of the solid deformation and fluid velocity field at different time instants.

In Figure 4.7, we have reported some snapshots of the wall deformation and the fluid velocity fields at different time instants. In Figure 4.8, it is shown that even in this complex case, the standard and Robin based semi-implicit coupling provide a prediction that compares well to the reference implicit solution.

In Table 4.2, we have reported the CPU-time consumption over 500 time-steps (two full cardiac cycles), for the different methods considered. Again, the standard and Robin based semi-implicit schemes are comparable in terms of computational cost. They are more than 10 times faster than the classical fully implicit algorithm.

Algorithm	CPU Time
Implicit	16.4
Standard semi-implicit (VR/FWI)	1.5/1.1
New semi-implicit (VR/FWI)	1.4/ 1

Table 4.2: Elapsed CPU Time (dimensionless)

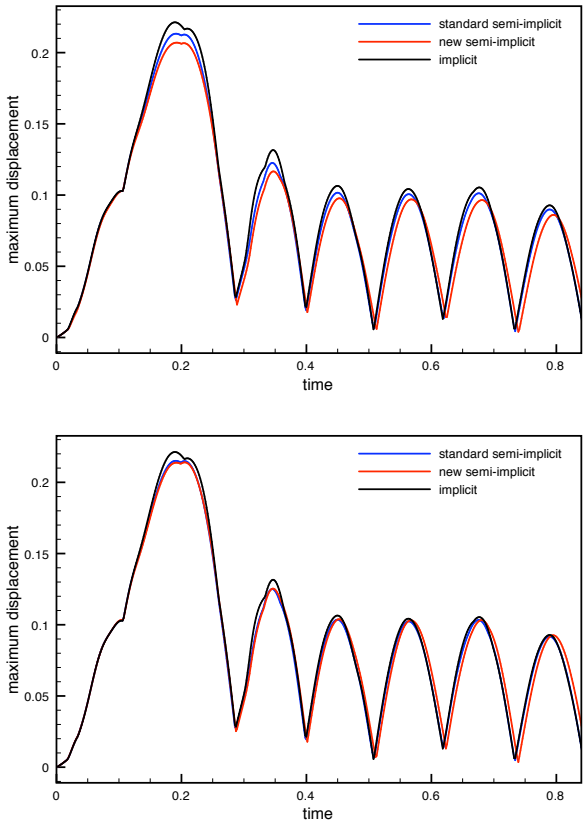

Figure 4.8: Comparison of the implicit, standard semi-implicit and Robin based semi-implicit coupling schemes: maximal displacement of the structure. Top: VR. Bottom: FWI.

4.6 Conclusion

We have proposed a Robin-based semi-implicit coupling scheme whose stability properties are independent of:

1. the added-mass effect in the system (fluid-solid density ratio and geometry of the domain);

2. the numerical dissipation of the solid time-discretization.

In particular, it allows for conservative time-stepping on the structure without compromising stability. The main idea consists in treating the explicit part of the coupling with a Robin based mortaring derived from Nitsche's method. Numerical tests confirm the theoretical results.

Part II

Numerical simulation of fluid-structure interaction problems with cardiac valves

Chapter 5

A partitioned scheme for FSI and multi-body contact

M. Astorino, J.-F. Gerbeau, O. Pantz and K.-F. Traoré. *Fluid-structure interaction and multi-body contact. Application to the aortic valves.* Comput. Methods Appl. Mech. Engng., Vol. 198, Num. 45-46, pp. 3603-3612, 2009.

Contents

5.1 Introduction

The numerical simulation of cardiac valves offers many challenges: the constitutive laws of the valves are very complex, the blood interacts with the valves and the wall, the valves are submitted to kinematic constraints like contact between leaflets or attachments to the *chordae tendineae* (for the mitral valves).

In this chapter we are interested in the development of a partitioned strategy for the management of fluid-structure interaction in presence of contacts, in which we suppose that the structure solvers do not include contact capabilities. Here, we focus on the interaction of several elastic bodies immersed in an incompressible viscous fluid. Clearly cardiac valves are the main motivation of the present study, but the proposed algorithms can address more general configurations.

A number of articles has been devoted to fluid-structure interaction around artificial or natural cardiac valves. As already mentioned in Section 1.2, p. 9, they can be roughly divided in three groups: the approaches based on the Immersed Boundary (IB) methods (see for example [GHMP07] and the references therein),

those based on the Arbitrary Lagrangian Eulerian (ALE) formulation (see *e.g.* [JDS96, MYWS07, DVD+09]), and those based on Fictitious Domains (FD) formulations (see *e.g.* [Baa01, dHPSB03, dH04, dSGB08]). The algorithm we present is based on the FSI approach proposed in [dSGB08] which belongs to the third group.

The most common approach in mechanical contacts is known as the master/slave formulation [Lau92, Lau02, LS93]. Initially designed to prevent a deformable body (the slave) to penetrate a rigid foundation (the master), it has been extended to the case of contacts between different deformable bodies. The master/slave approach can be also adapted to more complicated cases such as contacts and self-contacts between deformable thin structures (see [HASM93]), though it is no more completely consistent from a mathematical viewpoint. As a matter of fact, *ad hoc* modifications have to be added in order to correctly handle the inconsistent situations in which the standard master/slave approach may fail. Here, we propose to follow a totally different path, which allows us to consider contact, self-contact among thin or thick structures in a single setting. For more details about the state of the art in contact mechanics we refer to [HGB85], [KO88] and [Wri02] (see also [Wri95, Kla95]).

A few works have considered both fluid-structure interaction and the contact problem among the leaflets. For example, in [vLAvdV06], contact is taken into account with a rigid wall (convex constraint) and the algorithm is monolithic: fluid, structure and contact are governed by a unique *ad hoc* solver. In [dSGB08], the same kind of "simple" contact has been investigated but with a partitioned algorithm. In [CBHP06], the contact is handled directly in the structure solver. In [TS07], the "SENCT" contact algorithm has been introduced to preserve the quality of the fluid mesh between the structural surfaces coming into contact. Compared to the existing studies, the main characteristics of the present work are the following: (i) the solvers are kept independent; (ii) the structure solvers are not supposed to manage contact by themselves; (iii) the contact occurs among several leaflets (non-convex constraint), which can be thin structures; (iv) self-contact is automatically managed.

In Section 5.2, we briefly recall the fluid and structure models and their discretizations. In Section 5.3, we present the general algorithm. The fluid-structure coupling is handled with a standard fixed-point algorithm accelerated by an Aitken extrapolation (see Algorithm 2.1, p. 51). The constraint of non-penetration among the immersed structures defines a *non-convex* optimization problem which is solved following an algorithm proposed in [Pan08]. This approach is in particular able to manage the cases of thin structures and self-contacts. The proposed strategy allows to consider the fluid and structure solvers as "black-boxes" which only exchange forces and displacements.

In Section 5.4, the algorithm is applied to the simulation of an idealized aortic valve. The proposed test case is far from the complexity of the real problem. Several simplifications should be removed to address the problem with more realism. In particular, the fluid boundary conditions and the constitutive laws should be improved, and the elasticity of the aorta should be taken into account. The purpose

is only to illustrate the algorithm in a configuration which is not trivial, in spite of all the simplifications.

5.2 Modeling and discretization

5.2.1 Fluid and solid models

The fluid is governed by the incompressible Navier-Stokes equations. The approximation is performed with the finite element method. In view of the ratio thickness/size of the leaflets, it is necessary to consider robust structural models in order to avoid the well-known locking phenomena. In this study the solids are modeled by MITC4 "General shell element" [CB03], for which the internal energy (2.21) is assumed. The fluid and solid meshes are independent: the continuity of the fluid and solids velocities is enforced through Lagrange multipliers, as presented in Section 2.4.3. We refer to [dSGB08] for the details of the partitioned FSI approach.

5.2.2 Contact model

The contact is assumed to be frictionless and soft. In addition, we do not apply any specific treatment due to the presence of the fluid (no lubrication forces are added). In spite of these simplifications, the problem is quite complicated since the contact constraints are non-convex, as will be shown in the sequel.

5.3 General algorithm

We give in this section the details of the general algorithm used to handle fluid-structure interaction and contact. Note that, since in this chapter we consider only the space-discrete structure problem, in the presentation of the algorithm the subscript H is omitted for the sake of simplicity.

We denote by M the family of immersed solids $M = (M_1, M_2, \dots)$ and by $\mathcal{T}_H$ a $\mathbb{P}_1$ finite element mesh of M:

$$X = \{\boldsymbol{\varphi} \in \mathcal{C}^0(M; \mathbb{R}^d), \boldsymbol{\varphi}|_T \in \mathbb{P}_1, \forall T \in \mathcal{T}_H\},$$

d being 2 or 3. The quantity $\boldsymbol{\varphi}(\mathbf{x}_i)$ is the current position of the i^{th} node of the structure. We denote by $\boldsymbol{\varphi}_\Sigma$ the restriction of $\boldsymbol{\varphi}$ to the fluid-structure interface Σ.

The structure "discrete energy" is denoted by J. The energy J includes in particular the terms resulting from the discretization of the acceleration and the load exerted by the fluid. The deformation $\boldsymbol{\varphi} : \cup_i M_i \to \mathbb{R}^d$ is determined by solving at each time step the following minimization problem:

$$\inf_{\boldsymbol{\varphi} \in \mathcal{U}} J(\boldsymbol{\varphi}), \tag{5.1}$$

with

$$\mathcal{U} = \{\boldsymbol{\varphi} \in X, \mathrm{dist}(\boldsymbol{\varphi}(T_1), \boldsymbol{\varphi}(T_2)) \geq \varepsilon_g, \forall T_1, T_2 \in \mathcal{T}_H \text{ such that } T_1 \cap T_2 = \emptyset\},$$

where dist is the standard Euclidean distance and ε_g denotes a gap between the solids. Note that the set $\mathcal{U}$ defining the constraints is non-convex which makes the minimization problem (5.1) difficult. This difficulty will be circumvented by transforming the problem with non-convex constraints into a sequence of problems with convex constraints.

The proposed algorithm is made of three nested loops. The external loop (loop 1) solves the fluid-structure coupling. The first inner loop (loop 2) build a sequence of convex sets $\mathcal{C}(\boldsymbol{\varphi}^k)$ which are used in place of $\mathcal{U}$. The purpose of the most inner loop (loop 3) is to solve problem (5.1) on the convex sets $\mathcal{C}(\boldsymbol{\varphi}^k)$. Figure 5.1 summarizes this algorithm. In the three next sections, we give the details of each loop.

Loop 1: Fluid-Structure

Iterate on j until $\|\boldsymbol{\varphi}_\Sigma^{j+1} - \boldsymbol{\varphi}_\Sigma^j\| \leq \varepsilon_{\text{fsi}}$:

1. Solve the fluid problem: given the structures deformation $\boldsymbol{\varphi}_\Sigma^j$, compute the fluid velocity and pressure $(\mathbf{u}^j, p^j)$.

2. Compute the load exerted by the fluid $\boldsymbol{\sigma}^{\text{f},j}$.

3. Loop 2: Sequence of convex minimization problems

Iterate on k until $\|\boldsymbol{\varphi}^{j,k+1} - \boldsymbol{\varphi}^{j,k}\| \leq \varepsilon_{\mathcal{C}}$:

3.1. Definition of a convex neighborhood $\mathcal{C}(\boldsymbol{\varphi}^{j,k})$ of $\boldsymbol{\varphi}^{j,k}$.

3.2. Loop 3: Minimization with convex constraints

Uzawa algorithm (tolerance ε_{cvx}) to solve the structure problem:

$$J(\boldsymbol{\varphi}^{j,k+1}) = \inf J(\boldsymbol{\psi})$$

under the convex constraint $\boldsymbol{\psi} \in \mathcal{C}(\boldsymbol{\varphi}^{j,k})$.

Figure 5.1: General algorithm

5.3.1 Fluid-structure interaction (loop 1)

Several techniques have been proposed to solve the mechanical interaction between blood flow and arterial walls (among many references see *e.g.* [GV03, FM05, FGG06, TOK+06, FVCJ+06, BNV08]). For these problems, we know that naive partitioned schemes can be either unstable or very inefficient. As a matter of fact, an accelerated fixed point algorithm may need up to 40 iterations to converge. Explanations of this fact are provided in [CGN05, FWR06].

In the present study, we are not interested in the coupling with the wall but with an immersed valve. In this specific case, we observed that an accelerated fixed point algorithm typically converges in about 5 (max. 10) iterations. Thus, we adopted this simple algorithm for the fluid-valve interaction.

The accelerated fixed-point method, based on the Aitken formula, is given in

Algorithm 2.1, p. 51, and it has been first applied to FSI problems in [MWR01]. Noticing that $\boldsymbol{d}(\mathbf{x},t) \stackrel{\text{def}}{=} \boldsymbol{\varphi}(\mathbf{x},t) - \mathbf{x}$, $\mathbf{x}$ being the reference configuration, the scheme can be rewritten as

Algorithm 5.1 *Loop 1: Fluid-Structure.*

Initialize $\boldsymbol{\varphi}_\Sigma^0$ (prediction of the position of the interface);
Do

Step 1 : (fluid sub-problem)
- Solve the fluid problem, given $\boldsymbol{\varphi}_\Sigma^j$ at the interface;
- Compute the load $\boldsymbol{\sigma}^{\mathrm{f},j}$ exerted by the fluid on the structure;

Step 2 : (solid sub-problem)
Solve the structure to obtain a new deformation $\tilde{\boldsymbol{\varphi}}^{j+1}$;
Step 3 : (Aitken acceleration formula)
Correct the position of the interface:

$$\boldsymbol{\varphi}_\Sigma^{j+1} = \omega^j \tilde{\boldsymbol{\varphi}}_\Sigma^{j+1} + (1-\omega^j)\boldsymbol{\varphi}_\Sigma^j,$$

with

$$\omega^j = \frac{(\boldsymbol{\varphi}_\Sigma^j - \boldsymbol{\varphi}_\Sigma^{j-1}) \cdot (\boldsymbol{\varphi}_\Sigma^j - \tilde{\boldsymbol{\varphi}}_\Sigma^{j+1} - \boldsymbol{\varphi}_\Sigma^{j-1} + \tilde{\boldsymbol{\varphi}}_\Sigma^j)}{|\boldsymbol{\varphi}_\Sigma^j - \tilde{\boldsymbol{\varphi}}_\Sigma^{j+1} - \boldsymbol{\varphi}_\Sigma^{j-1} + \tilde{\boldsymbol{\varphi}}_\Sigma^j|^2}; \tag{5.2}$$

While $\|\boldsymbol{\varphi}_\Sigma^{j+1} - \boldsymbol{\varphi}_\Sigma^j\| > \varepsilon_{\text{fsi}}$;

Remark 5.1 *If the interaction with the aorta was also taken into account (which is not the case in this work), it would be necessary to use more sophisticated algorithms to avoid prohibitive computational costs. For example, the method proposed in [FGG06] could be extended to deal with both types of interaction (wall and valve). A step in this direction is presented in [dS07, Chapter 6].*

5.3.2 Definition of a convex neighborhoods (loop 2)

Loop 2 is based on an original idea proposed in [Pan08]. Its purpose is to replace the non-convex optimization problem (5.1) with a sequence of convex ones. For the sake of clarity, we drop the index j related to the FSI iteration in Figure 5.1. Suppose the current deformation of the structure is $\boldsymbol{\varphi}^k$. To compute the state $\boldsymbol{\varphi}^{k+1}$, we solve the structure problem (5.1) replacing $\mathcal{U}$ with a convex set denoted by $\mathcal{C}(\boldsymbol{\varphi}^k)$. Each convex set $\mathcal{C}(\boldsymbol{\varphi}^k)$ contains the element $\boldsymbol{\varphi}^k$ and is included in the initial admissible set $\mathcal{U}$. Moreover, if $\boldsymbol{\varphi}^k$ belongs to the interior of $\mathcal{U}$, the set $\mathcal{C}(\boldsymbol{\varphi}^k)$ is a convex (closed) neighborhood of the element $\boldsymbol{\varphi}^k$. In the following, $\mathcal{C}(\boldsymbol{\varphi}^k)$ will be often referred to a "neighborhood" of $\boldsymbol{\varphi}$ by language abuse. The precise definition of the convex neighborhood in 2D and 3D is given in the two following sections. Here is a sketch of the algorithm:

Algorithm 5.2 *Loop 2: Sequence of convex minimization problems.*

Initial guess: $\boldsymbol{\varphi}^0$;
Do

Solve

$$J(\boldsymbol{\varphi}^{k+1}) = \inf_{\boldsymbol{\psi}\in\mathcal{C}(\boldsymbol{\varphi}^k)} J(\boldsymbol{\psi}),$$

where $\mathcal{C}(\boldsymbol{\varphi}^k)$ is a convex neighborhood of $\boldsymbol{\varphi}^k$ (defined below);

While $\|\boldsymbol{\varphi}^{k+1} - \boldsymbol{\varphi}^k\| > \varepsilon_{\mathcal{C}}$;

As $\mathcal{C}(\boldsymbol{\varphi}^k)$ always contains $\boldsymbol{\varphi}^k$, the sequence $J(\boldsymbol{\varphi}^k)$ in the loop 2 of the algorithm is non-increasing, and therefore convergent if bounded from below. The resolution of the new minimization problem (where the solution is searched in $\mathcal{C}(\boldsymbol{\varphi}^k)$) is the purpose of the third loop and will be explained later on.

Note that, at convergence, the optimality conditions of the original non-convex problem are not exactly satisfied. Nevertheless, it can be proved that they are satisfied up to an error $O(H)$, where H is the discretization step in the structure (see [Pan08]).

5.3.2.1 Definition of $\mathcal{C}(\boldsymbol{\varphi}^k)$ in 2D

In 2D, the convex neighborhood is defined as follows:

$$\mathcal{C}(\boldsymbol{\psi}) = \Big\{\boldsymbol{\varphi} \in X, \min_{\mathbf{x}_e\in e} \mathbf{n}_{e,\mathbf{x}}(\boldsymbol{\psi}) \cdot (\boldsymbol{\varphi}(\mathbf{x}_e) - \boldsymbol{\varphi}(\mathbf{x})) \geq \varepsilon_g, \\ \text{for all edges } e \text{ and all nodes } \mathbf{x} \notin e\Big\},$$

where $\varepsilon_g > 0$ and $\mathbf{n}_{e,\mathbf{x}}(\boldsymbol{\psi})$ is defined by:

$$\min_{\mathbf{x}_e\in e} \mathbf{n}_{e,\mathbf{x}}(\boldsymbol{\psi}) \cdot (\boldsymbol{\psi}(\mathbf{x}_e) - \boldsymbol{\psi}(\mathbf{x})) = \operatorname{dist}(\boldsymbol{\psi}(e), \boldsymbol{\psi}(\mathbf{x})).$$

Loosely speaking, $\mathbf{n}_{e,\mathbf{x}}(\boldsymbol{\psi})$ is the normal to the edge e pointing to the node $\mathbf{x}$. See Figure 5.2 for two typical configurations.

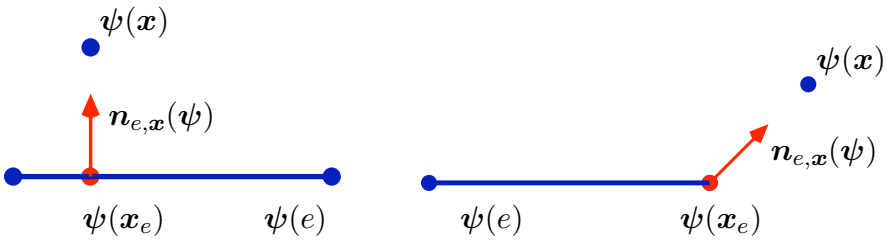

Figure 5.2: Definition of $\mathbf{n}_{e,\mathbf{x}}$ in two configurations.

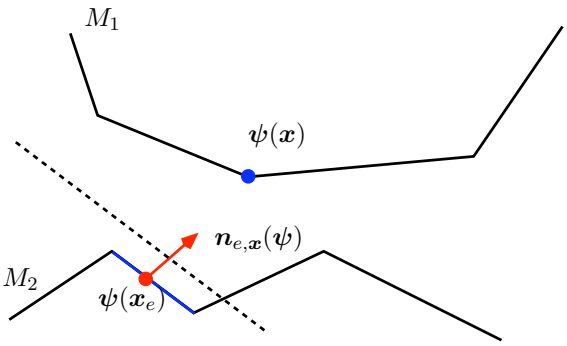

Figure 5.3: An example of convex constraint approximating the non-convex one: all the couples edge/vertex can be separated by a straight line (dashed-line), with a gap ε_g.

We denote by e^+ and e^- the vertices of an edge e. It is convenient to notice that the convex neighborhood can also be rewritten as:

$$\mathcal{C}(\psi) = \Big\{ \varphi \in X, F^-_{e,\mathbf{x}_i}(\varphi) \leq 0, F^+_{e,\mathbf{x}_i}(\varphi) \leq 0, \\ \text{for all edges } e \text{ and all nodes } \mathbf{x}_i \notin e \Big\}, \tag{5.3}$$

where

$$F^{\pm}_{e,\mathbf{x}_i,\psi}(\varphi) = \varepsilon_g - \mathbf{n}_{e,\mathbf{x}_i}(\psi) \cdot (\varphi(e^{\pm}) - \varphi(\mathbf{x}_i)),$$

Under this form, we see that the convex constraints consist in imposing that, after deformation, any edges and vertices can be separated by a straight line, with a gap ε_g (see Figure 5.3).

If loop 2 converges to $\varphi \in X$, then there exist $\lambda^+_{e,i} \geq 0$ and $\lambda^-_{e,i} \geq 0$ (for all e and i such that node i does not belong to edge e) such that $\forall \boldsymbol{\xi} \in X$:

$$\begin{cases} \langle J'(\varphi), \boldsymbol{\xi} \rangle - \\ \displaystyle\sum_e \sum_{\mathbf{x}_i \notin e} \mathbf{n}_{e,\mathbf{x}_i} \cdot \big((\lambda^-_{e,\mathbf{x}_i} + \lambda^+_{e,\mathbf{x}_i}) \boldsymbol{\xi}(\mathbf{x}_i) - \lambda^-_{e,\mathbf{x}_i} \boldsymbol{\xi}(e^-) - \lambda^+_{e,\mathbf{x}_i} \boldsymbol{\xi}(e^+) \big) & = & 0, \\ \lambda^-_{e,\mathbf{x}_i} F^-_{e,\mathbf{x}_i,\psi}(\varphi) & = & 0, \\ \lambda^+_{e,\mathbf{x}_i} F^+_{e,\mathbf{x}_i,\psi}(\varphi) & = & 0. \end{cases} \tag{5.4}$$

The Lagrange multipliers $\lambda^{\pm}_{e,\mathbf{x}_i}$ represent the contact pressure acting on the nodes of the solids mesh and are added to the hydrodynamic force acting on the structure. The computation of $\lambda^{\pm}_{e,\mathbf{x}_i}$ will be explained in Section 5.3.3.

Note that self-contact is automatically handled since the non-penetration condition is tested among two generic independent elements that can also belong to the same solid.

5.3.2.2 Definition of $\mathcal{C}(\boldsymbol{\varphi}^k)$ in 3D

In 3D, two possible contacts can occur:

1. contacts among edges (Figure 5.4.a),
2. contacts among triangles and vertices (Figure 5.4.b).

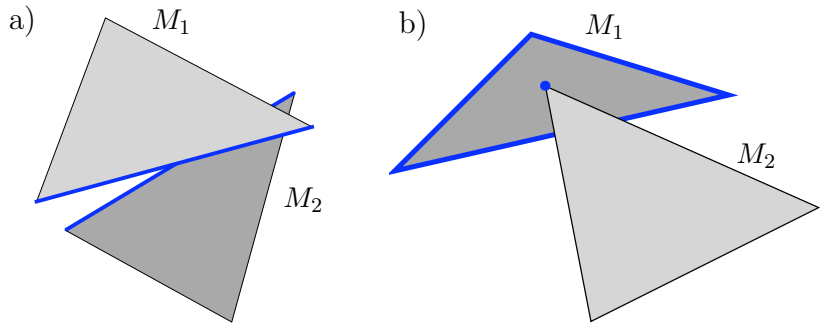

Figure 5.4: Possible contacts between two solids M_1 and M_2 in three dimensions. a) Contact between two edges. b) Contact between a vertex and a triangle.

Therefore the convex neighborhood $\mathcal{C}(\boldsymbol{\varphi}^k)$ is defined as the set of admissible deformations subjected to the constraints associated with each couple edge/edge and triangle/vertex:

$$\mathcal{C}(\boldsymbol{\psi}) = \Big\{ \begin{array}{l} \boldsymbol{\varphi} \in X, \min\limits_{\mathbf{x}_a \in a, \mathbf{x}_b \in b} \mathbf{n}_{a,b}(\boldsymbol{\psi}) \cdot (\boldsymbol{\varphi}(\mathbf{x}_a) - \boldsymbol{\varphi}(\mathbf{x}_b)) \geq \varepsilon_g, \\ \text{for all edges } a \text{ and } b \text{ of } \mathcal{T}_H \text{ such that } a \cap b = \emptyset \\ \text{and } \min\limits_{\mathbf{x}_T \in T} \mathbf{n}_{T,\mathbf{x}}(\boldsymbol{\psi}) \cdot (\boldsymbol{\varphi}(\mathbf{x}_T) - \boldsymbol{\varphi}(\mathbf{x})) \geq \varepsilon_g, \text{for all} \\ \text{triangle } T \text{ and all vertex } \mathbf{x} \text{ of } \mathcal{T}_H \text{ such that } \mathbf{x} \notin T \Big\}, \end{array}$$

where $\mathbf{n}_{a,b}(\boldsymbol{\psi})$ and $\mathbf{n}_{T,\mathbf{x}}(\boldsymbol{\psi})$ are defined by:

$$\min_{\mathbf{x}_a \in a, \mathbf{x}_b \in b} \mathbf{n}_{a,b}(\boldsymbol{\psi}) \cdot (\boldsymbol{\psi}(\mathbf{x}_a) - \boldsymbol{\psi}(\mathbf{x}_b)) = \text{dist}(\boldsymbol{\psi}(a) - \boldsymbol{\psi}(b))$$

and

$$\min_{\mathbf{x}_T \in T} \mathbf{n}_{T,\mathbf{x}}(\boldsymbol{\psi}) \cdot (\boldsymbol{\psi}(\mathbf{x}_T) - \boldsymbol{\psi}(\mathbf{x})) = \text{dist}(\boldsymbol{\psi}(T) - \boldsymbol{\psi}(\mathbf{x})).$$

For the sake of completeness, we now give a few details on the computations of $\mathbf{n}_{a,b}(\boldsymbol{\psi})$. Let us first denote by a_0, a_1 and b_0, b_1 the corresponding endpoints of the edges a and b, and by $\boldsymbol{\psi}(p_{a,b}) \in \boldsymbol{\psi}(a)$ and $\boldsymbol{\psi}(p_{b,a}) \in \boldsymbol{\psi}(b)$ the set of points that minimize the distance between $\boldsymbol{\psi}(a)$ and $\boldsymbol{\psi}(b)$ (Figure 5.5):

$$\begin{gathered} \boldsymbol{\psi}(p_{a,b}) = \alpha \boldsymbol{\psi}(a_0) + (1-\alpha)\boldsymbol{\psi}(a_1), \\ \boldsymbol{\psi}(p_{b,a}) = \beta \boldsymbol{\psi}(b_0) + (1-\beta)\boldsymbol{\psi}(b_1), \\ \text{with } \alpha, \beta \in \mathbb{R},\ 0 \leq \alpha, \beta \leq 1. \end{gathered}$$

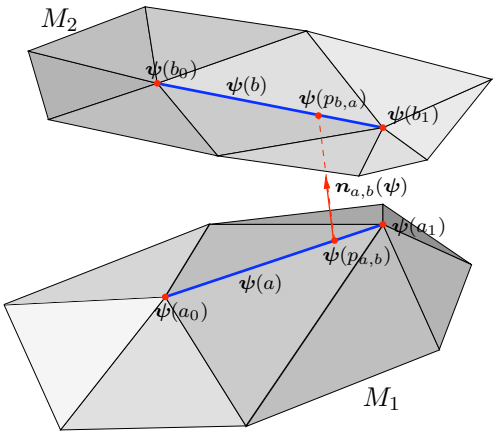

Figure 5.5: Computation of the unit vector $\mathbf{n}_{a,b}(\boldsymbol{\psi})$ for the edge/edge couple (a, b).

The coefficients α and β represent respectively the barycentric coordinates for $\boldsymbol{\psi}(p_{a,b})$ and $\boldsymbol{\psi}(p_{b,a})$ and are evaluated analytically by solving the following minimization problem:

$$(\alpha, \beta) = \underset{0\leq\alpha,\beta\leq 1}{\arg\min}\, f(\alpha, \beta) = \underset{0\leq\alpha,\beta\leq 1}{\arg\min}\, \|\boldsymbol{\psi}(p_{b,a}) - \boldsymbol{\psi}(p_{a,b})\|. \tag{5.5}$$

Note that problem (5.5) admits always a unique solution, except when $\boldsymbol{\psi}(a)$ and $\boldsymbol{\psi}(b)$ are colinear, *i.e.* when

$$\|a\|^2\|b\|^2 - (a_1 - a_0, b_1 - b_0)^2 = 0.$$

From a practical point of view it is convenient to solve first the corresponding unconstrained minimization problem and then evaluate the fulfillment of the constraints. If one of the constraints is not satisfied or if the edges are colinear, the solution of problem (5.5) is equivalent to

$$(\alpha, \beta) = \underset{\alpha,\beta\in\{0,1\}}{\arg\min}\, f(\alpha, \beta) = \underset{\alpha,\beta\in\{0,1\}}{\arg\min}\, \|\boldsymbol{\psi}(p_{b,a}) - \boldsymbol{\psi}(p_{a,b})\|.$$

Once the couple $(\boldsymbol{\psi}(p_{a,b}), \boldsymbol{\psi}(p_{b,a}))$ is computed, the normal vector $\mathbf{n}_{a,b}(\boldsymbol{\psi})$ is finally obtained by

$$\mathbf{n}_{a,b}(\boldsymbol{\psi}) = \frac{\boldsymbol{\psi}(p_{b,a}) - \boldsymbol{\psi}(p_{a,b})}{\|\boldsymbol{\psi}(p_{b,a}) - \boldsymbol{\psi}(p_{a,b})\|}.$$

Some possible configurations of $\mathbf{n}_{a,b}(\boldsymbol{\psi})$ for two generic edges a and b are represented in Figure 5.6.

Let us now consider the definition of the normal vector $\mathbf{n}_{T,\mathbf{x}}(\boldsymbol{\psi})$. In a similar way to the edge/edge contact case, we introduce the vertices (t_0, t_1, t_2) of the triangle T

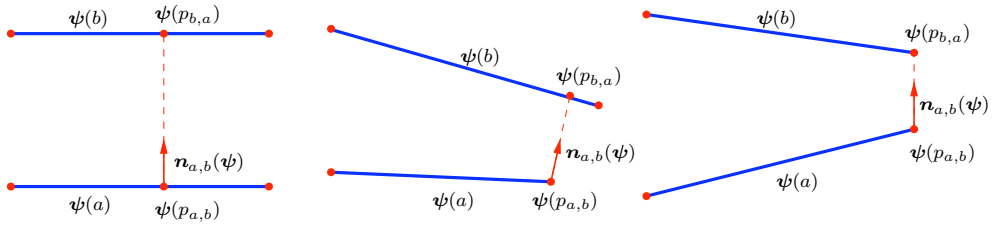

Figure 5.6: Possible configurations of the unit vector $\mathbf{n}_{a,b}(\boldsymbol{\psi})$.

and the barycentric coordinates for the point $\boldsymbol{\psi}(p_{T,\mathbf{x}}) \in \boldsymbol{\psi}(T)$ that minimizes the distance from the vertex $\boldsymbol{\psi}(\mathbf{x})$ (Figure 5.7):

$$\boldsymbol{\psi}(p_{T,x}) = \alpha\boldsymbol{\psi}(t_0) + \beta\boldsymbol{\psi}(t_1) + (1-\alpha-\beta)\boldsymbol{\psi}(t_2),$$
$$\text{with } \alpha,\beta,\gamma \in \mathbb{R},\ 0 \leq \alpha,\beta,\gamma \leq 1 \text{ and } \gamma = 1-\alpha-\beta.$$

The coefficients α, β and γ are determined by

$$(\alpha,\beta) = \underset{\substack{0\leq\alpha,\beta,\gamma\leq 1\\ \gamma=1-\alpha-\beta}}{\arg\min}\ g(\alpha,\beta) = \underset{\substack{0\leq\alpha,\beta,\gamma\leq 1\\ \gamma=1-\alpha-\beta}}{\arg\min}\ \|\boldsymbol{\psi}(p_{T,\mathbf{x}}) - \boldsymbol{\psi}(\mathbf{x})\|, \tag{5.6}$$

and $\mathbf{n}_{T,\mathbf{x}}(\boldsymbol{\psi})$ is obtained from:

$$\mathbf{n}_{T,\mathbf{x}}(\boldsymbol{\psi}) = \frac{\boldsymbol{\psi}(p_{T,\mathbf{x}}) - \boldsymbol{\psi}(\mathbf{x})}{\|\boldsymbol{\psi}(p_{T,\mathbf{x}}) - \boldsymbol{\psi}(\mathbf{x})\|}.$$

From a computational point of view, instead of solving directly the constrained

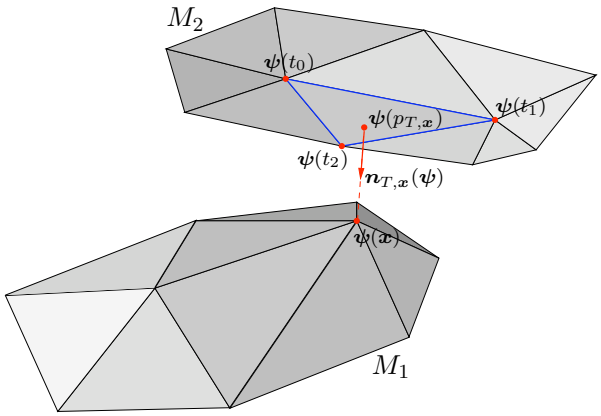

Figure 5.7: Computation of the unit vector $\mathbf{n}_{T,\mathbf{x}}(\boldsymbol{\psi})$ for the triangle/vertex couple $(T,\mathbf{x})$.

problem (5.6), it is easier to determine first the relative position of the point $\boldsymbol{\psi}(\mathbf{x})$ with respect to $\boldsymbol{\psi}(T)$ and then solve a subproblem to calculate $\boldsymbol{\psi}(p_{T,\mathbf{x}})$. In particular, considering the triangle in Figure 5.8.a, $\boldsymbol{\psi}(p_{T,\mathbf{x}})$ will be computed as the

projection of $\boldsymbol{\psi}(\mathbf{x})$ on the edge $\boldsymbol{\psi}(e_i)$ $(\forall i \in \{0,1,2\})$ if $\boldsymbol{\psi}(\mathbf{x})$ is in the part of the space opposed to $\boldsymbol{\psi}(t_i)$ with respect to the plane perpendicular to $\boldsymbol{\psi}(T)$ that contains $\boldsymbol{\psi}(e_i)$. Therefore, in this case, the triangle/vertex problem is equivalent to an edge/vertex problem in three dimensions. On the other hand (Figure 5.8.b), if $\boldsymbol{\psi}(\mathbf{x})$ belongs to the cylinder determined by the intersection of the three perpendicular planes previously defined, $\boldsymbol{\psi}(p_{T,\mathbf{x}})$ will be determined by the analytical solution of the unconstrained problem

$$(\alpha, \beta) = \arg\min g(\alpha, \beta) = \arg\min \|\boldsymbol{\psi}(p_{T,\mathbf{x}}) - \boldsymbol{\psi}(\mathbf{x})\|,$$

which is equivalent to the projection of the vertex $\boldsymbol{\psi}(\mathbf{x})$ on the infinite plane defined by (t_0, t_1, t_2).

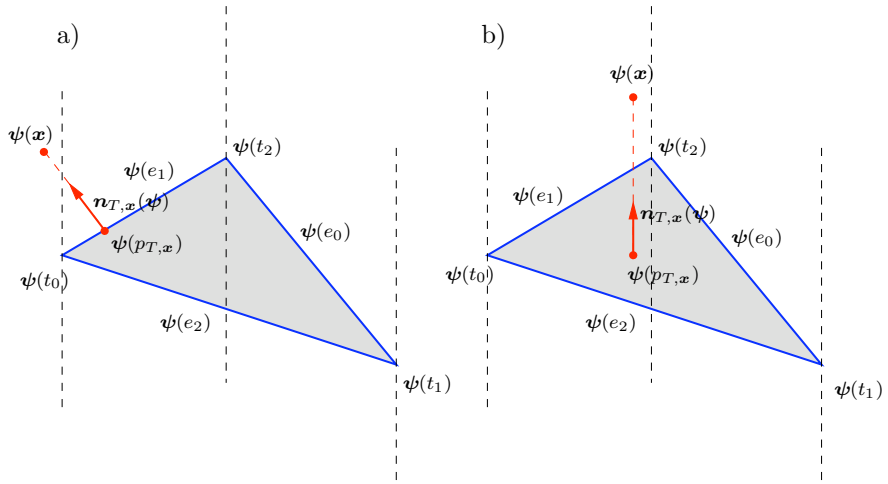

Figure 5.8: Possible configurations of the unit vector $\mathbf{n}_{T,\mathbf{x}}(\boldsymbol{\psi})$. a) $\boldsymbol{\psi}(\mathbf{x})$ is in the part of the space opposed to $\boldsymbol{\psi}(t_1)$ with respect to the plane that contains $\boldsymbol{\psi}(e_1)$. b) $\boldsymbol{\psi}(\mathbf{x})$ is inside the cylinder determined by the intersection of the three perpendicular planes to $\boldsymbol{\psi}(T)$.

As in the two-dimensional case, we observe that the convex neighborhood can also be rewritten as:

$$\mathcal{C}(\boldsymbol{\psi}) = \Big\{ \begin{array}{l} \boldsymbol{\varphi} \in X, F^{j,k}_{a,b}(\boldsymbol{\varphi}) \leq 0 \ \forall j,k \in \{0,1\}, \\ \text{for all edges } a \text{ and } b \text{ of the mesh } \mathcal{T} \text{ such that } a \cap b = \emptyset \\ \text{and } F^{k}_{T,\mathbf{x}_i}(\boldsymbol{\varphi}) \leq 0 \ \forall k \in \{0,1,2\}, \text{for all triangle } T \\ \text{and all vertex } x \text{ of the mesh } \mathcal{T} \text{ such that } x \notin T \Big\}, \end{array} \tag{5.7}$$

where

$$F^{j,k}_{a,b,\boldsymbol{\psi}}(\boldsymbol{\varphi}) = \varepsilon_g - \mathbf{n}_{a,b}(\boldsymbol{\psi}) \cdot (\boldsymbol{\varphi}(a_j) - \boldsymbol{\varphi}(b_k)),$$

and

$$F^{k}_{T,\mathbf{x}_i,\boldsymbol{\psi}}(\boldsymbol{\varphi}) = \varepsilon_g - \mathbf{n}_{T,\mathbf{x}_i}(\boldsymbol{\psi}) \cdot (\boldsymbol{\varphi}(t_k) - \boldsymbol{\varphi}(\mathbf{x}_i)).$$

If loop 2 converges, the limit satisfies the following optimality system:

$$\left\{\begin{array}{rcl} \langle J'(\boldsymbol{\varphi}),\boldsymbol{\xi}\rangle & - & \displaystyle\sum_{a}\sum_{\substack{b\\ a\cap b=\emptyset}} \mathbf{n}_{T,\mathbf{x}_i}\cdot\Big(\sum_{j=0}^{2}\sum_{k=0}^{2}\lambda_{a,b}^{j,k}\boldsymbol{\xi}(a_j)-\lambda_{a,b}^{j,k}\boldsymbol{\xi}(b_k)\Big) \\ & - & \displaystyle\sum_{T}\sum_{\mathbf{x}_i\notin T}\mathbf{n}_{T,\mathbf{x}_i}\cdot\Big(\sum_{k=0}^{3}\lambda_{T,\mathbf{x}_i}^{k}\boldsymbol{\xi}(\mathbf{x}_i)-\lambda_{T,\mathbf{x}_i}^{k}\boldsymbol{\xi}(t_k)\Big)=0 \qquad \forall\boldsymbol{\xi}\in X, \\ & & \lambda_{a,b}^{j,k}F_{a,b,\boldsymbol{\psi}}^{j,k}(\boldsymbol{\varphi})=0 \qquad \forall j,k\in\{0,1\}, \\ & & \lambda_{T,\mathbf{x}_i}^{k}F_{T,\mathbf{x}_i,\boldsymbol{\psi}}^{k}(\boldsymbol{\varphi})=0 \qquad \forall k\in\{0,1,2\}. \end{array}\right. \tag{5.8}$$

where $\lambda_{a,b}^{j,k}\geq 0$ and $\lambda_{T,\mathbf{x}}^{k}\geq 0$ represent respectively the four Lagrange multipliers associated with the (a,b) edge/edge problem and the three ones associated with the $(T,\mathbf{x}_i)$ triangle/vertex problem.

5.3.3 Minimization with convex constraints (loop 3)

The most inner loop aims at solving an optimization problem with convex constraints: given an hydrodynamic force $\boldsymbol{\sigma}^{\mathrm{f},j}$ (loop 1), given a convex neighborhood $\mathcal{C}(\boldsymbol{\psi})$ of the current solid deformation $\boldsymbol{\psi}=\boldsymbol{\varphi}^{j,k}$ (loop 2), we have to solve

$$\inf_{\boldsymbol{\varphi}\in\mathcal{C}(\boldsymbol{\psi})} J(\boldsymbol{\varphi}), \tag{5.9}$$

The convex set $\mathcal{C}(\boldsymbol{\psi})$ being defined by (5.3) in 2D and by (5.7) in 3D.

To solve problem (5.9), various methods – like penalization or relaxation with projection – may yield substantial changes of the structure solver. Here we adopt a method which consists in maximizing a dual energy. We present it in 2D, the extension in 3D being obtained *mutatis mutandis*.

Denoting by ζ the vector $(\zeta_{e,\mathbf{x}_i}^{\pm})$, where $(e,\mathbf{x}_i)$ describes all the couples edge/nodes such that $\mathbf{x}_i\notin e$, we look for the maximum of the dual energy

$$G(\zeta)=\inf_{\boldsymbol{\varphi}\in X}\left[J(\boldsymbol{\varphi})+\sum_{e}\sum_{\mathbf{x}_i\notin e}\big(\zeta_{e,\mathbf{x}_i}^{-}F_{e,\mathbf{x}_i,\boldsymbol{\psi}}^{-}(\boldsymbol{\varphi})+\zeta_{e,\mathbf{x}_i}^{+}F_{e,\mathbf{x}_i,\boldsymbol{\psi}}^{+}(\boldsymbol{\varphi})\big)\right],$$

under the constraint $\zeta_{e,\mathbf{x}_i}^{\pm}\geq 0$. In a gradient method with projection, these constraints are very easy to implement, whereas the original one, namely $\boldsymbol{\varphi}\in\mathcal{C}(\boldsymbol{\psi})$, is complicated. This is the usual motivation of the dual approach. In our specific framework, this method has another advantage: during the resolution by a gradient method of the dual problem, the structure solver exchanges the same kind of information as for the coupling with the fluid (it receives loads, it sends displacements, see Figure 5.9). The contact treatment can therefore be easily included as an inner-loop in the global algorithm without any change in the structure solvers. Even if other optimization methods are known to perform better than the gradient method, the possibility to use the structure solver as a "black-box" is a strong motivation for the proposed approach.

We can summarize the loop 3 as follows:

Algorithm 5.3 *Loop 1: Fluid-Structure.*

Initial guess: λ^0;
Do

Step 1 : (Structure problem)
Find $\boldsymbol{\varphi}^l \in X$ such that $\forall \boldsymbol{\xi} \in X$,

$$\langle J'(\boldsymbol{\varphi}^l), \boldsymbol{\xi} \rangle = -\sum_e \sum_{\mathbf{x}_i \notin e} \lambda^-_{e,\mathbf{x}_i} \langle (F^-_{e,\mathbf{x}_i,\psi})'(\boldsymbol{\varphi}^l), \boldsymbol{\xi} \rangle + \lambda^+_{e,\mathbf{x}_i} \langle (F^+_{e,\mathbf{x}_i,\psi})'(\boldsymbol{\varphi}^l), \boldsymbol{\xi} \rangle$$
$$= \sum_e \sum_{\mathbf{x}_i \notin e} \mathbf{n}_{e,\mathbf{x}_i}(\psi) \cdot \big((\lambda^-_{e,\mathbf{x}_i} + \lambda^+_{e,\mathbf{x}_i}) \boldsymbol{\xi}(\mathbf{x}_i) - \lambda^-_{e,\mathbf{x}_i} \boldsymbol{\xi}(e^-) - \lambda^+_{e,\mathbf{x}_i} \boldsymbol{\xi}(e^+) \big).$$

Step 2 : (Gradient iteration with projection)

$$\lambda^{l+1,\pm}_{e,\mathbf{x}_i} = \mathbf{P}_{\mathbb{R}^+} \left(\lambda^{l,\pm}_{e,\mathbf{x}_i} + \alpha^l F^{\pm}_{e,\mathbf{x}_i}(\boldsymbol{\varphi}^l) \right); \tag{5.10}$$

While $\|\lambda^{l+1} - \lambda^l\| > \varepsilon_{\text{cvx}}$;

The projection operator introduced in step 2 is defined by:

$$\mathbf{P}_{\mathbb{R}^+}(x) = \begin{cases} x & \text{if} \quad x > 0 \\ 0 & \text{if} \quad x \leq 0. \end{cases}$$

Remark 5.2 *In Algorithm 5.3, the choice of the descent step α^l is critical to ensure the convergence (possibly fast) of the scheme. Nonetheless, the identification of a "good" α^l is in general not trivial if we assume that deformations are the only output of the structure solvers. Indeed, in the logic of a non-linear optimization algorithm, we would be tempted to demand for the evaluation of the discrete energy J in order to apply a line search procedure. Constraining ourselves to use only information on $\boldsymbol{\varphi}$, two approaches have been considered:*

1. *A first possibility is to assume the descent step constant during the simulation. A heuristic argument based on the steepest descent method suggests to take this constant of order H/τ^2, being τ the time-step. This approach provides a very good estimate of α^l, especially for τ small, and remarkably reduces the efforts to identify by trials the magnitude of the constant.*

2. *A second possibility, currently under investigation, is based on the reinterpretation of (5.10) as a fixed-point problem in λ. Within this idea, it seems possible to retrieve an automatic choice of α^l for example with a simple Aitken extrapolation. Preliminary numerical tests are very promising and indicate a fast convergence of the algorithm, however further investigations from the theoretical viewpoint are needed.*

Remark 5.3 *For efficiency, it is of course recommended to restrict the sets edge/vertex in 2D or edge/edge, triangle/vertex in 3D to those elements which can actually experience contact.*

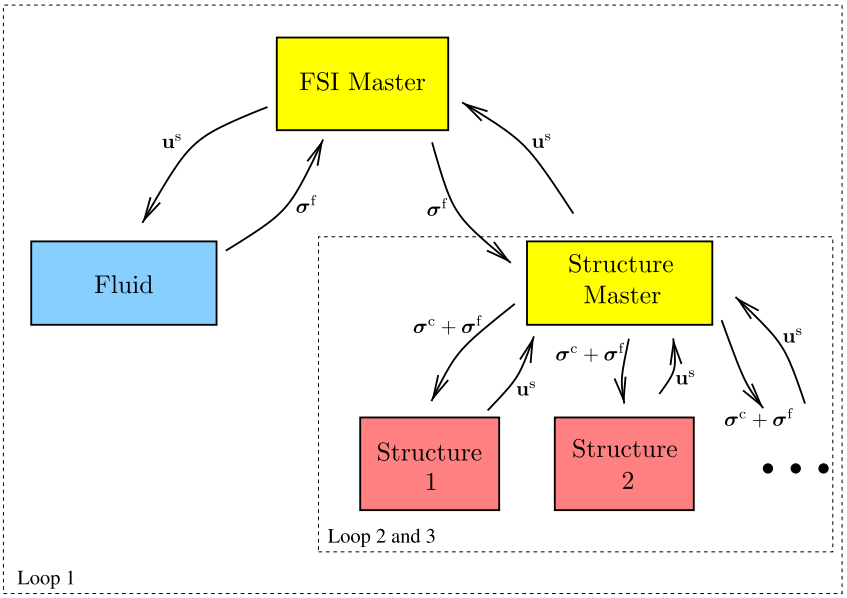

Figure 5.9: FSI with multi-body contacts: $\boldsymbol{\sigma}^f$ stands for the hydrodynamic force, and $\boldsymbol{\sigma}^c$ for the contact force.

Remark 5.4 [chordae tendineae] *Contacts are not the only relevant constraints in the applications to cardiac valves. For example, the* chordae tendineae *prevent the leaflet of the mitral valves from everting into the atrium. We have also implemented the capability to deal with such constraints in our framework. More precisely, let C be a point on the ventricular wall, and let M be the point of the valve to which a* chorda *(length L) is attached. It is straightforward to adapt the dual algorithm presented above to the constraint:*

$$dist(C, M) \leq L.$$

The Lagrange multiplier corresponds in this case to the tension applied on the valve by the string. Once again, the structure codes have not been modified which is an additional illustration of the versatility of the method.

5.3.4 Remarks on implementation

The independent solvers are coupled by exchanging "messages" (through PVM or MPI). The organization is sketched in Figure 5.9: a "fluid-structure master" manages the FSI coupling algorithm (loop 1), while a "structure master" manages the contact (loop 2 and 3). Whatever the coupling algorithm (loosely coupled, strongly coupled, *etc.*), whatever the fluid formulation (ALE, fictitious domains, or both), whatever the number and the kind of structures (valves, walls), in presence of contact or not, the only modification to perform in existing solvers are as limited as possible: for the fluid, it only consists in sending a load and receiving displacements whereas, for the structure it only consists in sending displacements and receiving a load.

5.4 Numerical experiments

In this section we present some numerical results obtained on a realistic geometry of an aortic valve with the aim of testing the proposed algorithm.

The aortic valve lets the blood flow in the ascending aorta, and prevents its back flow to the heart. It is composed of three semilunar leaflets attached to the aortic root. Behind them, three anatomic dilatations define the Valsalva sinuses in which the two coronary arteries are attached. A two-dimensional sketch of the valve is presented in Figure 5.10. Some anatomical characteristics and mechanical properties of the valve can be found in [dHPSB03, Thi08b].

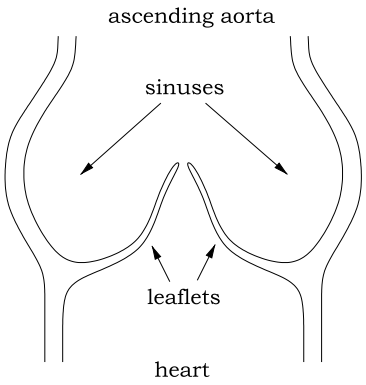

Figure 5.10: Two-dimensional representation of the aortic valve.

Since the target of the numerical simulation is to test the multi-body contact algorithm, only the leaflets of the valve are considered flexible (red colored in Figure 5.11); the remaining part, blue colored, is the fluid domain boundary, which is assumed fixed. The discretized FSI domain contains approximately 80000 tetrahedra for the fluid (Figure 5.12) and 2500 shell elements for the solid (Figure 5.13).

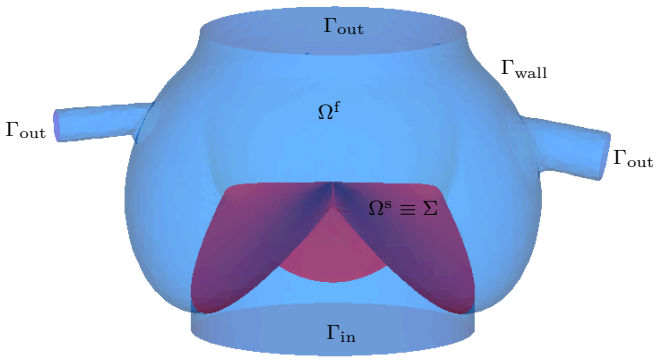

Figure 5.11: Computational domain.

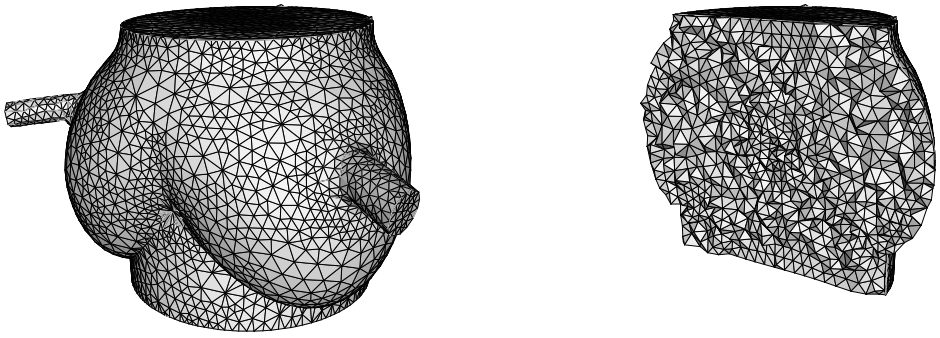

Figure 5.12: Fluid computational domain. On the left: surface mesh. On the right: inside clipping to show the spatial discretization step.

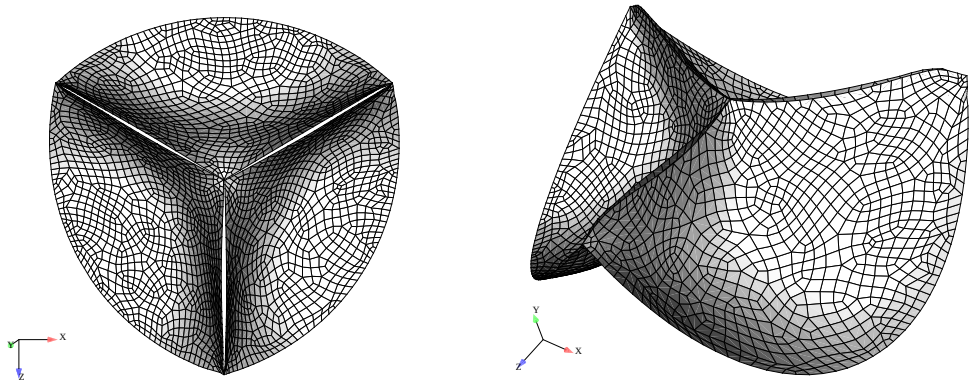

Figure 5.13: Structure computational domain from two different viewpoints.

From the mathematical viewpoint, the issue of contacts between bodies immersed in a viscous fluid is complicated and can lead to paradoxical results. For example, it is proved in [Hil07] that an immersed body cannot reach in finite time the boundary of the cavity surrounding the fluid. This interesting problem is beyond the scope of this work. From the computational viewpoint, it clearly appears that contacts do occur and have to be handled. To illustrate this point, we propose two simulations: the first one without handling the contact, the second one handling it with the contact algorithm proposed above.

We provide here the details of the test case. A periodic pressure difference is applied between the inlet and outlet of the fluid domain. On Γ_{in} the following pressure function is imposed:

$$p_{in} = \begin{cases} A & \text{if} \quad 0 \leq t \leq \frac{13T}{28} \\ -A & \text{if} \quad \frac{13T}{28} \leq t \leq T \end{cases},$$

with amplitude $A = 130\,\text{dyn/cm}^2$ and period $T = 0.28\,\text{s}$. Note that the duration of the systolic phase roughly corresponds to the physiological one. But, in order to test the robustness of the algorithm over several opening and closure cycles, we have

artificially reduced the duration of the diastole. On Γ_{out} free boundary conditions are set: $\boldsymbol{\sigma}^{\text{f}} \cdot \mathbf{n}^{\text{f}} = 0$; while on Γ_{wall} a no slip boundary condition is imposed. For the fluid, the density ρ^{f} and the dynamic viscosity μ are respectively $1.0\,\text{g/cm}^2$ and $0.03\,\text{poise}$. For the solid, a valve thickness of $0.65\,\text{mm}$ has been considered. The structure density ρ^{s} and the Young modulus E are respectively $1.2\,\text{g/cm}^2$ and $10000\,\text{dyn/cm}^2$. Both the simulations run with a time-step τ of $10^{-3}\,\text{s}$ for a total time of $3T$ to attend the periodic condition; the fluid-structure tolerance ε_{fsi} is finally set to 10^{-4}. For the contact algorithm a gap of $10^{-3}\,\text{cm}$ is imposed and the tolerances $\varepsilon_{\mathcal{C}}$ and ε_{cvx} are respectively fixed to $5.\ 10^{-6}$ and $5.\ 10^{-7}$.

At the closure of the valve, if the contact is not handled, a non-physical overlap of the leaflets is observed, as illustrated in Figure 5.14. This of course results in a dramatic change of the flow and the structure displacements. Moreover, in this case, locking phenomena among the leaflets or numerical instabilities can also happen, as noticed in [dS07]. These observations confirm the importance of managing the contact correctly.

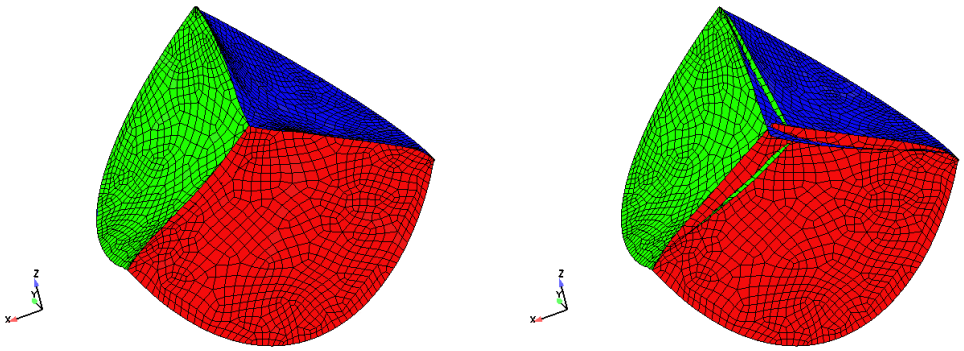

Figure 5.14: Comparison between the two simulations at $t = 0.259\,s$. On the left side, the contact among leaflets is handled with the contact algorithm, on the right side, it is not.

In Figures 5.15 and 5.16, the valve displacements, the blood velocity and pressure are reported for different time-steps in the case of contact handling. A maximum velocity of approximatively $20\,\text{cm/s}$ has been obtained during the simulation. At time-steps 0.212 and 0.268, the velocity vectors show in particular the blood recirculations that happen behind the aortic valve. Moreover, a pressure jump across the valve could be observed during the closure period.

5.5 Conclusion

The presented partitioned strategy allows the solution of FSI problems in which contact among multiple deformable bodies can occur. The scheme is conceived to address the problem with existing structure solvers that are not supposed to handle contact by themselves. From the mathematical viewpoint, the hypothesis of non-penetration among solid objects defines a non-convex constraint optimization

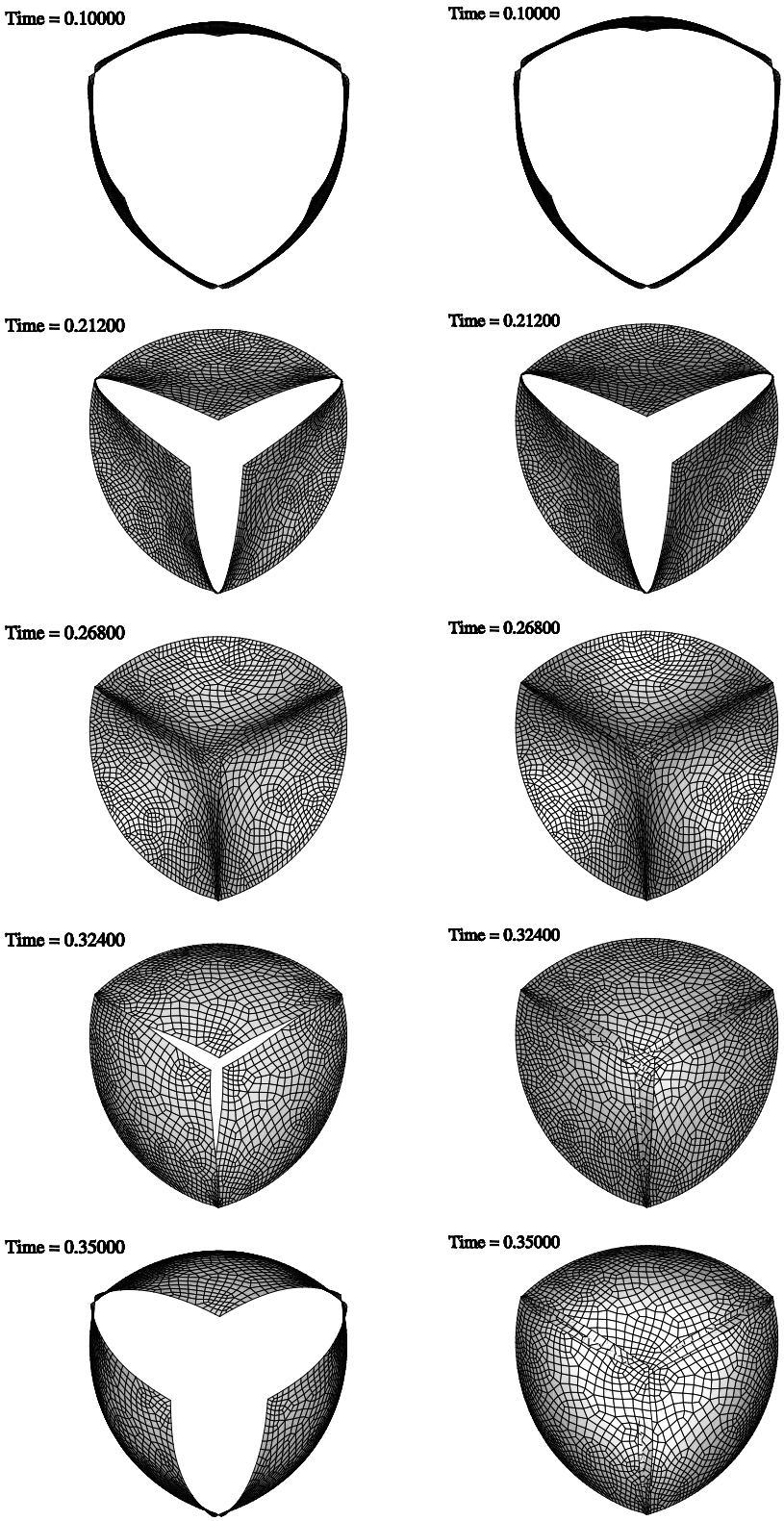

Figure 5.15: Valve displacements for five different time-steps in the simulations with (left) and without (right) contact handling. Note the dramatic difference between them at the reopening of the valve.

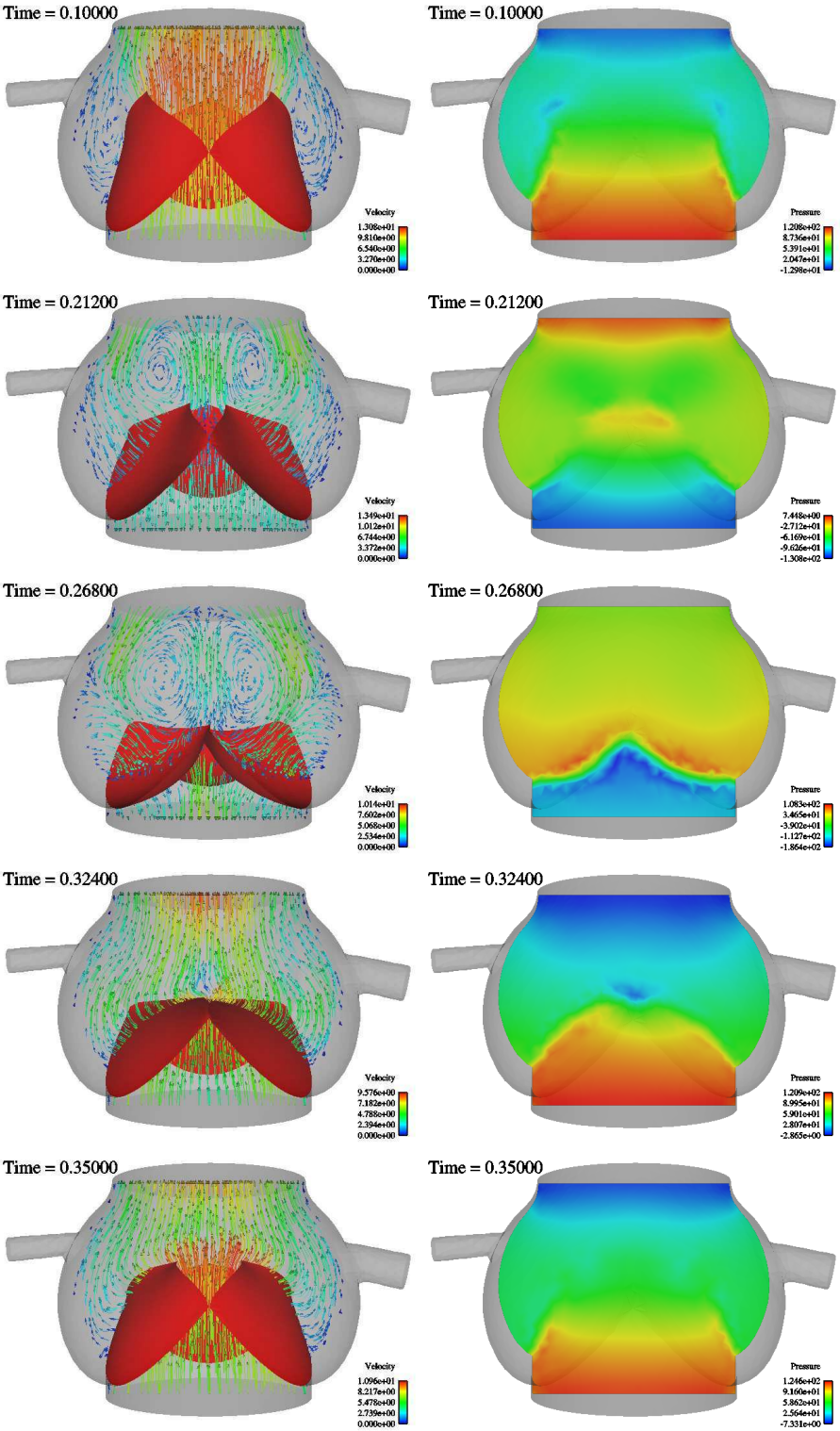

Figure 5.16: Blood velocity vectors (left) and pressure field (right) for 5 different time-steps.

problem that has been solved with an iterative approach. The bidimensional and tridimensional formulations are introduced and details on the implementation are given.

With the purpose of illustrating the coupling algorithm, the dynamics of an idealized aortic valve has been simulated for simplified flow conditions. In the proposed test case, several simplifications have been done, nonetheless important qualitative differences due to the use of the contact algorithm are already remarkable. In the next section, the same algorithm is applied to more realistic conditions in terms of peak velocity, opening and closure time of the valve.

Chapter 6

Computational analysis of an aortic valve jet with Lagrangian coherent structures

M. Astorino, J.-F. Gerbeau, S. Shadden, I.E. Vignon-Clementel. *Realistic blood flow through the aortic valve: simulation and analysis.* Conference Proceedings CMBE, 2009. Editors: P, Nithiarasu, R. Lohner, R. van Loon. Swansea, ISBN 978-0-9562914-0-0

S. Shadden, M. Astorino, J.-F. Gerbeau. *Computational analysis of an aortic valve jet with Lagrangian coherent structures.* Chaos, Vol. 20, 017512, 2010. doi:10.1063/1.3272780

Contents

6.1 Introduction

The aortic valve releases pressurized blood from the left ventricle into the ascending aorta during the systolic phase of the cardiac cycle and prevents possible back flow during the diastolic refilling phase. In normal anatomy, this valve is composed of three semilunar leaflets (cusps) that move apart or mate together in response to the pressure gradients imposed by the blood pumped from the heart.

Among the pathologies that may affect the functioning of the valve, aortic stenosis (AS) is one of the most common (see Section 1.1, p. 7). AS is an abnormal narrowing of the aortic valve opening, which can result from various causes such as calcification, congenital or rheumatic diseases [GD06, BHB+09]. Depending on the severity of the AS, different medical treatments are used. For example, valve replacements are usually recommended for severe stenoses, and for mild or moderate stenoses, therapies to control symptoms and restriction of strenuous activities are often advised.

Over the past years, the medical community broadly accepted that reliable assessment of AS requires estimates of the aortic valve area (AVA) [GD06]. Direct

visualization of the anatomical area of the stenotic orifice, the so-called geometric orifice area (GOA), has been considered a theoretically ideal way to assess the AS. Nonetheless, as observed in [Bau06], proper delineation of the orifice circumference by means of image-based planimetry has been found to be difficult and moreover it has been noticed that GOA doesn't characterize the flow properties related to the stenosis. Hence, the development of good clinical indices to accurately assess the AS is still an active research field.

Depending on the employed diagnostic technique, different indices to assess the AVA have been developed - the most popular among them being based on the Gorlin formula [GG51] and the continuity equation [RCMC86]. The Gorlin formula requires an evaluation of the pressure gradient across the valve to estimate the AVA. The index, called Gorlin area, can be obtained either with invasive measurements of pressure, done with micromanometer catheters, or by applying the classical Bernoulli equation to Doppler velocity measurements. Instead the continuity equation, based on the law of conservation of mass, provides an estimate of the AVA, the so-called effective orifice area (EOA), from noninvasive Doppler echocardiography measurements of the blood velocity.

Although the GOA, the Gorlin area and the EOA were initially believed to provide a similar estimation of the AVA, extensive comparison between the three quantities (*e.g.* see [DY91, CSC+92]) revealed important differences among them. As a matter of fact, the Gorlin formula and the continuity equation asses the stenosis severity taking into account the associated flow properties with some basic physical principles, such as Torricelli's law, Bernoulli's law and conservation of mass, while the GOA is a purely geometrical measure. In practice, the Gorlin area and the EOA provide an estimate of the minimal cross-sectional area of the jet formed downstream of the valve by the blood ejected during systole (Figure 6.1). We refer to [GK06] for a detailed discussion about these indices.

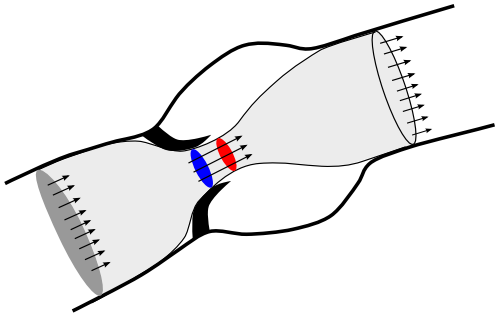

Figure 6.1: Schematic representation of the aortic valve and of the corresponding jet flow (grey). In blue the geometric orifice area (GOA), in red the effective orifice area (EOA).

The importance of the flow dependence in AS characterization has been widely investigated and is now well-established. As a consequence, the Gorlin area and the

EOA are usually preferred to the GOA, which is no longer considered a reliable index for AS. Important efforts are currently underway on improving clinical indices to better diagnose AS. Among them, for example, is the energy loss coefficient, E_LCo, proposed in [GPD+00], which reflects the energy loss induced by the aortic stenosis and aims to better describe the increased overload imposed on the left ventricle.

In this chapter, we focus on the EOA, which is the most common index for the assessment of AS, as it can be derived from noninvasive Doppler echocardiography [Bau06]. This index aims to assess AS by quantifying the size of the jet of ejected fluid from the heart. However, as a downside, it does not provide any direct, physical understanding of the actual geometry and dynamics of the jet. The analysis demonstrates a computational method to directly measure the jet size, shape and dynamics, which we believe provides a better and more clinically-relevant description of the jet.

The application of mathematical models and numerical tools to assess AS is a rather new field. In previous work, reduced models and simplified multi-dimensional models [DSVC98, GBP+05] have been proposed to test the validity and quality of clinical indices. More recently, progress in numerical simulation of fluid-structure interaction (FSI) around cardiac valves (see for example [MP01, dHPSB03, vLADB04, WKM07a, dSGB08, AGPT09] and Chapter 5) has enabled multi-dimensional FSI models to be applied to the analysis of aortic valve stenosis [GDP07, CDdSG+05, vL09]. In [vL09], instantaneous Eulerian measures obtained from a 3D FSI model of the aortic valve were used to compare different clinical indices for various stenotic geometries. Instantaneous Eulerian metrics are convenient since they can be directly obtained from the FSI simulations, but many important flow features are more easily comprehended using Lagrangian metrics.

Here we utilize the computation of Lagrangian coherent structures, LCS, to post-process results from multi-dimensional FSI simulations of the aortic valve. The LCS method is an advanced post-processing technique for examining unsteady fluid transport in a clearer way than with the visualization of instantaneous Eulerian quantities. Within this method, special moving boundaries - the LCS - are computed in the fluid domain, and can be used to reveal dominant flow features, such as vortex boundaries or separation profiles, or uncover kinematic processes organizing fluid mixing. Knowledge of transport mechanics in the cardiovascular system is particularly compelling. Disturbed flow conditions, including vortical or separated flow, are known to influence health maintenance and disease progression [WK99]. Therefore, strong motivation exists to utilize LCS to better understand transport in the cardiovascular system [ST08, XCS+09]. In the particular case of aortic valve stenosis, LCS can characterize flow separation downstream of the valve and identify the time-dependent bounding surface of the blood flow jet. As a consequence, a precise measure of the "effective orifice area", or jet size, can be evaluated.

The chapter is organized as follows: in Section 6.2, we discuss the major challenges in the numerical simulation of FSI problems with cardiac valves. Next, a detailed description of the computation of the LCS is provided in Section 6.3. In Section 6.4, two different test cases, one two-dimensional and one three-dimensional,

are used to illustrate the computational framework. A discussion on the results is contained in Section 6.5.

6.2 Challenges in FSI simulations with cardiac valve

In the last decades, many important progresses have been made in the simulation of the blood - valve interaction. These advances covered various interesting aspects such as the mathematical modeling, the mechanical characterization of valves and the numerical methods for the resolution of the corresponding problems (see Sections 1.2, 2.2.2 and 5.1). Although the progresses, various difficulties still make these simulations very challenging. Before presenting the numerical results obtained, a discussion on the numerical difficulties experienced in the numerical simulation of cardiac valves is in order.

Let us follow the sequence of technical steps needed to realize a numerical simulation of native valves. The first difficulty we encounter is the correct definition of the valve shape in its zero-energy configuration. This information is extremely important for the correct simulation of the dynamics of the valve during the whole cardiac cycle but it is in general very difficult to retrieve from a bioengineering viewpoint. Indeed, it is well-known that properties of biological tissues change whether they are tested *in vivo* or *in vitro*. Some work is devoted to the characterization of the geometrical properties and shape of the valves, we recall for example [SC74, Thu90, Tra06] for the aortic valves.

A second difficulty is the definition of a correct test case. In Chapter 5, Neumann-type boundary conditions are used at the inlet and outlet of the aortic root in order to retrieve the opening and closure dynamics of the valves. Nonetheless, when more physiological values of velocity and pressure are involved, the prescription of these boundary conditions seems to be extremely delicate because of the fluid dynamics instabilities (not necessarily related to the FSI problem) that frequently develop at the inlet or outlet of the fluid domain. As a consequence a flow boundary condition is usually imposed to improve the robustness of the numerical simulations. It must be observed however that, in a fluid domain like the one we consider in Section 5.4, this type of condition is appropriate during the opening - closure phase but is inadequate when the valve is closed. A brief explanation of this statement is in order. Let us observe first that a "perfectly closed" valve separates the fluid domain into two sub-domains (one below and the other above). The assumption of Dirichlet boundary condition at the inlet, automatically implies that the fluid contained in the lower sub-domain has to satisfy Dirichlet conditions all over the boundary when the valve is closed. To be precise, we have a no-slip condition on the wall, $\mathbf{u} = \mathbf{u}^{\mathrm{s}}$ on the valve, and $\mathbf{u} = \mathbf{u}_D$ on the inlet boundary. For the fluid incompressibility constraint, the flow imposed must be neither positive, otherwise the valves open, nor negative, otherwise the valves "reverse". When the valves are closed, the imposed flow must be zero (assuming fixed walls). However, in order to set it to be zero, it is necessary to know a priori when the valve is fully closed, which

is not straightforward for native valves. Notice however, that numerical simulations with an imposed flow at the inlet are commonly - and correctly - performed for the analysis of the opening and closing dynamics of valves during the systolic phase (see for example [dH02, vL05]). In this chapter, we focus on the systolic phase to investigate blood flow jet across the aortic valve, as a consequence, in the numerical simulations a flow is imposed at the inlet in order to retrieve physiological values of the peak velocity across the valve.

For mechanical valves, a strategy that circumvents the previous difficulty is given in [HNP+06]. The authors proposed to simulate the systolic phase of the cardiac cycle imposing a flow boundary condition and then to "switch" to a Neumann condition only at the end of the systole. At the beginning of the diastole, a pressure curve that mimics the pressure in the ventricle is applied at the inlet. Note that, the initial imposed pressure is chosen to be consistent, in magnitude and temporal slope, with that computed at the end of the systole. This choice is justified by the fact that that the heart tends over the longer term to adjust pressure and ventricular volume to achieve an appropriate systolic ejection. This method is in principle applicable to the numerical simulation of all types of valves. Nevertheless, other major difficulties, like incertitude related to the geometric shape and to the mechanical properties, make the simulation of native valves still very difficult.

A third difficulty, related to the numerical method in use, must be pointed out. The fictitious domain method, like the immersed boundary method, is a *diffused interface method* (see [SB09]), which means in practice that the pressure jump across the interface is slightly smeared. From a numerical viewpoint, the smearing of very high pressure jumps, like the one experienced during the diastole by the aortic valves, may lead to inaccuracies in the flow distribution and instabilities in the worst case. On the contrary, during the systole, because of the small pressure difference, this smearing is negligible and the results do not seem to be affected.

In the following, the algorithm proposed in Chapter 5 is used to simulate the flow across an aortic valve. A two-dimensional test case and a three-dimensional one are presented. In both cases a $(d-1)$-dimensional model is used, the corresponding internal energies are given in Section 2.2.2, equation (2.24) for the 1D structure model, equation (2.21) for the shell model. For the fluid, a flow is imposed at the inlet, a resistance at the outlet. On the remaining boundaries, we have a no-slip boundary condition. Note that these conditions are comparable to the ones imposed in other works on aortic valve simulations (see for example [dH02]). As mentioned before, it is difficult with such boundary conditions to retrieve the exact physiological behavior of the valves during the whole cardiac cycle. In particular the phase when the valves are totally closed is specially delicate. Nevertheless, we succeeded in getting correct valve opening and closing time, physiological ejection time and peak velocity [RBM+06]. As a result, these simulations allow to study the evolution of the blood jet profile downstream of the aortic valve.

Remark 6.1 *The problems discussed, together with the high computational costs of the numerical simulations, make this kind of numerical simulation very challenging.*

Considering all the difficulties, it may be interesting to explore also alternative solutions - more efficient and robust - that can be applied in all those clinical applications where a precise description of the leaflet mechanics is not stricly required. A step in this direction is made in Chapter 7, where we present a new reduced model for heart valves that offers a compromise between standard lumped parameter models and fully FSI problems.

6.3 Computation of LCS

The identification of the Lagrangian Coherent Structures (LCS) can be effectively achieved from the computation of finite-time Lyapunov exponent (FTLE) fields. The FTLE field is a scalar quantity which characterizes the amount of stretching about the trajectory of a point $\mathbf{x} \in \Omega^{\mathrm{f}}$ over the time interval $[t, t+T]$. The FTLE fields are computed by postprocessing the results obtained from the FSI simulation. In practice, they are obtained by integrating dense meshes of Lagrangian particles and LCS are extracted as codimension-one structures that maximize the FTLE measure (see *e.g.* [Hal01, SLM05, LSM07]). Due to complex geometries and highly transient flow conditions, care must be taken in computing LCS in cardiovascular applications. Below, practical considerations relevant to the computation of FTLE from blood flow data obtained by the finite element method are discussed. In particular, the handling of large data sets and efficient integration on unstructured velocity meshes is addressed. The focus is on 3D data; minor modifications are needed to address 2D data.

Kinematic model. An essential step in the computation of the FTLE field is the computation of particle trajectories. In reality, blood is a composition of water containing various dissolved substances and suspended cells. However, it is reasonable to treat blood as a homogenous fluid over the length scales considered given the small size of the cells and nearly uniform density of the suspension. Furthermore, the time scales considered are sufficiently short (on the order of 1 second) that inter-cellular interactions and diffusion may typically be neglected. For example the diffusion coefficient of platelets is estimated to be on the order of 10^{-6} to 10^{-7} cm^2/s [CPSS78], whereas $\mathbf{u}$ is typically on the order of 10^1 to 10^2 cm/s. Therefore, it is reasonable to assume that advection dominates transport and the equation governing particle trajectories is

$$\mathbf{x}(t+T) = \mathbf{x}(t) + \int_t^T \mathbf{u}(\mathbf{x}(\tau), \tau) d\tau \ . \tag{6.1}$$

When defining the FTLE, it is convenient to rewrite the solution to Eq. (6.1) as a mapping $\phi(\mathbf{x}, t, T) : \mathbf{x}(t) \mapsto \mathbf{x}(t+T)$, as details of the trajectory itself are inconsequential. A discrete approximation for the spatial variation of this flow map can be obtained by integrating a mesh of particles, from which the linearization of

the flow map can be computed. The FTLE is then obtained as

$$\sigma(\mathbf{x}, t, T) = \frac{1}{\|T\|} \ln \left\| \frac{d\phi(\mathbf{x}, t, T)}{d\mathbf{x}} \right\| , \tag{6.2}$$

where the induced L_2 norm is used. It is not difficult to show (see [SLM05]) that

$$\|\mathbf{y}(t+T) - \mathbf{x}(t+T)\| \approx \exp^{\sigma(\mathbf{x},t,T)T} \|\mathbf{y}(t) - \mathbf{x}(t)\| \tag{6.3}$$

for small $\|\mathbf{y}(t) - \mathbf{x}(t)\|$. Thus, strongly hyperbolic trajectories will have a high FTLE values.

The utility of LCS computations is founded on the building computational and experimental evidence that complex fluid motion encountered in nature is often dictated by locations of strong hyperbolicity, which force the dynamics of surrounding fluid to quickly converge or diverge. The computation of attracting LCS (obtained from FTLE fields when $T < 0$) and repelling LCS (obtained from FTLE fields with $T > 0$) enables us to understand these major flow features throughout the fluid domain.

Data management. Velocity data is specified over a tetrahedral mesh at times t^k, for $k = 1, \ldots, N_t$. Typically, the mesh size or temporal resolution is such that the velocity data is too large for the entire time history to be loaded into memory at once. Velocity is interpolated linearly in time, thus only data for two time points need be loaded concurrently. Using this strategy, the window of data loaded into memory is regularly shifted as the integration of particle trajectories proceeds.

The FTLE mesh is defined by a Cartesian grid with resolution N_x, N_y and N_z. A new mesh of particles is regenerated for each time the FTLE field is computed. Suppose t^r, $r = 1, \ldots, N_r$, denotes the times at which the FTLE field is to be determined. A new mesh of $N_\mathbf{x} = N_x \times N_y \times N_z$ particles is released N_r times. The total number of particles to be tracked, $N_\mathbf{x} \times N_r$, can be quite large. Thus, for each new window of velocity data loaded into memory, each release is processed over that time window sequentially to avoid high memory usage; for example, starting from $t^{k=1} \leq t^{r=1}$, the general algorithm would be as follows:

```
Load velocity data from t^k to t^{k+1}
For each release r = 1, ..., N_r
    If t^r < t^{k+1} and t^r + T > t^k
        Load data for release r into memory
        For each particle j = 1, ..., N_x
            Solve for x_r^j(t) from t = max(t^k, t^r) to t = min(t^{k+1}, t^r + T)
        EndFor
        Write data for release r to file
    EndIf
EndFor
```

New velocity data is loaded as needed to integrate all FTLE releases. Here, we have assumed that $T > 0$. Appropriate modifications should be made for backward-time integration, *i.e.* $T < 0$, used to compute attracting LCS.

Parallelization. Since the particles are non-interacting, the integration of particle trajectories can readily be parallelized. When N_r is commensurate with the number of CPUs, N_p, the most straightforward parallelization is distributing each release to a separate process. This parallelization can be done in a cyclic fashion when $N_r > N_p$. When $N_r \ll N_p$, then it is more efficient to distribute blocks of particles to each process. For simulations where it is expected that particles will not readily exit the domain (as with most cardiovascular applications), a straightforward block partitioning of the FTLE mesh is reasonable. In applications where particles readily leave the domain, a cyclic domain decomposition or dynamic assignment of work is needed for load balancing.

Velocity interpolation. Let $\bar{e}(\mathbf{x}(t))$ define the element bounding the particle $\mathbf{x}(t)$ at time t. To interpolate the velocity at $\mathbf{x}(t)$, the velocities at the nodes of $\bar{e}(\mathbf{x}(t))$ are first interpolated in time by

$$\mathbf{u}_n^{\bar{e}}(t) = [1 - \delta_t]\mathbf{u}_n^{\bar{e}}(t^k) + \delta_t \mathbf{u}_n^{\bar{e}}(t^{k+1}) \,, \tag{6.4}$$

where $\mathbf{u}_n^{\bar{e}}$ denotes the velocity at node n of element $\bar{e}$, $t \in [t^k, t^{k+1}]$ and $\delta_t = [t - t^k]/[t^{k+1} - t^k]$.

For spatial interpolation, natural coordinates are utilized, *i.e.* a coordinate transformation $\mathbf{x} \mapsto \boldsymbol{\xi}$ is employed so that the nodes of $\bar{e}(\mathbf{x}(t))$ are located at $(0,0,0), (1,0,0), (0,1,0), (0,0,1)$, see Figure 6.2. In this frame, the velocity at location $\boldsymbol{\xi} = (\xi, \eta, \zeta)$ inside the element is given by

$$\mathbf{u}(\boldsymbol{\xi})(t) = \mathbf{u}_1^{\bar{e}}(t) + [\mathbf{u}_2^{\bar{e}}(t) - \mathbf{u}_1^{\bar{e}}(t)]\xi + [\mathbf{u}_3^{\bar{e}}(t) - \mathbf{u}_1^{\bar{e}}(t)]\eta + [\mathbf{u}_4^{\bar{e}}(t) - \mathbf{u}_1^{\bar{e}}(t)]\zeta \,. \tag{6.5}$$

Note that $\mathbf{u}(\mathbf{x})(t) = \mathbf{u}(\boldsymbol{\xi})(t)$, so to evaluate $\mathbf{u}(\mathbf{x})(t)$ from Eq. (6.5), the mapping $\mathbf{x} \mapsto \boldsymbol{\xi}$ is needed.

For tetrahedral elements, the transformation $\boldsymbol{\xi} \mapsto \mathbf{x}$ takes the same form as Eq. (6.5), that is,

$$\mathbf{x}(\boldsymbol{\xi}) = \mathbf{x}_1^{\bar{e}} + [\mathbf{x}_2^{\bar{e}} - \mathbf{x}_1^{\bar{e}}]\xi + [\mathbf{x}_3^{\bar{e}} - \mathbf{x}_1^{\bar{e}}]\eta + [\mathbf{x}_4^{\bar{e}} - \mathbf{x}_1^{\bar{e}}]\zeta \,, \tag{6.6}$$

where $\mathbf{x}_n^{\bar{e}}$ denotes the coordinates of node n of element $\bar{e}$. This mapping can be inverted to provide ξ, η, and ζ as a function of the nodal coordinates, $\mathbf{x}_n^{\bar{e}}$ (see [KL96]). These values can then be plugged into Eq. (6.5) to solve for $\mathbf{u}(\mathbf{x})(t)$.

Therefore, to interpolate the velocity at location $\mathbf{x}$ in physical coordinates we must (1) find the element containing $\mathbf{x}(t)$ at time t and (2) transform $\mathbf{x}$ to the element's natural coordinates. Since the particle at $\mathbf{x}(t)$ is constantly moving, in practice we work from a "guess", e_g, for the element we believe contains $\mathbf{x}(t)$ at time t and (1) transform $\mathbf{x}$ to the natural coordinate frame of e_g, (2) evaluate if indeed $\bar{e}(\mathbf{x}(t)) = e_g$, and (3) interpolate velocity if $\bar{e}(\mathbf{x}(t)) = e_g$, otherwise restart at step (1) using a new guess element, which is chosen as described next.

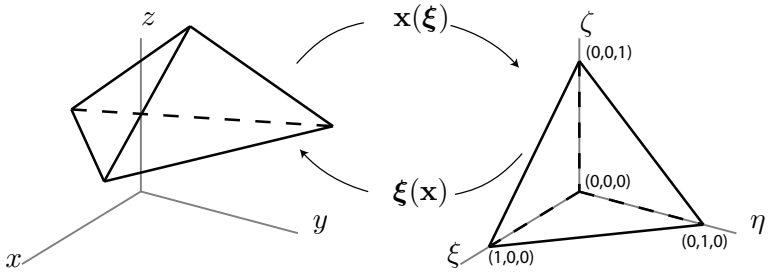

Figure 6.2: Transformation of tetrahedtral between physical coordinates (x, y, z) and natural coordinates (ξ, η, ζ).

Element search. Another advantage of mapping $\mathbf{x}(t)$ to natural coordinates is to simplify the search for $\bar{e}(\mathbf{x}(t))$. In the natural coordinates of e_g, $\mathbf{x}$ is bounded by e_g if all of the following are satisfied:

$$\xi \geq 0, \qquad \eta \geq 0, \qquad \zeta \geq 0, \qquad \text{and} \qquad 1 - \xi - \eta - \zeta \geq 0. \tag{6.7}$$

If any of these conditions are not satisfied, then a neighboring element is considered. Whichever condition is not satisfied indicates the neighbor to consider. For example, if $\xi < 0$, then the neighbor sharing the $\xi = 0$ face is used as the next guess. If more than one condition is not satisfied, the condition that is in greatest violation is used to determine the neighbor to search. In this way, the search progresses in the direction of the point and will readily converge to $\bar{e}(\mathbf{x}(t))$. Performing a local search in this manner requires adjacency information; this is usually available from the velocity mesh generation step, or can be computed as a preprocessing step. Also note that elements along the boundary of the velocity domain will have faces that are not shared with another element. If the local search tries to progress in the direction of a boundary face, the search returns a failure. When integrating a particle's trajectory, this occurs when the particle leaves the domain. When a particle leaves the domain, the integration for that particle is terminated.

Initialization. The efficiency of the local search method depends on the choice of the guess element. Before particles are integrated, the element containing each point in the FTLE mesh is determined. Roughly, this is performed as follows:

```
Globally search until ē(x^1) is found
For all FTLE nodes j = 2, ..., N_x
    Locally search for ē(x^j) using ē(x^{j-1}) as guess
    If above local search fails
        Use an alternative search method to locate ē(x^j)
    EndIf
EndFor
```

We have assumed that $\mathbf{x}^j$ neighbors $\mathbf{x}^{j-1}$ since the mesh is structured. If the intersection of the FTLE domain and velocity domain forms a non-convex set, then the local search protocol can fail for FTLE nodes located inside the velocity domain. Alternative search method(s) should be used when the local search fails (*e.g.* herein we used a local search from a seed location, but a global search, or other alternatives, may be needed for more complicated models). If any nodes in the FTLE mesh are located outside of the velocity domain, the alternative search method should be relatively robust at distinguishing these points while maintaining low computational expense. Additionally, one should ensure that the local search for $\bar{e}(\mathbf{x}^j)$ uses an appropriate guess element if $\mathbf{x}^{j-1}$ is located outside of the velocity domain.

Integration. The trajectory of each point in the FTLE mesh is obtained by solving Eq. (6.1). The integral on the right-hand side is evaluated using the 4th-order Runge-Kutta scheme or the adaptive time-stepping of the Runge-Kutta-Fehlberg method. The nominal time step size h (or limits for the adaptive stepping) is chosen from consideration of the CFL condition

$$\frac{h\mathbf{u}_{\max}}{\bar{d}} < C, \tag{6.8}$$

where $\bar{d}$ is the nominal edge size of the tetrahedral elements in the velocity field mesh and $\mathbf{u}_{max}$ is the maximum velocity occurring in space and time. Typically, $0.1 \leq C \leq 1$ is used in determining the nominal step size.

Once $\bar{e}(\mathbf{x}^j)$ has been computed for all FTLE nodes located inside the velocity domain, the integration of particles from $\mathbf{x}^j$ can readily proceed since the element bounding each particle is known. As the integration proceeds, the variation in the interpolation location (particle position) from one step to the next is small enough that the local element search typically only proceeds over, at most, a few elements, making the element search highly efficient.

Due to the discrete nature of the integration, special techniques are often needed to ensure particles do not cross vessel walls or get stuck near a no-slip wall. These problems are often minimized if boundary layer meshing is used when generating the velocity field mesh. To prevent particles from crossing the vessel wall, inlet and outlet faces can be tagged. When the local element search fails for a particle, one can difference the position of the particle before and after the integration step to determine if it crossed a vessel wall or an inlet/outlet face. If it is determined that the particle crossed a vessel wall, the integration procedure or interpolation can be modified. For example, the step size can be adapted or the component of the interpolated velocity vector in the direction of the wall can be removed or modified (used herein). Furthermore, higher order basis functions can be used when interpolating inside wall (no-slip boundary) elements to prevent particles stagnating near the wall due to linear interpolation underestimating tangential flow.

LCS extraction. Commonly, LCS are identified by visual inspection from the FTLE field. However, it is convenient to parameterize these structures, especially

when they are used for further postprocessing or analysis. In order to parameterize the LCS, we use the technique described in [Sha06]. Based on the definitions presented in [SLM05, LSM07], LCS are co-dimension one objects (lines in 2D, surfaces in 3D) that, generally speaking, satisfy the two conditions for each point $\mathbf{x}$ on the LCS:

D1 The gradient of $\sigma(\mathbf{x}, t, T)$ is aligned with the LCS.

D2 The principle direction (eigenvector) corresponding to the minimum eigenvalue of the Hessian of $\sigma(\mathbf{x}, t, T)$ is orthogonal to the LCS.

For these two conditions, the first and second derivatives of $\sigma(\mathbf{x}, t, T)$ must be computed from the FTLE field. When the field is "noisy" or contains many LCS, approximating these derivatives can be challenging and smoothing the field, or refining the computation of the FTLE field near the LCS, becomes necessary.

Let $\mathbf{e}_{\min}(\mathbf{x})$ denote the direction of minimum principle curvature (**D2**) in order to define the function $\alpha(\mathbf{x}) = \nabla_{\mathbf{x}}\sigma \cdot \mathbf{e}_{\min}$. LCS can be defined by the points $\mathbf{x}$ such that $\alpha(\mathbf{x}) = 0$. In practice, one may check for certain conditions at these points and exclude sections of the $\alpha(\mathbf{x}) = 0$ level set. For example, one can extract "well-defined" ridges by requiring the magnitude of the minimum principal curvature be above a certain threshold. For the case of 3D problems, one should also check that the finite-time deformation tensor

$$\left(\frac{d\phi(\mathbf{x}(t), t, T)}{d\mathbf{x}(t)}\right)^{\mathrm{T}} \left(\frac{d\phi(\mathbf{x}(t), t, T)}{d\mathbf{x}(t)}\right)$$

has only a single negative eigenvalue (see [LSM07, Definition 2.1]).

6.4 Numerical experiments

6.4.1 Two-dimensional simulation

Although flow through the aortic valve is inherently 3D, it is instructive to visualize the structure of the flow in the simple 2D case. For illustration purposes, flow through an idealized 2D heart valve model was investigated. The geometry of the aortic root shown in Figure 6.3 was used. The fluid domain was discretized by 5902 triangular elements. The two leaflets are of length 1.728 cm and each one was discretized by 54 Hermit elements. We considered a rather thick valve (thickness $= 0.1\,\mathrm{cm}$) characterized by a flexrual stiffness $EI = 3\,\mathrm{g\,cm^3/s^2}$. At the inflow boundary, the flow profile shown in Figure 6.3 is imposed. At the outflow boundary, a resistance boundary condition is prescribed, with resistance $R = 3500$ dyn·s/cm^3. Flow was simulated over multiple cardiac cycles with a time-step size of $2 \cdot 10^{-3}$ s to reach a periodic regime.

The velocity field following peak systole is shown in Figure 6.4.a. Figure 6.4.b shows the backward time FTLE field following peak systole, which approximately corresponds to the point in time where the jet is near maximum strength and fully-developed. As blood is rapidly ejected from the valve, flow separation occurs near

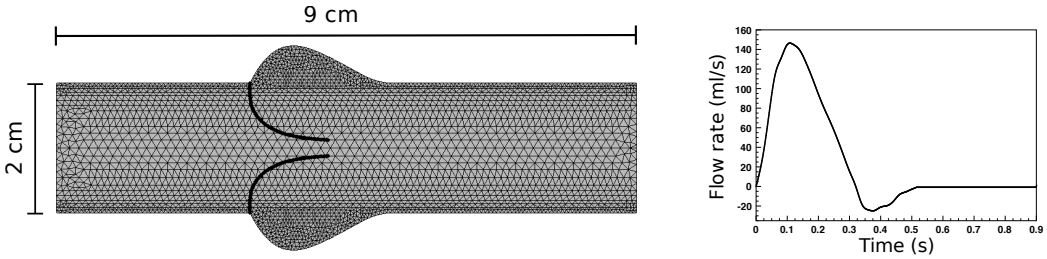

Figure 6.3: 2D computational domain and inflow waveform..

the tips of the leaflets. Each repelling LCS extending from the leaflets is a material boundary between the jet of ejected blood and the region of separated, recirculating flow. In addition, other LCS can be detected in the separated flow regions, which bound vortical structures (in the same sense as in [SDM06]) of recirculating flow.

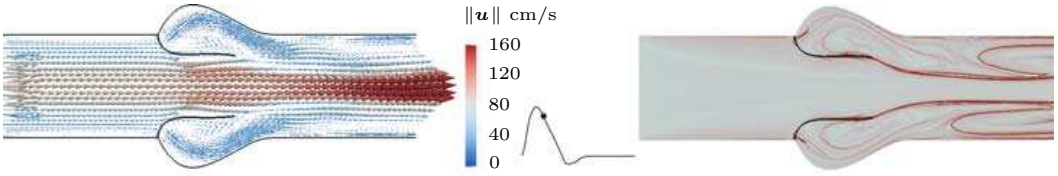

(a) Velocity field (b) FTLE field

Figure 6.4: (a) Velocity field following peak systole ($t = 0.16$ s) (b) FTLE field following peak systole ($t = 0.16$ s). Curves of high FTLE (dark) extending from leaflet tips demarcate boundary between jet and separated flow regions.

6.4.2 Three-dimensional simulation

For the 3D simulation we considered part of the idealized 3D geometry of the aortic root described in [Tra06]. The fluid and structure computational domains, as well as the pulsatile periodic flow waveform imposed at the inlet, are shown in Fig 6.5. To take into account the downstream vasculature, a resistance $R = 500$ dyn s/cm^5 was prescribed as the outlet boundary condition. Fluid and structure domains were discretized, respectively, by 216692 tetrahedral and 4814 shell elements. Leaflets were characterized by a density $\rho^s = 1.2$ g/cm^3, an elastic modulus $E = 10^6$ dyn/cm^2, a Poisson ratio of 0.3 and a thickness of 0.05 cm.

Flow was simulated over 2 cardiac cycles with a time-step size of $2.5 \cdot 10^{-4}$ s and data from the last cardiac cycle was used for analysis. The velocity field during systole is shown in Figure 6.6. For visualization purposes, only vectors from a subset of the nodes of the finite-element mesh are plotted. Also shown is the location of the valve over time.

The backward-time FTLE field was computed in the vicinity of the 3D aortic valves from the FSI simulation data shown in Figure 6.6. A section of the FTLE field, spanning from the root of the valve to 1 cm downstream from the leaflet tips

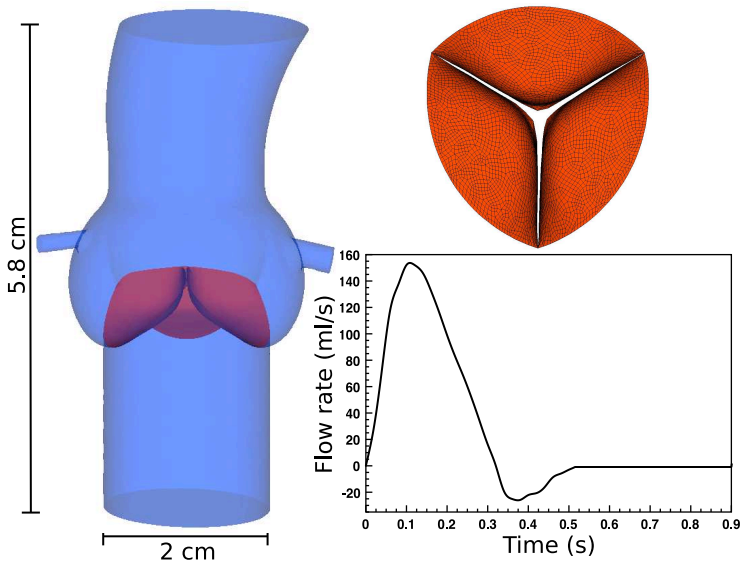

Figure 6.5: 3D computational domain and inflow waveform. The vessel is partially transparent and leaflets are opaque. A top view of the tricuspid valve is shown in upper right.

when fully opened, is shown in Figure 6.7 at four time instances during systole. This cross-section roughly corresponds to the location where minimal cross-sectional area of the jet occurs shortly after peak systole; however this location of minimum area continually changes. Initially, a single attracting LCS, shown as the white surface in panels (a) and (b) of Figure 6.7, bounds the region of blood being ejected as the valve opens. Near peak systole, flow separation from the leaflets occurs. The LCS shown in panels (c) and (d) of Figure 6.7 capture these separation profiles. Note that attracting LCS approximately coincide with each leaflet and thus these LCS *appear* fragmented along the leaflet when visualizing both structures together. From the LCS, we can see that as the flow separates from the leaflets, it rolls up along the edges. A similar separation profile was identified in studying flow separation in the carotid bifurcation in [ST08].

Since the LCS extending from the leaflets define the boundary of the jet, we can readily obtain an accurate measure of jet area from the LCS. This was done at a location 1 cm distal to the leaflet tips in the fully open state. The location chosen roughly corresponds to the region where the minimal cross-sectional area of the jet occur. Even if a more accurate selection could be done, for example through an optimization algorithm, we consider this level of accuracy reasonable in view of the uncertainties of the model. The cross-section of the FTLE field at this location is shown in Figure 6.8.a during systole. We used the algorithm described in Section 6.3, p. 154, to extract a parametrization for the cross-section of LCS at a series of points in time. The area bound by these curves was then computed at these time points and the results are shown in Figure 6.8.b. Time 0 corresponds to the start of

systole (the opening of the valve) and peak systole occurs after approximately 0.11 seconds. The size of the jet at this cross-section reaches approximately 1.63 cm^2, with the peak cross-sectional area occurring around $t = 0.17$ s, which does not correspond to peak systole. The reason for this is twofold. First, it takes a finite amount of time for the jet to develop. Second, it takes a finite amount of time for the jet to propagate downstream.

It is interesting to compare the (precise) size of the jet obtained from LCS with that obtained using the continuity equation, a popular formula typically used in clinical practice to estimate the EOA. The continuity equation states that the flow rate in the left ventricular outflow tract (LVOT) equals the one in the vena contracta (VC), that is

$$\text{EOA} \times \text{VTI}_{\text{VC}} = \text{A}_{\text{LVOT}} \times \text{VTI}_{\text{LVOT}} \, .$$

The quantity VTI_{VC} is the velocity time integral at the level of the vena contracta, while A_{LVOT} and VTI_{LVOT} represent, respectively, the subvalvular cross-sectional area (see Figure 6.1) and the corresponding velocity time integral. In clinical practice, the VTI on a prescribed cross-section is obtained from an integration in time of Doppler velocity measurements over the systolic phase of the cardiac cycle. Therefore, to estimate the EOA the following integral relationship is evaluated

$$\text{EOA} = \frac{\text{A}_{\text{LVOT}}\text{VTI}_{\text{LVOT}}}{\text{VTI}_{\text{VC}}} \, , \tag{6.9}$$

where we can think of the numerator as the stoke volume and the denominator as the integral of the velocity at the center of the vena contracta of the jet. Evaluating equation (6.9) from the 3D FSI velocity data at the cross-sectional location in Figure 6.8 gives EOA = 1.53 cm^2. This value is in the range of the measurements obtained with LCS (see Figure 6.8.b) but underestimates the true (peak) area of about 5%.

6.5 Discussion

In this chapter we demonstrated a novel approach for understanding the geometry and dynamics of the jet produced by the aortic valve. In particular, flow through the aortic valve was simulated using a robust FSI scheme to provide highly resolved velocity data in the vicinity of the aortic valve over serval cardiac cycles. This data was used to perform LCS computations, which revealed flow separation from the valve leaflets during systole, and correspondingly, the boundary between the jet of ejected fluid and the regions of separated, recirculating flow.

Advantages of computing LCS in multi-dimensional FSI models of the aortic valve are twofold. For one, the quality and effectiveness of existing clinical indices used to measure aortic jet size can be tested in different stenotic scenarios by taking advantage of the accurate measure of the jet area derived from LCS. Secondly, as an ultimate goal, a reliable computational framework for the assessment of the aortic valve stenosis could be developed. For this latter point, however, it must be

recognized that a precise knowledge of the mechanical and geometrical properties of the system could be needed for patient-specific medical planning.

As shown in Section 6.4, LCS provide clear, unambiguous boundaries to the jet. Currently, in practice, the size of the aortic jet is measured by the EOA. However, the computation of the EOA provides little insight into the actual geometry or dynamics of the jet since these computations are based on simplifying assumptions. It is conceivable, and most likely, that jets with dissimilar geometry and dynamics could produce similar indices. Since the local blood flow mechanics (recirculation, separations, mixing, etc.) is known to strongly influence pathophysiology (see *e.g.* [KGZG85, WK99]), the computation of LCS has the clear benefit of providing insight into these conditions. Furthermore, as shown in Section 6.4, clinical indices, such as the one based on the continuity equation, provide only averaged information.

As for practical concerns, note that to obtain the jet area, the entire 3D FTLE field is not needed. Only the section of the FTLE field at the location where the area measurement has to be made is needed. This is an important consideration since it greatly reduces the computational cost needed to compute the jet area. Additionally, as shown above, automatic extraction of the LCS is possible, which, for one, removes user bias (which is currently an issue for EOA calculations), and secondly, makes these methods potentially accessible to the medical community either from numerical or clinical data. Additionally, a better understanding of the 3D flow geometry of the jet could enable improved techniques for measuring flow conditions or developing more effective metrics for accessing the severity of AS from current and subsequent modalities and technologies.

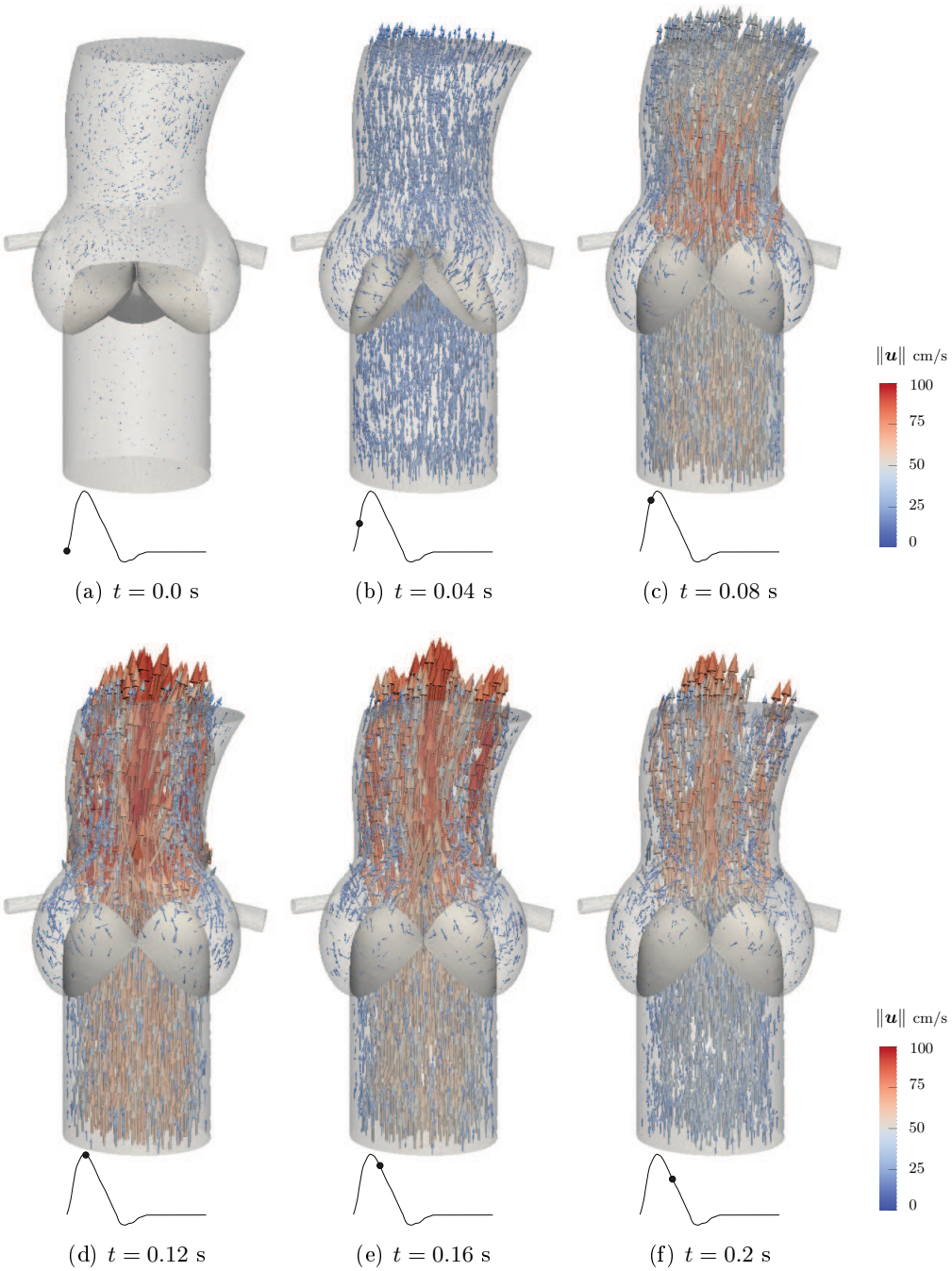

(a) $t = 0.0$ s (b) $t = 0.04$ s (c) $t = 0.08$ s

(d) $t = 0.12$ s (e) $t = 0.16$ s (f) $t = 0.2$ s

Figure 6.6: Velocity field during systolic phase.

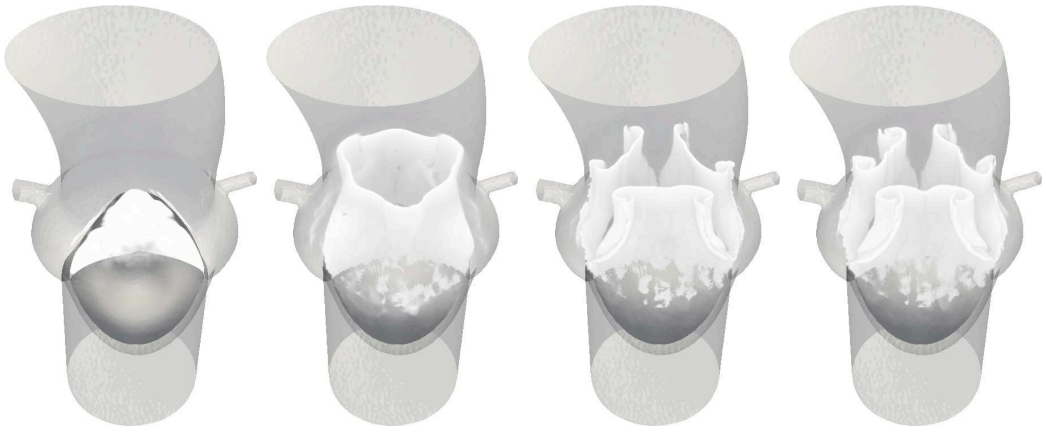

(a) $t = 0.05$ s (b) $t = 0.08$ s (c) $t = 0.11$ s (d) $t = 0.14$ s

Figure 6.7: Backward time FTLE reveals attracting LCS (white) that bound the blood ejected from the tricuspid valve as it opens.

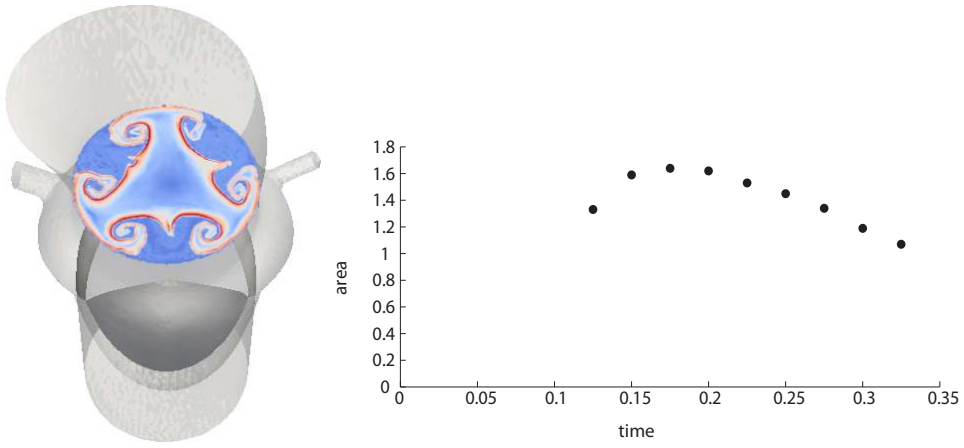

(a) (b)

Figure 6.8: (a) Cross-section of 3D FTLE field at location 1 cm distal from aortic valve leaflet tips. (b) Jet area at location 1 cm distal from aortic valve leaflet tips over time.

Part III

Towards the fluid-structure interaction in the heart

Chapter 7

Resistive immersed surfaces for heart valves modeling

Contents

7.1 Introduction

Heart valve models can be roughly divided in two groups: *lumped parameter* and *multidimensional* models. Both of them have inherent limitations for effective heart valve simulations. In lumped parameter models, the choice of the artificial boundaries, where the reduced models are used, is rather challenging since their position and their simplified geometrical shape dramatically affect the computational results. Moreover, numerical instabilities can also be experienced if sudden variations in time and/or space of the physical quantities occur at the artificial boundary. As for three-dimensional models, in spite of the remarkable progress made in the last decade, FSI valve simulation remains an extremely challenging task, even when it is performed in a limited portion or aorta (see Section 6.2 for a discussion). Among the other difficulties, we recall the complex mechanical constitutive laws involved, the high pressure jump experienced when the valves are closed and the modification of the nature of boundary conditions in the fluid problem, when we switch from an open valve configuration to a closed one. On the one hand, including a three-dimensional valve computation in more complex FSI problems, such as the simulation of the heart ventricles, is feasible, but it could become so computationally intensive that it may not be the best option to address some clinical problems for which a precise description of the leaflet biomechanics is not required. On the other hand, the use

of lumped parameter models may induce to many inaccuracies in the flow and pressure fields in critical fluid dynamics regions. In those cases, it may be interesting to explore alternative solutions.

In this chapter we propose a new reduced model for heart valves, which improves the accuracy of standard lumped models and the robustness and efficiency of 3D fluid-structure models. In this approach, the mechanics of the leaflets is neglected. Instead, the valve is replaced by an immersed surface acting as resistance on the fluid. The geometry of the resistive immersed surface (RIS) is fixed in space and can be defined as the real three-dimensional valve geometry in its closed configuration. The magnitude of the resistance varies when the valve opens or closes. A straightforward choice could be for example to set the resistance equal to zero when the valve is open and different from zero (typically a high value) otherwise. When the valve is open, the zero resistance makes the immersed surface "invisible" to the fluid. When the valve is closed, the resistance induces a jump of the stress across the surface which may raise numerical issues if not correctly handled. As a consequence, attention must be given for a proper choice of the space discretization. On the one hand, continuous approximations of the pressure may give inaccurate results, on the other hand, discontinuous approximations typically lead to expensive simulations. To circumvent these issues, we employ the mathematical formulation proposed in [FGM08] to deal with immersed stents. There, the stent has been modeled as a resistive surface that introduces a "fissure" in the fluid mesh. From the implementation viewpoint, the "fissure" is generated by duplicating the stent surface: the degrees of freedom of the fluid unknowns are therefore doubled on the stent. This allows for a precise computation of the pressure discontinuity even with the use of continuous finite element approximations. The continuity of the fluid velocity at the interface is eventually satisfied by imposing a periodic boundary condition for the velocity unknowns on the immersed surface.

For the sake of completeness in Section 7.2 an overview of the most common lumped parameter models for heart valves is given; we refer to the previous chapters for a review of the multidimensional models. In Section 7.3, we recall the mathematical formulation of the resistive immersed surface proposed in [FGM08], and we present a possible reduced model for the computation of the variable resistance. Details on the space discretization and on the time-advancing algorithm are also given. Finally in Section 7.4 various numerical simulations on realistic three dimensional geometries are performed in order to illustrate the flexibility and the efficiency of the RIS model for heart valves. In Section 7.5, a discussion on further developments and perspectives follows.

7.2 Lumped parameter models for heart valves: an overview

Lumped parameter models for valves can be divided in two groups: quasi-steady or time-dependent systems. Quasi-steady models have been chronologically the first

employed for the modeling of the valves of the circulatory system. Mathematically, they are described by algebraic equations that relate blood flow and pressure jump across the valve. Despite their simplicity and limited accuracy, they are still commonly used since they guarantee a very low computational cost. Time-dependent lumped parameter models are determined by linear or non-linear ordinary differential equations. The main advantage of the time-dependent lumped parameter models with respect to the quasi-steady ones is the ability to take into account the dynamics of the valve (opening and closing), at a minimal computational cost. In the presentation of the different models, we refer to a cardiac system like the one represented in Figure 7.1, where P_v is the pressure inside the ventricle, P_{ar} the pressure in the corresponding artery outlet and P_{at} the pressure in the corresponding atrium. All these quantities are averaged over a section or volume. Moreover, we denote with Q the blood flow leaving the ventricle.

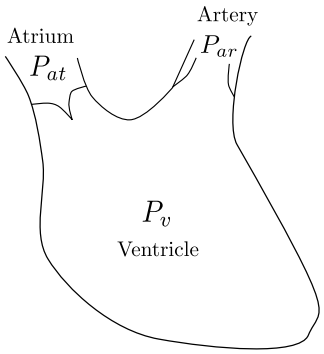

Figure 7.1: Schematic representation of the left ventricle.

Quasi-steady models. In the literature, it is common to derive quasi-steady models for valves by making an analogy between the circulatory system and an electrical circuit (see for example [JL06, FLTV06]). In this analogy, blood flow and pressure take respectively the role of current and voltage, while the valve is assimilated to an electrical diode. A perfect diode is an electrical element that allows a current only in one direction of the circuit and blocks it in the opposite one. In the same way, a valve allows the blood to flow in one specific direction of the circulatory system and prevents the potential backflow. Namely, considering the simplified system in Figure 7.1,

$$\begin{cases} Q \leq 0 & \text{when} \quad P_v = P_{at} \quad \text{(filling)}, \\ Q = 0 & \text{when} \quad P_{at} \leq P_v \leq P_{ar} \quad \text{(isovol. phases)}, \\ Q \geq 0 & \text{when} \quad P_v = P_{ar} \quad \text{(ejection)}. \end{cases} \tag{7.1}$$

However, relation (7.1) is not practical from a computational point of view since it is not regular. Various regularizations have been investigated. Here, for the sake of conciseness, we will only review the most commons.

A first possibility, proposed for example in [JL06], consists of replacing $(7.1)_1$ and $(7.1)_3$ by a sort of Ohm law, blood flow and pressure being related by means of a constant flow resistance R. Different values of R could be chosen for the filling and the ejection phase. However, since open valves in normal physiological condition offer a very small resistance to the flow, their values are usually rather small. To summarize, in [JL06] system (7.1) is rewritten as:

$$\begin{cases} Q = (P_v - P_{at})/R_{at} & \text{when} \quad P_v \leq P_{at}, \\ Q = 0 & \text{when} \quad P_{at} \leq P_v \leq P_{ar}, \\ Q = (P_v - P_{ar})/R_{ar} & \text{when} \quad P_v \geq P_{ar}, \end{cases} \tag{7.2}$$

where R_{at} and R_{ar} represent the resistances related to the atrioventricular and semilunar valves respectively.

The Ohm's law-like relation is not the only one conceivable. Indeed, using the classic Bernoulli equation and making the further assumption of blood at rest in the atria and ventricles, valves could be modeled as orifices. In this particular case we have

$$\begin{cases} Q = C_{at}\sqrt{P_{at} - P_v} & \text{when} \quad P_v \leq P_{at}, \\ Q = 0 & \text{when} \quad P_{at} \leq P_v \leq P_{ar}, \\ Q = C_{ar}\sqrt{P_v - P_{at}} & \text{when} \quad P_v \geq P_{ar}, \end{cases} \tag{7.3}$$

where C_{at} and C_{ar} are two constants respectively related to the atrioventricular and semilunar valves [KS06].

Quasi-steady models proposed in [SMCCS06, DZL07] also introduce a Ohm law for the isovolumetric phases, namely for $(7.1)_2$. In these models, valves behave like non-ideal diodes, that is, they could be affected by leaking: the smaller the corresponding resistance, the bigger the leaking. The final set of equations is:

$$\begin{cases} Q = (P_v - P_{at})/R_{at} & \text{when} \quad P_v \leq P_{at}, \\ Q = (P_v - P_{at})/R_c & \text{when} \quad P_{at} \leq P_v \leq P_{ar}, \\ Q = (P_v - P_{ar})/R_{ar} + (P_{ar} - P_{at})/R_c & \text{when} \quad P_v \geq P_{ar}, \end{cases} \tag{7.4}$$

where R_c represents the resistance when the valves are closed.

The models presented up to now assume that valves open and close only under the action of a pressure difference. However different assumptions could be made on the working conditions of valves. For example in [FLTV06], it is assumed that the closure of the valves is dictated by the flow reversal. The corresponding model is represented in the flow chart reported in Figure 7.2. In the RIS valve model similar conditions will be used to define the opening and closure of the valves; a detailed presentation of this choice is given below.

Dynamic models. Dynamic lumped parameter models represent a compromise between a detailed three-dimensional study and a simplified diode-like description

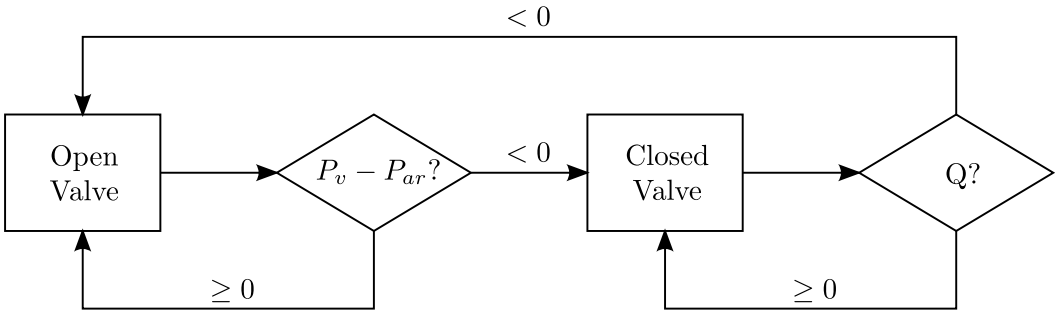

Figure 7.2: Flow chart representation of the aortic valve modeling in [FLTV06].

of the valve. Among others, we consider the model proposed in [KS06] for the aortic valve. In this work, the authors considered a simplified valve model, where a nominal leaflet opening angle is used as an average of the variation of angular position in the different parts of the elastic leaflet. The nominal opening angle is calculated by solving an ordinary differential equation and the blood-leaflet interaction is taken into account. In this model the pressure-flow relation in the aortic valve is

$$\begin{cases} Q = C_{ar} \cdot \mathrm{VO} \cdot \sqrt{P_v - P_{ar}} & \text{when} \quad P_v \geq P_{ar}, \\ Q = C_{ar} \cdot \mathrm{VO} \cdot \sqrt{P_{ar} - P_v} & \text{when} \quad P_v < P_{ar}, \end{cases} \tag{7.5}$$

where the valve opening VO is a scalar function that depends on the leaflet opening angle θ:

$$VO = \frac{(1 - \cos\theta)^2}{(1 - \cos\theta_{\max})^2}.$$

Zero degree for θ corresponds to the fully closed position, while the maximum opening angle $\theta_{\max}$ corresponds to the fully open leaflet position (see Figure 7.3). Note that if the function VO is simply defined by

$$VO = \begin{cases} 1 & \text{when} \quad P_v \geq P_{ar}, \\ 0 & \text{when} \quad P_v < P_{ar}, \end{cases}$$

then model (7.5) is equivalent to the quasi-steady model (7.3).

In order to compute θ, various factors that affect the leaflet motion could be considered. In practice in the proposed model, only the moment due to the pressure difference across the valve and the moment produced by the frictional force are considered. This leads to the following equation for the aortic leaflet motion:

$$\frac{d^2\theta}{dt^2} = K_{p,ar}(P_v - P_{ar})\cos\theta - K_{f,ar}\frac{d\theta}{dt}, \tag{7.6}$$

where $K_{p,ar}$ and $K_{f,ar}$ are parameters to be estimated. Note that a similar model could be also considered for the other heart valves and that different governing equations could be used (see for example the ones proposed in [MB05, SSG+04]).

The lumped parameter models provide an effective way to take into account the presence of the valve in numerical simulations. Nonetheless they all require the

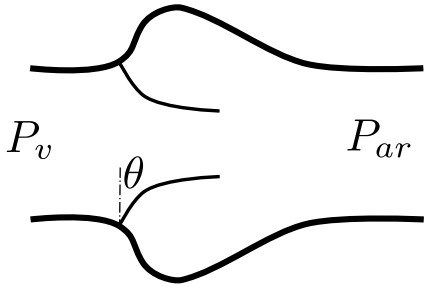

Figure 7.3: Schematic representation of the aortic valve and of the angle θ formed by its leaflets.

introduction of an artificial boundary to the fluid domain in regions where the velocity and the pressure experience a high variability in space and time. The resistive immersed surfaces for the valves get rid of the artificial boundaries. Moreover, the difficulties encountered in three-dimensional models during the diastole (*e.g.* high pressure jumps, contact, etc.) will be circumvented with this new formulation. As will be shown in the next section, the pressure jump is directly taken into account in a robust and accurate way with the "fissured" fluid mesh [FGM08].

7.3 Resistive immersed surface model for heart valves

The Navier-Stokes equation with a resistive immersed surface. In order to introduce the general theory, let us consider an incompressible fluid governed by the Navier-Stokes equations in a regular fixed domain $\Omega^{\mathrm{f}} \subset \mathbb{R}^d$, $d = 2$ or 3. Let $\Sigma \subset \mathbb{R}^{d-1}$ be the co-dimension one surface representing the resistive immersed interface. The latter divides the fluid domain in two connected subdomains (see Figure 7.4), *i.e.*

$$\Omega^{\mathrm{f}} \stackrel{\mathrm{def}}{=} \Omega_1^{\mathrm{f}} \cup \Sigma \cup \Omega_2^{\mathrm{f}} \quad \text{with} \quad \Omega_1^{\mathrm{f}} \cap \Omega_2^{\mathrm{f}} = \emptyset.$$

We also identify with $\mathbf{n}_1$, $\mathbf{n}_2$ the outgoing normals at the interface from each subdomain Ω_i^{f}, $i = 1, 2$.

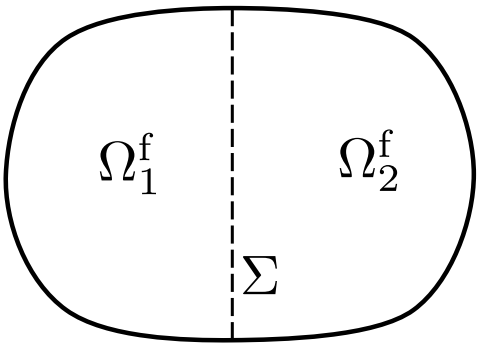

Figure 7.4: Sketch of the fluid domain.

The resistive immersed surface introduces an additional dissipative term in the momentum equation of the Navier-Stokes equation (2.1), the corresponding fluid model reads:

$$\begin{cases} \rho^{\mathrm{f}}\left(\partial_t \mathbf{u} + (\mathbf{u}\cdot\nabla)\mathbf{u}\right) - \operatorname{div}\boldsymbol{\sigma}^{\mathrm{f}}(\mathbf{u},p) + R_\Sigma \mathbf{u}\delta = \mathbf{f}, & \text{in} \quad \Omega^{\mathrm{f}}, \\ \operatorname{div}\mathbf{u} = 0, & \text{in} \quad \Omega^{\mathrm{f}}, \end{cases} \tag{7.7}$$

where δ is the Dirac measure on the immersed surface, and R_Σ denotes the variable resistance of the interface to the flow. Notice that equations (7.7) can be equivalently reformulated on the two separate sub-domains in the following way:

$$\begin{cases} \rho^{\mathrm{f}}\left(\partial_t \mathbf{u}_i + (\mathbf{u}_i\cdot\nabla)\mathbf{u}_i\right) - \operatorname{div}\boldsymbol{\sigma}^{\mathrm{f}}(\mathbf{u}_i,p_i) = \mathbf{f}_i, & \text{in} \quad \Omega_i^{\mathrm{f}}, \\ \operatorname{div}\mathbf{u} = 0, & \text{in} \quad \Omega_i^{\mathrm{f}}, \\ [\![\mathbf{u}]\!] = \mathbf{0}, & \text{on} \ \Sigma, \\ [\![\boldsymbol{\sigma}^{\mathrm{f}}(\mathbf{u},p)\mathbf{n}]\!] = -R_\Sigma \mathbf{u}, & \text{on} \ \Sigma, \end{cases} \tag{7.8}$$

where the operator $[\![\cdot]\!]$ defines the jump across Σ, that is:

$$[\![\mathbf{u}]\!] = \mathbf{u}_1 - \mathbf{u}_2 \ , \quad [\![\boldsymbol{\sigma}^{\mathrm{f}}(\mathbf{u},p)\mathbf{n}]\!] = \boldsymbol{\sigma}^{\mathrm{f}}(\mathbf{u}_1,p_1)\mathbf{n}_1 + \boldsymbol{\sigma}^{\mathrm{f}}(\mathbf{u}_2,p_2)\mathbf{n}_2.$$

The interface conditions express the fact that the velocity is continuous across the surface, while the normal stress is not. The equivalence of the two formulations can be easily shown in a variational framework [FGM08], where for $\boldsymbol{v} \in V^{\mathrm{f}}$, the dissipative term reads:

$$\langle R_\Sigma \mathbf{u}\delta, \boldsymbol{v}\rangle_\Sigma = \int_\Sigma R_\Sigma \mathbf{u}\cdot\boldsymbol{v}\,\mathrm{d}\boldsymbol{\gamma}.$$

Remark 7.1 *Note that from a mathematical point of view, the resistance R_Σ acts as a penalization parameter. When R_Σ is high, the solution $\mathbf{u} = \mathbf{0}$ is enforced on Σ; when it is low, the surface is more likely a porous surface [FGM08].*

In this work, for the space discretization we use the conforming stabilized finite element method proposed in [FGM08], that allows equal order interpolations, and for which optimal error estimates have been proved. The key ingredient consists of combining the techniques of [HFB86, TV96] with an interface based stabilization allowing pressure discontinuities through the interface Σ. We refer to [FGM08] for the details of the analysis. The time discretization of the Navier-Stokes equation is performed with a standard BDF1 scheme.

Remark 7.2 *Very recently in [CFGM10] a numerical method based on a fractional step formulation (Chorin-Temam projection scheme) has been proposed for the numerical simulation of an incompressible fluid through a porous interface* (e.g. *a stent). Clearly this scheme can be also used for the numerical simulation of valves in the RIS framework. Notice that this scheme, based on a peculiar stabilization term* à la Nitsche, *allows for very fast and stable computations, especially in problems where the fluid is also coupled with a structure (FSI problems).*

Variable resistance model. Let us now consider the model used to compute the variable resistance R_Σ. Clearly the way the resistance varies must mimic the behavior of a real valve. The magnitude of the resistance depends therefore on the flow conditions (*i.e.* on the velocity and pressure).

The model used is based on the following two simple physiological considerations:

1. The valves open when subjected to a positive pressure difference, *i.e.* $\delta P > 0$.
2. The valves close when a flow reversal happens, *i.e.* when $Q < 0$, being Q positive in the direction of the valves opening.

Before presenting the final algorithm for the update of the resistance magnitude, let us give some more details on the previous two statements.

Considering the first one, we can assume that the valve is closed until $\delta P < 0$ across it. When the pressure difference is zero, the valve is most likely in its zero-energy state and in the process to be opened with a further increase of δP. Note that at this point the flow across the valve is still zero, and only after the valve opening it will be positive. The evaluation of the pressure difference across the valve can therefore be used as a test condition for the opening of the valves. Two more considerations are now in order. On the one hand, the use of the fissured mesh technique introduced in [FGM08], allows for a computation of δP right across the valves (for example an averaged surface pressure difference can be used). On the other hand, it would not be correct to use information on the flow positivity across the valve as a condition for the valve opening, because theoretically when the valve is closed the flow is zero and won't be different until the valve is not open.

Considering the second statement, from a physiological viewpoint, the valve remains open as long as a positive flow occurs in the direction of the valves opening. Therefore the closure of the valves may only happens when $Q < 0$, which can be directly evaluated on the fissured surface. Note finally that in this case it wouldn't be correct to use information on the pressure across the valve to establish the valve closure. As a matter of fact, when the valve is open the fissured valve is "invisible" to the flow and the pressure difference would always be zero (or close to zero) across the valve.

The update of the resistance magnitude can be therefore summarized in the following lines of pseudo-code:

```
if(closed_valve == true){
  if(δP > α){
    R_Σ = R_ov;
    closed_valve == false;}}
else{
  if(Q < β){
    R_Σ = R_cv ;
    closed_valve == true;}}
```

where R_{cv} and R_{ov} are respectively the values of the resistance for the closed and open valve. The value of R_{cv} is usually high, for example in all simulations performed

this has been set equal to 10^6 dyn·s/cm^5. This choice of R_{cv} guarantees a very small flow across the closed valve, typically much less than 1% of the total flow, which is considered acceptable in the logic of the reduced model (see Remark 7.1). In normal conditions $R_{\text{ov}} = 0$, however it can be set different from zero to model pathological states of the valve. The parameters α and β are respectively non-negative and non-positive and are assumed equal to zero in normal conditions. In the remaining part of this chapter these will be assumed zero, nonetheless they can also be different from zero to model particular pathologies. For example a late opening can be modeled choosing $\alpha > 0$, similarly a late closure with $\beta < 0$.

Remark 7.3 *For the late closure, the condition $Q < \beta$ is only one of the possible conditions that can be used to establish the closure of the valve. Another possibility is to devise conditions based on the stroke volume. For example, valves close when the ratio between the inflowing and the outflowing blood volumes is larger than a prescribed percent value.*

Remark 7.4 *For the sake of simplicity, the RIS valve model has been presented assuming only two states for the valve. However, it is possible to associate different resistances to selected sub-regions of the valve and to compute the corresponding resistance values with respect to the local fluid dynamics. In all the simulations performed the variable resistance model presented is sufficient to get the main fluid dynamics phenomena of the problem under analysis. Nonetheless, other models for the computation of the resistances could be considered.*

Note finally that a further improvement to this valve model would be to add a second set of surfaces corresponding to the fully open leaflets. These surfaces would of course be equipped with a zero resistance, *i.e.* would be "invisible", when the valves are closed; different from zero otherwise. Doing so, the geometrical domain "seen by the fluid" is realistic for the most part of the cardiac cycle and only the intermediate dynamics, closed-to-open and open-to-closed, aren't taken into account.

The strategy employed for the update of the resistance makes the problem (7.7) highly non-linear. In a time-advancing scheme the problem can be linearized by computing the resistance with the velocity and pressure at the previous time-step. Nonetheless, this linearization introduces a delay in the update of R_Σ and hence in the valve opening and closure. Considering for instance the closure, the valve closes only after that the flow is already negative. A similar consideration can be done for the valve opening. In order to remove this delay, the time advancing scheme may be modified in the following way:

Algorithm 7.1 *Time-advancing scheme for the RIS valve model*

At time-step t^n, $(\mathbf{u}^k, p^k) = (\mathbf{u}^n, p^n)$
Do

- R_Σ^k = update_resistance$(\mathbf{u}^k, p^k)$:
- Solve problem (7.7) with R_Σ^k;

- `admissible = status_valve(`$\mathbf{u}^{n+1}, p^{n+1}$`);`
- $(\mathbf{u}^k, p^k) = (\mathbf{u}^{n+1}, p^{n+1})$;

`While(admissible == false)`

In the function named `update_resistance` it is implemented the valve model that computes the resistance magnitude. The procedure `status_valve` provides a test for the admissibility of the valve configuration (open or closed) with respect to the fluid dynamics state. In other words, it tells whether the prediction of the valve configuration made with the `update_resistance` function is still admissible after the solution of the fluid problem (7.7). If not, an update of the resistance, based on the latest velocity and pressure, is performed. The function `status_valve` depends on the specific RIS valve model considered. For instance, in our case this is defined in the following way:

```
if(closed_valve == true)
  if(δP > 0)    return false;
else
  if(Q < 0)     return false;
return true;
```

In practice this test simply states that the valve cannot be closed (resp. open) if the pressure difference is positive (resp. the flow is negative). Notice also that this strategy is very cheap. As a matter of fact the actual re-computation of the Navier-Stokes problem happens only when the valve changes configuration, *i.e.* from open to closed and from closed to open. In physiological flows this happens only twice for each valve per cardiac cycle.

Remark 7.5 *Note that the approach proposed differs remarkably from other existing approaches that use immersed surfaces for valve modeling* (e.g. *[NWY06]). Our method introduces new features not considered in previous works. Examples of these features are: the use of realistic geometries for the valves in their open and closed configurations, the precise capture of the pressure jump during the valve closure and a physiologically based resistance model.*

In the next section, different numerical experiments are presented in order to illustrate the capabilities of the proposed approach. All the simulations involve an incompressible viscous fluid either in a rigid domain or in a moving domain (with imposed displacements) and are performed with Algorithm 7.1. A preliminary example in fluid-structure interaction problems is also given for the sake of completeness in Section 7.5. Nonetheless for the latter, the standard advancing-scheme (without the `status_valve` procedure) is used. The application of Algorithm 7.1 in FSI problems has to be accurately analyzed and maybe related to the specific partitioned FSI scheme in use (see Section 2.5.3).

7.4 Numerical experiments

7.4.1 Pressure jump test.

In this first test case we intend to give a better insight into the properties of the RIS valve model, without the aim of providing physiologically relevant numerical simulations. We consider a simple rigid tube with a resistive immersed surface in the middle of it. The computational domain is given in Figure 7.5.a. The mesh is rather coarse and is made of 13818 tetrahedral elements. As usual, the fluid density ρ^{f} and the viscosity μ are assumed constant and equal to 1.0 g cm^{-3} and 0.035 g cm^{-1}s^{-1}, respectively. The fluid is assumed initially at rest and a sinusoidal pressure is imposed at the inlet, Figure 7.5.b. At the outlet the boundary condition $\boldsymbol{\sigma}^{\mathrm{f}}\mathbf{n}^{\mathrm{f}} = P_{\mathrm{out}}\mathbf{n}^{\mathrm{f}}$ is imposed, P_{out} is given by the RCR model described by the following ordinary differential equation [VC06]:

$$P_{\mathrm{out}} + R_d C \frac{dP_{\mathrm{out}}}{dt} = (R + R_d)Q + RR_d C \frac{dQ}{dt} + P_d + R_d C \frac{dP_d}{dt}, \tag{7.9}$$

where R is the proximal resistance, R_d the distal resistance, C the capacitance and P_d the distal pressure. In our case these parameters assume the values $R = 150$ dyn·s/cm^5, $R_d = 700$ dyn·s/cm^5, $C = 10^{-3}$ cm^5/dyn and $P_d = 0$.

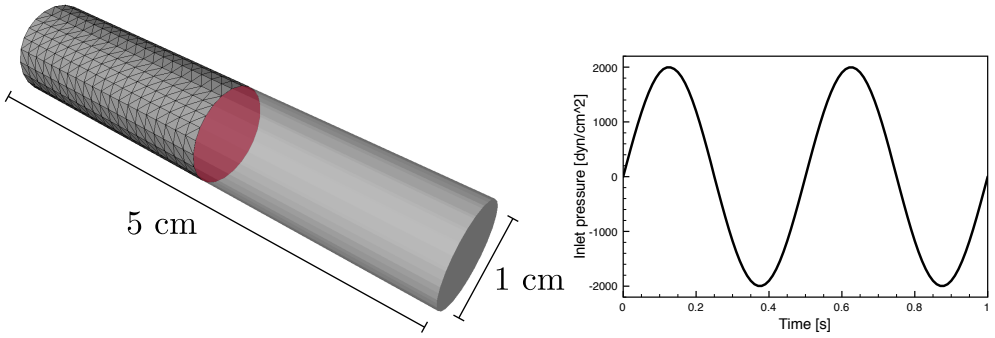

(a) (b)

Figure 7.5: Left: Computational domain and mesh discretization, the resistive immersed surface is represented in red. Right: Imposed pressure at the inlet ($\boldsymbol{\sigma}^{\mathrm{f}}\mathbf{n}^{\mathrm{f}} = 2000\sin(4\pi t)\mathbf{n}^{\mathrm{f}}$).

The simulation is carried out for 8 seconds with a time-step size of $5 \cdot 10^{-3}$ seconds. The computational results for the last two cycles are reported in Figures 7.6 and 7.7. In Figure 7.6 the elevated surface represents the pressure distribution in the longitudinal mid surface of the tube for two different points in time. On the one hand, when the valve is closed a precise pressure jump is given on the immersed surface by the resistive valve model. Note that this jump would be smeared at the interface with a continuous approximation for the pressure. On the other hand, when the valve is open, the resistance R_Σ is zero and the pressure assume the same

value on the two sides of the fissure. This is also confirmed by the pressure curves reported in Figure 7.7. The blue curve gives the pressure on the inlet side of the fissure, the red one on the outlet side. Note that when the valve is open, the flow is positive and the pressures coincide. On the contrary, when the valve is closed, the flow is zero and a pressure difference is present at the interface.

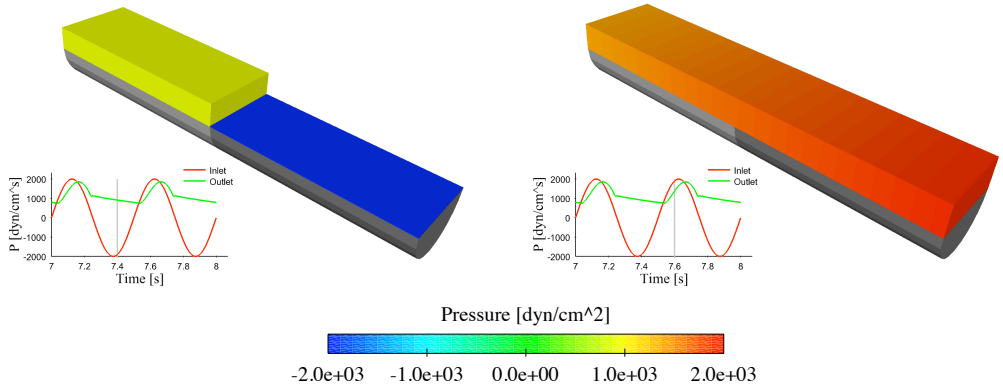

Figure 7.6: Left: Pressure distribution at time $t = 7.4$ s, the valve is closed. Right: Pressure distribution at time $t = 7.6$ s, the valve is open.

In Figure 7.7, four vertical grey lines indicate the successive opening and closure of the valve, respectively noted as OV and CV. It is important to observe that right after the closure of the valve a slight increase of the pressure is experienced at the outlet side of the fissure. This may be explained as the result of the inertia of the fluid, which causes a fluid motion from the outlet towards the fixed closed valve during its closure. Interestingly, this second peak of pressure seems to occur also in cardiac physiology. This is the so-called *dicrotic wave* (or *dicrotic nocht*), which happens in the early diastolic phase, right after the closure of the aortic valve (see Figure 1.4, Phase III in the pressure graph).

The origin of the dicrotic wave is very discussed in the medical community and it is more likely the result of multiple concomitant factors such as the closure of the aortic valves, the longitudinal recoil of the ascending aorta and the presence of coronaries [Yeo89, Sam12, Ale53, DTM73]. Here, we do not claim that this simple valve model is able to catch the whole complexity of this phenomenon. Nonetheless it is interesting to observe that the proposed model mimics the valve dynamics described in one of the first interpretations of the dicrotic wave. Quoting from G.F. Yeo's *A manual of physiology*, edition 1889:

> The dicrotic notch then most probably depends upon a negative centrifugal wave, caused by the sudden stoppage of the inflow and the momentary reflux of blood during the closure of the valves; and the dicrotic crest is, no doubt, produced by the completion of their closure, at which moment the sudden check given to the reflux of the blood column causes a positive centrifugal wave to follow the primary wave of the pulse.

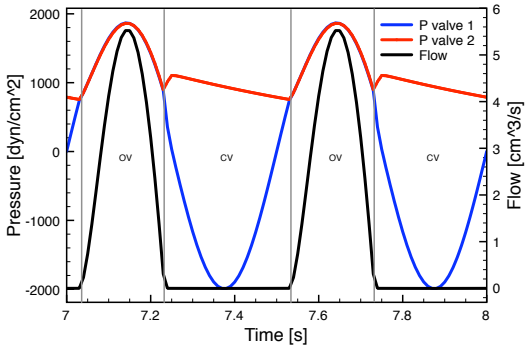

Figure 7.7: Pressures and flow on the resistive immersed surface. Valve 1 and Valve 2 identify respectively the inlet and the outlet side of the fissure.

7.4.2 Normal and stenotic configurations of the aortic valves.

This test case concerns the numerical simulation of the blood dynamics in the aortic root. Two different configurations of the valves are addressed. In the first one, the three leaflets opens normally, in the second one we suppose that one of the leaflets does not open. The two configurations are respectively named *normal* and *stenotic* for the sake of simplicity. Note that the condition reproduced in the second case is rather "extreme" from the medical viewpoint and it is used here as an example to illustrate the flexibility of the method. More realistic stenotic valve configurations can clearly be obtained from medical images.

Both the open and closed configurations have been used in the computations (see Figure 7.8). The open configuration, obtained from the 3D FSI simulation realized in Chapter 6, is green colored, the closed one is blue, finally the red leaflet in the stenotic valve is assumed fixed during the whole cardiac cycle.

The fluid domain is reported in Figure 7.9 and is made of approximatively 270000 tetrahedral elements for both the considered cases. As mentioned in Chapter 6, the simulations of the aortic root (with valves) have inherent difficulties related to the choice of the boundary conditions. We have also noticed how the prescription of Neumann-type boundary conditions, both at the inlet and at the outlet, may be difficult when physiological values of velocity and pressure are involved (see Section 6.2). In [HNP+06], where the closure of a mechanical heart valve has been studied, the authors suggested to switch between Dirichlet and Neumann conditions at the end of the systole. A similar approach is used here. During the systole, when the valves are open, a flow boundary condition is imposed at the inlet. During the diastole, when the valves are closed, we replace the flow condition with a pressure condition defined by a function that describes the pressure behavior in the left ventricle. Notice that, in order to easily switch from Dirichlet to Neumann and from Neumann to Dirichlet, the flow boundary condition is imposed by penalization. For the sake of simplicity, polynomial functions have been used to define the pressure behavior at the inlet during the diastolic phase. Nonetheless more complex (and

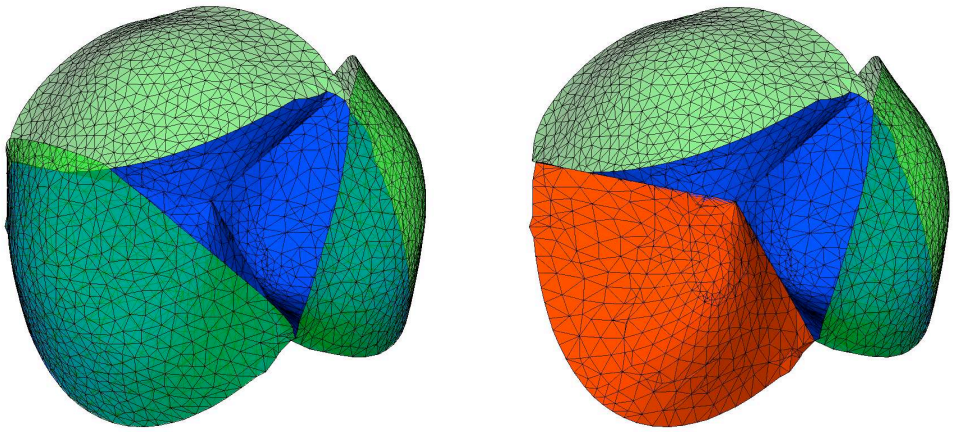

Figure 7.8: Left: Normal aortic valves. Right: Stenotic aortic valves, the red valve is fixed for the whole cardiac cycle.

realistic) models based for example on elastance model of the heart [SSW+03] could be imagined. On the outlet, Γ_{out}, the RCR model (7.9) is used. In both simulations its parameters are $R = 150$ dyn·s/cm^5, $R_d = 2300$ dyn·s/cm^5, $C = 9 \cdot 10^{-4}$ cm^5/dyn and $P_d = 0$. For both coronaries, Γ_{cor}, a resistance is imposed. Its magnitude is defined by a function that mimics the behavior of the heart contraction. Notice in fact that the resistance in the coronaries increases during systole, when the heart muscle contracts, and decreases during diastole, when the heart muscle relaxes.

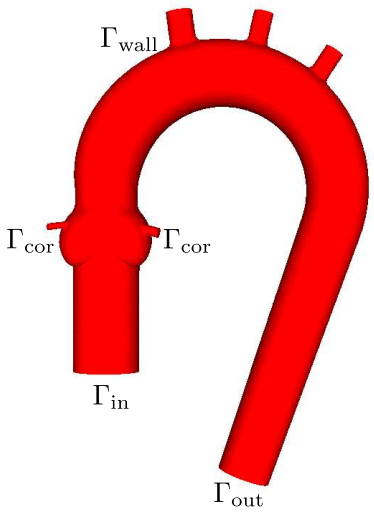

Figure 7.9: Computational fluid domain.

The simulations are run for 10 seconds with a time-step size of $5 \cdot 10^{-3}$ seconds.

The computational results for the last complete cycle are reported in Figures 7.10 for the normal and for the stenotic valves. As in the previous test case the opening and closure of the valve are identified by the grey lines in the pressure plots.

The use the RIS valve model leads to very robust computations even when physiological pressures are involved. In Figure 7.10.a, the variation in time of the pressure at the inlet and at the outlet are represented for the normal valve. Notice the physiological increase of the downstream pressure respect to the upstream, before the valve closure. In Figure 7.10.b a comparison among the pressures of the two simulations is given: the stenotic leaflet entails a higher pressure during the ejection phase.

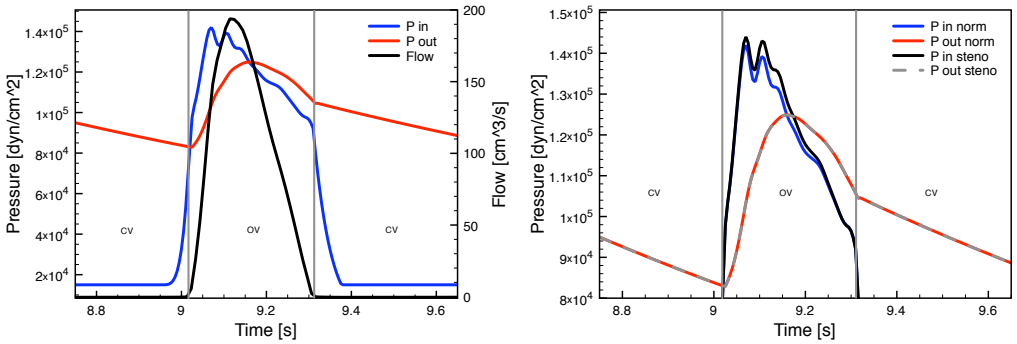

(a) (b)

Figure 7.10: Left: Variation of the pressure and flow for the normal case over a complete cardiac cycle. Right: Comparison among the pressures of the normal and stenotic cases.

During the systole, the open valve configuration replaces the closed one. The velocity distributions at time $t = 9.12$ s are reported in Figure 7.11 for the normal and for the stenotic cases. Notice the modification of the flow distribution and the increase of the peak velocity (approximatively 50 cm/s) induced by the fixed leaflet. This differences have been captured because of the second set of surfaces describing the open configurations of the valves. The use of this second set of surfaces is also appealing for providing a fast computation of the jet profile downstream of the valve, for example with the Lagrangian coherent structures (LCS) technique presented in Chapter 6. In Figure 7.12, the LCS surfaces have been computed for the two configurations. Qualitatively, two aspects are remarkable: first, the influence of the fixed "stenotic" valve in the development of the jet profile across the valve; second, the resemblance between the 3D FTLE field computed in Figure 6.7.d and the one of the normal case.

7.4.3 Left ventricle with imposed analytical displacements.

The problem we consider now is the flow dynamics in the left ventricle of the heart. The numerical experiment is performed by imposing analytical displacements on the

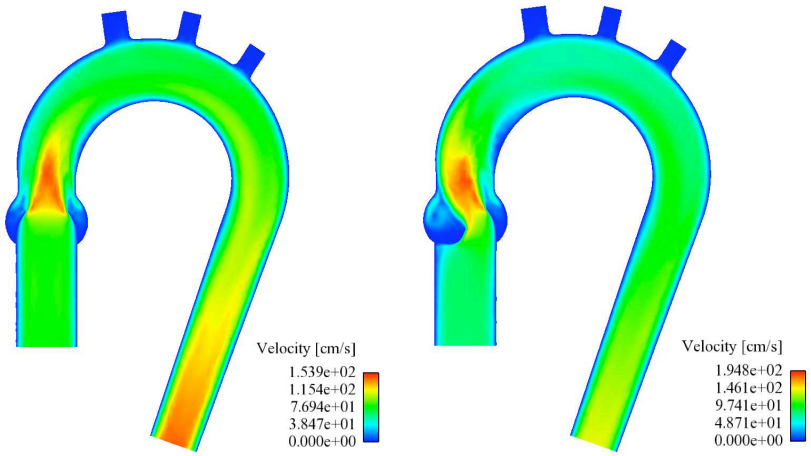

Figure 7.11: Velocity distribution for the normal (left) and stenotic (right) aortic valve at time $t = 9.12$ s (peak flow).

Figure 7.12: LCS computation of the blood flow jet at time $t = 9.12$ s for the normal (left) and stenotic (right) aortic valve.

heart wall. In Section 7.4.4, we also briefly discuss some preliminary result obtained with the use of realistic displacements, derived by an electromechanical simulation of the heart [CFG+09].

The surface geometry of the heart has been acquired by *Zygote Media Group* and is part of the project *3D Science*. Most likely, this geometry has been obtained from the post-processing of highly resolved CT (Computer Tomography) data. Before the actual use of this geometry for numerical computations, important works of re-modeling and re-meshing have been done by engineers and researchers of MACS and REO teams at INRIA. Concerning this test case, the closed configurations of the aortic and mitral valves, as well as the aortic root and a simplified geometry of the atrium, have been included to the left ventricle mesh. In Figure 7.13 the geometries of the two valves are given. All the operations of modeling and meshing have been

performed with the software *3-matic* distributed by the society *Materialise*.

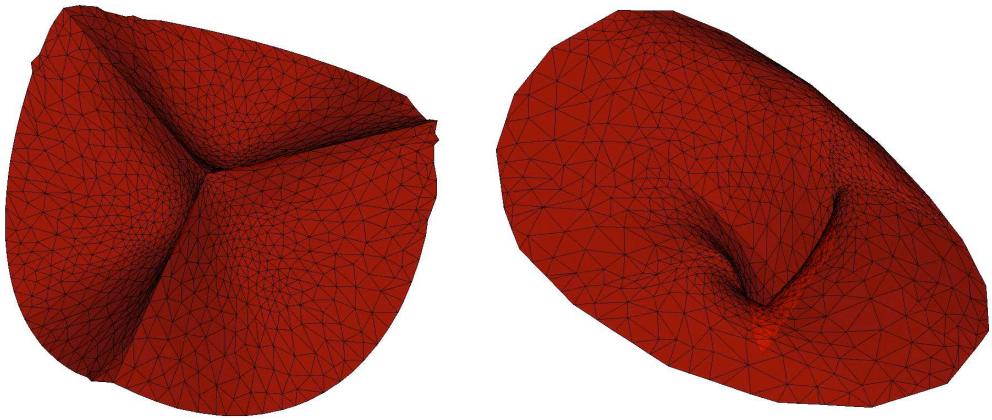

Figure 7.13: Left: Closed aortic valve mesh. Right: Closed mitral valve mesh.

The computational domain is represented in Figure 7.14.a and is made of 267917 tetrahedral elements. For what concerns the displacements, they are governed in space by the parabolic function $\pi(t)$ constructed with respect to the fix axis α. The amplitude of $\pi(t)$ varies in time with the periodic sinusoidal function given in Figure 7.14.b.

The displacements defined by the function $\pi(t)$ are imposed on the blue part of Γ_{wall}, the ventricle wall. This is indicated in the following by Γ_d. In the red and green parts of Γ_{wall}, corresponding respectively to the atrium and the aortic root, the displacements are implicitly given in the mesh update step of the ALE problem by solving the following problem:

$$\begin{cases} -\Delta \boldsymbol{d}^{\text{f}} = \mathbf{0}, & \text{in} \quad \Omega^{\text{f}}, \\ \boldsymbol{d}^{\text{f}} = \mathbf{0}, & \text{on} \quad \Gamma_{\text{in}} \text{ and } \Gamma_{\text{out}}, \\ \boldsymbol{d}^{\text{f}} = \boldsymbol{d}(\pi(t)), & \text{on} \quad \Gamma_d, \\ \nabla \boldsymbol{d}^{\text{f}} \cdot \mathbf{n} = 0; & \text{on} \quad \Gamma_{\text{wall}} \backslash \Gamma_d, \end{cases} \tag{7.10}$$

Note also that in the ALE formulation, if we let the RIS valves move with the fluid mesh, we have to rewrite problem (7.7) as follows:

$$\begin{cases} \rho^{\text{f}} \left(\partial_t \mathbf{u}|_{\mathcal{A}} + (\mathbf{u} - \mathbf{w}) \cdot \nabla \mathbf{u} \right) - \operatorname{div} \boldsymbol{\sigma}^{\text{f}}(\mathbf{u}, p) + R_\Sigma(\mathbf{u} - \mathbf{w})\delta = \mathbf{f}, & \text{in} \quad \Omega^{\text{f}}, \\ \operatorname{div} \mathbf{u} = 0, & \text{in} \quad \Omega^{\text{f}}, \end{cases} \tag{7.11}$$

$\mathbf{w}$ being the mesh velocity. Of course in that case, the movements of the surfaces representing the valves are not related to a physical velocity. Nevertheless, this artifact is necessary to follow the large movements of the heart. In addition, compared to the deformation of the myocardium, the deformation of these surfaces is relatively moderate. This approximation can therefore be considered as reasonable in the framework of this simplified model.

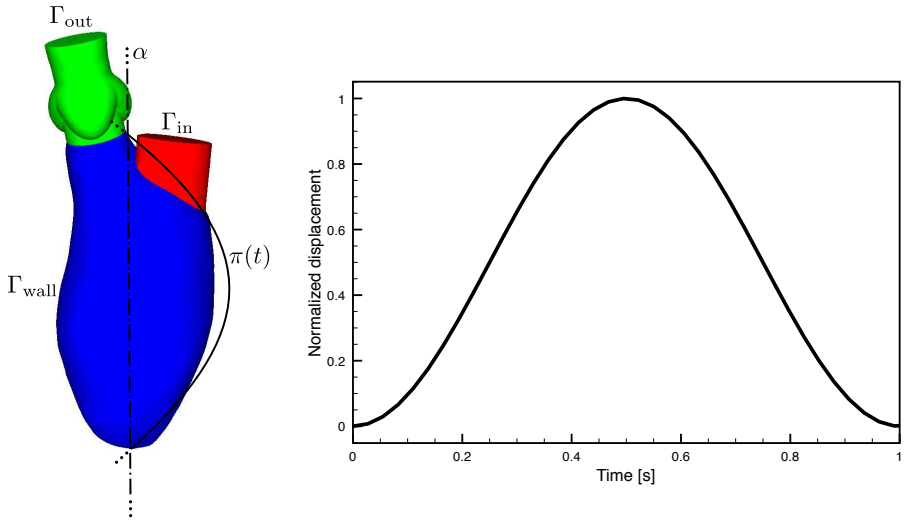

(a) (b)

Figure 7.14: Left: Computational fluid domain. Right: Normalized imposed displacement

For the boundary conditions on Γ_{in} a constant pressure of 15000 dyn/cm^2 is imposed, on Γ_{out} an RCR model is used, its parameters are the same of the previous test case. The simulation is carried out for 10 seconds with a time-step size of $5 \cdot 10^{-3}$ seconds.

In Figure 7.15, the fluid dynamics in the left ventricle is given for different points in time of the last cardiac cycle. The initial configuration of the left ventricle is represented in black, in the background, to better illustrate the amplitude of the displacements. The red and blue colors of the aortic and mitral valves are used to indicate the valves closure and opening, respectively.

Although the simple choice of the displacement function, the analysis of the results highlights high vorticity in the flow field during the diastolic phase (Figures 7.15.e and 7.15.f). This phenomenon has been observed also in other computational studies focused on the re-filling of the left ventricle (see *e.g.* [DPB05] and references therein). Clearly, further analysis in this direction require more realistic displacements.

For the pressure, results similar to that obtained in the previous test case are retrieved, the only aspect that is worth noticing is that the isovolumic contraction and relaxation seem to be missing in the pressure curves. This is probably related to the simple imposed dynamics. Nonetheless, for the considered choice of R_Σ, preliminary results indicate that the RIS valve model handles the two phases without difficulties. An example where the left-ventricle pressure varies smoothly between the aortic and the atrium pressures (isovolumic relaxation) is given in the next section.

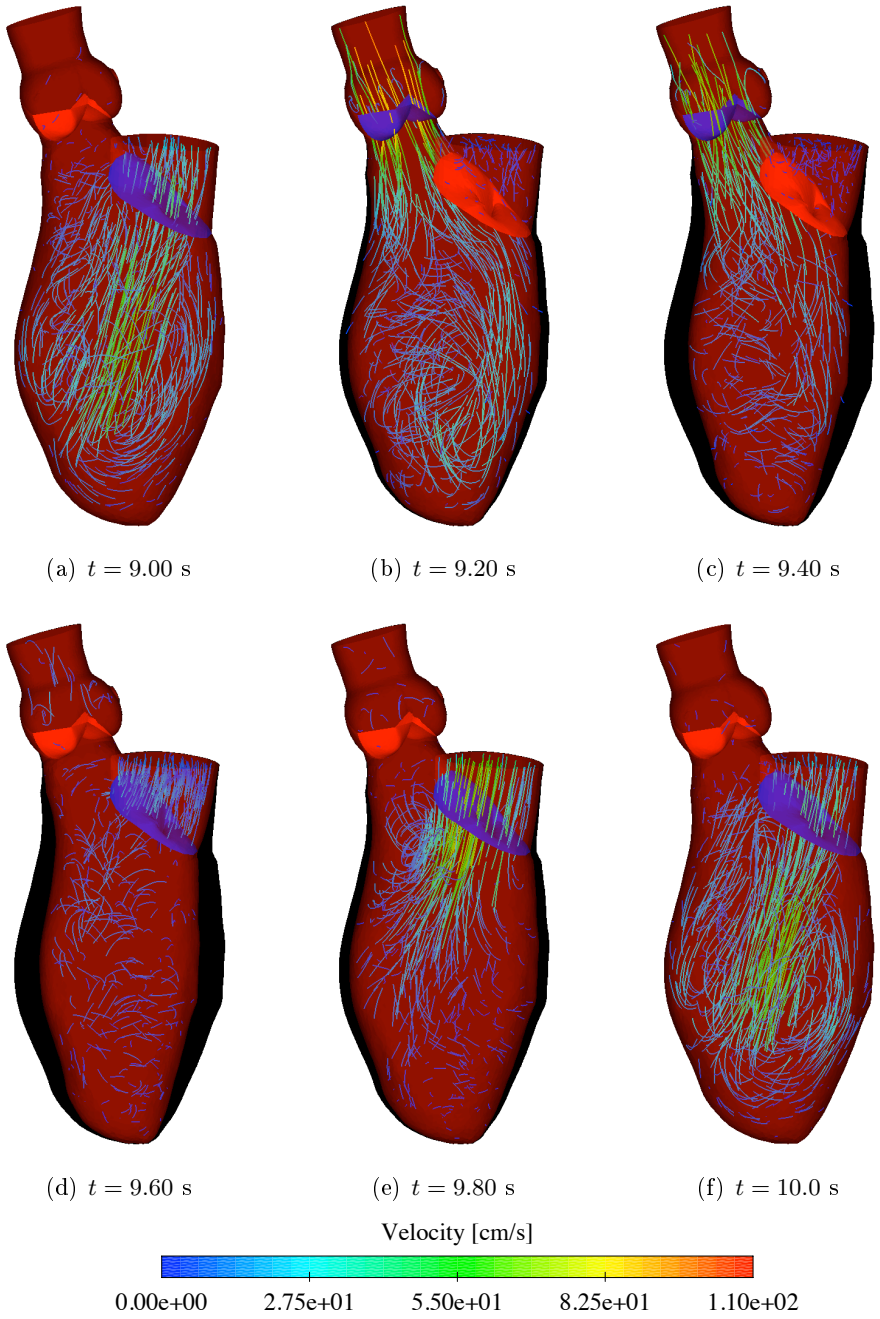

(a) $t = 9.00$ s (b) $t = 9.20$ s (c) $t = 9.40$ s

(d) $t = 9.60$ s (e) $t = 9.80$ s (f) $t = 10.0$ s

Figure 7.15: Fluid dynamics in the left ventricle for different points in time of the cycle. Open valves are represented in blue, closed valves in red.

7.4.4 Left ventricle with imposed realistic displacements.

In this last section, we discuss some preliminary results on the simulation of the fluid dynamics in the left ventricle, where the imposed displacements are given by an eletromechanical simulation of the heart, similar to the one performed in [CFG+09]. The displacements imposed on the heart lead to a physiological variation of the volume of the left ventricle, represented in Figure 7.16 (see [Moi08, CFG+09] for the details of the electromechanical simulation).

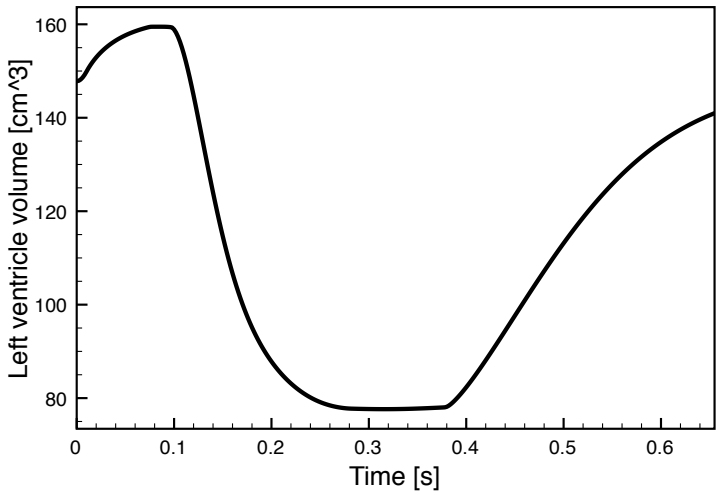

Figure 7.16: Variation of the left ventricle volume over a cardiac cycle.

For this computation, we have used the same fluid domain presented in the previous section. The displacements have been imposed both on the left ventricle wall and on the aortic wall (respectively blue and green in Figure 7.14.a). For the atrium wall, the red part, the displacements have been computed during the ALE step, as already discussed in Section 7.4.3. As before, the resistive immersed surface model is used for both the valves, aortic and mitral.

The simulation has been run only for one cardiac cycle with a time-step of 10^{-3} seconds. In this preliminary test a simplified choice for the boundaries conditions on Γ_{in} and Γ_{out} is made (see Figure 7.14.a for the notation). A constant pressure is imposed on both boundaries: on Γ_{in} equal to 15000 dyn/cm^2, on Γ_{out} equal to 90000 dyn/cm^2.

Although a single cardiac cycle is not sufficient to remove the effects of the initial conditions and that the boundary conditions could be improved (for example using *ad hoc* reduced models), some positive considerations on the results can already be done. First, the ALE formulation is able to handle without difficulties the large displacements that characterize the heart wall mechanics. This gives an important confirmation on the future use of the ALE formulation for the simulation of the fluid-structure interaction with the heart wall. Second, the RIS valve model ensures very robust and efficient computations also in physiological flow conditions. The velocity

distribution for different points in time is given in Figure 7.17. Third, within the RIS approach, using more physiological displacements than the one constructed in the previous section, it is possible to easily handle the isovolumic phases of the cardiac cycle. A confirmation of this last point is given in Figure 7.18, where successive phases of an isovolumic relaxation are represented. In Figure 7.18.a the aortic valve is open and the mitral valve is closed, the pressure in the left ventricle is equal to the one of the aorta. From Figure 7.18.b to Figure 7.18.e both of the valves are closed, and the pressure slowly reduces as soon as the volume of the ventricle increases. In Figure 7.18.f the mitral valve opens while the aortic valve is still closed. The pressure in the ventricle is now equal to the one of the atrium.

More extensive tests, with multiple cardiac cycles and more physiological boundary conditions, are planned in the very short future. After that, the fluid-structure interaction problem in the heart will be considered.

7.5 Discussion

In this chapter we presented a new reduced model for the modeling of heart valves. Within this approach, the valve is replaced by an immersed surface acting as a resistance on the fluid. The opening or the closure of the valve, *i.e.* the value of the resistance, is based on very simple fluid dynamics principles. Various tests have been presented to illustrate its efficiency and robustness in complex fluid dynamics problems (*e.g.* for three-dimensional ventricle blood flow simulations).

This approach represents a compromise between lumped parameter and multidimensional models. Although it cannot be considered to accurately describe the valve biomechanics, it nevertheless limits considerably the artifacts introduced by standard lumped parameter models, which require the introduction of artificial boundaries in region characterized by a strong variability, in space and time, of the fluid dynamics quantities. It allows also for very efficient and robust computations compared to full 3D FSI simulations and the introduction of two configurations, open and the closed, limits the inaccuracies due to the absence of the valve dynamics. Moreover, the RIS valve model seems to allow a certain flexibility in reproducing also pathological states of the valves. Pathologies such as regurgitation or stenosis can be included either in the mathematical model, or directly in the computational geometry.

As an ultimate goal, we plan to use this model for the numerical simulations of cardiac fluid-structure interaction problems where a precise description of the leaflet biomechanics is not required. A remarkable example is the fluid-structure interaction in left ventricle. To this end, the range of validity of the RIS valve model and the robustness of Algorithm 7.1 have to be accurately analyzed and intensively tested in FSI problems. Nonetheless, preliminary results, that confirm the applicability of the model in FSI problems, have already been obtained. In Figure 7.19 and Figure 7.20 are reported the results obtained for the pressure jump test (see Section 7.4.1) where half of the tube is flexible. The FSI coupled problem is solved with a strongly

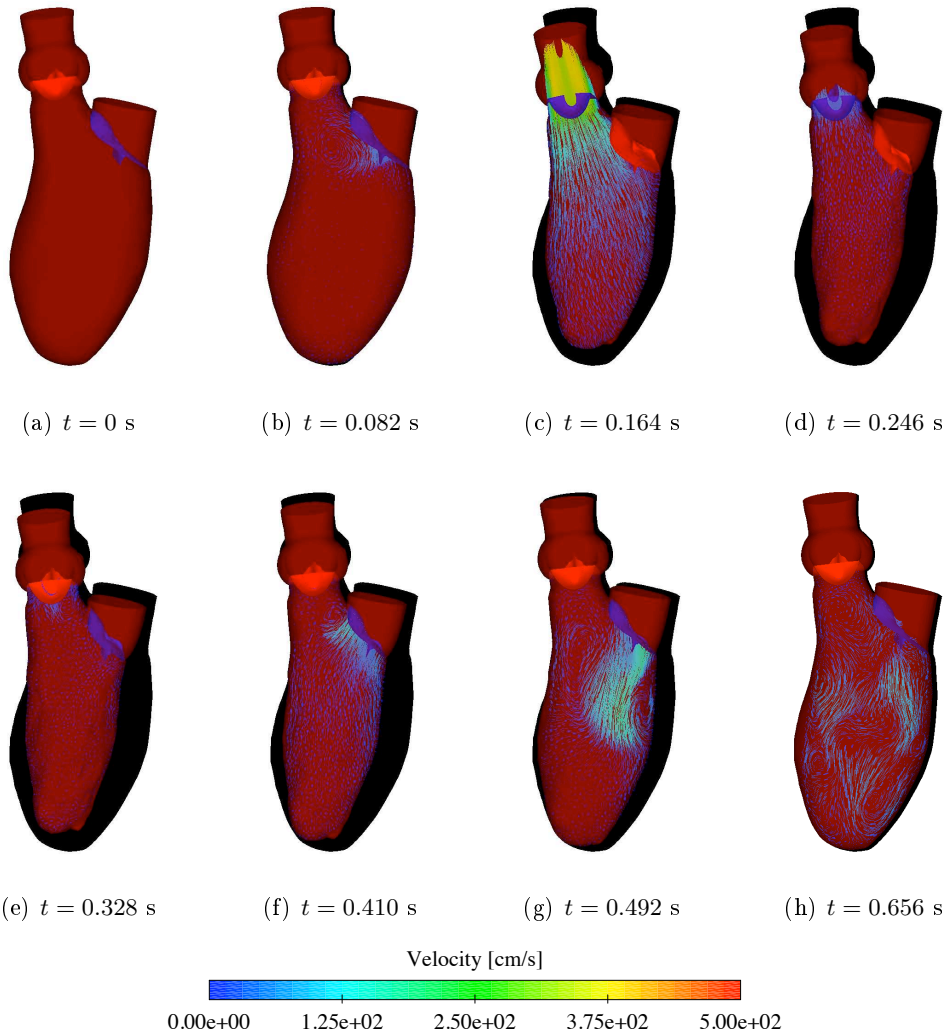

(a) $t = 0$ s (b) $t = 0.082$ s (c) $t = 0.164$ s (d) $t = 0.246$ s

(e) $t = 0.328$ s (f) $t = 0.410$ s (g) $t = 0.492$ s (h) $t = 0.656$ s

Figure 7.17: Fluid dynamics in the left ventricle for different points in time of the cardiac cycle. Open valves are represented in blue, closed valves in red.

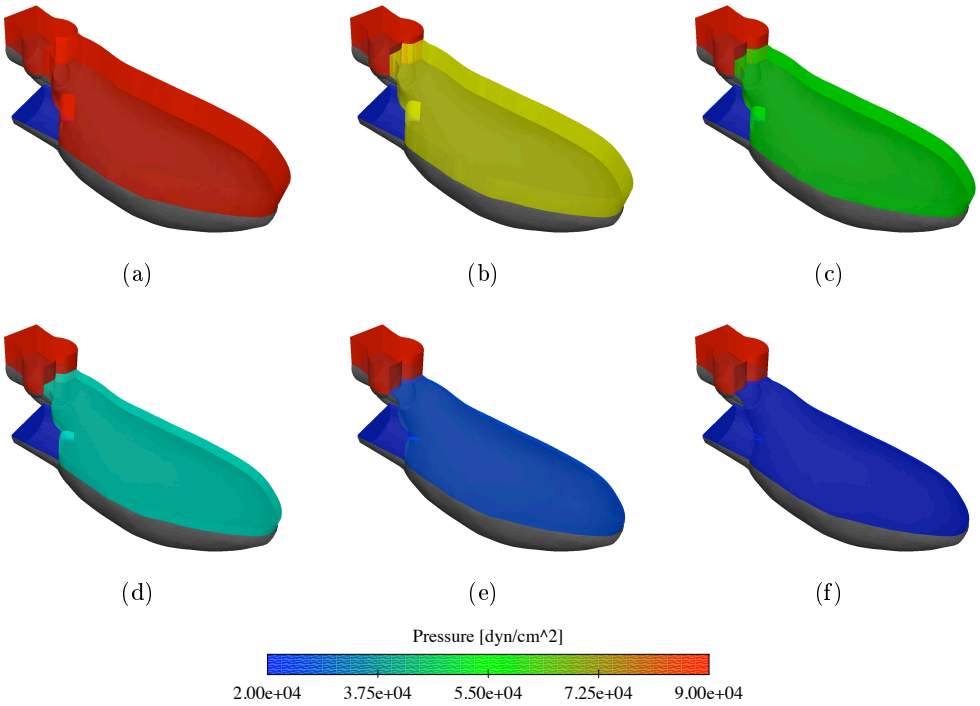

Figure 7.18: Successive time-steps of an isovolumic relaxation. The elevated surface represents the pressure.

coupled partitioned scheme based on a quasi-Newton iterative algorithm [GV03]. In this preliminary test case the update of the resistance for the RIS valve is based on the velocity and pressure at the previous time-step (*i.e.* on the standard version of the scheme).

For the fluid, we used the same computational domain, boundary conditions and initial conditions given in Section 7.4.1 [CB03]. The structure is discretized with the MITC4 "General Shell Elements". The thickness, the Young modulus and the Poisson ratio are respectively fixed to 0.1 cm, 10^6 dyn/cm^2 and 0.3. The structure mesh is conforming to the fluid mesh at the interface. We carried out the simulation for 8 seconds with a time-step size of $2{\cdot}10^{-3}$ s. The results obtained are qualitatively similar to the one of the fixed case. Nonetheless some differences in the pressure curves can be observed at the closure of the valve (Figure 7.20). Clearly, among the causes of these differences, the flexible structure has a primary responsability, but also the updating strategy of the resistance may play a role. Further investigations on this last point are required.

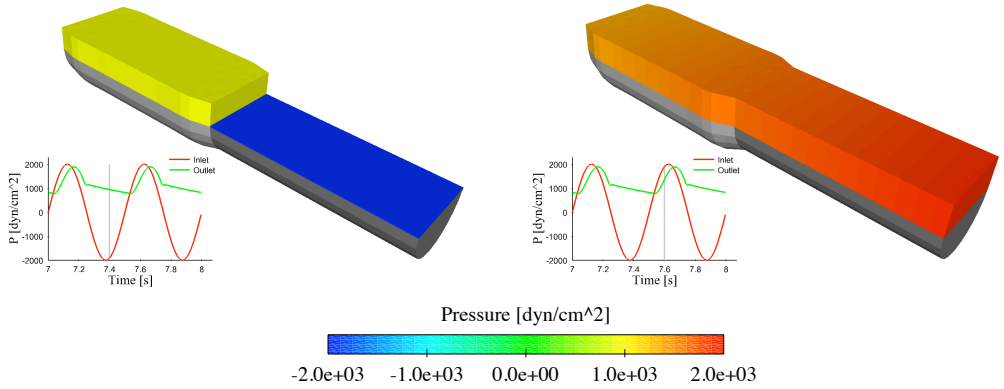

Figure 7.19: Left: Pressure distribution at time $t = 7.4$ s, the valve is closed. Right: Pressure distribution at time $t = 7.6$ s, the valve is open.

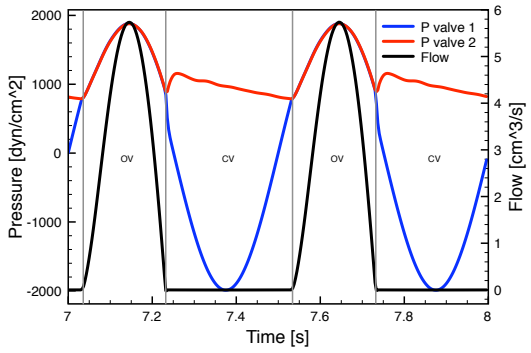

Figure 7.20: Pressures and flow on the resistive immersed surface. Valve 1 and Valve 2 identify respectively the inlet and the outlet side of the fissure.

Conclusions and perspectives

Conclusions and perspectives

In the cardiovascular system, the mechanical interactions of the blood with the vessels, the valves and the heart, give rise to complex fluid-structure interaction problems. In this thesis, we focused on the numerical analysis and the development of efficient partitioned algorithms for the resolution of these problems.

Among the various partitioned algorithms, the projection semi-implicit coupling scheme, proposed in [FGG06, FGG07], offers an excellent compromise between stability and efficiency in cardiovascular problems. In Part I, Chapter 3, we analyzed the convergence properties of the scheme both theoretically and numerically. From a theoretical point of view, we proved the convergence of the scheme in the case of a non-conforming space discretization at the fluid-structure interface. We discussed the optimality in space of the error estimates for different choices of the structure model (linearized elasticity, membrane and shell), for different choices of the interface matching operator (pointwise and matching) and with respect to the polynomial degree of the fluid approximation. In time we proved that the scheme is at least $\sqrt{\tau}$ accurate and we supported this result with a numerical test where a small reduction of the convergence rate is observed for pressure and displacements.

In Chapter 4, we replaced the strong Dirichlet-Neumann coupling enforced on the explicit step of the projection semi-implicit scheme with a Robin-Robin coupling derived from the Nitsche's interface method [BHS03, HHS04, BF07, BF09]. The resulting Robin-based semi-implicit coupling improves the stability properties of the original algorithm, in particular the new method is stable under a stability condition independent of:

1. the added-mass effect in the system (fluid-solid density ratio and geometry of the domain);

2. the numerical dissipation of the solid time-discretization.

The validity of this approach was illustrated with various numerical experiments, in particular an idealized abdominal aortic aneurysm.

In Part II, we have considered the numerical simulation of fluid-structure interaction problems with cardiac valves. A modular algorithm for the numerical simulation of fluid-structure interaction problems, where contact among multiple elastic solids can occur, was presented in Chapter 5. The contact algorithm, implemented in an independent C++ software, can handle multi-structure and auto contacts. This procedure has been tested for different problems in two and three dimensions and has been applied in Chapter 6 to the investigation of the blood jet downstream of the aortic valve. In the same chapter, we made use of an advanced post-processing technique based on the computation of Lagrangian coherent structures to better

identify the evolution of the jet profile. This technique allows to precisely characterize major flow features, such as vorticity, separation, stagnation and mixing, which are known to influence health maintenance and disease progression.

The computational costs and the numerical difficulties underling the numerical simulation of cardiac valves, moved us to explore also alternative solutions - more efficient and robust - to perform numerical simulations with cardiac valves. In Part III, Chapter 7, we have presented a new reduced valve model based on resistive immersed surfaces. This model represents a compromise between standard lumped parameter models and fully 3D FSI computations. Its main characteristics are here recalled:

- when the valve is closed, the pressure jump across the valve is accurately captured with the use of the "fissure" technique proposed in [FGM08].
- when the valve is open, the use of a second set of surfaces in the fluid domain allows to capture the main flow features of the cardiac cycles.
- the opening and closure of the valve relies on simple physiological considerations that ensure reliability and robustness to the model.

We conclude this thesis discussing some aspects of the present work that might lead to future developments.

Considering the convergence analysis of the projection semi-implicit scheme, some differences between the theoretical estimate and the convergence results obtained numerically can be observed. The origin of these differences must be accurately investigated in order to improve the understanding of the mathematical and numerical properties of the semi-implicit coupling scheme in fluid-structure interaction. With the same purpose, it will be also interesting to perform a theoretical analysis of the convergence properties of the incremental semi-implicit scheme - Algorithm 3.4, p. 93 - and of the Robin based semi-implicit scheme - Algorithm 4.1, p. 101.

The reinterpretation of the Nitsche's interface method as a particular Robin-Robin coupling might also lead to new insights in the development of fluid-structure interaction coupling schemes, and more in general for the coupling in multiphysics interface problems (see for example [Han05]).

In the framework of the numerical simulation of cardiac valves, two possible research directions can be addressed: one more numerical oriented, the other more clinically relevant.

From the numerical viewpoint, in 3D FSI simulations we are currently studying how to extend the different formulations of the projection semi-implicit coupling within the Fictitious Domain formulation, in order to reduce the computational costs of fully 3D numerical simulations. Preliminary steps in this direction have been made in [dS07]. Note that the coupling algorithm in the FD formulation

is non-trivial for the pressure-Poisson formulation of the semi-implicit scheme (see Section 2.5.3, p. 53). In addition, considering the contact algorithm, further analysis on the choice of the descent step in the Uzawa algorithm (see Remark 5.2) might also lead to new interesting mathematical results.

Currently, much effort is made to extend the "reduced immersed surface" (RIS) valve model to fluid-structure interaction problems. The results presented in Section 7.5 are promising, but more subtile analyses have to be made for the development of robust and reliable numerical procedures. In particular, an essential element will be the extension of the updating strategy presented in Algorithm 7.1 to FSI problems. Comparisons between fully 3D and RIS valves in term of performance and reliability are also contemplated. With regard to this point, the Lagrangian Coherent Structures (LCS) method offers an excellent framework for the comparisons.

From the clinical viewpoint, we are also planning to study relevant stenotic conditions using the RIS valve model and to analyze the corresponding results with the LCS post-processing technique.

As an ultimate goal, we plan to use robust and efficient partitioned FSI schemes together with the RIS valve model to simulate the fluid-structure interaction in the heart.

Appendix A

External tissue support for FSI simulations

During the last decade, the numerical modeling of three-dimensional blood flows in compliant arteries has become a very active field of research. For obvious reasons, it is not possible to model the entire arterial tree with three-dimensional models. Therefore, artificial truncations must be introduced in the computational domains and some adequate corresponding boundary conditions considered. In the fluid domain, much work has already been done for what concerns flow and pressure boundary conditions (see for example [FVCJ+06, FGNQ01, FMN07]) but few simulations take into account the effects of the tissues surrounding the solid domain. In fact, in all the FSI studies we are aware of, a constant pressure (or normal stress) is applied on the outer part of the structure wall. This simple boundary condition is not able to sustain the artery and typically results in an artificial global bending motion. In practice, this global movement induces inaccuracies (and in the worst case instabilities) much greater than those introduced by spurious reflections on artificial boundaries. A possible idea is thus to introduce a boundary condition along the external solid wall that consists of an elastic and a viscoelastic term, which represents the support provided by the surrounding tissues. From a mathematical viewpoint, this corresponds to the following generalized Robin boundary condition on the wall

$$\mathbf{\Pi n}^{\mathrm{s}} = -k_{\mathrm{s}}(\boldsymbol{d} - \boldsymbol{d}_b) - c_{\mathrm{s}}(\mathbf{u}^{\mathrm{s}} - \mathbf{u}_b), \tag{A.1}$$

where $\boldsymbol{d}_b$ and $\mathbf{u}_b$ are the reference displacement and velocity of the boundary. The parameters k_{s} and c_{s}, possibly distributed in space and time, can be adjusted to mimic the elastic and viscoelastic response of various physiological external tissues. This technique can model a wide range of contact (from very stiff external tissue to very soft external tissue). Along the artery the model aims at representing the external organs, for example the spine that supports the descending aorta. On the inlet or outlet ending, it should represent the rest of the cardiovascular tree: the vessels but also the moving heart when considering the ascending aorta. We also point out that time dependent parameters can be imagined for instance to model the effect of the change of mechanical properties of the lungs during respiration.

In the preliminary results presented below, the parameters have been chosen to reproduce the expected qualitative behavior for the structure. Clearly in more realistic situations, more accurate techniques, based for instance on parameter estimation procedures, should be considered.

An example on a carotid bifurcation. The simple FSI test presented here, made on an idealized carotid bifurcation, is representative of various tests made

to illustrate the qualitative differences between the use of a "standard" constant pressure and the boundary condition (A.1) for the external structure wall.

The geometry considered is made of 11426 hexahedral elements (see Figure A.1.a). The flow profile given in Figure A.1.b is imposed on Γ_{in}. On Γ_{out_1} and Γ_{out_2}, two resistance boundary conditions have been used, both of them equal to 550 dyn·s/cm^5. The structure matches the fluid mesh on Γ_{wall} and is described by the same non-linear shell model used in Section 7.5 for the pressure jump test. In this case the thickness, the Young modulus and the Poisson ratio are respectively fixed to 0.05 cm, $3 \cdot 10^6$ dyn/cm^2 and 0.3. For the coupling, the semi-implicit projection coupling algorithm is used.

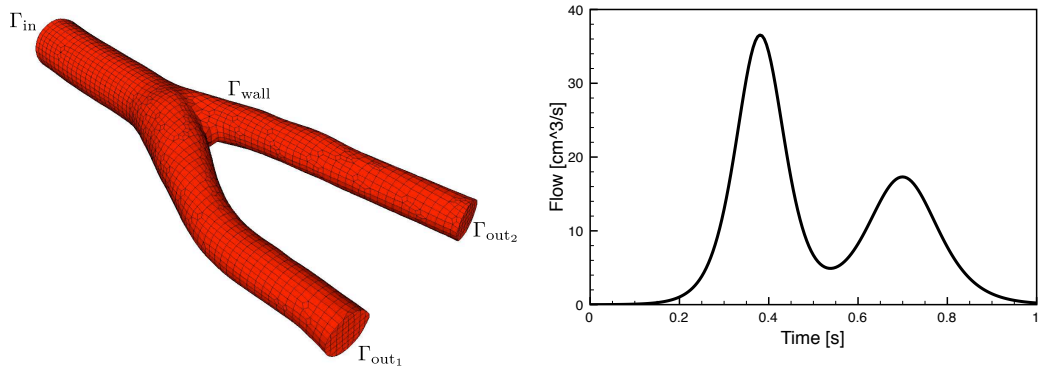

(a) (b)

Figure A.1: Left: Computational fluid domain. Right: Imposed flow profile.

Two simulations are presented: one doesn't include boundary condition (A.1), the other does. For the one that incorporates the external tissue, we set $k_{\text{s}} = 500$ dyn/cm^3 and $c_{\text{s}} = 1000$ dyn/cm^3. The results for three different time-steps are given in Figure A.2, the magnitude of the displacements is represented. On the one hand, the effect of an unphysical bending can be observed in the simulation that doesn't use the external tissue support (on the left in Figure A.2). Notice in fact how the maximum value of the displacements changes side of the carotid for successive time-steps. On the other hand, the use of a reduced model for the external tissue circumvents this problem and allows for more reliable numerical simulations. Other tests, on different idealized geometries and with different structure solvers, have been performed. In all the considered cases, the improvement on the results were remarkable. In [MXA+], a more physiological investigation is currently under analysis for the simulation of the aortic arch.

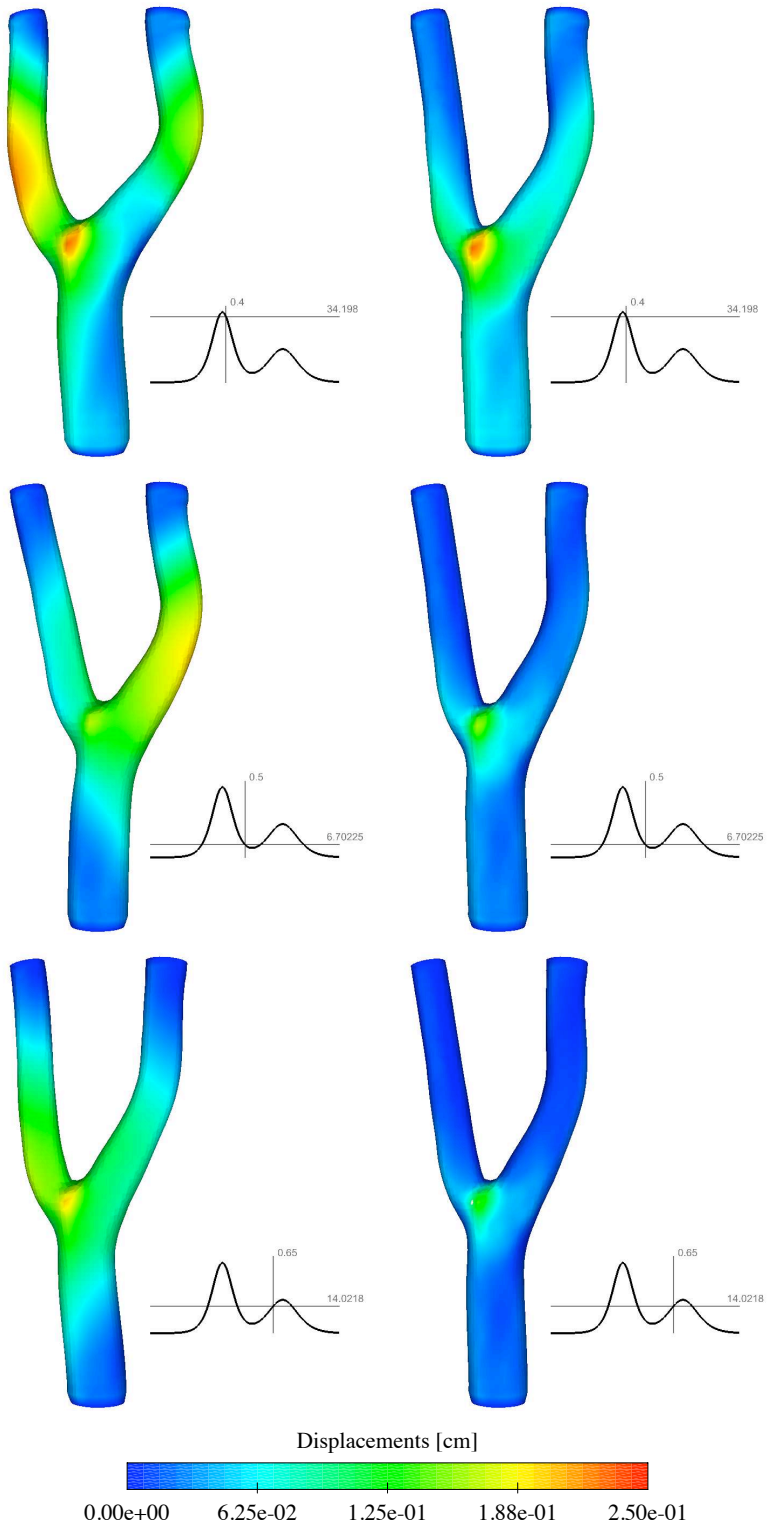

Figure A.2: Displacement in the cases of a constant pressure (left) and of boundary condition (A.1) (right) applied to the structure wall.

Bibliography

[ABL+95] R.L. Armentano, J.G. Barra, J. Levenson, A. Simon, and R.H. Pichel. Arterial wall mechanics in conscious dogs: assessment of viscous, inertial, and elastic moduli to characterize aortic wall behavior. *Circ. Res.*, 76(3):468, 1995.

[ACF09] M. Astorino, F. Chouly, and M.A. Fernández. An added-mass free semi-implicit coupling scheme for fluid-structure interaction. *C. R. Math. Acad. Sci. Paris*, 347(1-2):99–104, 2009.

[AG09] M. Astorino and C. Grandmont. Convergence analysis of a projection semi-implicit coupling scheme for fluid-structure interaction problems. Technical report, INRIA, July 2009.

[AGPT09] M. Astorino, J.-F. Gerbeau, O. Pantz, and K.-F. Traoré. Fluid-structure interaction and multi-body contact. Application to the aortic valves. *Comput. Methods Appl. Mech. Eng.*, 198(45-46):3603–3612, 2009.

[Ale53] R.S. Alexander. The genesis of the aortic standing wave. *Circ. Res.*, 1:145–151, 1953.

[Baa01] F. Baaijens. A fictitious domain/mortar element method for fluid-structure interaction. *Int. J. Numer. Methods Fluids*, 35:743–761, 2001.

[Bat96] K.J. Bathe. *Finite Element Procedures.* Prentice Hall, 1996.

[Bau06] H. Baumgartner. Hemodynamic assessment of aortic stenosis. *J. Am. Coll. Cardiol.*, 47(1):138–140, 2006.

[BB99] F. Ben Belgacem. The mortar finite element method with Lagrange multipliers. *Numer. Math.*, 84(2):173–197, 1999.

[BBM97] F. Ben Belgacem and Y. Maday. The mortar element method for three-dimensional finite elements. *RAIRO Modél. Math. Anal. Numér.*, 31(2):289–302, 1997.

[BC07] S. Badia and R. Codina. Convergence analysis of the FEM approximation of the first order projection method for incompressible flows with and without the inf-sup condition. *Numer. Math.*, 107:533–557, 2007.

[BCS01] J. Bestel, F. Clément, and M. Sorine. A biomechanical model of muscle contraction. In *Lect. Notes Comput. Sci.*, volume 2208. Eds W.J. Niessen and M.A. Viergever, Springer-Verlag, 2001.

[BCZH06] Y. Bazilevs, V.M. Calo, Y. Zhang, and T.J.R. Hughes. Isogeometric fluid–structure interaction analysis with applications to arterial blood flow. *Comput. Mech.*, 38(4):310–322, 2006.

[BF91] F. Brezzi and M. Fortan. *Mixed and hybrid finite element methods.* Springer-Verlag, New York, 1991.

[BF07] E. Burman and M.A. Fernández. Stabilized explicit coupling for fluid-structure interaction using Nitsche's method. *C. R. Math. Acad. Sci. Paris*, 345(8):467–472, 2007.

[BF09] E. Burman and M.A. Fernández. Stabilization of explicit coupling in fluid-structure interaction involving fluid incompressibility. *Comput. Methods Appl. Mech. Eng.*, 198(5-8):766–784, 2009.

[BGH+09] Y. Bazilevs, J.R. Gohean, T.J.R. Hughes, R.D. Moser, and Y. Zhang. Patient-specific isogeometric fluid–structure interaction analysis of thoracic aortic blood flow due to implantation of the Jarvik 2000 left ventricular assist device. *Comput. Methods Appl. Mech. Eng.*, 198(45-46):3534–3550, 2009.

[BHB+09] H. Baumgartner, J. Hung, J. Bermejo, J.B. Chambers, A. Evangelista, B.P. Griffin, B. Iung, C.M. Otto, P.A. Pellikka, and M. Quinones. Echocardiographic assessment of valve stenosis: EAE/ASE recommendations for clinical practice. *J. Am. Soc. Echocardiogr.*, 22(1):1–23, 2009.

[BHS03] R. Becker, P. Hansbo, and R. Stenberg. A finite element method for domain decomposition with non-matching grids. *M2AN Math. Model. Numer. Anal.*, 37(2):209–225, 2003.

[BMP93] C. Bernardi, Y. Maday, and A.T. Patera. Domain decomposition by the mortar element method. In *Asymptotic and numerical methods for partial differential equations with critical parameters (Beaune, 1992)*, volume 384 of *NATO Adv. Sci. Inst. Ser. C Math. Phys. Sci.*, pages 269–286. Kluwer Acad. Publ., Dordrecht, 1993.

[BMP94] C. Bernardi, Y. Maday, and A.T. Patera. A new nonconforming approach to domain decomposition: the mortar element method. In *Nonlinear partial differential equations and their applications. Collège de France Seminar, Vol. XI (Paris, 1989–1991)*, volume 299 of *Pitman Res. Notes Math. Ser.*, pages 13–51. Longman Sci. Tech., 1994.

[BNV08] S. Badia, F. Nobile, and C. Vergara. Fluid-structure partitioned procedures based on Robin transmission conditions. *J. Comput. Phys.*, 227:7027–7051, 2008.

[BNV09] S. Badia, F. Nobile, and C. Vergara. Robin–Robin preconditioned Krylov methods for fluid–structure interaction problems. *Comput. Methods Appl. Mech. Eng.*, 198(33-36):2768–2784, 2009.

[BQQ08] S. Badia, A. Quaini, and A. Quarteroni. Splitting methods based on algebraic factorization for fluid-structure interaction. *SIAM J. Sci. Comput.*, 30(4):1778–1805, 2008.

[Bre74] F. Brezzi. On the existence, uniqueness and approximation of saddle-point problems arising from Lagrangian multipliers. *Rev. Française Automat. Informat. Recherche Opérationnelle Sér. Rouge*, 8(R-2):129–151, 1974.

[Bre83] H. Brezis. *Analyse fonctionnelle, Théorie et applications*. Masson, 1983.

[CB03] D. Chapelle and K.J. Bathe. *The Finite Element Analysis of Shells - Fundamentals*. Springer Verlag, 2003.

[CBHP06] C.J. Carmody, G. Burriesci, I.C. Howard, and E.A. Patterson. An approach to the simulation of fluid-structure interaction in the aortic valve. *J. Biomech.*, 39:158–169, 2006.

[CDdSG+05] P. Causin, N.M. Diniz dos Santos, J.-F. Gerbeau, C. Guiver, and P. Metier. An embedded surface method for valve simulation: Application to stenotic aortic valve estimation. *ESAIM Proc.*, 14:48–62, 2005.

[CFG+09] D. Chapelle, M.A. Fernández, J.-F. Gerbeau, Ph. Moireau, J. Sainte-Marie, and N. Zemzemi. Numerical simulation of the electromechanical activity of the heart. In *FIMH*, pages 357–365, 2009.

[CFGM10] A. Caiazzo, M. A. Fernández, J.-F. Gerbeau, and V. Martin. Projection schemes for fluid flows through a porous interface. In preparation, 2010.

[CGN05] P. Causin, J.-F. Gerbeau, and F. Nobile. Added-mass effect in the design of partitioned algorithms for fluid-structure problems. *Comput. Methods Appl. Mech. Eng.*, 194(42-44):4506–4527, 2005.

[Cho68] A.J. Chorin. Numerical solution of the Navier-Stokes equations. *Math. Comput.*, 22:745–762, 1968.

[Cho69] A.J. Chorin. On the convergence of discrete approximations to the Navier-Stokes equations. *Math. Comput.*, 23:341–353, 1969.

[Cia88] P.G. Ciarlet. *Mathematical elasticity. Vol. I*, volume 20 of *Studies in Mathematics and its Applications*. North-Holland Publishing Co., Amsterdam, 1988.

[CL91] P.G. Ciarlet and J.-L. Lions, editors. *Handbook of Numerical Analysis, Vol. 2, Finite Element Methods (Part 1).* North-Holland, 1991.

[CLK04] R. Cheng, Y.G. Lai, and Chandran K.B. Three-dimensional fluid-structure interaction simulation of bileaflet mechanical heart valve flow dynamics. *Ann. Biomed. Eng.*, 32(11):1471–1483, 2004.

[CLW06] J. Chen, X.-Y. Lu, and Wang W. Non-newtonian effects of blood flow on hemodynamics in distal vascular graft anastomoses. *J. Biomech.*, 39:1983–1995, 2006.

[CPSS78] C.G. Caro, T.J. Pedley, R.C. Schroter, and W.A. Seed. *The Mechanics of the Circulation.* Oxford University Press, Oxford, 1978.

[CRCK+05] S. Canic, K. Ravi-Chandar, Z. Krajcer, D. Mirkovic, and S. Lapin. Mathematical Model Analysis of Wallstent® and AneuRx®: Dynamic Responses of Bare-Metal Endoprosthesis Compared with Those of Stent-Graft. *Texas Heart Institute Journal*, 32(4):502, 2005.

[CSC+92] J.B. Chambers, D.C. Sprigings, T. Cochrane, J. Allen, R. Morris, M.M. Black, and G. Jackson. Continuity equation and Gorlin formula compared with directly observed orifice area in native and prosthetic aortic valves. *Br. Heart J.*, 67:193–199, 1992.

[DDFQ06] S. Deparis, M. Discacciati, G. Fourestey, and A. Quarteroni. Fluid-structure algorithms based on Steklov-Poincaré operators. *Comput. Methods Appl. Mech. Eng.*, 195(41-43):5797–5812, 2006.

[DDQ04] S. Deparis, M. Discacciati, and A. Quarteroni. A domain decomposition framework for fluid-structure interaction problems. In *Proceedings of the Third International Conference on Computational Fluid Dynamics (ICCFD3)*, 2004.

[DFF03] S. Deparis, M.A. Fernández, and L. Formaggia. Acceleration of a fixed point algorithm for fluid-structure interaction using transpiration conditions. *M2AN Math. Model. Numer. Anal.*, 37(4):601–616, 2003.

[DGHL03] Q. Du, M.D. Gunzburger, L. S. Hou, and J. Lee. Analysis of a linear fluid-structure interaction problem. *Discrete Contin. Dyn. Syst.*, 9(3):633–650, 2003.

[dH02] J. de Hart. *Fluid-Structure Interaction in the Aortic Heart Valve: a three-dimensional computational analysis.* PhD thesis, Technische Universiteit Eindhoven, 2002.

[dH04] J. de Hart. Evaluation of a fictitious domain method for predicting dynamic response of mechanical heart valves. *J. Fluids Struct.*, 19:835–850, 2004.

[DHPRF04] J. Donea, A. Huerta, J.-Ph. Ponthot, and A. Rodríguez-Ferran. *Encyclopedia of Computational Mechanics*, volume 1: Fundamentals, chapter 14, pages 1–25. John Wiley & Sons, 2004.

[dHPSB03] J. de Hart, G.W.M. Peters, P.J.G. Schreurs, and F.P.T. Baaijens. A three-dimensional computational analysis of fluid-structure interaction in the aortic valve. *J. Biomech.*, 36:103–112, 2003.

[DPB05] F. Domenichini, G. Pedrizzetti, and B. Baccani. Three-dimensional filling flow into a model left ventricle. *J. Fluid Mech.*, 539:179–198, 2005.

[dS07] N.M.D. dos Santos. *Numerical methods for fluid-structure interaction problems with valves.* PhD thesis, Université Pierre et Marie Curie, Paris VI, 2007.

[dSGB08] N.M.D. dos Santos, J.-F. Gerbeau, and J.-F. Bourgat. A partitioned fluid-structure algorithm for elastic thin valves with contact. *Comput. Methods Appl. Mech. Eng.*, 197(19-20):1750–1761, 2008.

[DSVC98] C.G. DeGroff, R. Shandas, and L. Valdes-Cruz. Analysis of the effect of flow rate on the doppler continuity equation for stenotic orifice area calculations: A numerical study. *Circulation*, 97:1597–1605, 1998.

[DTM73] T.R. Dawber, H.E. Thomas, and P.M. McNamara. Characteristics of the dicrotic notch of the arterial pulse wave in coronary heart disease. *Angiology*, 24(4):244, 1973.

[DVD+09] S.K. Dahl, J. Vierendeels, J. Degroote, S. Annerel, B. Skallerud, and Hellevik L.R. Implicit interaction of two rigid mitral leaflets in a partitioned fluid-structure approach. In B. Skallerud and H.I. Andersson, editors, *MekIT'09. Fifth national conference on Computational Mechanics.*, 2009. ISBN: 9788251924214.

[DY91] J.G. Dumesnil and A.P. Yoganathan. Theoretical and practical differences between the Gorlin formula and the continuity equation for calculating aortic and mitral valve areas. *Am. J. Cardiol.*, 67:1268–1272, 1991.

[DZ07] C. D'Angelo and P. Zunino. A numerical study of the interaction of blood flow and drug release from cardiovascular stents. In *Proceedings of the Enumath Conference, Austria, September.* Springer, 2007.

[DZL07] V. Díaz-Zuccarini and J. LeFèvre. An energetically coherent lumped parameter model of the left ventricle specially developed for educational purposes. *Comput. Biol. Med.*, 37:774–784, 2007.

[EG04] A. Ern and J.-L. Guermond. *Theory and practice of finite elements.* Springer Verlag, New-York, 2004.

[FF92] L.P. Franca and S.L. Frey. Stabilized finite element methods : II. The incompressible Navier-Stokes equations. *Comput. Methods Appl. Mech. Eng.*, 99:209–233, 1992.

[FFGQ09] M.A. Fernández, L. Formaggia, J.-F. Gerbeau, and A. Quarteroni. *The derivation of the equations for fluids and structure*, chapter 3 of *Cardiovascular Mathematics*. Springer Verlag, 2009. L. Formaggia, A. Quarteroni, A. Veneziani editors.

[FFP79] Y.C. Fung, K. Fronek, and P. Patitucci. Pseudoelasticity of arteries and the choice of its mathematical expression. *Am. J. Physiol. - Heart Circ. Physiol.*, 237(5):H620–31, 1979.

[FG09] M.A. Fernández and J.-F. Gerbeau. *Fluid structure interaction problems in haemodynamics*, chapter 9 of *Cardiovascular Mathematics*. Springer Verlag, 2009. L. Formaggia, A. Quarteroni, A. Veneziani editors.

[FGG06] M.A. Fernández, J.-F. Gerbeau, and C. Grandmont. A projection algorithm for fluid-structure interaction problems with strong added-mass effect. *C. R. Math. Acad. Sci. Paris*, 342(4):279–284, 2006.

[FGG07] M.A. Fernández, J.-F. Gerbeau, and C. Grandmont. A projection semi-implicit scheme for the coupling of an elastic structure with an incompressible fluid. *Int. J. Numer. Meth. Eng.*, 69(4):794–821, 2007.

[FGGV08] M.A Fernández, J.-F. Gerbeau, A. Gloria, and M. Vidrascu. A partitioned Newton method for the interaction of a fluid and a 3D shell structure. Technical Report RR-6623, INRIA, August 2008.

[FGM08] M.A. Fernández, J.-F. Gerbeau, and V. Martin. Numerical simulation of blood flows through a porous interface. *M2AN Math. Model. Numer. Anal.*, 42:961–990, 2008.

[FGNQ01] L. Formaggia, J.-F. Gerbeau, F. Nobile, and A. Quarteroni. On the coupling of 3D and 1D Navier-Stokes equations for flow problems in compliant vessels. *Comput. Methods Appl. Mech. Eng.*, 191(6-7):561–582, 2001.

[FLLT98] C. Farhat, M. Lesoinne, and P. Le Tallec. Load and motion transfer algorithms for fluid/structure interaction problems with non-matching discrete interfaces: Momentum and energy conservation, optimal discretization and application to aeroelasticity. *Comput. Methods Appl. Mech. Eng.*, 157:95–114, 1998.

[FLTV06] L. Formaggia, D. Lamponi, M. Tuveri, and A. Veneziani. Numerical modeling of 1D arterial networks coupled with a lumped parameters description of the heart. *Comput. Meth. Biomech. Biomed. Eng.*, 9(5):273–288, 2006.

[FM03] M.A. Fernández and M. Moubachir. An exact block-Newton algorithm for solving fluid-structure interaction problems. *C. R. Math. Acad. Sci. Paris*, 336(8):681–686, 2003.

[FM05] M.A. Fernández and M. Moubachir. A Newton method using exact Jacobians for solving fluid-structure coupling. *Comp. & Struct.*, 83:127–142, 2005.

[FMN07] L. Formaggia, A. Moura, and F. Nobile. On the stability of the coupling of 3D and 1D fluid-structure interaction models for blood flow simulations. *M2AN Math. Model. Numer. Anal.*, 41(4):743–769, 2007.

[FQV09] L. Formaggia, A. Quarteroni, and A. Veneziani, editors. *Cardiovascular Mathematics. Modeling and simulation of the circulatory system*, volume 1 of *Modeling, Simulation and Applications*. Springer, 2009.

[Fun93] Y.C. Fung. *Biomechanics: Mechanical properties of living tissues.* Springer, 1993.

[FVCJ+06] C.A. Figueroa, I.E. Vignon-Clementel, K.E. Jansen, T.J.R. Hughes, and C.A. Taylor. A coupled momentum method for modeling blood flow in three-dimensional deformable arteries. *Comput. Methods Appl. Mech. Eng.*, 195(41-43):5685–5706, 2006.

[FvdZG06] C. Farhat, K. van der Zee, and Ph. Geuzaine. Provably second-order time-accurate loosely-coupled solution algorithms for transient nonlinear aeroelasticity. *Comput. Methods Appl. Mech. Eng.*, 195(17-18):1973–2001, 2006.

[FWR06] C. Förster, W.A. Wall, and E. Ramm. The artificial added mass effect in sequential staggered fluid-structure interaction algorithms. In P. Wessling, E. Onate, and J. Periaux, editors, *Prooceedings European Conference on Computational Fluid Dynamics ECCOMAS CFD*, 2006.

[FWR07] C. Förster, W.A. Wall, and E. Ramm. Artificial added mass instabilities in sequential staggered coupling of nonlinear structures and incompressible viscous flows. *Comput. Methods Appl. Mech. Eng.*, 196(7):1278–1293, 2007.

[GBP+05] D. Garcia, P. Barenbrug, P. Pibarot, A. Dekker, F.H. van der Veen, J.G. Maessen, J.G. Dumesnil, and L.G. Durand. A ventricular-vascular coupling model in presence of aortic stenosis. *Am. J. Physiol.*, 288:H1874–H1884, 2005.

[GD06] D. Garcia and L.G. Durand. *Wiley Encyclopedia of Biomedical Engineering*, chapter Aortic stenosis and systemic hypertension, Modeling of. John Wiley & Sons, Inc., 2006.

[GDP07] C. Guivier, V. Deplano, and P. Pibarot. New insights into the assessment of the prosthetic valve performance in the presence of subaortic stenosis through a fluid-structure interaction model. *J. Biomech.*, 40:2283–2290, 2007.

[GG51] R. Gorlin and S.C. Gorlin. Hydraulic formula for calculation of the area of the stenotic mitral valve, other cardiac valves, and central circulatory shunts. *Am. Heart J.*, 41:1–29, 1951.

[GGC+09] G. Guidoboni, R. Glowinski, N. Cavallini, S. Canic, and S. Lapin. A kinematically coupled time-splitting scheme for fluid-structure interaction in blood flow. *Appl. Math. Lett.*, 22(5):684–688, 2009.

[GGCC09] G. Guidoboni, R. Glowinski, N. Cavallini, and S. Canic. Stable loosely-coupled-type algorithm for fluid–structure interaction in blood flow. *J. Comput. Phys.*, 228(18):6916–6937, 2009.

[GHMP07] B.E. Griffith, R.D. Hornung, D.M. McQueen, and C.S. Peskin. An adaptive, formally second order accurate version of the immersed boundary method. *J. Comput. Phys.*, 223(1):10–49, 2007.

[GK06] D. Garcia and L. Kadem. What do you mean by aortic valve area: Geometric orifice area, effective orifice area or Gorlin area? *J. Heart. Valve Dis.*, 15:601–608, 2006.

[GM98] C. Grandmont and Y. Maday. Nonconforming grids for the simulation of fluid-structure interaction. In *Domain decomposition methods, 10 (Boulder, CO, 1997)*, volume 218 of *Contemp. Math.*, pages 262–270. Amer. Math. Soc., Providence, RI, 1998.

[GM00] C. Grandmont and Y. Maday. Existence for an unsteady fluid-structure interaction problem. *M2AN Math. Model. Numer. Anal.*, 34(3):609–636, 2000.

[GMS06] J. L. Guermond, P. Minev, and J. Shen. An overview of projection methods for incompressible flows. *Comput. Methods Appl. Mech. Eng.*, 195(44-47):6011–6045, 2006.

[GPD+00] D. Garcia, P. Pibarot, J.G. Dumesnil, F. Sakr, and L.G. Durand. Assessment of aortic valve stenosis severity: A new index based on the energy loss concept. *Circulation*, 101:765–771, 2000.

[GPH+01] R. Glowinski, T.-W. Pan, T.I. Hesla, D.D. Joseph, and J. Périaux. A fictitious domain approach for the direct simulation of incompressible fluid flow past moving rigid bodies: Application to particulate flow. *J. Comput. Phys.*, 169:363–426, 2001.

[GPHJ99] R. Glowinski, T.W. Pan, T.I. Hesla, and D.D. Joseph. A distributed Lagrange mutiplier/fictitious domain method for particulate flows. *Int. J. Multiphas. Flow*, 25:755–794, 1999.

[GPP94] R. Glowinski, T.W. Pan, and J. Périaux. A fictitious domain method for Dirichlet problem and applications. *Comput. Methods Appl. Mech. Eng.*, 111(3-4):283–303, 1994.

[GQ98a] J.-L. Guermond and L. Quartapelle. On stability and convergence of projection methods based on pressure Poisson equation. *Int. J. Numer. Methods Fluids*, 26(9):1039–1053, 1998.

[GQ98b] J.-L. Guermond and L. Quartapelle. On the approximation of the unsteady Navier-Stokes equation by finite element projection methods. *Numer. Math.*, 80(2):207–238, 1998.

[Gra98] C. Grandmont. *Analyse mathématiques et numérique de quelques problèmes d'interaction fluid-structure*. PhD thesis, Université Pierre et Marie Curie, Paris VI, 1998.

[Gue96] J.-L. Guermond. Some implementation of projection methods for Navier-Stokes equations. *M2AN Math. Model. Numer. Anal.*, 30:637–667, 1996.

[GV03] J.-F. Gerbeau and M. Vidrascu. A quasi-Newton algorithm based on a reduced model for fluid-structure interactions problems in blood flows. *M2AN Math. Model. Num. Anal.*, 37(4):631–648, 2003.

[GVF05] J.-F. Gerbeau, M. Vidrascu, and P. Frey. Fluid-structure interaction in blood flows on geometries based on medical imaging. *Comp. & Struct.*, 83(2-3):155–165, 2005.

[Hal01] G. Haller. Distinguished material surfaces and coherent structures in three-dimensional fluid flows. *Phys. Nonlinear Phenom.*, 149(4):248–277, 2001.

[Han05] P. Hansbo. Nitsche's method for interface problems in computational mechanics. *GAMM-Mitt.*, 28(2):183–206, 2005.

[HASM93] M.W. Heinstein, S.W. Attaway, J.W. Swegle, and F.J. Mello. A general-purpose contact detection algorithm for nonlinear structural analysis code. Sandia Report, 1993.

[Hec] F. Hecht. *FreeFem++, Third Edition, Version 3.0-1. User's Manual.* LJLL, University of Paris VI.

[Hei04] M. Heil. An efficient solver for the fully coupled solution of large-displacement fluid-structure interaction problems. *Comput. Methods Appl. Mech. Eng.*, 193(1-2):1–23, 2004.

[HFB86] T.J.R. Hughes, L.P. Franca, and M. Balestra. A new finite element formulation for computational fluid dynamics: V. circumventing the Babuska-Brezzi condition : a stable Petrov-Galerkin formulation of the Stokes problem accommodating equal-order interpolations. *Comput. Methods Appl. Mech. Eng.*, 59:85–99, 1986.

[HGB85] J.O. Hallquist, G.L. Goudreau, and D.J. Benson. Sliding interfaces with contact-impact in large-scale Lagrangian computations. *Comput. Methods Appl. Mech. Eng.*, 51(1-3):107–137, 1985.

[HGS02] G.A. Holzapfel, T.C. Gasser, and M. Stadler. A structural model for the viscoelastic behavior of arterial walls: continuum formulation and finite element analysis. *Eur. J. Mech. Solid.*, 21(3):441–463, 2002.

[HH03] P. Hansbo and J. Hermansson. Nitsche's method for coupling non-matching meshes in fluid-structure vibration problems. *Comput. Mech.*, 32(1–2):134–139, 2003.

[HHS04] P. Hansbo, J. Hermansson, and T. Svedberg. Nitsche's method combined with space-time finite elements for ALE fluid-structure interaction problems. *Comput. Methods Appl. Mech. Eng.*, 193:4195–4206, 2004.

[Hil07] M. Hillairet. Lack of collision between solid bodies in a 2D incompressible viscous flow. *Comm. Part. Differ. Equat.*, 32(9):1345–1372, 2007.

[HLZ81] T.J.R. Hughes, W.K Liu, and T.K. Zimmermann. Lagrangian-eulerian finite element formulation for incompressible viscous flows. *Comput. Methods Appl. Mech. Eng.*, 29:329–349, 1981.

[HNP+06] D.R. Hose, A.J. Narracott, J.M.T. Penrose, D. Baguley, I.P. Jones, and P.V. Lawford. Fundamental mechanics of aortic heart valve closure. *J. Biomech.*, 39(5):958 – 967, 2006.

[Hor97] U. Hornung, editor. *Projection and Quasi-compressibility Methods for Solving the Incompressible Navier-Stokes Equations.* Springer-Verlag, New York, 1997.

[HPS03] P.J. Hunter, A.J. Pullan, and B.H. Smaill. Modeling Total Heart Function. *Annu. Rev. Biomed. Eng.*, 5(1):147–177, 2003.

[HR90] J.G. Heywood and R. Rannacher. Finite-element approximations of the nonstationary Navier-Stokes problem. Part IV: error estimates for second-order time discretization. *SIAM J. Numer. Anal.*, 27(2):353–384, 1990.

[JDS96] Z. Jianhai, C. Dapeng, and Z. Shengquan. ALE finite element analysis of the opening and closing process of the artificial mechanical valve. *Appl. Math. Mech.*, 17(5):403–412, 1996.

[JL06] E. Jung and W. Lee. Lumped parameter models of cardiovascular circulation in normal and arrhythmia cases. *J. Kor. Math. Soc.*, 43(4):885–897, 2006.

[Ken79] D.E. Kenyon. A mathematical model of water flux through aortic tissue. *Bull. Math. Biol.*, 41(1):79–90, 1979.

[KGF+09] U. Küttler, M. Gee, C. Förster, A. Comerford, and W.A. Wall. Coupling strategies for biomedical fluid-structure interaction problems. *Comm. Numer. Meth. Eng.*, 2009. DOI: 10.1002/cnm.1281.

[KGZG85] D.N. Ku, D.P. Giddens, C.K. Zarins, and S. Glagov. Pulsatile flow and atherosclerosis in the human carotid bifurcation: positive correlation between plaque location and low and oscillating shear-stress. *Arteriosclerosis*, 5(3):293–302, 1985.

[KL96] D.N. Kenwright and D.A. Lane. Interactive time-dependent particle tracing using tetrahedral decomposition. *IEEE Trans. Visual. Comput. Graph.*, 2(2):120–129, 1996.

[Kla95] A. Klarbring. Large displacement frictional contact: a continuum framework for finite element discretization. *Eur. J. Mech. Solid.*, 14(2):237–253, 1995.

[KMP01] S.J. Kovács, D.M. McQueen, and C.S. Peskin. Modelling cardiac fluid dynamics and diastolic function. *Phil. Trans. R. Soc. Lond. A*, 359:1299–1314, 2001.

[KO88] N. Kikuchi and J.T. Oden. *Contact problems in elasticity: a study of variational inequalities and finite element methods*, volume 8 of *SIAM Studies in Applied Mathematics*. Society for Industrial and Applied Mathematics (SIAM), Philadelphia, PA, 1988.

[KS06] T. Korakianitis and Y. Shi. A concentrated parameter model for the human cardiovascular system including heart valve dynamics and atrioventricular interaction. *Med. Eng. Phys.*, 28:613–628, 2006.

[Lau92] T.A. Laursen. Formulation and treatment of frictional contact problems using finite elements. *SUDAM Report*, 92(6), 1992.

[Lau02] T.A. Laursen. *Computational contact and impact mechanics. Fundamentals of modeling interfacial phenomena in nonlinear finite element analysis*. Springer-Verlag, Berlin, 2002.

[LBMZ08] P. Libby, R. Bonow, D.L. Mann, and D.P. Zipes. *Braunwald's Heart Disease: a textbook of cardiovascular medicine.* WB Saunders Company, 2008.

[Lio69] J.-L. Lions. *Quelques méthodes de résolution des problèmes aux limites non linéaires.* Dunod, 1969.

[LS93] T.A. Laursen and J.C. Simo. A continuum-based finite element formulation for the implicit solution of multibody, large deformation frictional contact problems. *Int. J. Numer. Meth. Eng.*, 36(20):3451–3485, 1993.

[LSM07] F. Lekien, S.C. Shadden, and J.E. Marsden. Lagrangian coherent structures in n-dimensional systems. *J. Math. Phys.*, 48(6):065404, 2007.

[LTM00] P. Le Tallec and S. Mani. Numerical analysis of a linearised fluid-structure interaction problem. *Numer. Math.*, 87(2):317–354, 2000.

[LTM01] P. Le Tallec and J. Mouro. Fluid structure interaction with large structural displacements. *Comput. Methods Appl. Mech. Eng.*, 190:3039–3067, 2001.

[MÖ9] J.-D. Müller. Heart valve fluid-structure interaction using weak coupling. In P Nithiarasu, R Löhner, and R. van Loon, editors, *CMBE09.* Wiley, 2009.

[MB05] B.H. Maines and C.E. Brennen. Lumped parameter model for computing the minimum pressure during mechanical heart valve closure. *J. Biomech. Eng.*, 127:648–655, 2005.

[Moi08] Ph. Moireau. *Filtering based data assimilation for second order hyperbolic PDE. Applications in cardiac mechanics.* PhD thesis, Ecole Polytechnique, 2008.

[MP00] D.M. McQueen and C.S. Peskin. A three-dimensional computer model of the human heart for studying cardiac fluid dynamics. *ACM SIGGRAPH Computer Graphics*, 34(1):56–60, 2000.

[MP01] D.M. McQueen and C.S. Peskin. Heart simulation by an immersed boundary method with formal second-order accuracy and reduced numerical viscosity. In H. Aref and J.W. Phillips, editors, *Mechanics for a New Mellennium*, 2001.

[MPY82] D.M. McQueen, C.S. Peskin, and E.L. Yellin. Fluid dynamics of the mitral valve: physiological aspects of a mathematical model. *Am. J. Physiol. - Heart Circ. Physiol.*, 242(6):1095–1110, 1982.

[MS02] H.G. Matthies and J. Steindorf. Partitioned but strongly coupled iteration schemes for nonlinear fluid-structure interaction. *Comp. & Struct.*, 80(27–30):1991–1999, 2002.

[MS03] H.G. Matthies and J. Steindorf. Partitioned strong coupling algorithms for fluid-structure interaction. *Comp. & Struct.*, 81:805–812, 2003.

[MvBdB05] C. Michler, E.H. van Brummelen, and R. de Borst. An interface Newton-Krylov solver for fluid-structure interaction. *Int. J. Numer. Methods Fluids*, 47(10-11):1189–1195, 2005.

[MWR99] D. P. Mok, W.A. Wall, and E. Ramm. Partitioned analysis approach for the transient, coupled response of viscous fluids and flexible structures. In W. Wunderlich, editor, *Proceedings of the European Conference on Computational Mechanics*. ECCM'99, TU Munich, 1999.

[MWR01] D.P. Mok, W.A. Wall, and E. Ramm. Accelerated iterative substructuring schemes for instationary fluid-structure interaction. In K.J. Bathe, editor, *Computational Fluid and Solid Mechanics*, pages 1325–1328. Elsevier, 2001.

[MXA+] Ph. Moireau, N. Xiao, M. Astorino, C.A. Figueroa, D. Chapelle, C.A. Taylor, and J.-F. Gerbeau. External tissue support and fluid-structure simulation in blood flows. In preparation.

[MYWS07] Y.S. Morsi, W.W. Yang, C.S Wong, and Das S. Transient fluid-structure coupling for simulation of a trileaflet heart valve using weak coupling. *J. Artif. Organs*, 10:96–103, 2007.

[NH00] M.P. Nash and P.J. Hunter. Computational mechanics of the heart. *J. Elasticity*, 61(1):113–141, 2000.

[Nit71] J. Nitsche. Über ein Variationsprinzip zur Lösung von Dirichlet-Problemen bei Verwendung von Teilräumen, die keinen Randbedingungen unterworfen sind. *Abh. Math. Sem. Univ. Hamburg*, 36:9–15, 1971.

[Nob01] F. Nobile. *Numerical approximation of fluid-structure interaction problems with application to haemodynamics.* PhD thesis, EPFL, Switzerland, 2001.

[NV08] F. Nobile and C. Vergara. An effective fluid-structure interaction formulation for vascular dynamics by generalized Robin conditions. *SIAM J. Sci. Comput.*, 30(2):731–763, 2008.

[NWY06] M. Nakamura, S. Wada, and T. Yamaguchi. Influence of the opening mode of the mitral valve orifice on intraventricular hemodynamics. *Ann. Biomed. Eng.*, 34(6):927–935, 2006.

[Pan08] O. Pantz. A frictionless contact algorithm for deformable bodies. SIAM preprint CMAP, Ecole Polytechnique, R.I. 647, 2008.

[Pes02] C.S. Peskin. The immersed boundary method. *Acta numerica*, 11:479–519, 2002.

[PFL95] S. Piperno, C. Farhat, and B. Larrouturou. Partitioned procedures for the transient solution of coupled aeroelastic problems. Part I: Model problem, theory and two-dimensional application. *Comput. Methods Appl. Mech. Eng.*, 124:79–112, 1995.

[PSH07] V. Prot, B. Skallerud, and G.A. Holzapfel. Transversely isotropic membrane shells with application to mitral valve mechanics. constitutive modeling and finite element implementation. *Int. J. Numer. Meth. Eng.*, 71(8):987–1008, 2007.

[QQ07] A. Quaini and A. Quarteroni. A semi-implicit approach for fluid-structure interaction based on an algebraic fractional step method. *Math. Model. Methods Appl. Sci.*, 17(6):957–983, 2007.

[Qua08] A. Quaini. *Algorithms for fluid-structure interaction problems arising in hemodynamics*. PhD thesis, EPFL, Switzerland, 2008.

[QV97] A. Quarteroni and A. Valli. *Numerical Approximation of Partial Differential equations*. Springer, 1997.

[QV99] A. Quarteroni and A. Valli. *Domain decomposition methods for partial differential equations*. Numerical Mathematics and Scientific Computation. The Clarendon Press Oxford University Press, 1999. Oxford Science Publications.

[Ran91] R. Rannacher. On Chorin's projection method for the incompressible Navier-Stokes equations. *Lect. Notes Math.*, 1530:167–183, 1991.

[RBM+06] A. Ranga, O. Bouchot, R. Mongrain, P. Ugolini, and C. Raymond. Computational simulations of the aortic valve validated by imaging data: evaluation of valve-sparing techniques. *Interact. Cardiovasc. Thorac. Surg.*, 5:373–378, 2006.

[RCMC86] K.L. Richards, S.R. Cannon, J.F. Miller, and M.H. Creawford. Calculation of aortic valve area by doppler echocardiography: A direct application of the continuity equation. *Circulation*, 73:964–969, 1986.

[RRLJ01] P. Råback, J. Ruokolainen, M. Lyly, and E. Järvinen. Fluid-structure interaction boundary conditions by artificial compressibility. In *EC-COMAS Computational Fluid Dynamics Conference, Swansea, UK*, 2001.

[RT83] P.A. Raviart and J.M. Thomas. *Introduction à l'Analyse Numérique des Equations aux Dérivées Partielles.* Masson, Paris, 1983.

[Sac04] F.B. Sachse. *Computational Cardiology, Modeling of Anatomy, Electrophysiology, and Mechanics*, volume 2966 of *Lecture Notes in Computer Science.* Springer, 2004.

[Sam12] D.W. Samways. The genesis of the dicrotic pulse wave. *Br. Med. J.*, pages 774–775, 1912.

[SB05] F. Sotiropoulos and I. Borazjani. Flow in prosthetic heart valves: state-of-the-art and future directions. *Ann. Biomed. Eng.*, 33(12):1689–1694, 2005.

[SB09] F. Sotiropoulos and I. Borazjani. A review of the state-of -the-art numerical methods for simulating flow through mechanical heart valves. *Med. Biol. Eng. Comput.*, 47:245–256, 2009.

[SC74] W.M. Swanson and R.E. Clark. Dimensions and geometric relationships of the human aortic value as a function of pressure. *Circ. Res.*, 35(6):871, 1974.

[SDM06] S.C. Shadden, J.O. Dabiri, and J.E. Marsden. Lagrangian analysis of fluid transport in empirical vortex ring flows. *Phys. Fluids*, 18(4):047105, 2006.

[SFCLT05] A.-V. Salsac, M.A. Fernández, J.M. Chomaz, and P. Le Tallec. Effects of the flexibility of the arterial wall on the wall shear stresses and wall tension in abdominal aortic aneurysms. In *Bull. Am. Phys. Soc.*, 2005.

[SH06] H. Schmid and P.J. Hunter. Biomechanical modelling at the molecular, cellular, and tissue levels. Lectures Notes – 14th CISM-IUTAM Summer School, 2006.

[Sha06] S.C. Shadden. *A dynamical systems approach to unsteady systems.* PhD thesis, California Institute of Technology, 2006.

[She92] J. Shen. On error estimates of projection methods for the navier-stokes equations: First-order schemes. *SIAM J. Numer. Anal.*, 29:55–77, 1992.

[SLM05] S.C. Shadden, F. Lekien, and J.E. Marsden. Definition and properties of Lagrangian coherent structures from finite-time Lyapunov exponents in two-dimensional aperiodic flows. *Phys. Nonlinear Phenom.*, 212(3-4):271–304, 2005.

[SM08] S. Soyibou and C.M. Murea. A stable time advancing scheme for solving fluid-structure interaction problem at small structural displacements. *Comput. Methods Appl. Mech. Eng.*, 198(2):210–222, 2008.

[SMCCS06] J. Sainte-Marie, D. Chapelle, R. Cimrman, and M. Sorine. Modeling and estimation of the cardiac electromechanical activity. *Comp. & Struct.*, 84:1743–1759, 2006.

[SSCL06] A.-V. Salsac, S.R. Sparks, J.M. Chomaz, and J.C. Lasheras. Evolution of the wall shear stresses during the progressive enlargement of symmetric abdominal aortic aneurysms. *J. Fluid Mech.*, 550:19–51, 2006.

[SSG+04] G. Szabò, D. Soans, A. Graf, C.J. Beller, L. Waite, and S. Hagl. A new computer model of mitral valve hemodynamics during ventricular filling. *Eur. J. Cardio. Thorac. Surg.*, 26:239–247, 2004.

[SSW+03] P. Segers, N. Stergiopulos, N. Westerhof, P. Wouters, P. Kolh, and P. Verdonck. Systemic and pulmonary hemodynamics assessed with a lumped-parameter heart-arterial interaction model. *J. Eng. Math.*, 47(3):185–199, 2003.

[ST08] S.C. Shadden and C.A. Taylor. Characterization of coherent structures in the cardiovascular system. *Ann. Biomed. Eng.*, 36(7):1152–1162, 2008.

[Tak02] T. Takahashi. *Analyse des équations modélisant le mouvement des systémes couplant des solides rigides et des fluides visqueux.* PhD thesis, Université Henri Poincaré - Nancy I, 2002.

[TBL92] T.E. Tezduyar, M. Behr, and J. Liou. A new strategy for finite element computations involving moving boundaries and interfaces - the deforming-spatial-domain/space-time procedure: I. the concept and the preliminary numerical tests. *Comput. Methods Appl. Mech. Eng.*, 94:339–351, 1992.

[Tem68] R. Temam. Une méthode d'approximation de la solution des équations de Navier-Stokes. *Bull. Soc. Math. France*, 96:115–152, 1968.

[Tez01] T.E. Tezduyar. Finite element methods for fluid dynamics with moving boundaries and interfaces. *Arch. Comput. Meth. Eng.*, 8:83–130, 2001.

[TF09] C.A. Taylor and C.A. Figueroa. Patient-Specific Modeling of Cardiovascular Mechanics. *Annu. Rev. Biomed. Eng.*, 11:109–134, 2009.

[Thi08a] M. Thiriet. *Biology and Mechanics of Blood Flows, Part I: Biology.* Springer, New York, 2008.

[Thi08b] M. Thiriet. *Biology and Mechanics of Blood Flows, Part II: Mechanics and Medical Aspects of Blood Flows.* Springer, New York, 2008.

[Tho06] V. Thomée. *Galerkin finite element methods for parabolic problems*, volume 25 of *Springer Series in Computational Mathematics*. Springer-Verlag, Berlin, second edition, 2006.

[Thu90] M. Thubrikar. *The aortic valve*. Informa HealthCare, 1990.

[TOK+06] R. Torii, M. Oshima, T. Kobayashi, K. Takagi, and T.E. Tezduyar. Computer Modeling of Cardiovascular Fluid-Structure Interactions with the Deforming-Spatial-Domain/Stabilized Space-Time Formulation. *Comput. Methods Appl. Mech. Eng.*, 70:1885–1895, 2006.

[TOK+08] R. Torii, M. Oshima, T. Kobayashi, K. Takagi, and T.E. Tezduyar. Fluid–structure interaction modeling of a patient-specific cerebral aneurysm: influence of structural modeling. *Comput. Mech.*, 43(1):151–159, 2008.

[Tra06] T.-D. Tran. Construction d'un modéle 3d comprenant les sinus de valsalva, la valve aortique et l'arche aortique. Master's thesis, École Polytechnique Montreal, 2006.

[TS07] T.E. Tezduyar and S. Sathe. Modeling of Fluid-Structure Interactions with the Space-Time Finite Elements: Solution Techniques. *Int. J. Numer. Methods Fluids*, 54:855–900, 2007.

[TV96] L. Tobiska and R. Verfürth. Analysis of a streamline diffusion finite element method for the Stokes and Navier-Stokes equations. *SIAM J. Numer. Anal.*, 33(1):107–127, 1996.

[VC06] I.E. Vignon-Clementel. *A Coupled Multidomain Method for Computational Modeling of Blood Flow*. PhD thesis, Department of Mechanical Engineering, Stanford University, 2006.

[VCMP08] E.J. Vigmond, C. Clements, D.M. McQueen, and C.S. Peskin. Effect of bundle branch block on cardiac output: A whole heart simulation study. *Prog. Biophys. Mol. Biol.*, 97(2-3):520–542, 2008.

[VD03] R.P. Vito and S.A. Dixon. Blood Vessel Constitutive Models. *Annu. Rev. Biomed. Eng.*, 5:413–439, 2003.

[Vid08] M. Vidrascu. Shell based robust numerical procedures for the solution of real-life problems. In *WCCM8 - ECCOMAS08 Conference Proceedings*, 2008.

[vL05] R. van Loon. *A 3D method for modelling the fluid-structure interaction of heart valves.* PhD thesis, Eindhoven University of Technology, 2005.

[vL09] R. van Loon. Towards computational modelling of aortic stenosis. *Comm. Numer. Meth. Eng.*, 2009.

[vLADB04] R. van Loon, P.D. Anderson, J. De Hart, and F.P.T. Baaijens. A combined fictitious domain/adaptative meshing method for fluid-structure interaction in heart valves. *Int. J. Numer. Methods Fluids*, 46:533–544, 2004.

[vLAvdV06] R. van Loon, P.D. Anderson, and F.N. van de Vosse. A fluid-structure interaction method with solid-rigid contact for heart valve dynamics. *J. Comput. Phys.*, 217(2):806–823, 2006.

[VVA+00] A.I. Veress, D.G. Vince, P.M. Anderson, J.F. Cornhill, E.E. Herderick, J.D. Klingensmith, B.D. Kuban, N.L. Greenberg, and J.D. Thomas. Vascular mechanics of the coronary artery. *Z. Kardiol.*, 89(14):92–100, 2000.

[WH99] J.Z. Wu and W. Herzog. Modelling concentric contraction of muscle using an improved cross-bridge model. *J. Biomech.*, 32(8):837–848, 1999.

[WHS+02] H. Watanabe, T. Hisada, S. Sugiura, J. Okada, and H. Fukunari. Computer simulation of blood flow, left ventricular wall motion and their interrelationship by fluid-structure interaction finite element method. *JSME International Journal Series C*, 45(4):1003–1012, 2002.

[WK99] D.M. Wootton and D.N. Ku. Fluid mechanics of vascular systems, diseases, and thrombosis. *Annu. Rev. Biomed. Eng.*, 1:299–329, 1999.

[WKM05] E.J. Weinberg and M.R. Kaazempur Mofrad. On the constitutive models for heart valve leaflet mechanics. *Cardiovasc. Eng.*, 5(1):37–43, 2005.

[WKM07a] E.J. Weinberg and M.R. Kaazempur Mofrad. A finite shell element for heart mitral valve leaflet mechanics, with large deformations and 3D constitutive material model. *J. Biomech.*, 40(3):705–711, 2007.

[WKM07b] E.J. Weinberg and M.R. Kaazempur Mofrad. Transient, three-dimensional, multiscale simulation of the human aortic valves. *Cardiovasc. Eng.*, 7(4):140–155, 2007.

[WKM08] E.J. Weinberg and M.R. Kaazempur Mofrad. A multiscale computational comparison of the bicuspid and tricuspid aortic valves in relation to calcific aortic stenosis. *J. Biomech.*, 41:3482–3487, 2008.

[WLY+08] P.N. Watton, X.Y. Luo, M. Yin, G.M. Bernacca, and D.J. Wheatley. Effect of ventricle motion on the dynamic behaviour of chorded mitral valves. *J. Fluids Struct.*, 24(1):58–74, 2008.

[Wri95] P. Wriggers. Finite element algorithms for contact problems. *Arch. Comput. Meth. Eng.*, 2(4):1–49, 1995.

[Wri02] P. Wriggers. *Computational Contact Mechanics.* J. Wiley & Sons, New York, 2002.

[WSKH04] H. Watanabe, S. Sugiura, H. Kafuku, and T. Hisada. Multiphysics simulation of left ventricular filling dynamics using fluid-structure interaction finite element method. *Biophys. J.*, 87(3):2074–2085, 2004.

[XCS+09] Z. Xu, N. Chen, S.C. Shadden, J.E. Marsden, M.M. Kamocka, E.D. Rosen, and M. Alber. Study of blood flow impact on growth of thrombi using a multiscale model. *Soft Matter*, 5:769–779, 2009.

[Yeo89] G.F. Yeo. *A manual of physiology.* P. Blakiston, Son & Co., 1889.

[YG08] F. Yilmaz and M.Y. Gundogdu. A critical review on blood flow in large arteries; relevance to blood rheology, viscosity models, and physiologic conditions. *Korea-Aust. Rheol. J.*, 20(4):197–211, 2008.

[Yu05] Z. Yu. A DLM/FD method for fluid/flexible-body interactions. *J. Comput. Phys.*, 207(1):1–27, 2005.

[Zem09] N. Zemzemi. *Etude Théorique et Numérique de l'activité électrique du coeur: Applications aux Électrocardiogrammes.* PhD thesis, Université Paris-Sud, Paris XI, 2009.

[ZZJ+03] H. Zhang, X. Zhang, S. Ji, Y. Guo, G. Ledezma, N. Elabbasi, and H. deCougny. Recent development of fluid-structure interaction capabilities in the ADINA system. *Comp. & Struct.*, 81(8–11):1071–1085, 2003.